

See discussions, stats, and author profiles for this publication at: <https://www.researchgate.net/publication/350098972>

Practical Magnetic and Electromechanical Design

Book · September 2020

CITATION

1

READS

230

1 author:



Mark Juds
MAJ Engineering LLC
13 PUBLICATIONS 112 CITATIONS

[SEE PROFILE](#)

Some of the authors of this publication are also working on these related projects:

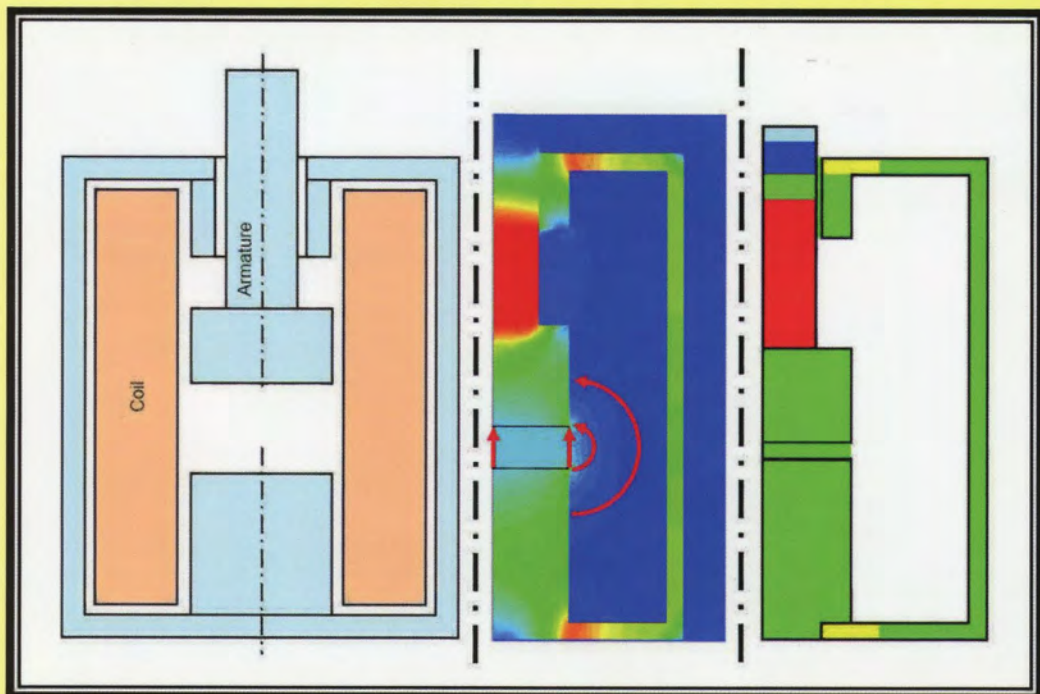
 DC Circuit Breaker [View project](#)

 Motor Soft Starter [View project](#)

Practical Magnetic and Electromechanical Design

Solenoids, Actuators, Transformers, Inductors

“If I were a flux line, where would I go?”



Mark A. Juds

This Book is About

- Developing an intuitive understanding of the magnetic fields in solenoids, actuators, transformers, inductors, sensors, and materials.
- Showing that, armed only with a spreadsheet, one can quickly and accurately evaluate a wide array of magnetic designs that are consistent with finite element simulations and prototype tests.

Praise for the Book

Practical Magnetic and Electromechanical Design

“Mark’s experience and technical competencies make him an endangered species; it is absolutely critical to document his vast knowledge and share it with the technical community in advanced magnetics design and research. Mark’s book is a must-read for younger and experienced technologists who need to better understand the intricacies of Mechanisms, Electricity, and Magnetism concepts.” **Antonio Trujillo**, Global Technology Director, Power Systems Technologies, Eaton Research Labs.

“Scientists, Engineers, Inventors, and Educators will find Mark’s latest work on magnetics, extraordinary. Mark Juds has a natural talent for teaching. His book is comprehensive yet easy to understand and practical to apply. From basic to advanced magnetics, Mark’s *“Practical Magnetic and Electromechanical Design”*, is a seminal work. Research and Engineering managers will find this work essential to all magnetic designs and inventions. It is the “Go to” book for magnetics. Educators and students will find a straight clear path to understanding the field of magnetics.” **Jerome Hastings**, President, Electric Power Management Consulting, Division Engineering Manager Eaton – Retired.

“This book is a very valuable aid to designers of electromechanical devices. It focuses on calculations of magnetic fields via the reluctance method, which can be implemented on computer spreadsheets.” **Dr. John Brauer**, Adjunct Professor, Department of Electrical Engineering and Computer Science, Milwaukee School of Engineering.

- - More Testimonials Inside - -

ISBN 978-1-09833-355-3



9 781098 333553

Practical Magnetic and Electromechanical Design

Solenoids, Actuators, Transformers, Inductors

“If I were a flux line, where would I go?”

Mark A. Juds

MAJ Engineering, LLC
markajuds@ieee.org
New Berlin, Wisconsin

This book is available at Book Baby as well as other sources ...
<https://store.bookbaby.com/book/practical-magnetic-and-electromechanical-design>

Practical Magnetic and Electromechanical Design

Copyright © 2020 Mark A. Juds

No part of this publication may be reproduced, stored in a retrieval system or transmitted in any form or by any means, electronic, mechanical, photocopying, recording, scanning or otherwise, except as permitted under Section 107 or 108 of the 1976 United States Copyright Act, without written permission of the author and publisher (markajuds@ieee.org).

Limit of Liability/Disclaimer of Warranty: While the author has used the best efforts in preparing this book, no representations or warranties are made with respect to the accuracy or completeness of the contents of this book and specifically disclaim any implied warranties of merchantability or fitness for a particular purpose. No warranty may be created or extended by sales representatives or written sales materials. The advice and strategies contained herein may not be suitable for your situation. You should consult with a professional where appropriate. The author and publisher shall not be liable for any loss of profit or any other commercial damages, including but not limited to special, incidental, consequential, or other damages.

ISBN: 978-1-09833-355-3

Printed in the USA by BookBaby (www.BookBaby.com)

Contents

Preface	7
1. Magnetic Fundamentals.....	11
a. Visualizing Magnetic Flux Lines	11
b. Magnetic System – Circuit Theory	14
c. Material Properties	16
d. System Properties	17
e. DC vs AC – Voltage vs Current.....	18
f. Air Flux Paths.....	23
g. Permeance of Air Flux Paths	24
h. Leakage Flux Paths	29
i. Parasitic Inductance and Capacitance	31
j. Example-1 – Solid Core.....	33
2. Magnetic Forces.....	35
a. Energy and Force	35
b. Normal Force	37
c. Tangential Force	41
d. Pole Shaping	42
e. Lorentz Force	43
f. Magnetic Actuator Configurations	44
g. Actuator Technologies	50
h. Example-2 – Gapped Core.....	51
i. Example-3 – Effect of Permeability	56
3. Magnetic Materials.....	57
a. Basics – Soft and Hard Materials	57
b. Soft Magnetic Materials.....	59
c. Curie Temperature	61
d. Effect of Alloying Elements	62
e. BH Curve – 3-Factor Curve Fit	64
f. Hard Magnetic Materials	67
g. Permanent Magnet Performance	71
h. Losses, Eddy Currents, Skin Effect	75
i. Imaginary Permeability and Loss Tangent	79
j. Permanent Magnet Model – Magnetic Moment	81
k. Example-4 – PM Model.....	84
4. Coil Design	89
a. Wire Resistivity and Size	89
b. DC Coil.....	91
c. AC Coil	92
d. Copper Area Ratio Method	94
e. Coil Design Trade-Offs.....	95
f. Example-5 – DC Coil Design	97
g. Example-6 – AC Coil Design	99
5. Temperature Rise	101
a. Steady-State Heat Transfer	101

b. Transient Heat Transfer	105
c. Magnet Wire Insulation Life	108
d. Example-7 – DC Coil Temperature	109
- Still Air (No Fan) (natural or free convection).....	109
- Moving Air (With a Fan) (forced convection)	111
e. Example-8 – AC Coil Temperature	112
- Still Air (No Fan) (natural or free convection).....	113
- Moving Air (With a Fan) (forced convection)	113
6. Solenoid Design and Pole Shaping	115
a. Simplified Solenoid Geometry.....	115
b. Solenoid Flux Paths	116
c. Reluctance Network	116
d. Estimated Armature Cross Section	118
e. Magnetic Calculations, Linear Model.....	119
f. Comparison of Analysis Methods	122
g. Pole Shaping	125
7. Solenoid Pull-In Dynamics.....	129
a. Mechanical Dynamics.....	129
b. DC Circuit and Motion Dynamics	130
c. Capacitor and Motion Dynamics.....	133
8. Rectification and Shading	137
a. Rectified AC Electromagnets.....	137
b. Shaded Pole AC Electromagnets	140
9. Transformer, Inductors	147
a. Transformer (No Leakage).....	147
b. Special Cases (No Leakage)	149
- Inductor	150
- Current Transformer (CT)	150
- Rogowski Coil.....	151
- Ideal Current Transformer (Ideal CT)	151
c. Transformer (with Leakage).....	153
d. Core-Type, Shell-Type, and Leakage	155
e. Core Loss (with Leakage)	160
f. Performance Charts (with Leakage)	166
g. Example-9 – Inductor Design	173
10. BH Curve Measurement	183
a. Basic Test Characteristics	183
b. Ring Sample.....	185
c. Examples – Core-Type Transformer.....	186
11. Air Core Inductor	189
a. Air Core Coil Geometry	189
b. Ansys Maxwell Simulation Results	189
c. Accurate Wide Range Correlation	190
d. Other Air-Core Correlations	191
12. Forces on Permanent Magnets and Coils	195

a. Biot-Savart Law	196
- Circular Loop Flux Density.....	197
- Air-Core Coil Inductance	197
b. Torque on a Magnetic Moment.....	198
c. Force on a Magnetic Moment	199
13. Slot Motor.....	201
a. Reverse Loop Conductors	201
b. Reverse Loop with Slot Motor.....	202
c. Slot Motor Saturation.....	205
d. Example-10 – Slot Motor Force.....	206
e. Contact Forces and Constriction	208
f. Slot Motor Configuration Options.....	210
14. Thomson Coil.....	211
a. Flux Paths, Permeance, Inductance.....	213
b. System Model Equations	216
- Approximate Formulae for Verification.....	219
c. Solutions and Results	223
- Comparison to Linear RLC System	226
- Effect of Mechanical Motion.....	226
d. Comparison to FEA and Testing.....	227
15. Magnetic Field Sensors.....	231
a. Variable Inductor and Transformer.....	231
b. CT, Rogowski Coil, Search Coil.....	231
c. Wiegand Wire	233
d. Hall Sensor.....	234
e. SQUID	235
f. Fluxgate	235
g. Magnetoimpedance (MI)	237
h. Magnetoresistance (MR or AMR)	238
i. Giant Magnetoresistance (GMR)	238
j. Other MR (TMR, CMR, BMR, EMR)	239
Appendix-A: Constants	241
Appendix-B: Units	242
Appendix-C: Electrical & Thermal Material Properties	245
Appendix-D: Soft Magnetic Materials	246
Appendix-E: BH Curve Fit	247
Appendix-F: Hard-Magnetic Permanent Magnet Materials	248
Appendix-G: Low Core Loss Magnetic Materials	249
Appendix-H: Wire Insulation	255
Appendix-I: Magnet Wire.....	256
Appendix-J: Summary of Physics Equations	258
Appendix-K: Range of Magnetic Field Values.....	260

References	261
Index	264
About the Author.....	270
More Praise for the Book	271

Preface

This book is written for students and practicing engineers involved in the design of magnetic and electromechanical devices. The material presented is a compilation of the practical approaches used over the author's 37-year career at Eaton Research Labs and is intended to help the reader gain a "feel" for locations and strengths of magnetic fields and an intuitive insight into what magnetic fields do and how to use them. This book makes magnetics easy to understand and practical to apply in magnetic research, experimentation, and analysis of magnetic fields encountered in engineering challenges.

Accurate and reliable methods are presented for the design of magnetic sensors, actuators, controls, and other electromechanical devices with the notable exclusion of rotating machines that are well covered by various authors and courses in university Electrical Engineering departments. Actuators, solenoids, and magnetic sensors have been around in various forms for over a century, and they are critical components of control and protection systems including relays and circuit breakers.

This book has a strong foundation in the methods developed by H. C. Roters [1] with additional topics in the areas of permanent magnet materials and permanent magnet performance in particular. The methodologies also take full advantage of complex spreadsheet capabilities, as well as finite element analysis as a counterpart to the calculations. Design examples include calculations for losses and temperature rise, which are critical for all electromagnetic systems. The smallest design usually has the highest temperature rise. The best design usually considers the trade-off between size and temperature rise.

The author holds a bachelor's degree in mechanical engineering with specialties in dynamic systems, kinematics, strain energy, and numerical optimization, and a master's degree in heat transfer and fluid dynamics. He was a practicing engineer throughout his career. During the past 37 years, he focused on designing magnetic and electromechanical devices and was granted 123 US and foreign patents. This book reflects the practice-oriented perspective that benefits from many years in the development of practical calculations for numerous applications.

The design calculations presented are practical in the sense that they can be quickly and accurately applied in a spreadsheet model using the permeance method (also known as reluctance method or magnetic circuit method). The permeance method evaluates the magnetic field from the perspective of a magnetic circuit, analogous to an electric circuit. Chapter 1 describes this in detail and aims to provide an understanding of magnetic flux paths based on the simple question, "If I were a magnetic flux line, where would I go?" The permeance method is most accurately utilized by having a physical feeling or visualization of the magnetic flux. The accuracy of the permeance method is demonstrated with comparisons to measurements and finite element simulations.

Practical methods also address the issues of time and effort. Some ideas need only “feasibility” level accuracy, while other design-specific challenges require high-level accuracy. This relates directly to budget and schedule issues on engineering projects. Increased effort (model detail, complexity, size, time) is needed to achieve increased accuracy. The best strategic approach is to use a method that is quick and provides enough accuracy to make a valid design decision. A spectrum of calculation methods can be considered 1) a hand calculation, 2) a simple spreadsheet model, 3) a complex spreadsheet model, 4) a 2D or axisymmetric finite element model, 5) a 3D finite element model. A spreadsheet model can also be used to quickly determine the starting size for a finite element model.

A critical step for gaining confidence in the validity of any analysis is to check the results against those of a simple calculation. In general, when doing a complex analysis (such as a finite element simulation), the first step should be a simple calculation (such as a spreadsheet calculation) and a visualization of the magnetic field. The finite element simulation results can then be quickly reviewed for the shape of the magnetic field and the magnitude of the flux density, current and force, to judge if the results are reasonable. Finite element models have many input values and boundary conditions that are prone to typographical errors (such as a decimal point error, or a dimensional units error). Errors can be quickly detected when compared to a simple calculation and magnetic field visualization.

Chapter 2 discusses the mechanical force produced by actuators (reluctance force and Lorentz force), as a result of electromechanical energy conversion (the transfer of magnetic field energy into mechanical energy). The reluctance force is produced across an air gap. The Lorentz force is produced when a current interacts with a magnetic field.

Chapter 3 covers magnetic materials and highlights the relationship between magnetic properties (permeability, coercivity), crystal structure, and atomic spacing. Magnetic materials are critical in the performance of actuators and transformers. A lower saturation flux density limits the force and power output or requires larger parts. A lower magnetic permeability requires more coil current or a larger permanent magnet to achieve the desired magnetic flux. A higher coercivity increases losses and leads to issues involving remanent magnetic flux. Magnetic properties are directly affected by the material crystal structure and atomic spacing, which is dependent on the alloying elements and residual mechanical strain. Additional topics include soft magnetic materials, permanent magnets, skin effect, and losses due to hysteresis and eddy currents.

Chapters 4-8 address solenoid design, including coil design, coil temperature rise, solenoid dynamic performance, back EMF, and the use of rectification and shading to prevent zero flux and zero force in AC actuators.

Chapters 9 and 10 discuss transformers, inductors, inductive current sensors, core loss, and BH curve measurement. Transformer characteristics are presented for a simple transformer with no leakage, including the special cases of inductors and inductive current sensors. Characteristics are also

presented for a transformer with leakage, including the design trade-offs for leakage and core loss.

Chapters 11 and 12 cover the topics of air-core coil inductance, the Biot-Savart law, and the force between coils and permanent magnets. The inductance of an air-core coil is not trivial to calculate because the magnetic flux path in the air is not well defined. The Biot-Savart law makes it possible to calculate the magnetic field at any point in space due to a current. The force between permanent magnets and coils can be determined from the Lorentz force by using the magnetic moment characteristics of a permanent magnet with the Biot-Savart law or with the derivative of the mutual inductance.

High-speed actuators are discussed in chapters 13 and 14, including repulsion between current-carrying conductors and eddy currents, which are utilized in circuit breakers, slot motors, and Thomson coils. Circuit breakers use the repulsion effect of opposite currents in adjacent conductors to achieve fast opening electrical contacts at high current. A slot motor is a u-shaped magnetic material with a slot that encompasses the adjacent conductors and increases the magnetic field and the Lorentz force. A Thomson coil is an actuator based on the repulsion effect between the current in a coil and the induced eddy currents in an electrically conductive plate or ring. Chapter 15 gives a summary of magnetic field sensors, including position sensors and current sensors based on the magnetic field.

The visualization concepts in this book should empower the reader to contribute in a positive way to ideation discussions, where the best two responses to new ideas are, “Yes, that should work, and here are a couple thoughts on how to make it better,” and “That probably won’t work because of these issues, but if it’s modified in these ways it has a good chance to work.”

Thanks to my many colleagues at Eaton for their positive support, excellent discussions, and brilliant contributions on numerous projects (77 US patents with 92 colleagues and 46 European patents with 75 colleagues). Thanks to my mentors, Jim Bigelow, Jerome Hastings, and John Brauer for their encouragement and advice. Thanks also to my reviewers for their critical and meticulous evaluation and suggestions; Dr. John Brauer, Dr. Bruno Lequesne, Dr. Paul Ohodnicki Jr., Dr. Armen Baronian, Mary Jo VanderHeiden, Jerome Hastings, and Scott Juds.

markajuds@ieee.org
New Berlin, Wisconsin

Mark A. Juds
MAJ Engineering, LLC

1. Magnetic Fundamentals

This chapter describes the basic characteristics of magnetic flux (total magnetic field passing through a given area) and the calculation of the magnetic flux path permeance (the ease of carrying magnetic flux through a volume, analogous to electrical conductance). Permeance can often be accurately calculated when the magnetic flux paths can be visualized. The approach for visualizing magnetic flux paths is based on the simple question, “If I were a magnetic flux line, where would I go?”

a. Visualizing Magnetic Flux Lines

The RIGHT-HAND RULE (**Fig. 1.1.a**) is stated as follows for current in a wire: When pointing the Thumb of your Right Hand in the direction of the Current, your Fingers curl in the direction of the Magnetic Field.

Also, the RIGHT-HAND RULE (**Fig. 1.1.b**) can be stated as follows for current in a coil (or electromagnet): When curling the Fingers of your Right Hand in the direction of the Current, your Thumb points in the direction of the Magnetic Field.

The RIGHT-HAND RULE is based on the following conventions [6]:

- Current is the flow of positive charges from “+” to “-”
- Magnetic flux lines flow out from the “North” pole of a Compass Needle, or Permanent Magnet (PM), or Electromagnet

In **Fig. 1.2**, a current-carrying wire is shown passing through a plane covered in compass needles or small permanent

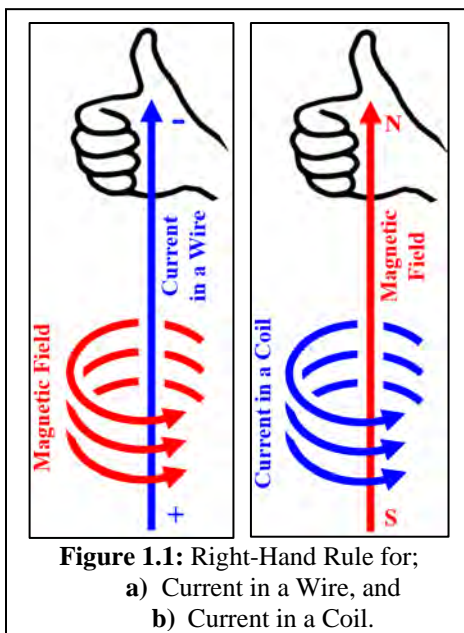


Figure 1.1: Right-Hand Rule for;
a) Current in a Wire, and
b) Current in a Coil.

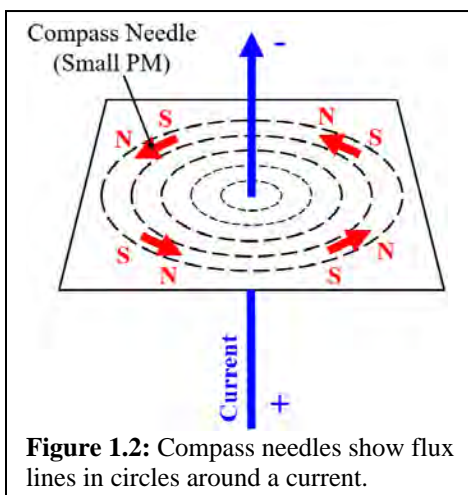


Figure 1.2: Compass needles show flux lines in circles around a current.

magnets (PM). The compass needles align to form circles around the wire. The magnetic field around a current-carrying wire is in the shape of circles centered on the wire in a plane perpendicular to the wire. This also shows that magnetic flux lines are continuous loops. They don't start and they don't end. When visualizing a magnetic field, it's important to look at the entire flux path (flux leaving and flux returning).

In **Fig. 1.3**, Magnetic flux lines flow out from the NORTH magnetic pole of a permanent magnet (this could also be an electromagnet as in **Fig. 1.1.b**), and they flow into the SOUTH magnetic pole. The magnetic flux lines don't stop or end, and they pass through the magnet from South to North forming closed loops.

A magnetic pole (N or S) can be visualized as a small region at each end of a permanent magnet or electromagnet (**Fig. 1.3**) where the flux lines converge. In high energy permanent magnets (such as NdFeB or SmCo), the distance between the poles is about 95% of the permanent magnet length. In low energy permanent magnets (such as AlNiCo), the distance between the poles is about 70% of the permanent magnet length.

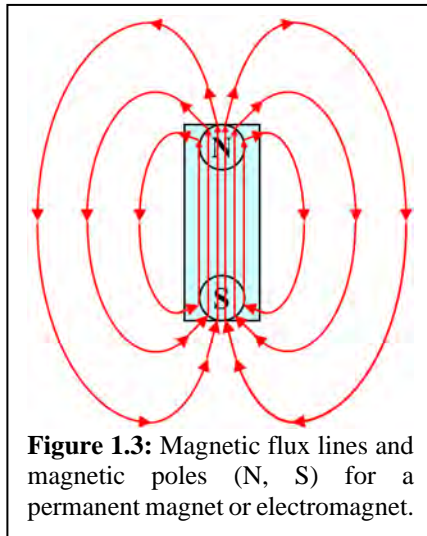
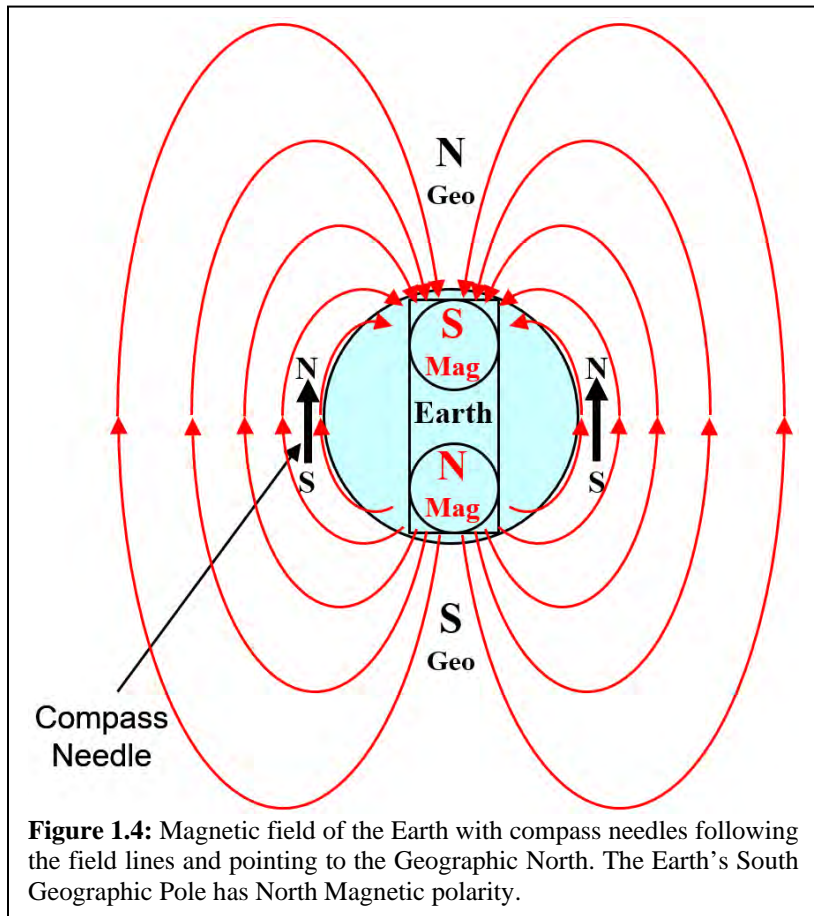


Figure 1.3: Magnetic flux lines and magnetic poles (N, S) for a permanent magnet or electromagnet.

The Earth's magnetic field is shown in **Fig. 1.4**, where the earth can be visualized as containing a large permanent magnet. Also, 2 compass needles are shown, where the NORTH magnetic pole of the compass needle points to the Earth's Geographic North Pole. Compass needles are permanent magnets that align with the Earth's magnetic field. The original compass materials were minerals such as lodestone or magnetite, which when suspended, would align with the earth's magnetic field and point toward the north. A lodestone is magnetized in the earth's magnetic field. Therefore, when the lodestone aligns with the earth's magnetic field, the north end of the lodestone will point toward the north. The discussion in **Ch. 12.b** describes the torque on a magnetic moment in a uniform magnetic field (such as the magnetic moment of a permanent magnet or a compass needle), which causes the compass needle to align with the earth's local magnetic field.

The north and south magnetic poles are depicted on the large internal permanent magnet (**Fig. 1.4**), as the representation of the earth's magnetic field source. As discussed for a permanent magnet in **Fig. 1.3**, the magnetic flux lines emerge from the NORTH Magnetic pole and return to the SOUTH Magnetic pole. Based on this convention for polarity, the Earth's SOUTH Geographic pole has a NORTH Magnetic polarity.

The earth's magnetic field is produced by the circulating flow of the liquid iron layer between the core and the crust. The liquid iron is not magnetic, because the temperature is well above the Curie temperature for iron. However, the iron is electrically conductive and it does carry ionic charges. The fluid flow within the liquid iron layer results in very large electric currents, which behave like an electromagnet to produce the earth's magnetic field. Therefore, the earth's magnetic field varies depending on the flow patterns and turbulence in the buoyancy-driven convective flow of the liquid iron layer. The earth's magnetic field varies relative to location and relative to time. There is also evidence indicating that the earth's magnetic field has flipped directions from time to time (the last time was about 780,000 years ago).



b. Magnetic System – Circuit Theory

The system performance equations for a magnetic field can be developed and visualized from the image in Fig. 1.5.

Fig. 1.5 shows an ampere-turn source (NI) pushing magnetic flux (ϕ) through a material that has a length (l) and cross-sectional area (a), and the magnetic flux flows from (N) to (S).

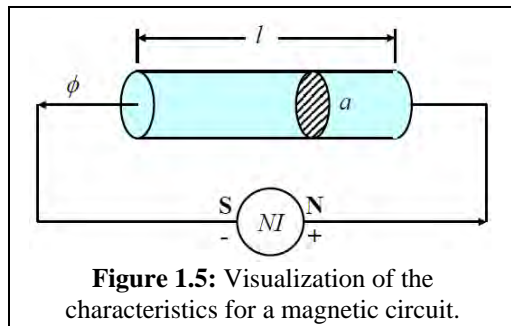


Figure 1.5: Visualization of the characteristics for a magnetic circuit.

The characteristics of a magnetic system are listed, as follows.

ϕ	=	Magnetic Flux
NI	=	Magnetizing Force, Magnetomotive Force, MMF
\mathcal{R}	=	Reluctance
P	=	Permeance
λ	=	Flux Linkage
L	=	Inductance

The physical characteristics for magnetic flux (reluctance, permeance, and magnetic ohm's law) are shown below with the analogous equivalent physical characteristics for electric current.

Magnetic Flux System		Electric Current System
Reluctance	$\mathcal{R} = \frac{NI}{\phi}$ (1.1)	Resistance $R_e = \frac{V}{I}$ (1.4)
Permeance	$P = \frac{1}{\mathcal{R}} = \frac{\phi}{NI}$ (1.2)	Conductance $G = \frac{1}{R_e} = \frac{I}{V}$ (1.5)
Mag. Ohm's Law	$NI = \phi \mathcal{R}$ (1.3)	Ohm's Law $V = I R_e$ (1.6)

In the magnetic flux system, it's the ampere-turns (NI) (a coil with several turns N and a current I) that acts as the source that pushes the flux (ϕ) through a reluctance (\mathcal{R}). Reluctance is the resistance of a material to the flow of magnetic flux. If a material has more reluctance, it will require more ampere-turns to push the same amount of flux through the material. In the electric current system, it's the voltage (V) that pushes the current (I) through a resistance (R_e). If a material has more resistance, it will require more voltage to push the same amount of current through the material.

Visualizing a magnetic system in this way helps to think of the magnetic flux as a closed-loop. Both the magnetic circuit and the electric circuit make a complete loop of flux and current.

The most unusual characteristic of magnetic fields is flux linkage (λ). There is nothing similar in any other area of physics. Flux linkage is shown in **Fig. 1.6**, where 6 turns (N) of a coil are linked with 10 Lines (10^{-7} Webers, **Appendix-B**) of magnetic flux (ϕ). The resulting flux linkage (λ) is:

$$\lambda = N\phi \text{ Wb-turns} \quad (1.7)$$

$$\lambda = 60 \text{ Line-turns}$$

$$\lambda = 6.0E-7 \text{ Weber-turns}$$

Inductance (L) is defined as the flux linkage (λ) per ampere of current (I).

Inductance	$L = \frac{\lambda}{I} = \frac{N\phi}{I}$	(1.8)
------------	---	-------

Flux Linkage	$\lambda = N\phi = LI$	(1.9)
--------------	------------------------	-------

Faraday's Law states that a coil voltage will produce a change in flux linkage, or a change in flux linkage will produce a voltage.

Faraday's Law	$V = \frac{d\lambda}{dt} = \frac{d(LI)}{dt} = \frac{d(N\phi)}{dt}$	(1.10)
---------------	--	--------

The last 2 terms in Faraday's Law (**Eq. 1.10**) can be expanded for a varying inductance or varying turns for actuators with moving armatures or coils and the chain rule can be applied to the derivatives of inductance and turns. The armature is a moveable ferromagnetic part of the magnetic circuit assembly.

$$V = \frac{d(LI)}{dt} = L \frac{dI}{dt} + I \frac{dL}{dt} = L \frac{dI}{dt} + I \frac{dL}{dx} \frac{dx}{dt} \quad (1.11)$$

$$V = \frac{d(N\phi)}{dt} = N \frac{d\phi}{dt} + \phi \frac{dN}{dt} = N \frac{d\phi}{dt} + \phi \frac{dN}{dx} \frac{dx}{dt} \quad (1.12)$$

Substituting the velocity of the armature ($v = dx/dt$) gives the velocity-dependent Back EMF (electromotive force, or voltage) as the 2nd term. The 1st term is the well-known relationship for inductors with constant inductance.

$V = \frac{d(LI)}{dt} = L \frac{dI}{dt} + vI \frac{dL}{dx}$	(1.13)
---	--------

$V = \frac{d(N\phi)}{dt} = N \frac{d\phi}{dt} + v\phi \frac{dN}{dx}$	(1.14)
--	--------

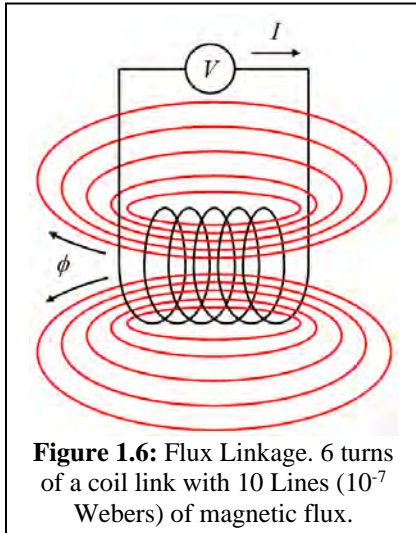


Figure 1.6: Flux Linkage. 6 turns of a coil link with 10 Lines (10^{-7} Webers) of magnetic flux.

c. Material Properties

The magnetization curve (B - H curve) characterizes the properties for magnetic materials, shown in **Fig. 1.7**. The vertical axis is the magnetic flux density (B), which is a measure of the magnetic flux (ϕ) per unit of cross-sectional area (a) in the magnetic material. The horizontal axis is the magnetic field intensity (H), which is a measure of the ampere-turns (NI) pushing the magnetic flux through the material per unit length (l) of the magnetic material. The H -value can also be regarded as the ampere-turns (NI) lost or dropped across the material per unit length (l) for a given flux density (B). This is the same concept as a voltage drop per unit length across a material for a given electric current density.

The slope (μ) of the curve is the ratio of magnetic flux density (B) per unit of magnetic field intensity (H), which is initially somewhat linear and steep. Saturation begins at the “knee” of the curve, where the slope (μ) diminishes as the magnetic field intensity (H) increases. When a material is magnetized, the domains (group of atoms with the same electron spin) rotate into alignment. The domain walls move as the aligned domains get larger and the misaligned domains get smaller (**Ch. 3**). At saturation, there are no more misaligned domains to rotate into alignment, and the magnetic material will not produce additional magnetic flux. At full saturation, the material behaves like air and the permeability approaches the value of μ_0 .

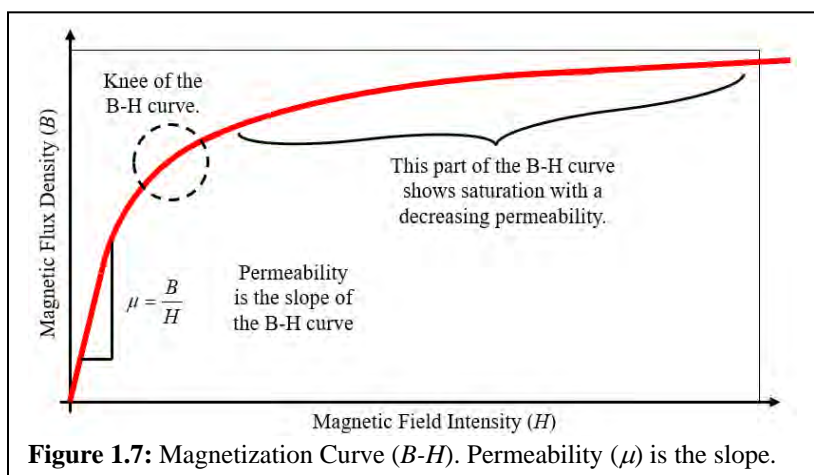


Figure 1.7: Magnetization Curve (B - H). Permeability (μ) is the slope.

The magnetic material properties are listed, as follows.

B = Magnetic Flux Density

H = Magnetic Field Intensity

μ = Magnetic Permeability

μ_0 = Permeability of Free Space (air and non-magnetic materials)

$\mu_0 = 4\pi E-7$ H/m

$$\mu_r = \frac{\mu}{\mu_0} = \text{Relative Permeability} \quad (1.15)$$

The magnetic material properties (magnetic flux density, magnetic field intensity, magnetic permeability) are shown below with the analogous equivalent electric material properties.

Magnetic Material

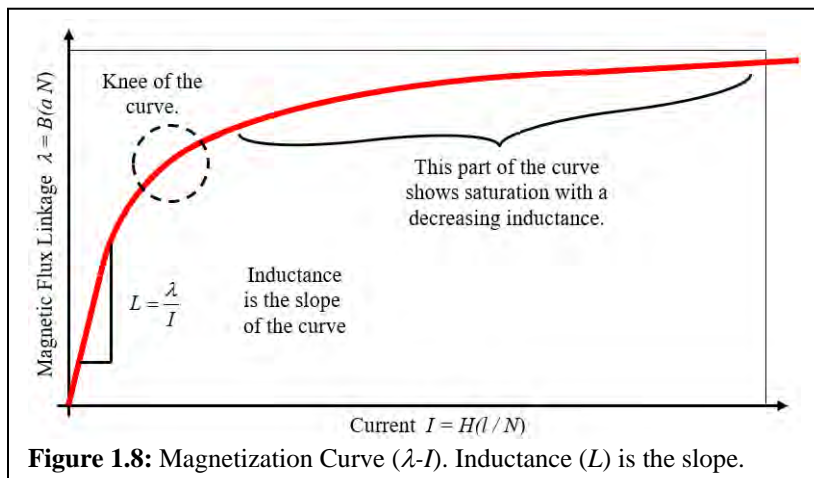
Flux Density	$B = \frac{\phi}{a}$	(1.16)
Field Intensity	$H = \frac{NI}{l}$	(1.17)
Permeability	$\mu = \frac{B}{H}$	(1.18)

Electric Material

Current Density	$J = \frac{I}{a}$	(1.19)
Field Intensity	$E = \frac{V}{l}$	(1.20)
Conductivity	$\sigma = \frac{J}{E}$	(1.21)

d. System Properties

The typical magnetization curve (λ - I Curve) for a magnetic system (or component) is shown in **Fig. 1.8**. This is identical to the B - H curve (**Fig. 1.7**) multiplied by some constants. The vertical axis (λ) represents the magnetic flux linkage, which is the magnetic flux density (B) multiplied by two constants, the cross-sectional area (a) and the turns (N). The horizontal axis (I) represents the current, which is the magnetic field intensity (H) multiplied by two constants, the length (l) and the inverse of turns ($1/N$). Note that inductance (L) is the slope of the curve.



The magnetic system properties are listed, as follows.

- \mathcal{R} = Reluctance
- \mathcal{P} = Permeance
- L = Inductance

The magnetic system properties (reluctance, permeance, inductance) are shown below with the equivalent properties for an electric system.

<u>Magnetic System</u>		<u>Electric System</u>	
Reluctance	$\mathcal{R} = \frac{l}{\mu a}$	(1.22)	Resistance $R_e = \frac{l}{\sigma a}$
Permeance	$\mathcal{P} = \mu \frac{a}{l}$	(1.23)	Conductance $G = \sigma \frac{a}{l}$
Inductance	$L = \frac{\lambda}{I} = \frac{N\phi}{I}$	(1.24)	

Inductance (L) can be described as a function only of geometry and magnetic permeability (a material property) by combining **Eq. 1.2**, **Eq. 1.8** and **Eq. 1.23**, as follows.

$$L = \frac{\lambda}{I} = \frac{N\phi}{I} = \frac{N^2\phi}{NI} = N^2\mathcal{P} = N^2\mu \frac{a}{l} \quad (1.27)$$

Inductance can be calculated based on the geometry and magnetic permeability, without knowing the voltage and current characteristics.

e. DC vs AC – Voltage vs Current

With this fundamental knowledge, the performance of some basic systems can be evaluated. Typically, DC or AC voltage-source systems have a sinusoidal voltage with a stiff source to supply the required current without reducing (drooping) the voltage. Also, DC or AC current-source systems have a sinusoidal current with a stiff source to supply the required voltage without reducing (drooping) the current. This is particularly interesting in inductive systems that saturate at high current. In general, these four systems have the following characteristics.

1. DC Voltage source:

- a. Current is defined by Coil Voltage and Coil Resistance.

$$I = \frac{V}{R} \quad (1.28)$$

- b. Magnetic Flux is defined by Coil Current, Turns, and system Permeance.

$$\phi = NI\mathcal{P} \quad (1.29)$$

- c. It will draw Current to support the Voltage.

2. AC Voltage source:

- a. Magnetic Flux is defined by Coil Voltage, Turns, and AC Frequency (ω) from the flux linkage ($N\phi$) in Faraday's law.

$$\phi_{PK} = \frac{V_{PK}}{N\omega} \dots \left[V = \frac{d(N\phi)}{dt} \quad \phi = \phi_{PK} \sin(\omega t) \right] \quad (1.30)$$

- b. Coil Current is defined by Magnetic Flux, Turns, and system Permeance (assume $R = \text{small}$).

$$I_{PK} = \frac{\phi_{PK}}{N\mathcal{P}} \quad (1.31)$$

- c. It will draw Current to support the Flux.

3. DC Current source:

- a. Magnetic Flux is defined by Coil Current, Turns, and system Permeance.

$$\phi = NI\mathcal{P} \quad (1.32)$$

- b. Coil Voltage is defined by Coil Current and Coil Resistance.

$$V = IR \quad (1.33)$$

- c. It will draw Voltage to support the Current.

4. AC Current source:

- a. Magnetic Flux is defined by Coil Current, Turns, and the system Permeance.

$$\phi = NI\mathcal{P} \quad (1.34)$$

- b. Coil Voltage is defined by Coil Current, Resistance, Turns & Flux rate of change.

$$V = IR + \frac{d(N\phi)}{dt} \quad (1.35)$$

- c. It will draw Voltage to support the Current and the Flux.

The most interesting cases are for AC Voltage and Current source systems with a saturating inductor, where the coil resistance is very small, so that all the voltage produces magnetic flux (a high resistance AC coil behaves like a DC coil, where the source voltage supports the resistive voltage drop). In this experiment (**Fig. 1.9**), a coil is wound on a ring of 1010 annealed steel, with an AC power supply, and a small Coil Resistance (Note: annealing relieves internal stresses and improves the magnetic properties).

$$I_{pk}R < V_{pk}/100$$

$$R < 0.15 \text{ ohm.}$$

Given:

$$D = 0.32 \text{ m}$$

$$l = \pi D = 1.00 \text{ m}$$

$$d = 0.02 \text{ m}$$

$$t = 0.02 \text{ m}$$

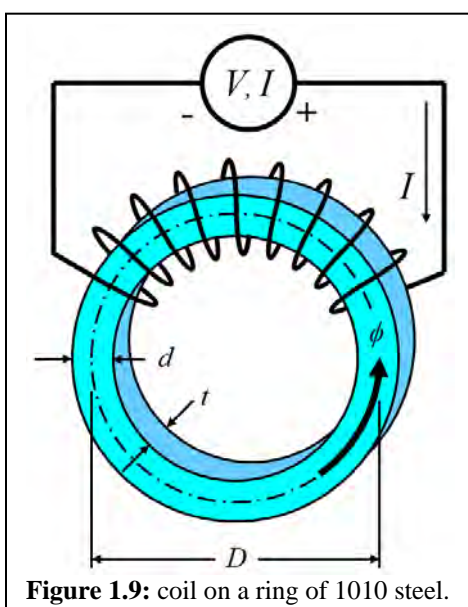
$$A = t d = 0.0004 \text{ m}^2$$

$$N = 300 \text{ turns}$$

$$V_{pk} = 70 \text{ volts}$$

$$f = 60 \text{ Hz}$$

$$\mu_0 = 4\pi E-7 \text{ H/m}$$



The system equation is shown below for a small coil resistance ($R \approx 0$):

$$V = IR + \frac{d(N\phi)}{dt} \approx \frac{d(N\phi)}{dt} = NA \frac{dB}{dt} \quad (1.36)$$

For an **AC Voltage source**, the following equations are used in sequence to define the magnetic flux density (B), the relative permeability (μ_r), the magnetic field intensity (H), and the current (I). (For **Eq. 1.39**, the k -values for 1010 annealed steel are, $k_1 = 4.847$, $k_2 = 1.908$, $k_3 = 227.3$, **Appendix-E**). The time step (Δt) is determined by adjusting Δt smaller until the results don't change.

$$\text{Source Voltage} \quad V = V_{PK} \sin(\omega t) \quad (1.37)$$

$$\text{Magnetic Flux Density} \quad B = \frac{1}{NA} \int V dt \quad (1.38)$$

$$\text{Relative Permeability (Appendix-E)} \quad \mu_r = \frac{1}{\mu_0 \left(k_1 e^{(k_2 B^2)} + k_3 \right)} + 1 \quad (1.39)$$

$$\text{Magnetizing Force (Field Intensity)} \quad H = \frac{B}{\mu_r \mu_0} \quad (1.40)$$

$$\text{Current} \quad I = \frac{H l}{N} \quad (1.41)$$

$$\text{Spreadsheet Iteration Time Step} \quad \Delta t = \frac{1}{1000 f} \quad (1.42)$$

For an **AC Current source**, the following equations are used in sequence to define the magnetic field intensity (H), the relative permeability (μ_r), the magnetic flux density (B), and the voltage (V).

$$\text{Source Current} \quad I = I_{PK} \sin(\omega t) \quad (1.43)$$

$$\text{Magnetizing Force (Field Intensity)} \quad H = \frac{NI}{l} \quad (1.44)$$

Relative Permeability (μ_r) ... an iterative approach is used on **Eq. 1.39** by making an initial guess for the flux density (B) and refining that guess until the error is small (Error < 36 μT).

$$\text{Magnetic Flux Density} \quad B = \mu H = \mu_r \mu_0 H \quad (1.45)$$

$$\text{Voltage} \quad V = NA \frac{dB}{dt} \quad (1.46)$$

The solution results on the next 2 pages show the non-sinusoidal wave shapes for the resulting current (**Fig. 1.12**) and voltage (**Fig. 1.15**) due to the saturation of the 1010 steel core.

Sinusoidal
Source
Voltage (V)

Sinusoidal
(B) Magnetic
Flux Density

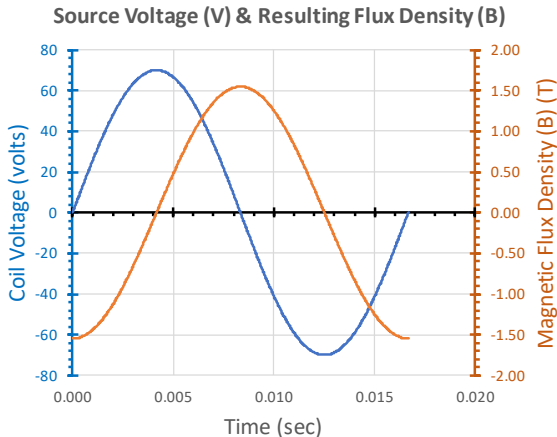


Figure 1.10: Source Voltage (V) and Flux Density (B).

B-H Curve
showing
Saturation

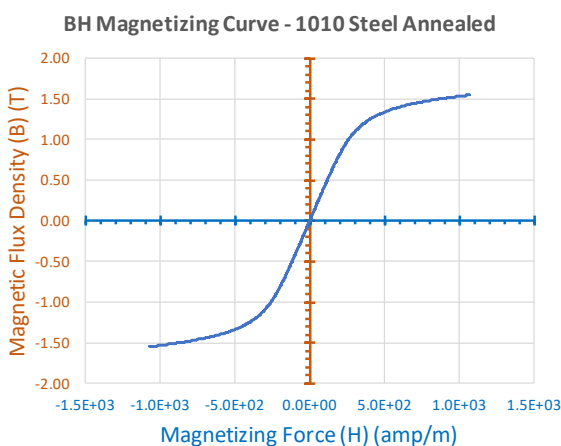


Figure 1.11: B-H Curve based on Eq. 1.39.

Resulting
Non-sine
Magnetizing
Force (H) &
Current (I)

Current (I)
spikes to
support (B)
Magnetic
Flux Density
at Saturation.

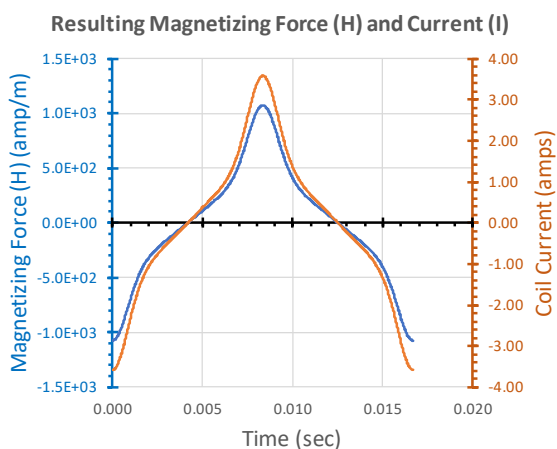


Figure 1.12: Magnetizing Force (H) and Current (I).

Sinusoidal Source Current (I)

Sinusoidal Magnetizing Force (H)

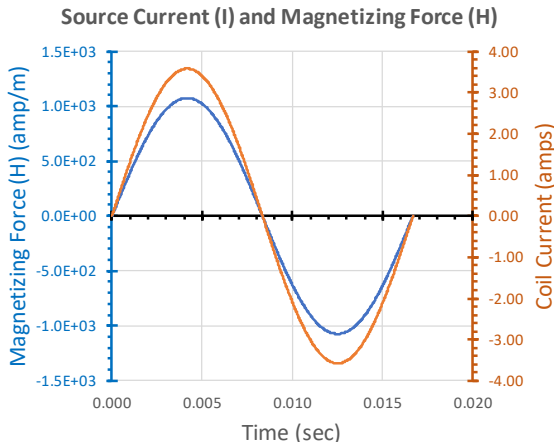


Figure 1.13: Source Current (I), Mag. Force (H).

B-H Curve showing Saturation

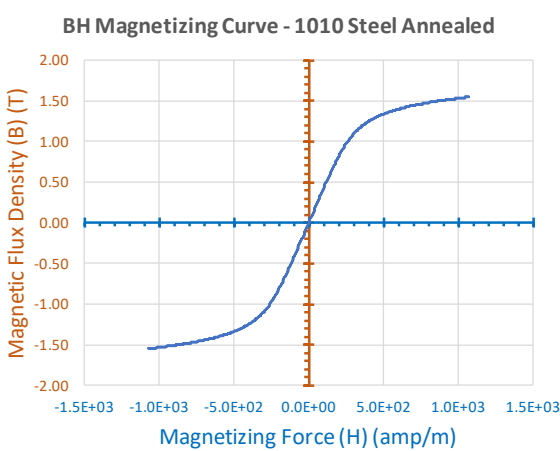


Figure 1.14: B - H Curve based on Eq. 1.39.

Resulting Non-sine (B) Flux Density, (V) Voltage.

Flux Density (B) is flat at the top.

Voltage (V) spikes on the steep slope of Flux Density.

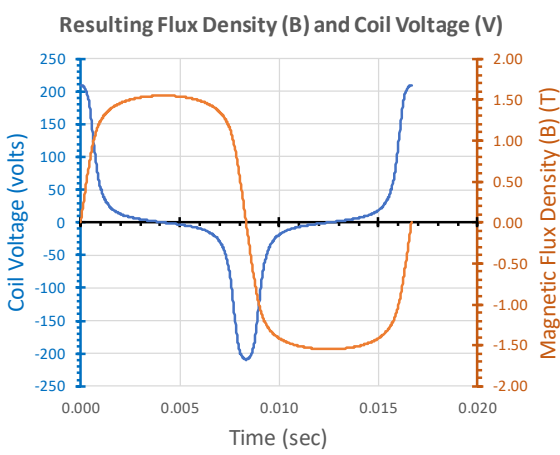


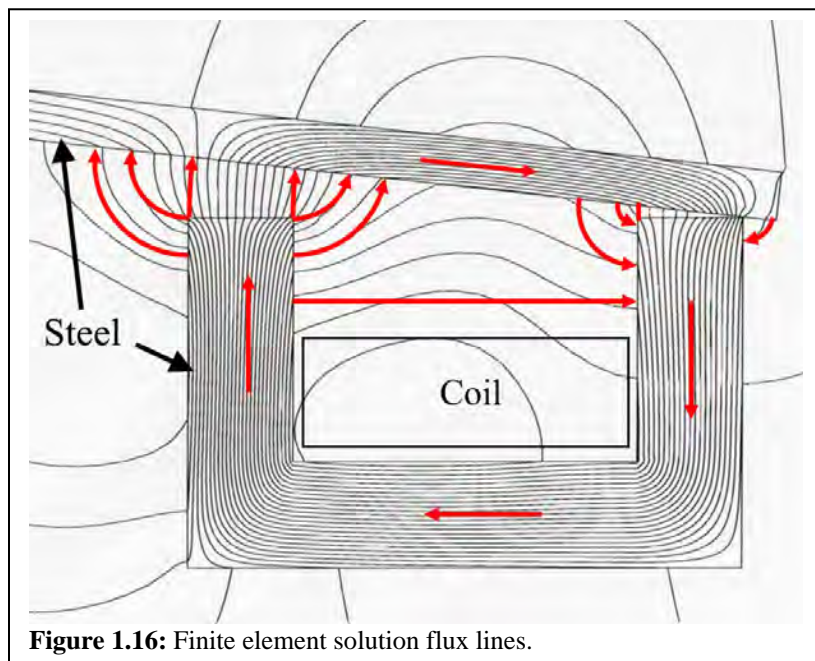
Figure 1.15: Voltage (V) and Flux Density (B).

f. Air Flux Paths

The objective here is to visualize more details of the magnetic flux lines so that flux paths can be defined and calculated. Again, the approach for visualizing magnetic flux paths is based on the simple question, “If I were a magnetic flux line, where would I go?”

A finite element flux plot (**Fig. 1.16**) demonstrates some important characteristics of flux lines. In this image, the coil contains current that is directed into the plane of the image, and the parts that contain most of the flux lines are made of a magnetic steel. In general, the magnetic flux will follow the path of least reluctance (analogous to least resistance for electric current).

1. Flux lines are continuous loops. All of the flux lines that aren't cut off at the edge of the plot are shown to form continuous loops.
2. Flux lines encircle a current. All of the flux lines encircle the coil.
3. Flux lines continue through the air between two pieces of magnetic steel. The finite element solution yields air flux lines that are almost normal to the adjacent steel, due to the large steel permeability.
 - a. Flux lines emerge from a piece of steel perpendicular to the steel surface.
 - b. Flux lines enter a piece of steel perpendicular to the steel surface.



The Red Lines and Circular Arcs that are drawn perpendicular to the steel surfaces (**Fig. 1.16**) do a very good job of approximating the path of flux lines

in the air. This is very important, because the length and area of regular geometric shapes (Lines, Circular Arcs) can be easily calculated.

Iron filing images are presented in Roters [1] to determine the shape of the magnetic field between two steel pole pieces. The contours of the traced magnetic field show that Lines and circular Arcs drawn normal to the steel surfaces do a very good job of estimating the shape of the magnetic flux path in the air.

This is the basis of estimating the air flux path permeance (\mathcal{P}), as will be shown in the next section.

g. Permeance of Air Flux Paths

Air flux paths can be accurately represented with straight lines and circular arcs, as shown in **Fig. 1.16**. The length (l) and area (a) of regions (**Fig. 1.17**) bounded by straight lines and circular arcs can be calculated, and the permeance (\mathcal{P}) of the air flux paths can be determined based on **Eq. 1.23**.

The permeance of the main air flux path (\mathcal{P}_1) is determined directly from **Eq. 1.23**.

1.23, as follows (for the air gap, $\mu_r = 1$). The length of the main flux path is equal to the air gap ($l = g$), and the cross-sectional area is a rectangular region of width (t) and depth (w), ($a = wt$), ($a = wt$).

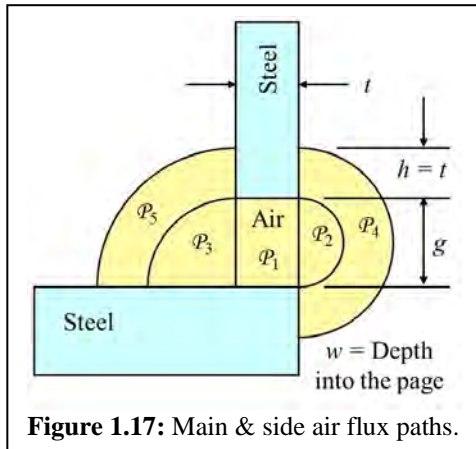


Figure 1.17: Main & side air flux paths.

$$\text{Permeance of Main air gap} \quad \mathcal{P}_1 = \mu_r \mu_0 \frac{a}{l} \quad \boxed{\mathcal{P}_1 = \mu_0 \frac{wt}{g}} \quad (1.47)$$

Electric and magnetic fields are linked by the speed of light ($c = 1/\sqrt{\mu_0 \epsilon_0}$).

The capacitance (C_1) of the main air gap (**Fig. 1.17**) can be calculated from **Eq. 1.47** by replacing the permeability (μ) with the permittivity (ϵ), where the relative permittivity (ϵ_r) is the dielectric constant of the air gap.

$$\text{Capacitance of Main air gap} \quad C_1 = \epsilon_r \epsilon_0 \frac{a}{l} \quad \boxed{C_1 = \epsilon_r \epsilon_0 \frac{wt}{g}} \quad (1.48)$$

The side flux paths ($\mathcal{P}_2, \mathcal{P}_3, \mathcal{P}_4, \mathcal{P}_5$) are also known as fringing flux paths. The half-cylindrical permeance (\mathcal{P}_2) (**Fig. 1.17**) is developed as follows. The cross-sectional area of the flux path (a_2) changes along the path, therefore the

permeance equation (**Eq. 1.23**) is modified by multiplying the numerator and denominator by the flux path length (l_2) to obtain the flux path volume (v_2).

$$\mathcal{P}_2 = \mu_0 \frac{a_2}{l_2} \frac{l_2}{l_2} = \mu_0 \frac{v_2}{l_2^2} \quad (1.49)$$

The radius of the cylinder is equal to half of the air gap ($r_2 = g/2$). The length of the flux path (l_2) is estimated as the average of the shortest straight-line path and the longest outside radius path (integrating over the various flux paths within the geometric shape would be more rigorous). The volume of the flux path (v_2) is the volume of the half-cylinder.

$$l_2 = \frac{1}{2}(g + \pi r_2) = 1.285 g \quad (1.50)$$

$$v_2 = \frac{w}{2} \pi r_2^2 = \frac{\pi}{8} w g^2 \quad (1.51)$$

$$\boxed{\mathcal{P}_2 = 0.24 \mu_0 w} \quad (1.52)$$

The quarter cylinder permeance (\mathcal{P}_3) (**Fig. 1.17**) is defined with the same procedure as the half-cylinder permeance (\mathcal{P}_2).

$$\mathcal{P}_3 = \mu_0 \frac{a_3}{l_3} \frac{l_3}{l_3} = \mu_0 \frac{v_3}{l_3^2} \quad (1.53)$$

$$r_3 = g \quad (1.54)$$

$$l_3 = \frac{1}{2} \left(g + \frac{\pi}{2} r_3 \right) = 1.285 g \quad (1.55)$$

$$v_3 = \frac{w}{4} \pi r_3^2 = \frac{\pi}{4} w g^2 \quad (1.56)$$

$$\boxed{\mathcal{P}_3 = 0.48 \mu_0 w} \quad (1.57)$$

Roters [1] uses a graphical method of field mapping to estimate the permeance of probable flux paths for \mathcal{P}_2 and \mathcal{P}_3 , which results in slightly different values for the constants, $\mathcal{P}_2 = 0.26 \mu_0 w \dots \mathcal{P}_3 = 0.52 \mu_0 w$. The difference is 7.7%, which validates this simple approach based on straight lines and circular arcs.

The half-cylindrical shell permeance (\mathcal{P}_4) (**Fig. 1.17**) is developed as follows. A differential permeance ($d\mathcal{P}_4$) is characterized by a flux path length (l_4) along the radius of the cylinder (r_4), and a differential flux path cross-sectional area (da_4) based on the differential radius (dr_4). The total permeance is determined by integrating across the radius from inside to outside.

$$d\mathcal{P}_4 = \mu_0 \frac{da_4}{l_4} \quad (1.58)$$

$$r_4 = \frac{g}{2} \quad \text{Inside Radius} \quad r_4 = \frac{g}{2} + h \quad \text{Outside Radius} \quad (1.59)$$

$$l_4 = \pi r_4 \quad (1.60)$$

$$da_4 = wdr_4 \quad (1.61)$$

$$dP_4 = \mu_0 \frac{w dr_4}{\pi r_4} \quad (1.62)$$

$$\mathcal{P}_4 = \mu_0 \frac{w}{\pi} \int_{\frac{g}{2}}^{\frac{g+h}{2}} \frac{dr_4}{r_4} \quad \boxed{\mathcal{P}_4 = \mu_0 \frac{w}{\pi} \ln \left(1 + 2 \frac{h}{g} \right)} \quad (1.63)$$

The quarter cylindrical shell permeance (\mathcal{P}_5) (Fig. 1.17) is defined with the same procedure as the half-cylindrical shell permeance (\mathcal{P}_4).

$$dP_5 = \mu_0 \frac{da_5}{l_5} \quad (1.64)$$

$$r_5 = g \quad \text{Inside Radius} \quad r_5 = g + h \quad \text{Outside Radius} \quad (1.65)$$

$$l_5 = \pi r_5 \quad (1.66)$$

$$da_5 = wdr_5 \quad (1.67)$$

$$dP_5 = \mu_0 \frac{w dr_5}{\pi r_5} \quad (1.68)$$

$$\mathcal{P}_5 = \mu_0 \frac{w}{\pi} \int_g^{g+h} \frac{dr_5}{r_5} \quad \boxed{\mathcal{P}_5 = 2 \mu_0 \frac{w}{\pi} \ln \left(1 + \frac{h}{g} \right)} \quad (1.69)$$

Roters [1] uses the same procedure for \mathcal{P}_4 and \mathcal{P}_5 and gives the same equations.

Additional **fringing flux paths** include the corner flux paths (\mathcal{P}_6 , \mathcal{P}_7) (spherical quadrant) shown in Fig. 1.18, and (\mathcal{P}_8 , \mathcal{P}_9) (spherical octant) shown in Fig. 1.19.

The flux paths are bounded by straight lines and circular arcs, and the permeances can be easily calculated based on the length and cross-sectional area of each region.

The permeance of the spherical quadrant air flux path (\mathcal{P}_6) is calculated similarly to (\mathcal{P}_3 and \mathcal{P}_4), where the cross-sectional area of the flux path (a_6) changes along the path and the flux path volume (v_6) is used. The length of the flux path (l_6) is the average of the shortest straight-line path and the longest outside radius path.

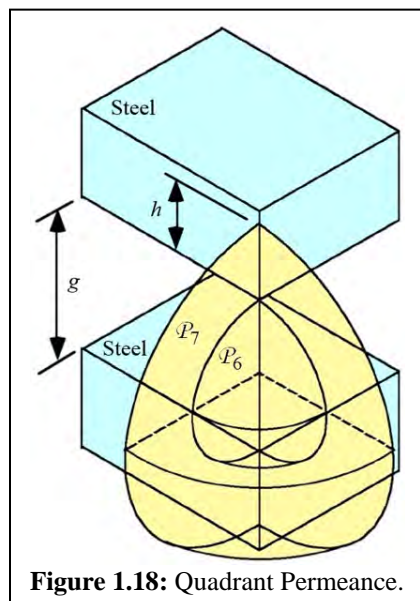


Figure 1.18: Quadrant Permeance.

$$\mathcal{P}_6 = \mu_0 \frac{a_6}{l_6} \frac{l_6}{l_6} = \mu_0 \frac{v_6}{l_6^2} \quad (1.70)$$

$$r_6 = \frac{g}{2} \quad (1.71)$$

$$l_6 = \frac{1}{2}(g + \pi r_6) = 1.285 g \quad (1.72)$$

$$v_6 = \frac{1}{4} \frac{4}{3} \pi r_6^3 = \frac{\pi}{24} g^3 \quad (1.73)$$

$$\boxed{\mathcal{P}_6 = 0.079 \mu_0 g} \quad (1.74)$$

The spherical quadrant shell permeance (\mathcal{P}_7) (Fig. 1.18) is developed similarly to the half-cylindrical shell permeance (\mathcal{P}_5). A differential permeance ($d\mathcal{P}_7$) is characterized by a flux path length (l_7) along the radius of the sphere (r_7). The differential flux path cross-sectional area (da_7) is not constant along the flux path, therefore a differential flux path volume is used (dv_7). The total permeance is determined by integrating across the radius from inside to outside.

$$d\mathcal{P}_7 = \mu_0 \frac{da_7}{l_7} \frac{l_7}{l_7} = \mu_0 \frac{dv_7}{l_7^2} \quad (1.75)$$

$$r_7 = \frac{g}{2} \quad \text{Inside Radius} \quad r_7 = \frac{g}{2} + h \quad \text{Outside Radius} \quad (1.76)$$

$$l_7 = \pi r_7 \quad (1.77)$$

$$dv_7 = \frac{1}{4} 4\pi r_7^2 dr_7 \quad (1.78)$$

$$\mathcal{P}_7 = \frac{\mu_0}{\pi} \int_{\frac{g}{2}}^{\frac{g+h}{2}} dr_7 \quad \mathcal{P}_7 = \mu_0 \frac{h}{\pi} \quad \boxed{\mathcal{P}_7 = 0.318 \mu_0 h} \quad (1.79)$$

Roters [1] uses a graphical method of field mapping to estimate the permeance of probable flux paths for \mathcal{P}_6 and \mathcal{P}_7 , giving slightly different proportional constants, $\mathcal{P}_6 = 0.077 \mu_0 g$... $\mathcal{P}_7 = 0.250 \mu_0 h$. The difference is 2.6% for \mathcal{P}_6 , and 26.8% for \mathcal{P}_7 . This is acceptable due to the small overall contribution (< 16.3%) for $g < t$, which validates this simple approach based on straight lines and circular arcs.

The permeance of the spherical octant air flux path (\mathcal{P}_8) (Fig. 1.19) is calculated similarly to (\mathcal{P}_3 , \mathcal{P}_4 , and \mathcal{P}_6), where the cross-sectional area of the flux path (a_8) changes along the path

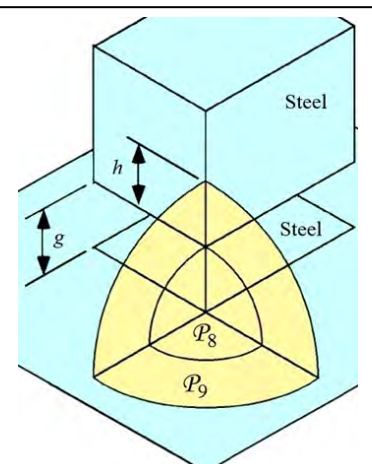


Figure 1.19: Spherical Octant Permeance.

and the flux path volume (v_8) is used. The length of the flux path (l_8) is the average of the shortest straight-line path and the longest outside radius path.

$$\mathcal{P}_8 = \mu_0 \frac{a_8}{l_8} \frac{l_8}{l_8} = \mu_0 \frac{v_8}{l_8^2} \quad (1.80)$$

$$r_8 = g \quad (1.81)$$

$$l_8 = \frac{1}{2} \left(g + \frac{\pi}{2} r_8 \right) = 1.285 g \quad (1.82)$$

$$v_8 = \frac{1}{8} \frac{4}{3} \pi r_8^3 = 0.5236 g^3 \quad (1.83)$$

$$\boxed{\mathcal{P}_8 = 0.317 \mu_0 g} \quad (1.84)$$

The permeance of the spherical octant shell air flux path (\mathcal{P}_9) (**Fig. 1.19**) is calculated similarly to the spherical quadrant shell (\mathcal{P}_7). Note that permeances \mathcal{P}_4 , \mathcal{P}_5 , \mathcal{P}_7 , and \mathcal{P}_9 use an integration of successive volumetric shells over the geometric shape because the thickness, the flux path length, and the differential volume are well defined with this technique.

$$d\mathcal{P}_9 = \mu_0 \frac{da_9}{l_9} \frac{l_9}{l_9} = \mu_0 \frac{dv_9}{l_9^2} \quad (1.85)$$

$$r_9 = g \quad \text{Inside Radius} \quad r_9 = g + h \quad \text{Outside Radius} \quad (1.86)$$

$$l_9 = \frac{\pi}{2} r_9 \quad (1.87)$$

$$dv_9 = \frac{1}{8} 4\pi r_9^2 dr_9 \quad (1.88)$$

$$d\mathcal{P}_9 = \mu_0 2 \frac{\pi r_9^2 dr_9}{\pi^2 r_9^2} = \mu_0 \frac{2}{\pi} dr_9 \quad (1.89)$$

$$\mathcal{P}_9 = \mu_0 \frac{2}{\pi} \int_s^{g+h} dr_9 \quad \mathcal{P}_9 = \mu_0 \frac{2}{\pi} h \quad \boxed{\mathcal{P}_9 = 0.637 \mu_0 h} \quad (1.90)$$

Roters [1] uses a graphical method of field mapping to estimate the permeance of probable flux paths for \mathcal{P}_8 and \mathcal{P}_9 , which results in slightly different values for the constants, $\mathcal{P}_8 = 0.308 \mu_0 g \dots \mathcal{P}_9 = 0.500 \mu_0 h$. The difference is 2.9% for \mathcal{P}_8 , and 27.4% for \mathcal{P}_9 . This is acceptable due to the small overall contribution (< 17.5%) for small gaps ($g < t/3$) that have higher force and inductance, which validates this simple approach based on straight lines and circular arcs.

Note that \mathcal{P}_2 , \mathcal{P}_3 , \mathcal{P}_7 , and \mathcal{P}_8 are independent of the gap (g), and \mathcal{P}_6 and \mathcal{P}_8 are proportional to the gap, and \mathcal{P}_1 , \mathcal{P}_4 , and \mathcal{P}_5 are inversely proportional to the gap. Therefore, only \mathcal{P}_1 , \mathcal{P}_4 , and \mathcal{P}_5 go to zero as the gap goes to infinity. For the other permeances, the width of the flux paths go to infinity and the length of the flux paths go to infinity, which results in an infinite flux path cross-section divided by an infinite flux path length. Therefore, this is a reasonable condition for a ridiculous limit.

h. Leakage Flux Paths

Leakage flux is the flux that is produced by a source (such as a coil or a permanent magnet) and does not show up at the armature air gap to produce force or torque, or does not link with the secondary coil in a coil actuator or does not link with the secondary coil in a transformer. It can be visualized as the flux that leaks away from the desired destination.

An actuator is shown

(**Fig. 1.20**) with a source of magnetic flux (a coil

or a permanent magnet (PM)). The 3 main flux paths can be visualized as follows, 1) the Black flux loops through the source and loops through the armature and the black permeance paths between the poles and the armature (this is where it is intended for the flux to go), 2) the Red flux loops through the source and loops across the poles at the bottom of the assembly, 3) the Red flux loops through the source and loops across the poles halfway between the source and the armature. There are also leakage flux paths in the 3rd dimension in and out of the page and corner flux paths, as described in the previous section. It helps to ask, “If I were a flux line where would I go?” when visualizing the flux paths.

Notice that each of the 3 flux paths are loops, and they all pass through the source, at least part of it. Flux path #2 (permeances P_{L4a} and P_{L4b}) and flux path #3 (permeance P_{L1}) are leakage flux paths, because the flux does not loop through the armature. The leakage flux path on the source (P_{L4a}) is estimated by dividing the source (coil or PM) into thirds.

Each leakage flux loop is in parallel with the armature flux loop. Therefore, an equivalent circuit can be created in which the source ampere-turns drives magnetic flux through a network of series and parallel reluctances (reluctance is the inverse of permeance).

Why does magnetic flux leak through the air, but the electric current does not leak through plastic? The ratio of magnetic permeability between iron and air is approximately $\mu_{Fe}/\mu_{air} = 10^4$. The ratio of electrical conductivity between copper and plastic is $\sigma_{Cu}/\sigma_{Plas} = 10^{22}$. Plastic as electrical insulation is 18 orders of magnitude better than air as magnetic insulation. However, this also allows the magnetic flux to cross air gaps in actuators and to produce a force.

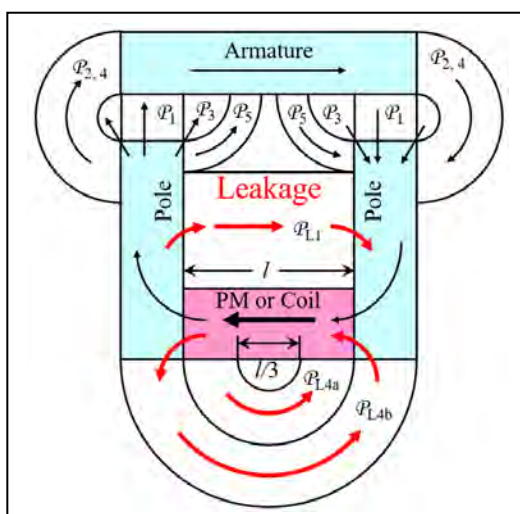


Figure 1.20: Leakage Flux in an actuator.

Fig. 1.20 shows the inner diameter of the coil leakage flux path permeance P_{L4a} as 1/3 of the length of the coil ($w = l/3$). This results in an approximation for the coil leakage permeance that is within 10% of the actual value. This can be shown based on the following analysis, with **Fig. 1.21**.

The actual coil leakage flux path permeance is calculated as follows.

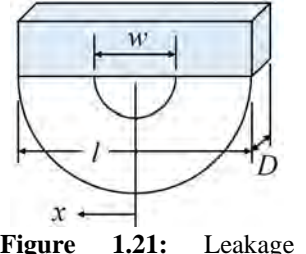


Figure 1.21: Leakage permeance for a coil.

$$NI_L = \frac{2x}{l} NI \quad \text{Ampere-turns driving the leakage flux at position } x \quad (1.91)$$

$$B_{Lx} = \mu_0 \frac{NI_L}{\pi x} = \mu_0 \frac{1}{\pi x} \frac{2x}{l} NI = \mu_0 \frac{2}{\pi} \frac{NI}{l} \quad \text{Leakage flux density at } x \quad (1.92)$$

$$\phi_L = B_{Lx} \frac{l}{2} D = \mu_0 \frac{2}{\pi} \frac{NI}{l} \frac{l}{2} D = \mu_0 NI \frac{D}{\pi} \quad \text{Total coil leakage flux} \quad (1.93)$$

$$\mathcal{P}_{Lcoil} = \frac{\phi_L}{NI} = \mu_0 \frac{D}{\pi} \quad \text{Coil Leakage flux path permeance} \quad (1.94)$$

The approximate coil leakage flux path permeance for P_{L4a} can be written as follows from **Eq. 1.63**. Note that the entire coil NI drives the leakage flux through P_{L4a} .

$$\mathcal{P}_{L4a} = \mu_0 \frac{D}{\pi} \ln \left(1 + 2 \frac{h}{g} \right) \quad h = \frac{l-w}{2} \quad g = w \quad (1.96)$$

$$\mathcal{P}_{L4a} = \mu_0 \frac{D}{\pi} \ln \left(\frac{l}{w} \right) \quad \text{Approximate coil leakage flux path permeance} \quad (1.97)$$

This approximation (**Eq. 1.97**) is within 10% of the actual coil leakage permeance (**Eq. 1.94**) when $w = l/3$. Also, for $w = l/2.7$ the Error = 0.7%.

$$\frac{\mathcal{P}_{L4a}}{\mathcal{P}_{Lcoil}} = \frac{\mu_0 \frac{D}{\pi} \ln \left(\frac{l}{w} \right)}{\mu_0 \frac{D}{\pi}} = \ln \left(\frac{l}{w} \right) \quad (1.98)$$

$$w = \frac{l}{2} \quad \ln \left(\frac{l}{w} \right) = \ln(2) = 0.693 \quad \text{Error} = -30.7\% \quad (1.99)$$

$$w = \frac{l}{3} \quad \ln \left(\frac{l}{w} \right) = \ln(3) = 1.099 \quad \text{Error} = +9.9\% \quad (1.100)$$

$$w = \frac{l}{4} \quad \ln \left(\frac{l}{w} \right) = \ln(4) = 1.386 \quad \text{Error} = +38.6\% \quad (1.101)$$

i. Parasitic Inductance and Capacitance

Parasitic (or stray) inductance is unplanned inductance in addition to the inductance of the circuit components. It increases impedance and adds stray resonance (when combined with stray capacitance). All current-carrying conductors (lead wires, circuit board traces) add stray inductance.

The stray inductance for each conductor can be reduced by decreasing the space between conductors (g), such as by twisting a pair of lead wires.

The inductance of lead wires per unit length (L/l) (Fig. 1.22) (with opposite current direction) can be calculated where, r_0 = conductor radius, g = conductor spacing,

I = current, B = magnetic flux density,

l = conductor length (not shown), $c = 2\pi r$ = circumference of the flux path.

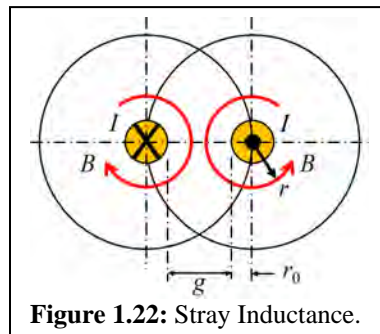


Figure 1.22: Stray Inductance.

$$B = \mu_0 H \quad (1.102)$$

$$H = \frac{NI}{c} = \frac{NI}{2\pi r} \quad B = \frac{\mu_0 I}{2\pi r} \quad N = 1 \quad (1.103)$$

$$d\phi = B da = B l dr \quad (1.104)$$

$$\phi = \int_{r_0}^{r_0+g} B l dr = \int_{r_0}^{r_0+g} \frac{\mu_0 I}{2\pi r} l dr = \frac{\mu_0 I l}{2\pi} \ln \left(1 + \frac{g}{r_0} \right) \quad (1.105)$$

$$L = \frac{N\phi}{I} = \frac{\mu_0 l}{2\pi} \ln \left(1 + \frac{g}{r_0} \right) \quad \boxed{\frac{L}{l} = \frac{\mu_0}{2\pi} \ln \left(1 + \frac{g}{r_0} \right)} \quad (1.106)$$

Similarly, parasitic or stray capacitance is an unplanned capacitance in addition to the capacitance of the circuit components. It decreases impedance, causes EMI (electromagnetic interference) on other conductors, and adds stray resonance (combined with stray inductance). The stray capacitance between lead wire conductors can be reduced by increasing the space between conductors (g) and by reducing the dielectric constant (ϵ_r) of the material in the space (g). Stray capacitance (C_1, C_2, C_4) (Fig. 1.23) can be estimated from the permeance equations (P_1, P_2, P_4) (Eq. 1.48, Eq. 1.52, Eq. 1.63) by replacing permeability (μ) with permittivity (ϵ). Note that permeance, capacitance, conductance, and elastic modulus (in Appendix-J, Eq. 9a – Eq. 9d) all represent system compliance in various areas of physics.

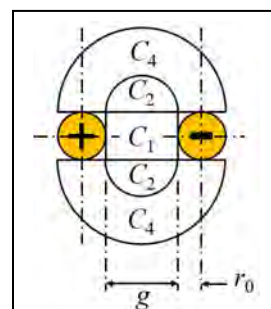


Figure 1.23: Stray Capacitance.

Also, the permeability and permittivity of free space (μ_0 , ϵ_0) are related by the speed of light (c) ... $c = 1/\sqrt{\mu_0 \epsilon_0}$.

The capacitance between conductors per unit length (C/l) can be calculated where, r_0 = conductor radius, g = conductor spacing, and l = conductor length (not shown).

$$C_1 = \epsilon_0 \epsilon_r \frac{a}{g} = \epsilon_0 \epsilon_r \frac{2r_0 l}{g} \quad a = 2r_0 l \quad (1.107)$$

$$C_2 = 0.24 \epsilon_0 \epsilon_r l \quad (1.108)$$

$$C_4 = \epsilon_0 \epsilon_r \frac{l}{\pi} \ln \left(1 + 2 \frac{2r_0}{g} \right) \quad (1.109)$$

$$C = C_1 + 2C_2 + 2C_4 = 2\epsilon_0 \epsilon_r \left(\frac{r_0 l}{g} + 0.24 l + \frac{l}{\pi} \ln \left(1 + 4 \frac{r_0}{g} \right) \right) \quad (1.110)$$

$$\boxed{\frac{C}{l} = 2\epsilon_0 \epsilon_r \left(\frac{r_0}{g} + 0.24 + \frac{1}{\pi} \ln \left(1 + 4 \frac{r_0}{g} \right) \right)} \quad (1.111)$$

Sample calculations are shown below for the parasitic inductance per unit length (L/l) and capacitance per unit length (C/l) of a pair of 4 AWG wires spaced apart (g) by 1.000 inches and 0.100 inches, to show how the inductance and capacitance vary relative to the space (g).

- The **parasitic inductance** decreases from 0.476 to 0.136 $\mu\text{H}/\text{m}$ when the space (g) is reduced from 1.000 to 0.100 inches.
- The **parasitic capacitance** increases from 7.99 to 31.5 pF/m when the space (g) is reduced from 1.000 to 0.100 inches.

Geometry				
Conductor Size	AWG	awg	4	
Conductor Diameter	d_0	inch	0.204	
Conductor Radius	r_0	inch	0.102	
Space between Conductors	g	inch	1.000	0.100
Parasitic Inductance per unit Length				
Permeability of Free Space	μ_0	H/m	1.26E-06	
Parasitic Inductance	L/l	H/m	4.76E-07	1.36E-07
Parasitic Capacitance per unit Length				
Permittivity of Free Space	ϵ_0	F/m	8.85E-12	
Dielectric Constant	ϵ_r	---	1	
Path-1	C_1/l	F/m	1.81E-12	1.81E-11
Path-2	C_2/l	F/m	2.12E-12	2.12E-12
Path-4	C_4/l	F/m	9.66E-13	4.58E-12
Parasitic Capacitance	C/l	F/m	7.99E-12	3.15E-11

j. Example-1 – Solid Core

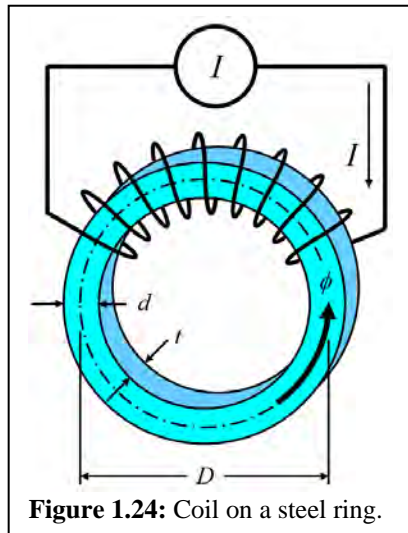
A coil is wound on a steel ring or toroid (Fig. 1.24). The power supply is DC constant current.

$$\begin{aligned}
 D &= 0.10 \text{ m} \\
 d &= 0.01 \text{ m} \\
 t &= 0.01 \text{ m} \\
 N &= 10. \text{ turns} \\
 I &= 5. \text{ amperes} \\
 \mu_r &= 5,000. \text{ ---} \\
 \mu_0 &= 4\pi E-7 \text{ T-m/A-t or H/m}
 \end{aligned}$$

Note: Ignore Leakage

Find: \mathcal{P} , \mathcal{R} , ϕ , B , L

Find: I and NI to saturate
($B = 1.6 \text{ T}$)



Calculations:

$$\text{Flux Area} \quad a = t d = (0.01)(0.01) = 1.0E - 4 \text{ m}^2 \quad (1.112)$$

$$\text{Flux Length} \quad l = \pi D = \pi(0.10) = 0.3142 \text{ m} \quad (1.113)$$

$$\text{Permeance} \quad \mathcal{P}_F = \mu_r \mu_0 \frac{a}{l} = (5000)(4\pi E - 7) \frac{0.0001}{0.3142} \quad (1.114)$$

Permeance	$\mathcal{P}_F = 2.0E - 6 \frac{\text{Wb}}{\text{A}}$	(1.115)
-----------	---	---------

Reluctance	$\mathcal{R}_F = \frac{1}{\mathcal{P}_F} = 0.5E + 6 \frac{\text{A}}{\text{Wb}}$	(1.116)
------------	---	---------

Magnetic Flux	$\phi = \frac{NI}{\mathcal{R}_F} = \frac{(10)(5)}{0.5E + 6} = 1.0E - 4 \text{ Wb}$	(1.117)
---------------	--	---------

Flux Density	$B = \frac{\phi}{a} = \frac{1.0E - 4}{1.0E - 4} = 1.0 \text{ T}$	(1.118)
--------------	--	---------

Inductance	$L = N^2 \mathcal{P}_F = (10^2)(2.0E - 6) = 200.E - 6 \text{ H}$	(1.119)
------------	--	---------

Calculations for Saturation:

$$\text{Flux} \quad \phi = B a = (1.6)(1.0E - 4) = 1.6E - 4 \text{ Wb} \quad (1.120)$$

$$\text{NI} \quad NI = \phi \mathcal{R} = (1.6E - 4)(0.5E + 6) = 0.8E + 2 \quad (1.121)$$

NI	$NI = 80.0 \text{ ampere-turns}$	(1.122)
----	----------------------------------	---------

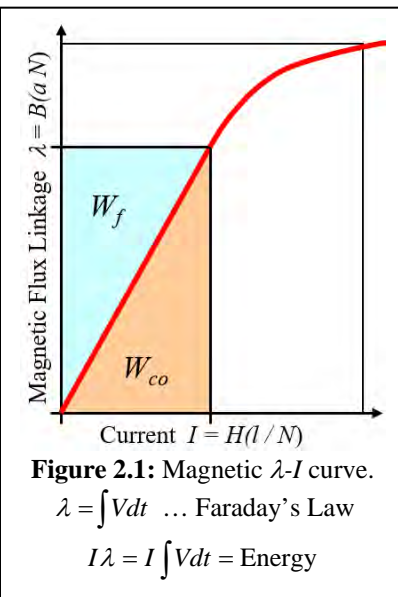
Current	$I = NI/N = 80/10 = 8.0 \text{ amperes}$	(1.123)
---------	--	---------

2. Magnetic Forces

a. Energy and Force

The magnetic force between two pieces of magnetic steel (such as an armature and a pole piece) is the result of electromechanical energy conversion, which is the transfer of magnetic field energy into mechanical energy. This is the basis of all actuators, solenoids and motors. In general, the change in magnetic field energy is equal to the change in mechanical energy, as shown in Eq. 2.5 and Eq. 2.6.

The magnetization curve (λ - I curve) (Fig. 1.8, Fig. 2.1) shows that the slope is equal to inductance ($L = \lambda/I$) and the area is equal to magnetic energy ($W_f = \lambda I$).



The electromechanical characteristics are as follows.

W_f = Magnetic Field Energy

W_{co} = Magnetic Co-Energy

W_m = Mechanical Energy

F_x = Mechanical Force in the x -direction

x = Mechanical Position in the x -direction

When evaluating the electromechanical energy conversion in an entire system (including the air gaps and the saturating magnetic components) the magnetic co-energy (W_{co}) must be used. When evaluating only the characteristics of an air gap ((NI)_g, P_g , R_g , ϕ_g) to determine the force across the air gap, the magnetic field energy (W_f) can be used. Co-energy is equal to magnetic field energy ($W_{co} = W_f$) for air because air has a constant magnetic permeability. Note that (NI)_g is the ampere-turns dropped across the air gap, and ϕ_g is the magnetic flux across the air gap.

$$\text{Basic Magnetics} \quad \phi_g = (NI)_g P_g \quad (NI)_g = \phi_g R_g \quad (2.1)$$

$$\text{Inductance} \quad L = \frac{\lambda}{I} = N^2 P = N^2 \mu_0 \frac{a}{g} \quad (2.2)$$

$$\text{Magnetic Field Energy} \quad dW_f = Id\lambda \quad W_f = \frac{1}{2} \lambda I = \frac{1}{2} LI^2 \quad (2.3)$$

$$\text{Magnetic Field Energy} \quad W_f = \frac{1}{2} (NI)_g \phi_g = \frac{1}{2} (NI)_g^2 P_g = \frac{1}{2} \phi_g^2 R_g \quad (2.4)$$

Electro-mechanical energy conversion on an air gap equates the change in magnetic field energy (ΔW_f) to the change in mechanical energy (ΔW_m) (see **Eq. 2.5** and **Eq. 2.6**). The magnetic field energy across the air gap changes as the armature moves because the magnetic flux and reluctance change (**Eq. 2.4**), and the mechanical energy changes as the armature force (F_x) moves through a distance (Δx). The force (F_x) in the direction of displacement (x) is obtained by differentiating the magnetic field energy (W_f) with respect to the displacement (x). The energy relationships can be written as follows to give the mechanical force (**Eq. 2.7**), also known as the reluctance force.

$$\text{Energy Balance} \quad \Delta W_{co} = \Delta W_f = \Delta W_m = F_x \Delta x \quad (2.5)$$

$$\text{Mechanical Force} \quad F_x = \frac{\Delta W_f}{\Delta x} \Big|_{\Delta x \rightarrow 0} = \frac{dW_f}{dx} \quad (2.6)$$

$$\boxed{\text{Mechanical Force} \quad F_x = \frac{1}{2} (NI_g)^2 \frac{d\mathcal{P}_g}{dx} = \frac{1}{2} \phi_g^2 \frac{d\mathcal{R}_g}{dx}} \quad (2.7)$$

Similarly, the electrostatic force between two dielectric materials (such as an electrostatically charged balloon and a non-conductive wall) is the result of electromechanical energy transfer from electric field energy into mechanical energy. In general, the change in electric field energy is equal to the change in mechanical energy.

The electrostatic q - V curve for a dielectric system (**Fig. 2.2**) shows that the slope is equal to capacitance (**Eq. 2.8**) and the area is equal to electric energy (**Eq. 2.9**).

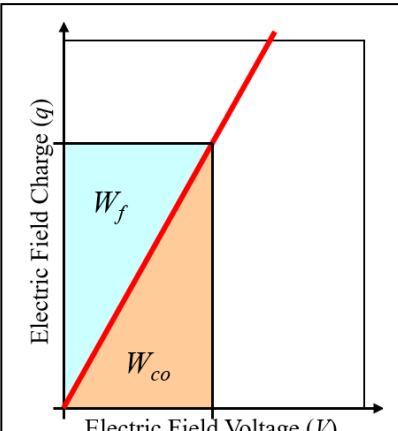


Figure 2.2: Electrostatic q - V curve for a dielectric system.

$$\text{Capacitance} \quad C = \frac{q}{V} = \epsilon_r \epsilon_0 \frac{a}{g} \quad q = CV \quad (2.8)$$

$$\text{Electric Field Energy} \quad W_f = \frac{1}{2} qV = \frac{1}{2} CV^2 \quad (2.9)$$

Electro-mechanical energy conversion on an air gap equates the change in electric field energy (ΔW_f) to the change in mechanical energy (ΔW_m). The energy relationships can be written in the same way as was done in **Eq. 2.5** and **Eq. 2.6** with the electric field energy from **Eq. 2.9**. The mechanical force due to an electric field across an air gap is shown in **Eq. 2.10**.

$$\boxed{\text{Electric Field Force} \quad F_x = \frac{1}{2} V^2 \frac{dC}{dx}} \quad (2.10)$$

b. Normal Force

In this section, the force normal (perpendicular) to the armature surface is calculated. In many actuators, this is the motive force than results in motion. The force tangential (parallel) to the armature surface is calculated in the next section.

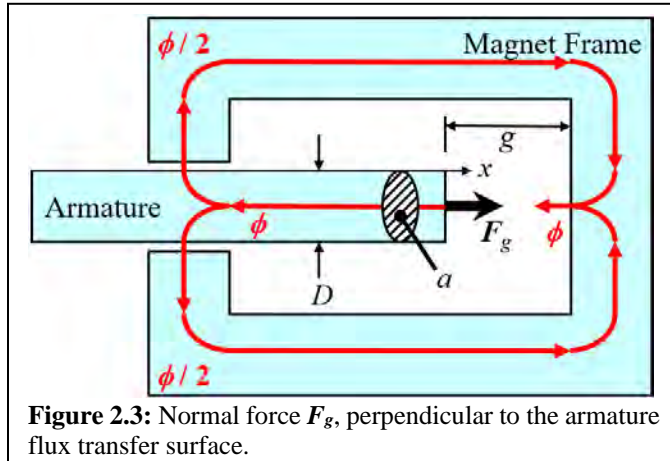


Figure 2.3: Normal force F_g , perpendicular to the armature flux transfer surface.

The force (F_x) (in the x -direction) is calculated by differentiating the magnetic field energy (W_f) with respect to g (air gap size in the x -direction). The force (F_x) in **Eq. 2.7** can be evaluated relative to the air gap permeance (P_g) or reluctance (R_g). The force (F_x) is always in the direction to increase the magnetic flux (ϕ), or to increase the permeance (P), or to decrease the reluctance (R). The magnetic force (**Eq. 2.7**) can be evaluated relative to the air gap permeance (P_g) as follows, where the main air gap permeance (P_1 , **Eq. 1.47**) is used alone. This is valid for small air gaps ($g < 0.001 D$), where the fringing permeances (P_2 through P_9) are insignificant. This simplification is useful here to illustrate the basic physics. The force details for a large air gap with fringing flux is shown in **Fig. 2.6**.

$$F_x = \frac{1}{2} (NI)_g^2 \frac{dP_g}{dg} = \frac{1}{2} \phi_g^2 \frac{dR_g}{dg} \quad (2.11)$$

$$P_g = \frac{\mu_0 a}{l} = \frac{\mu_0 a}{g} \quad \frac{dP_g}{dg} = \frac{\mu_0 a}{g^2} \quad (2.12)$$

$$F_x = \frac{1}{2} (NI)_g^2 \frac{\mu_0 a}{g^2} = \frac{1}{2} \frac{(NI)_g^2}{g^2} \mu_0 a \quad \begin{cases} \text{No Saturation} \\ g = \text{small ... } g < 0.001 D \end{cases} \quad (2.13)$$

The force (F_x) in **Eq. 2.13** is proportional to the inverse square of the air gap ($1/g^2$) and the square of the ampere-turns dropped across the air gap $(NI)_g^2$.

Therefore, if the magnetic flux is not saturated, the force (F_x) will rise proportionally with the inverse square of the air gap.

Similarly, the electric field force (**Eq. 2.10**) can be evaluated in the same way to give the force (F_x) (**Eq. 2.14**) across an air gap (g) due to the electrostatic field. This explains why an electrostatically charged balloon will stick to a non-conductive wall.

$$F_x = \frac{1}{2} V^2 \frac{dC}{dg} = \frac{1}{2} \left(\frac{V}{g} \right)^2 \epsilon a \quad \text{Electrostatic Force} \quad (2.14)$$

The magnetic force (**Eq. 2.7**) can be evaluated relative to the air gap reluctance (\mathcal{R}_g) as follows, where only the main air gap reluctance is used. This is valid for small air gaps ($g < 0.001 D$), where fringing is insignificant.

$$\mathcal{R}_g = \frac{l}{\mu_0 a} = \frac{g}{\mu_0 a} \quad \frac{d\mathcal{R}_g}{dg} = \frac{1}{\mu_0 a} \quad (2.15)$$

$$F_x = \frac{1}{2} \phi_g^2 \frac{1}{\mu_0 a} = \frac{B_g^2 a}{2\mu_0} \quad \begin{cases} \text{Saturation} \\ g = \text{small ... } g < 0.001 D \end{cases} \quad (2.16)$$

The force (F_x) in **Eq. 2.16** is constant relative to the air gap (g) and proportional to the square of the air-gap flux density (B_g^2). Saturation for many steel alloys is in the range of 1.60 T to 1.85 T. Evaluating **Eq. 2.16** at saturation for a small air gap ($g < 0.001 D$) gives the maximum possible magnetic force (F_g) and maximum possible magnetic pressure ($p = F_g/a$).

$$p = \frac{F_g}{a} = \frac{B_g^2}{2\mu_0} = \frac{(1.60)^2}{2(4\pi E - 7)} = 1.02E + 6 \frac{\text{N}}{\text{m}^2} = 148 \frac{\text{lb}}{\text{in}^2} \quad (2.17)$$

$$[p = 1.02 \text{ MPa} = 10.2 \text{ bar} = 148 \text{ psi}] \quad (B = 1.60 \text{ T}, g < 0.001 D) \quad (2.18)$$

$$p = \frac{F_g}{a} = \frac{B_g^2}{2\mu_0} = \frac{(1.85)^2}{2(4\pi E - 7)} = 1.36E + 6 \frac{\text{N}}{\text{m}^2} = 198 \frac{\text{lb}}{\text{in}^2} \quad (2.19)$$

$$[p = 1.36 \text{ MPa} = 13.6 \text{ bar} = 198 \text{ psi}] \quad (B = 1.85 \text{ T}, g < 0.001 D) \quad (2.20)$$

These calculations show that the maximum magnetic pressure across a small air gap at saturation is between approximately 1.0 MPa (10 bar, 150 psi) and 1.4 MPa (14 bar, 200 psi).

This shows that electromagnetic forces are limited due to magnetic saturation, and small compared to the pressure in a hydraulic system. For example, hydraulic systems in military aircraft typically operate at 5,000 psi (33 MPa). Hydraulic systems are popular because they can be very small. However, hydraulic systems are dirty (oil leaks) and they are difficult to control due to their nonlinear characteristics (pressure is proportional to the square of the flow rate). Electromagnetic systems are popular because they are clean and easy to control.

The minimum size (cross-sectional area) of a magnetic armature can be calculated from these values based on the required holding force. For

example, the armature cross-sectional area for a 1,000 N (224 lb_f) holding force (F_{Hold}) is in the range of 7 cm² to 10 cm² (**Eq. 2.22** and **Eq. 2.23**). This calculation is useful when evaluating the size of an armature for a holding force, which occurs at a small air gap ($g < 0.001 D$).

$$p = \frac{F_{Hold}}{a} \quad (2.21)$$

$$a = \frac{F_{Hold}}{p} = \frac{1000}{1.02E + 6} \quad \boxed{a = 9.80 \text{ cm}^2 = 1.52 \text{ inch}^2} \quad (2.22)$$

$$a = \frac{F_{Hold}}{p} = \frac{1000}{1.36E + 6} \quad \boxed{a = 7.35 \text{ cm}^2 = 1.14 \text{ inch}^2} \quad (2.23)$$

For a small air gap, the fringing permeances ($\mathcal{P}_2 - \mathcal{P}_9$) can be ignored because they are insignificant compared to the main permeance (\mathcal{P}_1). Therefore, the holding force calculation uses only the main permeance (\mathcal{P}_1 , **Eq. 1.47**). The holding force defines the maximum possible force for an actuator.

Larger air gaps need to be evaluated to determine the pull-in characteristics of an actuator, where an armature works against a spring or carries a mass against gravity. This refers to bringing the armature from the large air gap position (open) to the small air gap position (closed). The force at the open gap is much lower than the holding force at the closed gap (as suggested by **Eq. 2.13**).

When evaluating the force on larger air gaps, all of the fringing permeances ($\mathcal{P}_2 - \mathcal{P}_9$) become significant and cannot be ignored. The magnetic force across a large air gap is evaluated for two configurations, 1) **Fig. 2.4** is a cylindrical armature with an air gap to an equally sized cylindrical pole piece, 2) **Fig. 2.5** is a cylindrical armature with an air gap to a flat plate.

The cylindrical armature to pole piece configuration (**Fig. 2.4**) uses the main permeance \mathcal{P}_1 , the half-cylinder permeance \mathcal{P}_2 , and the half-cylindrical shell permeance \mathcal{P}_4 ($\mathcal{P}_g = \mathcal{P}_1 + \mathcal{P}_2 + \mathcal{P}_4$). The cylindrical armature to flat plate configuration (**Fig. 2.5**) uses the main permeance \mathcal{P}_1 , the quarter cylinder permeance \mathcal{P}_3 , and the quarter cylindrical shell permeance \mathcal{P}_5 ($\mathcal{P}_g = \mathcal{P}_1 + \mathcal{P}_3 + \mathcal{P}_5$).

The force (F_g) (**Eq. 2.11**) across a range of air gaps ($0.0001 < g/D < 100$) is calculated based on the air gap permeances ($\mathcal{P}_1 - \mathcal{P}_5$, from **Eq. 1.47 – Eq. 1.69**), the permeance derivatives with respect to the air gap ($d\mathcal{P}_g/dg$), and a flux density of 1.6 T (lightly saturated). The results are shown in **Fig. 2.6** for both configurations.

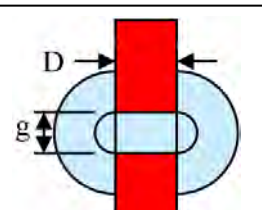


Figure 2.4: Armature to Cylindrical Pole.

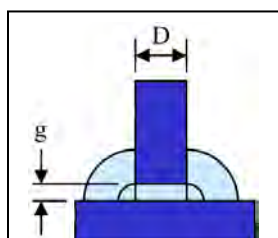


Figure 2.5: Armature to Flat Plate.

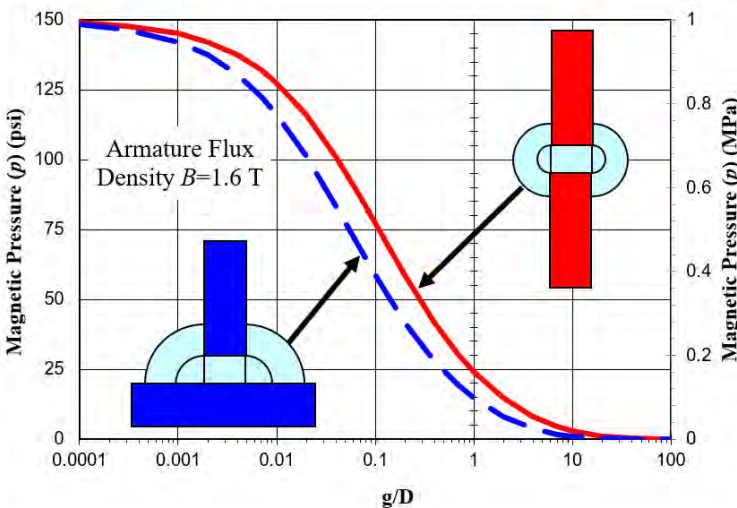


Figure 2.6: Magnetic force per unit pole area (p) versus g/D ratio. This includes the fringing permeance paths as depicted in the sketches.

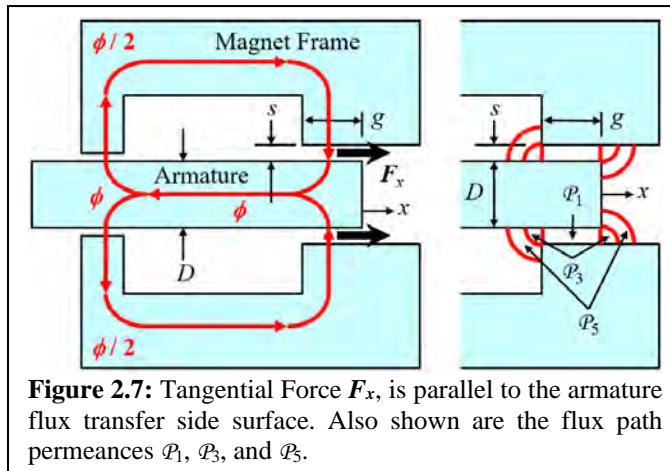
The armature to cylindrical pole configuration has a higher force because it has less fringing flux than the armature to flat plate configuration. Less fringing flux results in more flux through the main permeance path and a larger force. The curves in **Fig. 2.6** were curve-fit to the following equations (**Eq. 2.24**, **Eq. 2.25**) with high accuracy (Error < 4.6%). These equations can be used very effectively to calculate the armature force for large air gaps based on the magnetic flux density in the armature.

$$P_{\max} = \frac{1.02 \left(\frac{B}{1.6} \right)^2}{\left(1 + 4.96 \left(\frac{g}{D} \right)^{0.724} + 0.264 \left(\frac{g}{D} \right)^2 \right)} \text{ MPa} \quad \begin{bmatrix} \text{Armature to} \\ \text{Cylindrical} \\ \text{Pole Piece} \end{bmatrix} \quad (2.24)$$

$$P_{\max} = \frac{1.02 \left(\frac{B}{1.6} \right)^2}{\left(1 + 8.20 \left(\frac{g}{D} \right)^{0.725} + 1.055 \left(\frac{g}{D} \right)^2 \right)} \text{ MPa} \quad \begin{bmatrix} \text{Armature to} \\ \text{Flat Plate} \end{bmatrix} \quad (2.25)$$

c. Tangential Force

The tangential X-direction force (F_x) on an armature (Fig. 2.7) is parallel to the armature side surface, and the magnetic flux (ϕ) is normal to the armature side surface (in the s-direction or Y-direction).



The net normal force in the Y-direction (F_y) is zero because it is balanced between the top and bottom sides of the armature due to perfect symmetry (s at the top = s at the bottom). If the armature is not perfectly centered there will be a net Y-direction normal force. The Y-direction force (F_y) is calculated by differentiating the magnetic field energy (W_f) with respect to s (or with respect to the Y-direction).

The X-direction force (F_x) is calculated by differentiating the magnetic field energy (W_f) with respect to g (or with respect to the X-direction). The force is always in the direction of increasing magnetic flux (ϕ), or increasing permeance (\mathcal{P}), or decreasing reluctance (\mathcal{R}). For small air gaps ($s < 0.10 g$), the fringing permeances (P_3 and P_5) (Eq. 1.57, Eq. 1.69) are insignificant compared to the main air gap permeance (P_1) (Eq. 1.47), and the magnetic force can be evaluated relative to the main air gap permeance (P_1). Also, both P_3 and P_5 are independent of g (or x) and therefore they don't contribute to the tangential force (F_x).

$$\mathcal{P}_g = P_1 + 2P_3 + 2P_5 \quad \mathcal{P}_g \Big|_{s<0.10g} \approx P_1 = \frac{\mu_0 a}{l} = \frac{\mu_0 (\pi D g)}{s} \quad (2.26)$$

$$F_x = \frac{1}{2} (NI)^2 \frac{d\mathcal{P}_g}{dg} = \frac{1}{2} (NI)^2 \frac{\mu_0 \pi D}{s} \quad \begin{bmatrix} \text{Saturation} \\ s = \text{small ... } s < 0.10 g \end{bmatrix} \quad (2.27)$$

The tangential force (F_x) (Eq. 2.27) is constant relative to the armature position (g). The air gap permeance (\mathcal{P}_g) and the magnetic flux (ϕ) increase with the displacement (g). The armature will saturate at a large displacement.

d. Pole Shaping

Pole shaping can be visualized as modifying the shape of the face on the armature and pole piece (flat or conical or parallel) (Fig. 2.8) to optimize the force curve to more closely match the load profile.

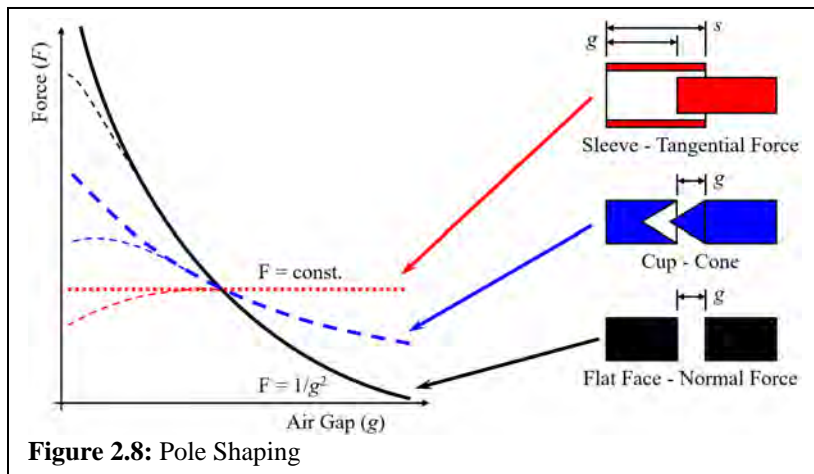


Figure 2.8: Pole Shaping

- A flat face armature has a normal force that is proportional to the inverse square of the air gap ($1/g^2$) (Eq. 2.13). The force is initially very low at a large air gap and increases to a very high value at a small gap. The magnetic flux increases with a decreasing air gap. Saturation causes the force to flatten as the air gap becomes small, as shown by the broken line on the figure.
- A parallel face (sleeve) armature has a tangential force that is constant and independent of the armature position (g, x) (Eq. 2.27). Compared to the flat face structure, this configuration has higher force at the open gap and lower force at a small gap. Saturation causes the force to fall off as the air gap becomes small.
- A cup-cone configuration can achieve a force characteristic that is between the flat face and the parallel face structures.

Pole shaping is very common in actuators and solenoids. When the force curve more closely matches the load profile, the actuator size can be reduced or the actuator input energy (ampere-turns) can be reduced.

e. Lorentz Force

Prior discussions on magnetic force were based on the energy transfer between the magnetic and the mechanical systems. The change in magnetic field energy was determined by differentiating the permeance or reluctance. Therefore, that force is known as a reluctance force.

The Lorentz force results from the interaction between an electric current and a magnetic field (**Fig. 2.9**). The Lorentz force vector (\vec{F}_x) is defined as the cross product of the current vector (\vec{I}_y) and the flux density vector (\vec{B}_z) and multiplied by the length (l_w) of the current path through the magnetic field (**Eq. 2.28**).

Figure 2.9: Lorentz Force on a current passing through a magnetic field.

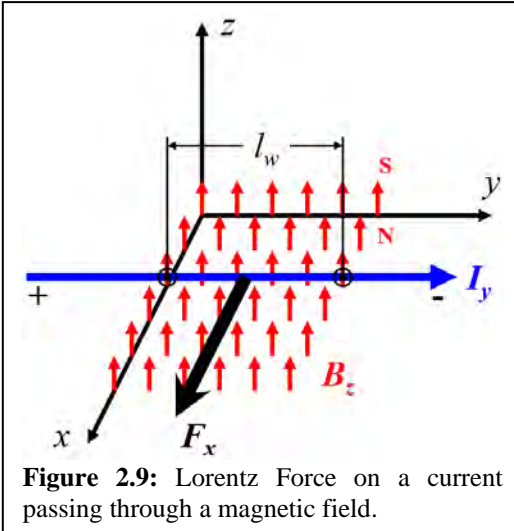


Figure 2.9: Lorentz Force on a current passing through a magnetic field.

$$\vec{F} = (\vec{I} \times \vec{B}) l_w \quad \text{Lorentz Force} \quad (2.28)$$

The Right-Hand Rule for Lorentz force is shown in **Fig. 2.10**. The thumb of the right-hand points in the direction of the current (I), the fingers point in the direction of the magnetic field (B), and the force (F) points out and normal to the palm. The following example demonstrates the Lorentz Force calculation and unit conversions.

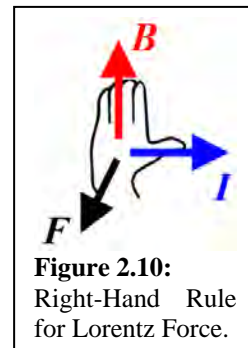


Figure 2.10:
Right-Hand Rule
for Lorentz Force.

$$\begin{aligned} I &= 1,000 \text{ A} \\ B &= 1.0 \text{ T} \\ l_w &= 0.4 \text{ m} \end{aligned}$$

$$\vec{F} = (\vec{I} \times \vec{B}) l_w = (1,000)(1.0)(0.4) = 400 \text{ A-T-m} \quad (2.29)$$

$$\vec{F} = 400 \text{ A-T-m} \frac{\text{Wb}}{\text{T-m}^2} \frac{\text{V-s}}{\text{Wb}} \frac{\text{J}}{\text{V-A-s}} = 400 \frac{\text{J}}{\text{m}} = 400 \frac{\text{J}}{\text{m}} \frac{\text{N-m}}{\text{J}} \quad (2.30)$$

$$\boxed{\vec{F} = 400 \text{ N}} \quad (2.31)$$

f. Magnetic Actuator Configurations

Multiple configurations of magnetic actuators are shown in **Fig. 2.11 – 2.22.**

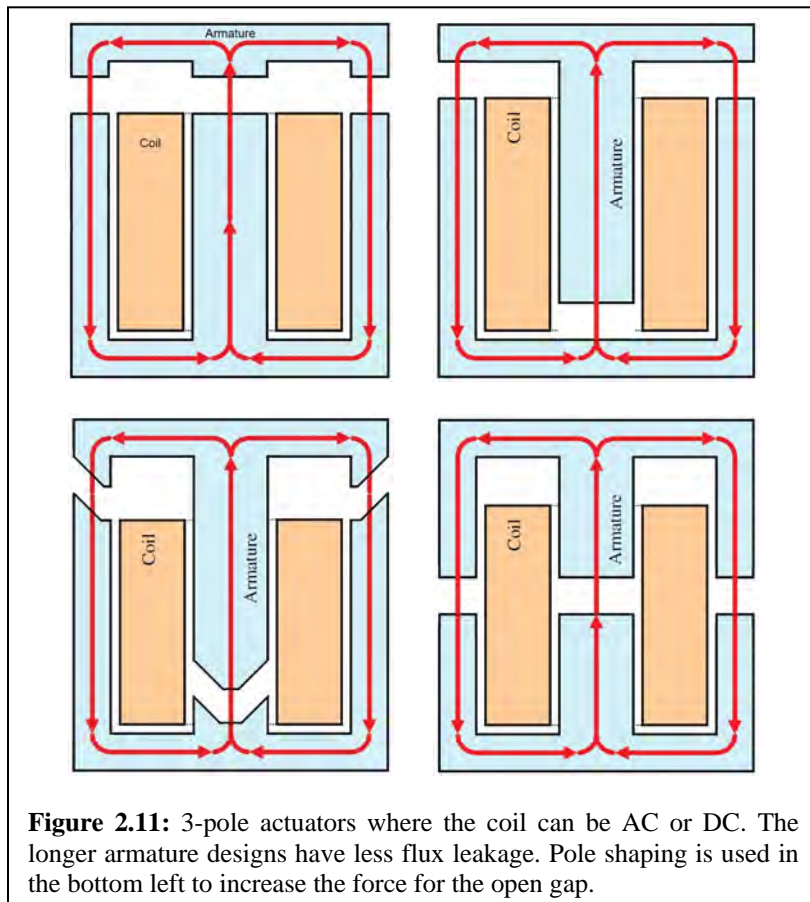


Figure 2.11: 3-pole actuators where the coil can be AC or DC. The longer armature designs have less flux leakage. Pole shaping is used in the bottom left to increase the force for the open gap.

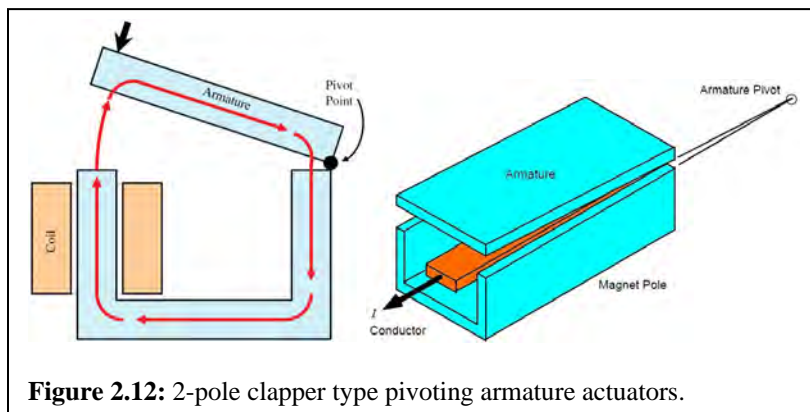


Figure 2.12: 2-pole clapper type pivoting armature actuators.

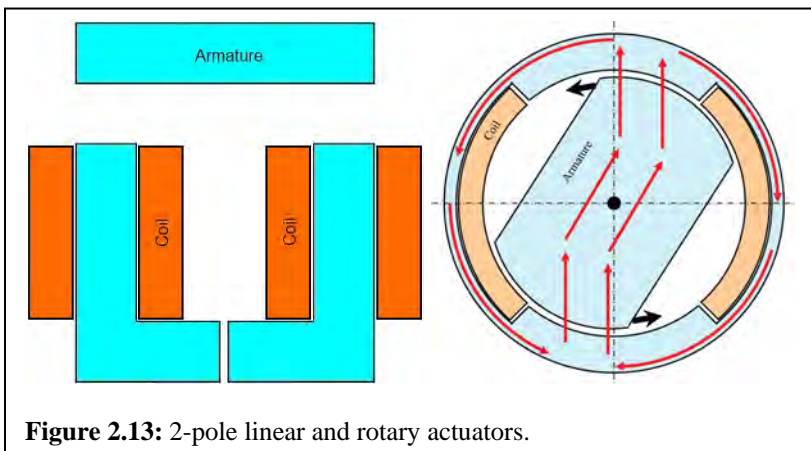


Figure 2.13: 2-pole linear and rotary actuators.

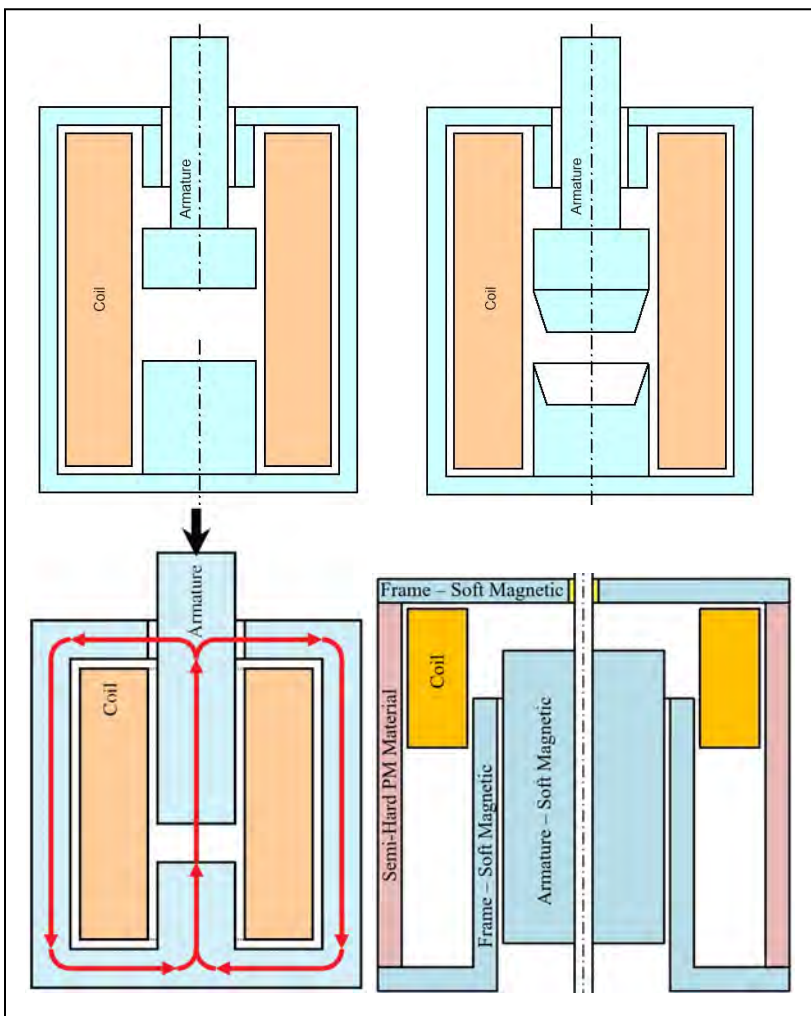


Figure 2.14: Axisymmetric Solenoids. The top 2 use pole shaping. The bottom right uses a semi-hard (easily magnetizable and de-magnetizable) material in the outer shell to hold it closed and to allow it to open.

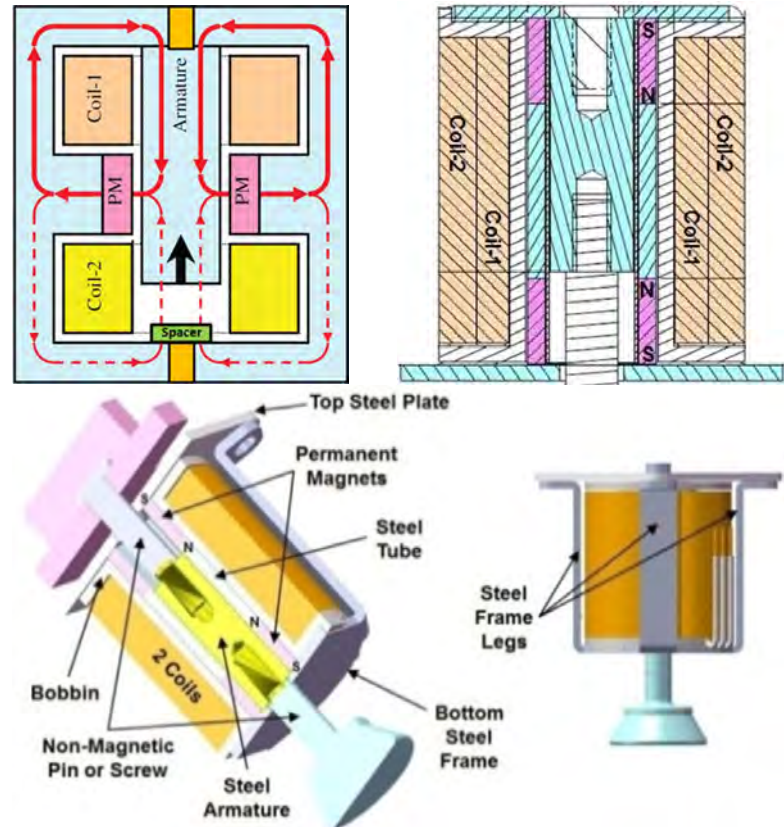


Figure 2.15: 2-way hold permanent magnet actuators. The top right and the bottom images are different views of the same actuator. The permanent magnet holds the armature at the top position. A coil pulse causes the armature to move to the bottom position. The permanent magnet then holds the armature at the bottom.

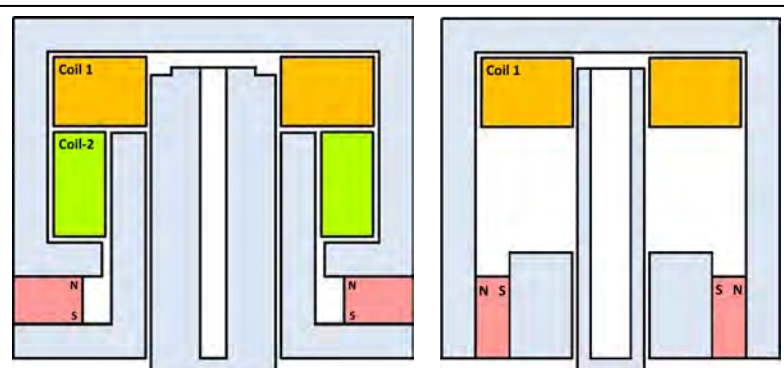


Figure 2.16: 1-way hold permanent magnet actuators. A coil pulse causes the armatures to move to the top position, where the permanent magnet holds it. A coil pulse cancels the permanent magnet holding flux and allows a spring to move the armature to the bottom.

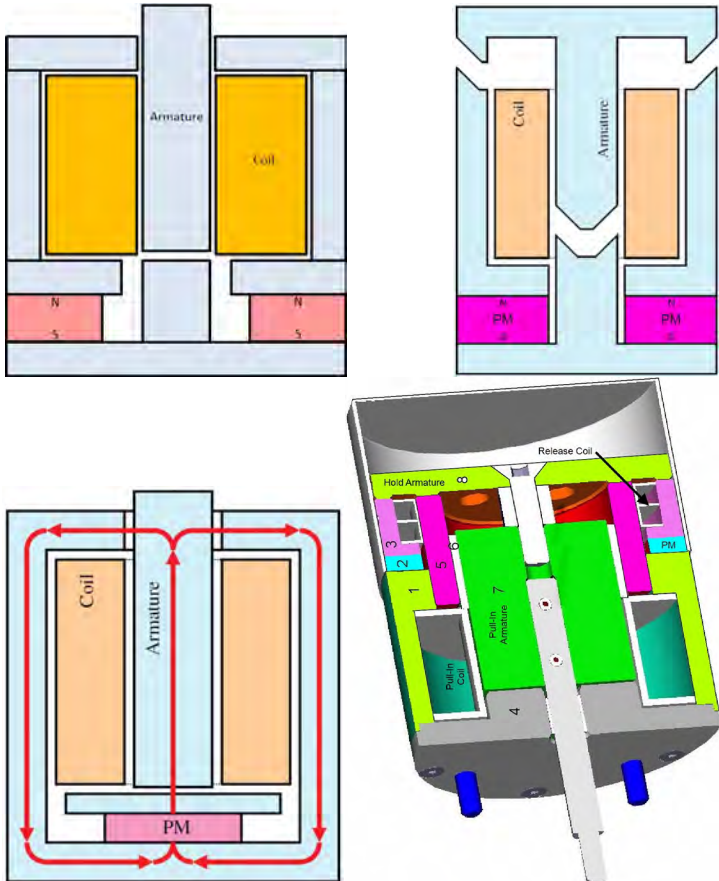


Figure 2.17: 1-way hold permanent magnet actuators. The top 2 and the bottom left actuators are designed to be closed with an external force. A coil pulse causes the actuators to open with a spring force. The bottom right actuator is designed to close with a coil pulse, hold with a permanent magnet, and open with a coil pulse.

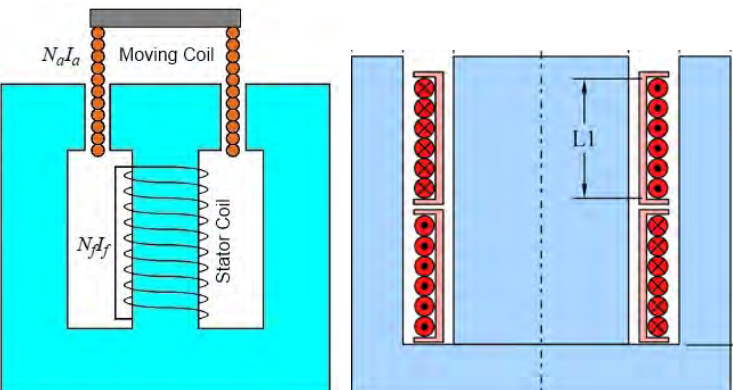


Figure 2.18: Axisymmetric moving coil (Voice Coil) actuators. The bottom coil produces magnetic flux on the top coil, and the current in the top coil interacts with the magnetic flux to produce a Lorentz force.

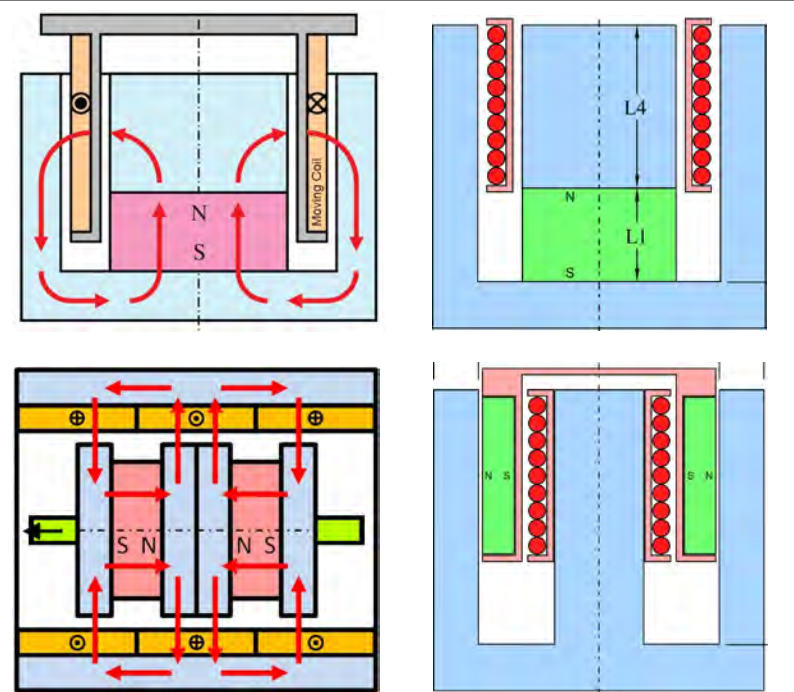


Figure 2.19: Axisymmetric moving coil actuators (Voice Coils) (Top). Coil current interacts with magnetic flux from the permanent magnets. Axisymmetric moving permanent magnet actuators (Bottom).

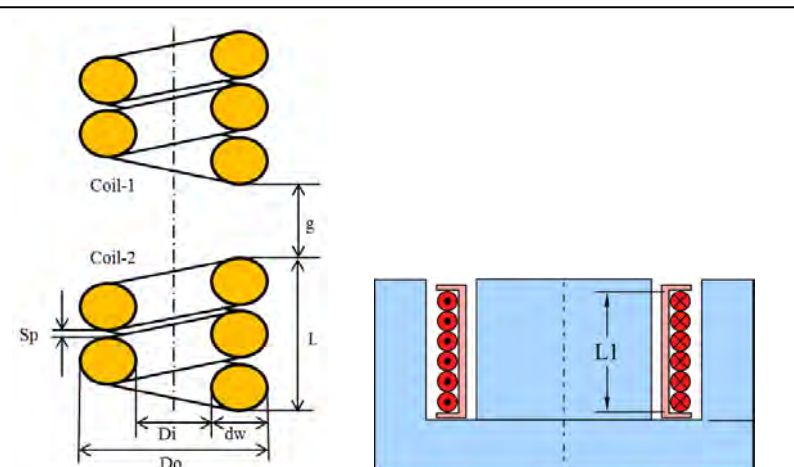


Figure 2.20: The current in the top coil of the left image interacts with the magnetic flux from the bottom coil. The right image is a slot motor in which the coil interacts with its own magnetic flux and moves down into the slot.

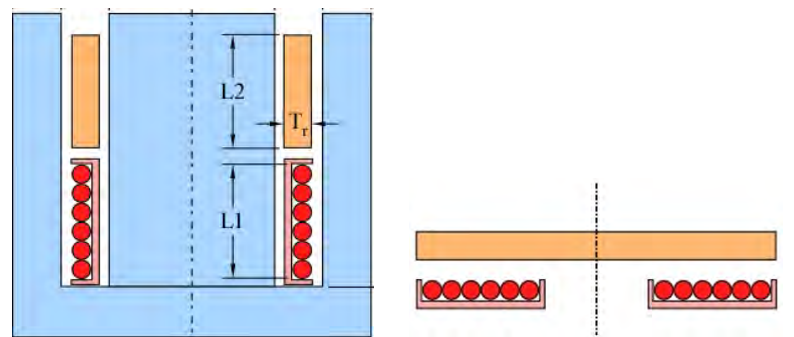


Figure 2.21: Eddy current actuators. The bottom coil produces a fast changing magnetic flux through a conductive ring or plate, which causes eddy currents that interact with the magnetic flux to produce an upward Lorentz force. The actuator on the right is called a Thomson coil.

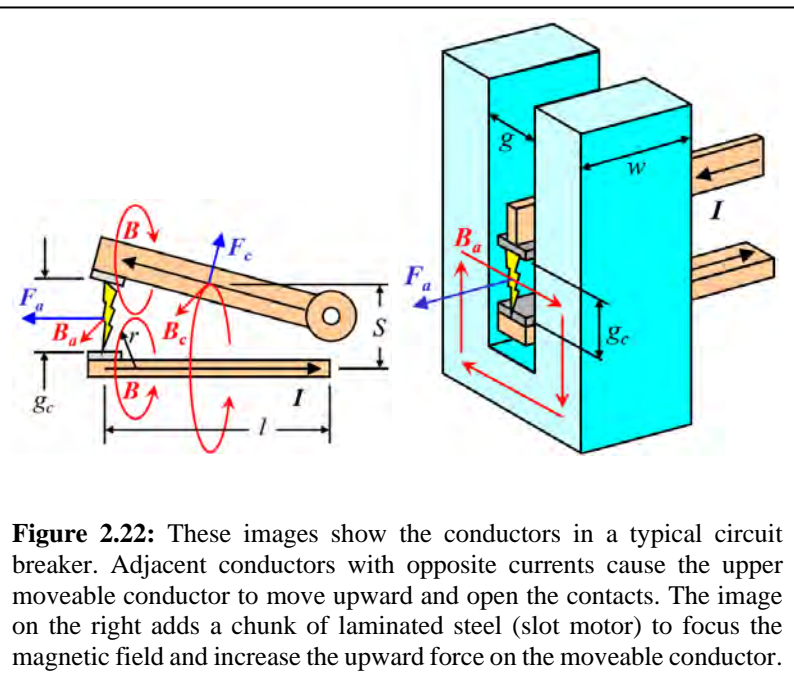


Figure 2.22: These images show the conductors in a typical circuit breaker. Adjacent conductors with opposite currents cause the upper moveable conductor to move upward and open the contacts. The image on the right adds a chunk of laminated steel (slot motor) to focus the magnetic field and increase the upward force on the moveable conductor.

g. Actuator Technologies

Actuator technologies are listed below (Fig. 2.23) showing the cost of a typical actuator per unit of mechanical energy delivered (Green Bars, \$/J), and the mechanical energy delivered for a typical actuator per unit volume (Orange Bars, Energy Density, J/m³). Note that the widely used actuator technologies have the lowest cost, but not always the highest energy density.

All of these performance values were calculated from manufacturer datasheet properties and characteristics. The strain for SMA materials is < 3% to get high fatigue life (fatigue life < 1,000 cycles at 8% strain). The PZT prototype is from an actuator that was tested with material from Kinetic Ceramics. The bimetal design and cost are from a production Eaton circuit breaker.

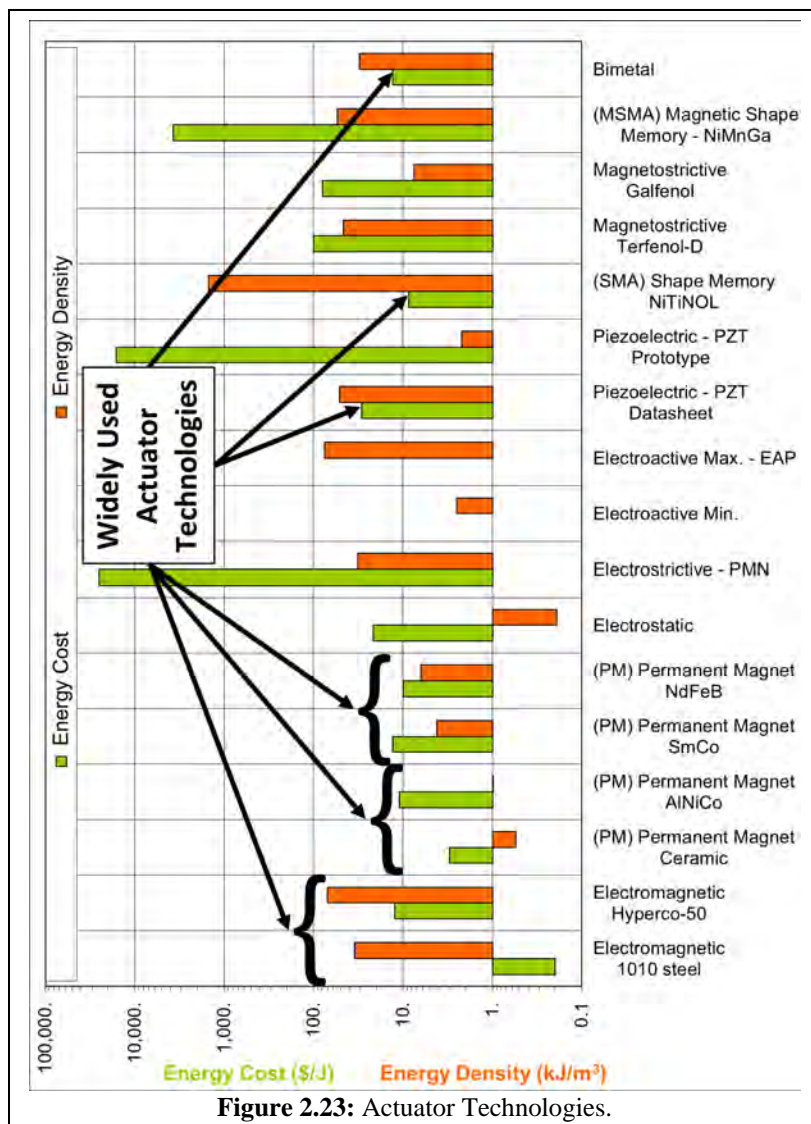


Figure 2.23: Actuator Technologies.

h. Example-2 – Gapped Core

A coil (**Fig. 2.24**) is wound on a steel ring, and the steel ring has an air gap (**Fig. 2.25**). Assume no flux leakage across the steel ring.

$$\begin{aligned} D &= 0.10 \text{ m} \\ d &= 0.01 \text{ m} \\ t &= 0.01 \text{ m} \\ g &= 0.001 \text{ m} \\ N &= 10. \text{ turns} \\ I &= 5. \text{ amperes-DC} \\ \mu_r &= 5,000. \text{ ---} \\ \mu_0 &= 4\pi E-7 \text{ T-m/A-t} \end{aligned}$$

Find: \mathcal{P} , \mathcal{R} , ϕ , B , L , F

Find: NI to saturate

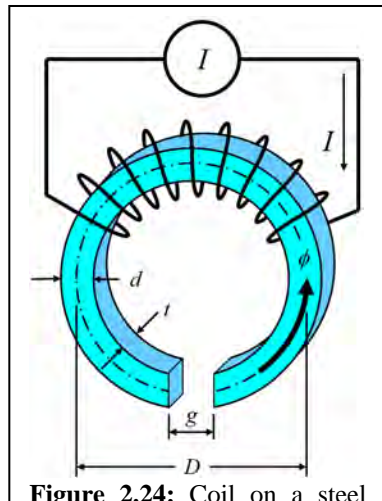


Figure 2.24: Coil on a steel core with an air gap.

The calculations for the permeance method are detailed below. The permeance results are summarized in **Fig. 2.26**. The permeance results are compared with the results from 4 finite element simulations (**Fig. 2.29**) to show validity for the permeance method and to show how small modeling details and can give varying results. The permeances \mathcal{P}_6 , \mathcal{P}_7 , \mathcal{P}_8 , \mathcal{P}_9 , are small and not calculated for simplification.

Calculations:

Air Gap Permeance:

$$\mathcal{P}_1 = \mu_0 \frac{a}{g} \quad (1.47)$$

$$\mathcal{P}_2 = 0.24 \mu_0 w \quad (1.52)$$

$$\mathcal{P}_4 = \mu_0 \frac{w}{\pi} \ln \left(1 + 2 \frac{h}{g} \right) \quad (1.63)$$

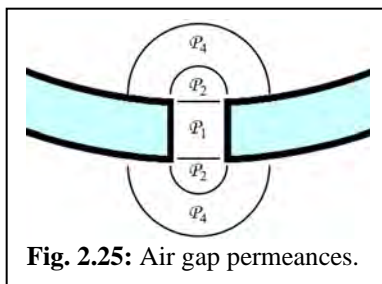


Fig. 2.25: Air gap permeances.

$$\text{Fringing Width: } w = 2d + 2t = 0.04 \text{ m} \quad (2.32)$$

$$\text{Path (1): } \mathcal{P}_1 = (4\pi E - 7) \frac{(0.01)(0.01)}{0.001} = 1.26E - 7 \frac{\text{Wb}}{\text{A}} \quad (2.33)$$

$$\text{Path (2): } \mathcal{P}_2 = (0.24)(4\pi E - 7)(0.04) = 1.21E - 8 \frac{\text{Wb}}{\text{A}} \quad (2.34)$$

$$\text{Path (4): } \mathcal{P}_4 = (4\pi E - 7) \frac{0.04}{\pi} \ln \left(1 + 2 \frac{0.01}{0.001} \right) = 4.87E - 8 \frac{\text{Wb}}{\text{A}} \quad (2.35)$$

Air Gap Permeance:	$\mathcal{P}_A = \mathcal{P}_1 + \mathcal{P}_2 + \mathcal{P}_4 = 1.864E - 7 \frac{\text{Wb}}{\text{A}}$	(2.36)
--------------------	---	--------

Air Gap Reluctance:	$\mathcal{R}_A = \frac{1}{\mathcal{P}_A} = 5.36E + 6 \frac{\text{A}}{\text{Wb}}$	(2.37)
---------------------	--	--------

Steel Reluctance:

Steel Path Length: $l_F = \pi D - g = 0.3132 \text{ m}$ (2.38)

Steel Permeance:

$$\mathcal{P}_F = \mu_r \mu_0 \frac{a}{l_F} = (5000)(4\pi E - 7) \frac{0.0001}{0.3132} = 2.01E - 6 \frac{\text{Wb}}{\text{A}}$$
 (2.39)

Steel Reluctance: $\mathcal{R}_F = \frac{1}{\mathcal{P}_F} = 0.498E + 6 \frac{\text{A}}{\text{Wb}}$ (2.40)

Total Reluctance: $\mathcal{R} = \mathcal{R}_A + \mathcal{R}_F = 5.862E + 6 \frac{\text{A}}{\text{Wb}}$ (2.41)

Total Permeance: $\mathcal{P} = \frac{1}{\mathcal{R}} = 1.71E - 7 \frac{\text{Wb}}{\text{A}}$ (2.42)

Results for ϕ, B, L : ($NI_c = 50 \text{ A-t}$)

Flux: $\phi = \frac{NI}{\mathcal{R}} = \frac{(10)(5)}{5.862E + 6} \quad \boxed{\phi = 8.53E - 6 \text{ Wb}}$ (2.43)

Core Flux Density: $B = \frac{\phi}{a} = \frac{8.53E - 6}{1.0E - 4} \quad \boxed{B = 0.085 \text{ T}}$ (2.44)

Inductance: $L = N^2 \mathcal{P} = (10^2)(1.71E - 7) = 17.1E - 6 \text{ H}$ (2.45)

$\boxed{L = 17.1 \mu\text{H}}$ (2.46)

Calculate Coil NI to saturate: ($B_{sat} = 1.6 \text{ T}$)

$$\phi = Ba = (1.6)(1.0E - 4) = 1.6E - 4 \text{ Wb}$$
 (2.47)

$$NI_c = \phi \mathcal{R} = (1.6E - 4)(5.862E + 6)$$
 (2.48)

$\boxed{NI_c = 938. \text{ ampere-turns}}$ (2.49)

Calculate Force F : ($NI_c = 50 \text{ A-t}$ $B = 0.085 \text{ T}$)

Force: $F = \frac{1}{2}(NI_A)^2 \frac{d\mathcal{P}_A}{dg} = \frac{1}{2}(NI_A)^2 \left(\frac{d\mathcal{P}_1}{dg} + \frac{d\mathcal{P}_4}{dg} \right)$ (2.50)

Note that \mathcal{P}_2 is not part of Eq. 2.50, because \mathcal{P}_2 is independent of g .

Path (1): $\frac{d\mathcal{P}_1}{dg} = \mu_0 \frac{a}{g^2} = \frac{\mathcal{P}_1}{g} = \frac{1.26E - 7}{0.001} = 1.26E - 4 \frac{\text{Wb}}{\text{A-m}}$ (2.51)

Path (4): $\frac{d\mathcal{P}_4}{dg} = \mu_0 \frac{w}{\pi} \left(\frac{2h/g}{1+2h/g} \right) \left(\frac{1}{g} \right)$ (2.52)

$$\frac{d\mathcal{P}_4}{dg} = (4\pi E - 7) \left(\frac{0.04}{\pi} \right) \left(\frac{20}{21} \right) \left(\frac{1}{0.001} \right) = 1.52E - 5 \frac{\text{Wb}}{\text{A}}$$
 (2.53)

$$NI_A = \phi \mathcal{R}_A = (8.53E - 6)(5.364E + 6) = 45.75 \text{ A-t}$$
 (2.54)

$$F = \frac{1}{2}(NI_A)^2 \left(\frac{d\mathcal{P}_1}{dg} + \frac{d\mathcal{P}_4}{dg} \right) = \frac{1}{2}(45.75)^2 (1.409E - 4)$$
 (2.55)

$\boxed{F = 0.148 \text{ N} = 0.0333 \text{ lb}_f} \quad (NI_c = 50 \text{ A-t} \quad B = 0.085 \text{ T})$ (2.56)

The air gap flux density B_1 can also be calculated, as follows:

Air Flux Density	$B_1 = \frac{\phi_1}{a_1} = \frac{NI_A \mathcal{P}_1}{a_1} = \frac{(45.75)(1.26E-7)}{0.0001} = 0.0576 \text{ T}$	(2.57)
------------------	--	--------

Check the Force calculation using Eq. 2.24 (Fig. 2.6):

$$\text{Force: } (B = 0.085 \text{ T}) \quad \left(\frac{g}{d} \right) = \frac{0.001}{0.01} = 0.10 \quad p_{\max} = 0.218 \text{ MPa} \quad (2.58)$$

$$\text{Force: } (B = 0.085 \text{ T}) \quad F = p_{\max} a = 0.218(d)^2 \text{ N} \quad (2.59)$$

$$\text{Force: } (B = 0.085 \text{ T}) \quad \boxed{F = 0.155 \text{ N} \quad F = 0.0348 \text{ lb}_f} \quad (2.60)$$

This is within 4.7% of the force from **Eq. 2.56** and confirms its validity. The force at saturation ($B_{sat} = 1.6 \text{ T}$) can be calculated as follows from **Eq. 2.60** and **Eq. 2.44**.

$$\text{Force: } (B_{sat} = 1.60 \text{ T}) \quad F_{sat} = F \left(\frac{B_{sat}}{B} \right)^2 = 0.148 \left(\frac{1.60}{0.085} \right)^2 \quad (2.61)$$

$$\text{Force: } (B_{sat} = 1.60 \text{ T}) \quad \boxed{F_{sat} = 52.44 \text{ N} \quad = 11.79 \text{ lb}_f} \quad (2.62)$$

Results ($NI_C = 50 \text{ A-t}$)			Perm-1 w / Fringing	Perm-2 No Fringing
Steel Relative Permeability		---	$\mu = 5,000$	$\mu = \text{Infinite}$
Air Gap Permeance	\mathcal{P}_1	Wb/A	$1.257E-7$	$1.257E-7$
Air Gap Permeance	\mathcal{P}_2	Wb/A	$0.121E-7$	0
Air Gap Permeance	\mathcal{P}_4	Wb/A	$0.487E-7$	0
Air Gap Permeance	\mathcal{P}_A	Wb/A	$1.864E-7$	$1.257E-7$
Air Gap Reluctance	\mathcal{R}_A	A/Wb	$5.364E+6$	$7.958E+6$
Steel Reluctance	\mathcal{R}_F	A/Wb	$4.980E+5$	0
Total Reluctance	\mathcal{R}	A/Wb	$5.862E+6$	$7.958E+6$
Total Permeance	\mathcal{P}	Wb/A	$1.706E-7$	$1.257E-7$
Core Magnetic Flux	ϕ	Wb	$8.529E-6$	$6.283E-6$
Core Flux Density	B_c	T	0.0853	0.0628
Air Gap Flux Den.	B_g	T	0.0576	0.0628
Inductance	L	μH	17.1	12.6
Air Gap NI	NI_A	A-t	45.75	50.00
Force	F	N	0.148	0.157
Force	F	lb _f	0.033	0.035
Results ($NI_C = 938 \text{ A-t}$)			Perm-1	Perm-2
Core Flux Density	B_c	T	1.60	---
Force	F	N	52.4	---
Force	F	lb _f	11.8	---

Figure 2.26: Permeance results summary. **Perm-1** is from the calculations above (**Eq. 2.32 – Eq. 2.62**). **Perm-2** is a simplified calculation with no steel reluctance and no fringing in the air gap.

The relative importance of the steel reluctance and the air gap fringing is shown in **Fig. 2.26**. The **Perm-1** results are from a detailed calculation. The **Perm-2** results are from a simplified calculation, with no steel reluctance (infinite permeability) and no air gap fringing permeance (using only the direct flux path permeance P_1). The total reluctance is increased by 8.5% due to the core reluctance, and reduced by 32.7% due to the air gap fringing permeance. The simplified calculation of **Perm-2** gives lower values for core flux density and inductance, and higher values for air gap flux density and force (highlighted in yellow). The **Perm-2** values for the core magnetic flux density and inductance are 26% lower than for **Perm-1**. The **Perm-2** values for the force across the air gap are 6% higher than for **Perm-1**.

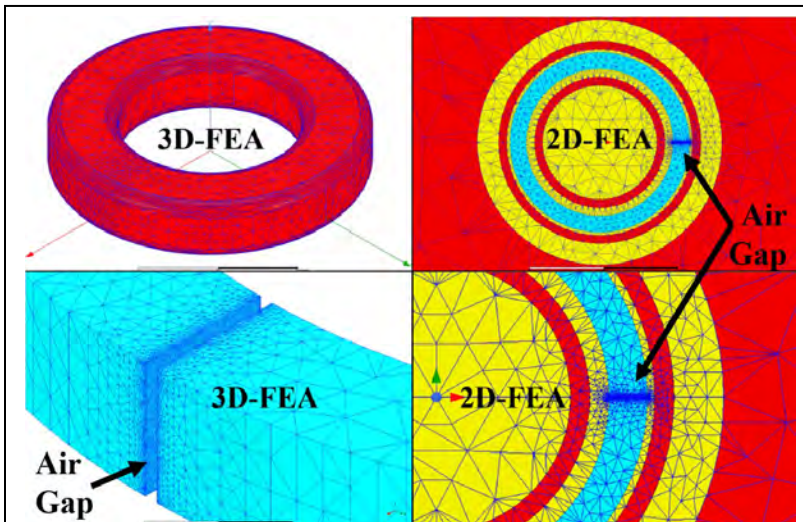


Figure 2.27: Mesh for the 3D and 2D finite element magnetic models.

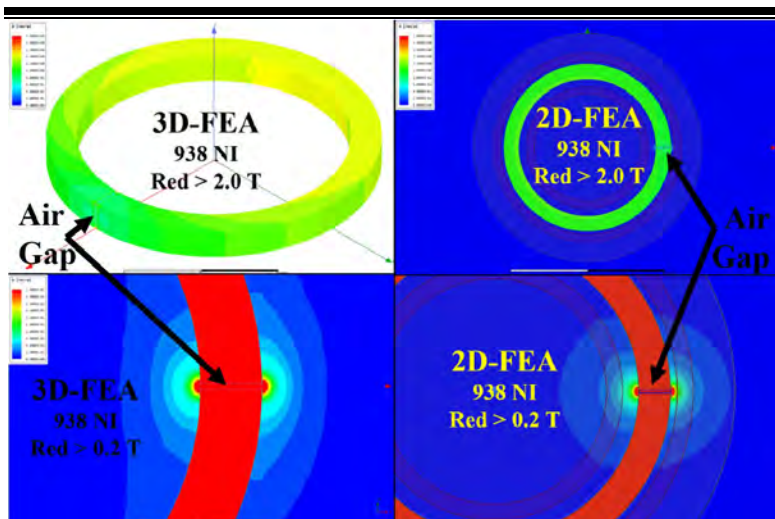


Figure 2.28: Core flux density distribution (top plots), and air gap density distribution showing fringing flux (bottom plots) at 938 NI.

Finite element simulations were performed with ANSYS Maxwell by Mary Jo Vander Heiden of Mag-Num Consulting Services, LLC. Finite element magnetic models were constructed in 2D and 3D, with a toroidal coil formed on the entire core circumference, as shown in **Fig. 2.27**. The results from both permeance models (**Perm-1**, **Perm-2**) and both FEA models (3D and 2D) are compared in **Fig. 2.29**. The permeance models ignore flux leakage. However, the 3D-FEA model shows some small flux leakage across the diameter of the core, indicated by the increased core flux density opposite to the core air gap (**Fig. 2.28**, top left, Green = 1.0 T, Yellow = 1.5 T). The 2D-FEA model shows no significant flux leakage and the difference in results (flux density, inductance, force) between the 3D and 2D FEA models is small, which validates the assumption to ignore flux leakage. Observations and conclusions from the analysis results are listed below.

1. The **Perm-2** calculation does not include air gap fringing permeance. Therefore, the overall permeance is smaller, which results in a smaller core flux density and a smaller inductance than **Perm-1**.
2. The force across the air gap is generally in good agreement between all models (Perm and FEA).
3. The 3D-FEA model has some flux leakage, as shown by the slightly higher core flux density opposite the air gap. Therefore, the 3D-FEA inductance is slightly higher than for the 2D-FEA model.
4. The inductance for the 3D-FEA and 2D-FEA models is low because the coil is wound across the air gap, which minimizes the air gap fringing flux. These inductance values are in good agreement with the **Perm-2** inductance, which ignored the fringing permeances.
5. All of the Permeance model results are generally in good agreement with the FEA model results.

Coil NI	NI	50			
Model		Perm-1	Perm-2	3D-FEA	2D-FEA
Bcore-max	T	0.085	0.063	0.077	0.053
Bgap-max	T	0.058	0.063	0.031	0.038
Inductance	μH	17.1	12.6	13.6	10.4
Force	lbf	0.033	0.035	0.046	0.040
Force	N	0.148	0.157	0.205	0.178
Coil NI	NI	938			
Model		Perm-1	Perm-2	3D-FEA	2D-FEA
Bcore-max	T	1.60	---	1.37	1.08
Bgap-max	T	1.09	---	0.57	0.77
Inductance	μH	17.1	12.6	13.2	11.2
Force	lbf	11.8	---	15.2	16.2
Force	N	52.5	---	67.7	72.2

Figure 2.29: Results summary for the Permeance and FEA models.

i. Example-3 – Effect of Permeability

The relative permeability (μ_r) of the core in **Example-2** is varied from 300 to 100,000, and the air gap (g) in the core is varied from 0.1 mm to 1.0 mm.

The calculations in **Example-2** are repeated for the different values of the core air gap (g) and the core relative permeability (μ_r). The objective is to determine how the coil NI varies for each value of the core air gap (g) and the core relative permeability (μ_r), to achieve a core magnetic flux density of 1.52 Tesla (95% of saturation).

Results (**Fig. 2.30**) show:

- At low relative permeability ($\mu_r < 3,000$) ... Increasing the permeability reduces the coil current and coil NI inversely proportional to the change in relative permeability.
- At high relative permeability ($\mu_r > 3,000$) ... Increasing the permeability has no significant effect on the coil current or coil NI .
- A larger air gap (g) increases the coil current and coil NI in proportion to the air gap, regardless of the core relative permeability (μ_r).

High permeability materials are typically high cost. Therefore, increasing the relative permeability of the material beyond $\mu_r = 3,000$, may not be economically practical.

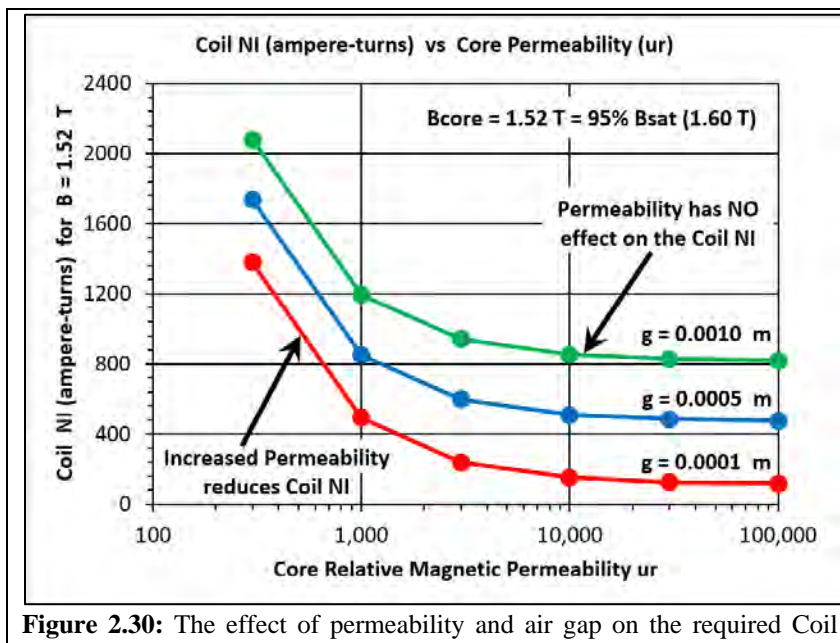


Figure 2.30: The effect of permeability and air gap on the required Coil current and Coil NI for a magnetic system with a gapped core.

3. Magnetic Materials

a. Basics – Soft and Hard Materials

Soft magnetic materials are defined as easy to magnetize and demagnetize, therefore they are soft relative to external magnetic fields. Soft magnetic materials also have a high magnetic permeability and low losses. Many soft magnetic materials are also characterized as physically soft, for example, iron alloys that exhibit the best soft magnetic properties tend to be annealed and contain a low alloy content of carbon and a hardness as low as 130 Brinell Hardness Number (BHN). However, ceramic materials are physically hard.

Materials that show soft magnetic characteristics include the following.

- Metal Alloys: Fe, FeC, Ni, Co, NiFe, FeCo, FeSiAl
- Steel Alloys: 1010, 1018, 1020, 1030, 12L14, 12L15
- Glassy Metals: Metglas-FeBSiC, Metglas-FeBMoNiCo
- Nano-Crystalline Metals: FeSiBCuNb
- Ceramic Ferrites: MnFeO, NiFeO, ZnFeO, MgFeO, MnZn, NiZn
 - Note that ceramic ferrites are physically very hard

Hard magnetic materials are generally referred to as permanent magnets. They are difficult to magnetize and demagnetize, therefore they are hard relative to external magnetic fields. Hard magnetic materials have a low magnetic permeability and high losses and are typically characterized as physically hard, for example, iron alloys that exhibit the best hard magnetic properties tend to be hardened by heat treatment and contain a high alloy content of carbon with a hardness as high as 690 BHN. Permanent magnet steel was available from China as early as 500 A.D. and highly alloyed cobalt steels were available with 1.2% carbon by 1920.

Materials that show hard magnetic characteristics include the following.

- Alloys: AlNiCo, SmCo, NdFeB
- Ceramic Ferrites: SrFeO, BaFeO
- Hardened Steel Alloys: 1090 (contain 0.9% carbon)

Magnetic materials are generally composed of atoms in a crystal structure, although glassy metals have no crystal structure. Magnetic property characteristics are produced in a magnetic material primarily as the result of electron spin. Magnetic properties are also produced by smaller effects from the electron orbit and nuclear spin [3, 10, 16].

- **Electron Spin:** Electrons spinning on their axis produce a magnetic field. Only electrons in shells that are partially filled produce a magnetic field. The electron spin is more than an order of magnitude larger than the magnetic field produced by the electron orbit.
- **Electron Orbit:** Electrons circulating atoms in orbits produce a magnetic field. This is not significant for ferromagnetic materials. It's significant only for diamagnetic and paramagnetic materials,

and for rare earth elements such as Gd. The magnetic properties of most materials (diamagnetic, paramagnetic, antiferromagnetic) are so weak that they are commonly considered to be nonmagnetic.

- **Nuclear Spin:** The spin of the nucleus is the basis for nuclear magnetic resonance imaging (MRI). This is not significant relative to the overall magnetic properties of materials.

A magnetic material such as low carbon steel contains about 10^{23} atoms per cubic centimeter. The atoms form groups called **domains**, each containing about 10^{15} atoms, in which all the atoms have the same electron spin. The atoms also form into regions called **grains**, in which all the atoms have the same crystal orientation. There are approximately 10^5 domains in a grain and about 10^3 grains per cubic centimeter. [13, 14, 20]

The **Exchange Force** [3, 10, 16] is an interaction (or coupling) between the spins of electrons in neighboring atoms, and it causes the electrons in neighboring atoms to have the same spin and produce magnetic properties. The exchange force is a quantum effect related to the indistinguishability of electrons. It can be positive or negative and it can be weakly or strongly coupled.

- **Negative Exchange Force:** Chromium and Manganese (in which each atom is strongly magnetic) have a strong negative exchange coupling, which forces the electron spins of neighboring atoms to be in opposite directions and results in antiferromagnetic (very weak) magnetic properties.
- **Positive Exchange Force:** Iron, Cobalt, and Nickel have unbalanced electron spins (in which each atom is strongly magnetic) and has a strong positive exchange coupling. Therefore, the spins of electrons in neighboring atoms point in the same direction and produce a large macroscopic magnetization. This largescale atomic cooperation is called ferromagnetism.

The exchange force in strongly magnetic atoms depends on the atomic spacing as shown in the Bethe-Slater curve (**Fig. 3.1**) [3, 7, 10, 16]. The atomic spacing can be changed with alloy elements or by mechanical strain. The magnetic permeability of Nickel increases when it is compressed and decreases when it is stretched, and the magnetic permeability of 68 permalloy (68% Ni 32% Fe) behaves oppositely. Ferritic stainless steel (400 series) is magnetic. Austenitic stainless steel (300 series) is not magnetic, but the relative permeability can reach $\mu_r = 10$ when it is strained. Also, alloys of MnBi, Cu₂MnSn, and Cu₂MnAl are ferromagnetic because of the increased atomic spacing between Mn atoms that results in a positive Exchange Force.

When a magnetic material is magnetized, the electron spins rotate into alignment. The aligned domains expand and the non-aligned domains shrink as the domain walls move through the atomic structure. Magnetizing a magnetic material can produce mechanical strain (known as magnetostriction). This mechanical strain is a change in atomic spacing as a

result of the magnetic field, which is very common in materials such as Fe, Ni, and in giant magnetostriction materials (TerFeNOL-D, GalFeNOL).

Magnetostriction is a Magneto-Elastic or Magneto-Mechanical effect that results from a balance between the magnetic energy and the mechanical strain energy and a rotation of the elliptical electron orbits. The energy balance produces a shift toward the peak of the Bethe-Slater curve. See references [3, 7, 10, 16] for complete details.

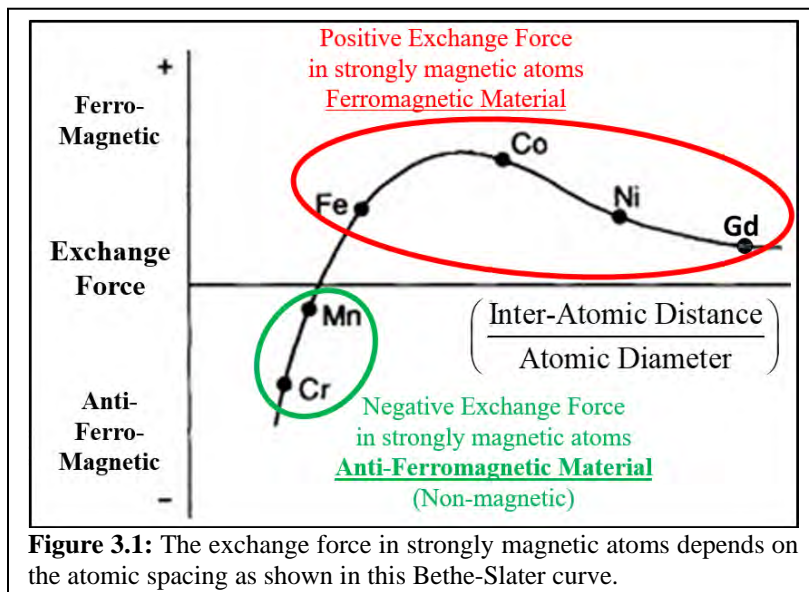


Figure 3.1: The exchange force in strongly magnetic atoms depends on the atomic spacing as shown in this Bethe-Slater curve.

The domain boundaries (or walls) move through the atomic structure during magnetization as the electron spins rotate into alignment [3, 5, 7, 16]. The energy required to align the electron spins and electron orbits of atoms depends on the local atomic structure, such as the strain energy in the crystal structure due to residual mechanical strain or the position of alloying atoms.

Quench hardening permanent magnet steels contain nonmagnetic carbide inclusions that form in the grain boundaries due to alloying elements. The motion of a domain wall through a nonmagnetic inclusion requires more energy, which makes it more difficult to magnetize and demagnetize. In some high energy permanent magnet materials, the domain walls are pinned at the grain boundaries by carbide or other intermetallic compounds. The energy required to move the domain wall in a pinned domain is very high. If the domain wall remains pinned, the entire domain will not rotate to align with the magnetizing field or demagnetizing field.

b. Soft Magnetic Materials

Soft magnetic materials have a narrow hysteresis loop (**Fig. 3.2**). The width of the hysteresis loop or coercivity (H_c) is small and the area or energy inside the hysteresis loop (BH) is small. A material with a smaller coercivity

requires less energy to magnetize and demagnetize. The area (energy) inside the hysteresis loop represents the energy that is dissipated during cyclic magnetizing and demagnetizing, such as in a motor or transformer or inductor. A material with a smaller hysteresis loop energy will dissipate less heat during cyclic applications.

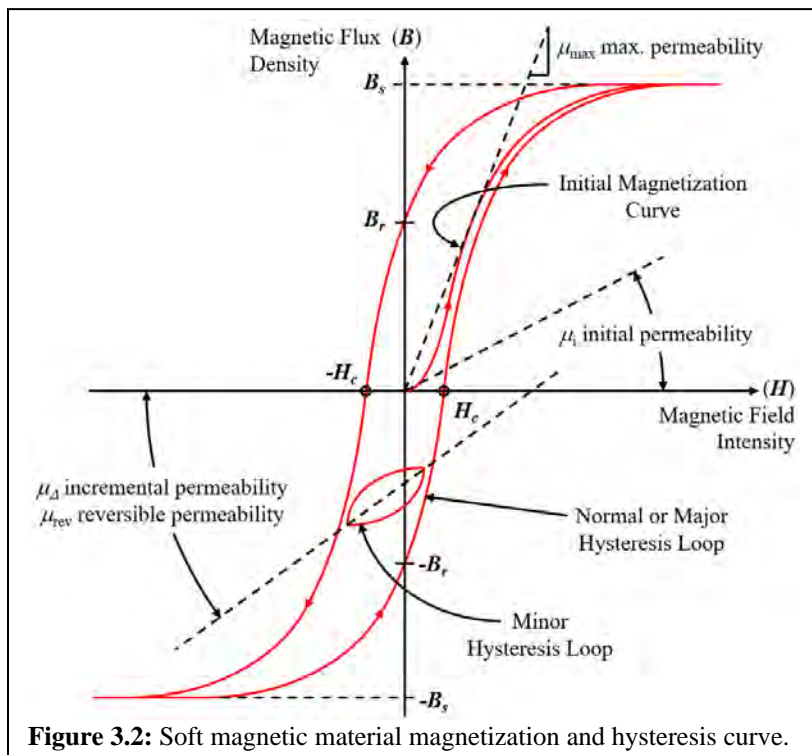


Figure 3.2: Soft magnetic material magnetization and hysteresis curve.

Residual mechanical strain or alloying elements add energy to the crystal structure (inclusions, dislocations, atomic space) that increases coercivity (H_c), reduces permeability (μ_{\max}), and increases the hysteresis loop energy (BH).

The hysteresis loop characteristics listed below are generally used in most magnetic performance calculations. Additional terminology (Fig. 3.2) includes the normal or major hysteresis loop, the minor hysteresis loop for partial magnetization and demagnetization (with the incremental (μ_Δ) and reversible (μ_{rev}) permeability), and the initial permeability (μ_i) at the start of magnetization.

Hysteresis Loop Characteristics

B_s = Saturation Flux Density (T)

B_r = Residual Flux Density (T)

H_c = Coercivity (A/m)

BH = Hysteresis Loop Area (T-A/m, J/m³)

μ_{\max} = maximum permeability (H/m)

c. Curie Temperature

Ferromagnetic properties of materials disappear when the Curie Temperature (T_C) is reached. This temperature is also called the Curie Point. Iron, Nickel, and Cobalt are the only ferromagnetic elements that have a Curie Point above room temperature, as shown in **Fig. 3.3**.

<u>Element</u>		T_C		<u>B_s, Intrinsic Saturation</u>	<u>Ref.</u>
		<u>Curie Temperature</u>	<u>Flux Density (T)</u>		
Cobalt	Co	1388 °K	1115 °C	1.790	[7]
Iron	Fe	1043 °K	770 °C	2.158	[7]
Nickel	Ni	631 °K	358 °C	0.608	[7]
Gadolinium	Gd	291.8°K	18.8°C	----	[11]
Terbium	Tb	221 °K	-52 °C	----	[11]
Dysprosium	Dy	92.1°K	-180.9°C	----	[11]
Thulium	Tm	32 °K	-241 °C	----	[12]
Holmium	Ho	20 °K	-253 °C	----	[11]
Erbium	Er	18.7°K	-254.3°C	----	[11]

Figure 3.3: Cure Temperature or Curie Point of the magnetic elements.

The saturation magnetic flux density as a function of temperature is shown in **Fig. 3.5** for 6 soft magnetic ferrite materials. The curves show that the saturation flux density falls off at a fairly constant slope. The constant slope ranges from -12 Gauss/°C to -22 Gauss/°C. The saturation flux density falls off fairly fast within about 25°C to 50°C of the Curie Point. The Curie Point ranges from 130°C to 280°C. These measurements were done in 1990 for materials from Ceramic Magnetics and TSC Ferrite International.

The saturation flux density temperature curves were fit to **Eq. 3.1**, and the coefficients are listed in **Fig. 3.4** for each of the 6 ceramic ferrite materials.

$$B_s = (B_{25} + S(T - 25)) \left(1 - e^{(2(T - T_c)/T_f)} \right) \quad (3.1)$$

<u>CMD5005</u>	<u>CN20</u>	<u>MN60</u>
$T_c = 130$ °C	$= 180$ °C	$= 170$ °C
$B_{25} = 3300$ G	$= 3100$ G	$= 4600$ G
$S = -16$ G/°C	$= -12$ G/°C	$= -22$ G/°C
$T_f = 19$ °C	$= 17$ °C	$= 15$ °C
<u>MN8CX</u>	<u>TSF-8040</u>	<u>MN67</u>
$T_c = 185$ °C	$= 227$ °C	$= 280$ °C
$B_{25} = 4300$ G	$= 4600$ G	$= 5200$ G
$S = -15.5$ G/°C	$= -15$ G/°C	$= -14$ G/°C
$T_f = 35$ °C	$= 26$ °C	$= 68$ °C

Figure 3.4: Ceramic ferrite material coefficients for **Eq. 3.1**.

The magnetic saturation flux density for ferrite materials (**Fig. 3.5**) decreases approximately linearly as temperature increases until the temperature is near the Curie point. Iron alloys have a similar temperature characteristic. This is described by more complex functions such as Langevin or Brillouin functions.

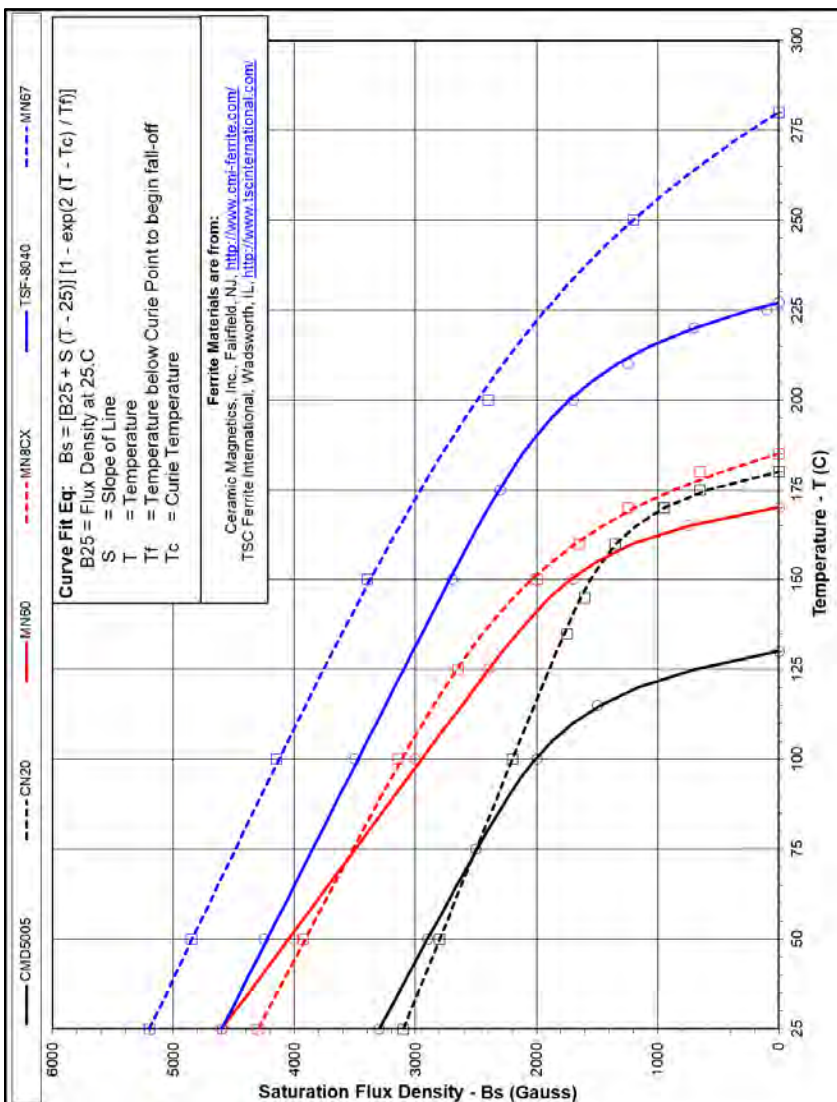


Figure 3.5: The saturation magnetic flux density (Gauss) as a function of temperature (°C) for several magnetic ferrite materials.

d. Effect of Alloying Elements

Alloying elements can have significant effects on magnetic properties. A change in atomic spacing (**Ch. 3.a**) can produce a change in magnetic properties. Adding N or Co to iron has been shown to increase the saturation

flux density. Adding other elements to iron increases the atomic spacing and can decrease the magnetic properties.

The addition of carbon into iron (**Fig. 3.6**) has a huge negative effect on the saturation flux density (reducing B_S by 37% per 1% of C) and coercivity (increasing H_C by 720% per 1% of C). The effect of all other elements is at least an order of magnitude smaller. This clearly shows why low carbon steel is used to achieve good magnetic properties. A typical low carbon steel for magnetic applications is 1010 steel, where the last 2 digits indicate the carbon content in 0.01% increments. Therefore, 1010 steel contains 0.10% carbon. Also, magnetic steel or iron is typically stress annealed to eliminate residual strain from the atomic structure and to minimize the coercivity.

Alloy	Sat. Flux Density Change in B_S per 1% of Alloy	Coercivity Change in H_C per 1% of Alloy
C	-37.0 %	720 %
Si	-2.9 %	---
Al	-2.7 %	---
< 7.7% Mn	-2.2 %	---
> 7.7% Mn	-22.9 %	---
Cr	-1.5 %	---
Cu	-1.1 %	---

Figure 3.6: Effect of alloying elements on the saturation flux density and coercivity of iron [14, 15].

The effect of many elements on the resistivity of iron is shown in **Fig. 3.7**. Both silicon and aluminum increase the resistivity of iron by more than 100% per 1% of content and both have very little effect on the magnetic saturation flux density.

This explains the alloy composition for motor lamination M-27 which contains 0.003% carbon and 2.0% silicon. Motor lamination M-4 contains 0.003% carbon and 3.1% silicon. Higher resistivity core materials significantly reduce eddy current losses (as will be discussed in **Ch. 3.h**).

Another very popular magnetic alloy for cyclic applications is Sendust, which contains 85% iron, 9% silicon, 6% aluminum, and no significant carbon.

Alloy	Resistivity Change in R per 1% of Alloy
Si	122.1 %
Al	107.5 %
Sn	83.5 %
Mn	56.4 %
V	51.2 %
Cr	44.9 %
Mo	37.6 %
Co	28.2 %
Ti	26.1 %
Ni	20.9 %
W	15.7 %

Figure 3.7: Effect of alloying elements on iron resistivity [14, 15].

Some motor lamination materials have been developed with 6.5% silicon. However, silicon content over 3% results in high hardness and brittleness that makes it difficult to manufacture and results in low tool life.

e. BH Curve – 3-Factor Curve Fit

The 3-Factor BH magnetization equation was initially reported by John Brauer in 1975 [4] and was later modified (**Eq. 3.2**) as reported in the 2nd edition of Brauer's book [9]. It is shown here in the form of relative permeability.

$$\mu_r = \frac{B}{\mu_0 H} = \frac{1}{\mu_o \left[k_1 e^{(k_2 B^2)} + k_3 \right]} + 1 \quad (3.2)$$

Listed in **Appendix-E** are the coefficients (k_1 , k_2 , k_3) for 40 materials based on a curve fit of magnetization curves from manufacturer datasheets. Also listed is the maximum relative permeability ($\mu_{r\text{-max}}$), the saturation flux density (B_{sat}) from the 3-Factor equation, and the RMS Error of the curve fit. Saturation is defined here as the point where the relative permeability is 10% of $\mu_{r\text{-max}}$. The minimum relative permeability (μ_r) tends toward 1 (like air) as the flux density becomes large ($B > B_{sat}$). The maximum permeability occurs at $B=0$, which reduces **Eq. 3.2** to the following form.

$$\mu_{r\text{-max}} = \frac{1}{\mu_o (k_1 + k_3)} + 1 \quad (3.3)$$

The following procedure is used to determine the k -values (k_1 , k_2 , and k_3).

1. $k_1 + k_3$ is based on the initial slope with points below the knee.
2. k_2 is based on the saturation level.
3. k_1 is based on the shape of the knee, using points near the knee.
4. k_2 is adjusted based on the saturation level.
5. k_1 is adjusted, using points near the knee.
6. k_2 is adjusted based on the saturation level.
7. k_1 is adjusted, using points near the knee.
8. k_2 is adjusted based on the saturation level.
9. Steps 1 through 8 are repeated to minimize the RMS Error.

Some of the curve fit results from **Appendix-E** are listed in **Fig. 3.8** for low carbon steel alloys, including the k -values, maximum relative permeability ($\mu_{r\text{-max}}$), saturation flux density (B_{sat}), and the RMS Error for the curve fit. The small RMS Error (less than 1.5%) demonstrates very good agreement between the datasheet points and the 3-Factor equation.

The maximum relative permeability ($\mu_{r\text{-max}}$) and saturation flux density (B_{sat}) are included in **Appendix-E** to aid in material selection.

Material	Curve Fit Coefficients			$\mu_{r\text{-max}}$	B_{sat} Tesla	RMS Error
	k_1	k_2	k_3			
US Steel® 1010 annealed	4.847E+00	1.9080	2.273E+02	3,429	1.79	1.00%
US Steel 1010 cold rolled	3.662E+01	1.3310	5.349E+02	1,393	1.93	0.80%
US Steel 1020 annealed	4.770E+00	2.0550	3.022E+02	2,593	1.77	1.40%
US Steel 1020 cold rolled	1.423E+01	1.6990	8.065E+02	971	1.92	1.20%
US Steel 1030 annealed	5.000E+01	1.3710	6.543E+02	1,146	1.88	1.50%
US Steel 1030 cold rolled	4.000E+01	1.4160	1.212E+03	636	2.00	0.70%

Figure 3.8: Curve fit results from Appendix-E with the RMS Error.

Graphical curve fit results are shown (Fig. 3.9, Fig. 3.10) to demonstrate the ability of the 3-Factor equation to accurately represent a wide range of magnetization curves (BH curves), including those with a gently rounded saturation knee and those with a sharp saturation knee. The black points in

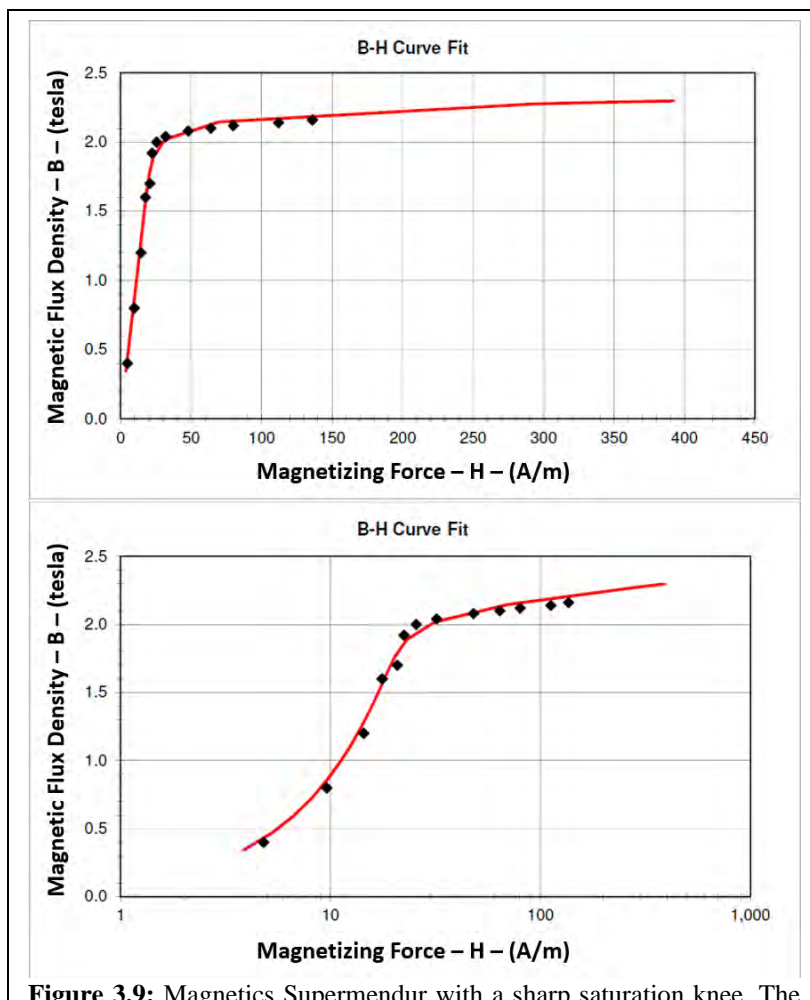


Figure 3.9: Magnetics Supermendur with a sharp saturation knee. The RMS Error of the curve fit is 4.0%. Both graphs show the same data. The bottom graph has a log scale on the horizontal axis (H -values).

the graphs are digitized datasheet values, and the red line is the 3-Factor curve. Each figure depicts two curves with identical data but with different horizontal scales to give a complete assessment of the curve fit quality.

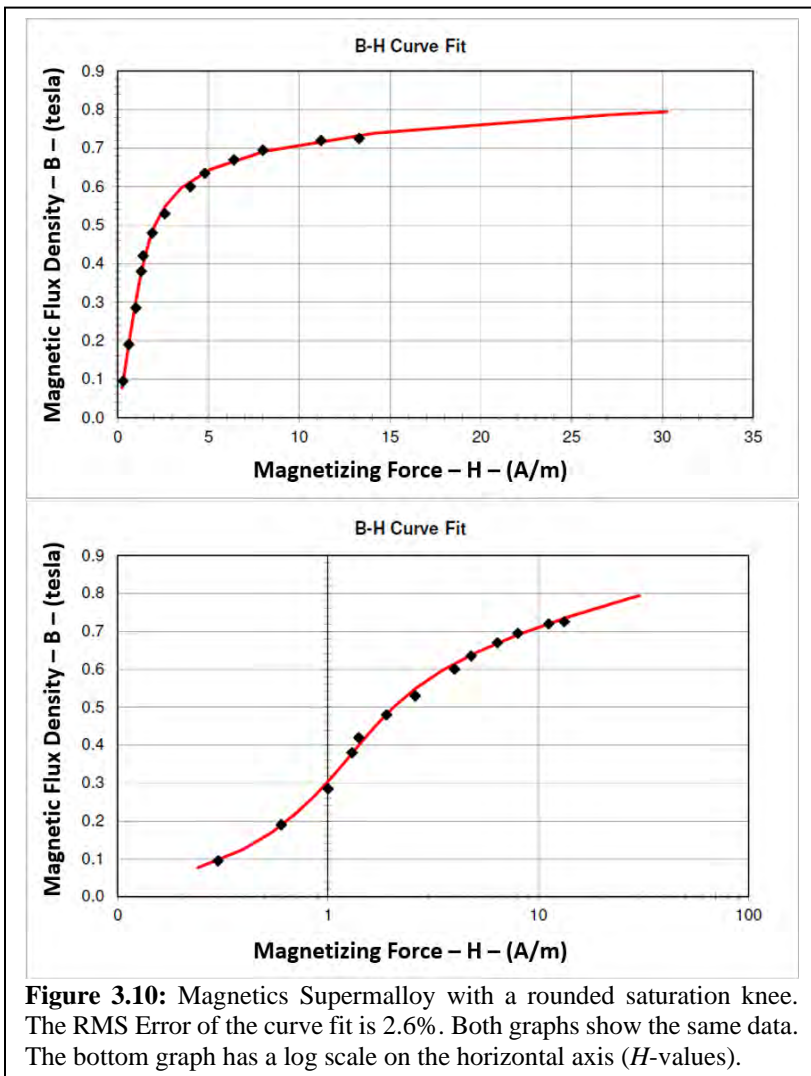
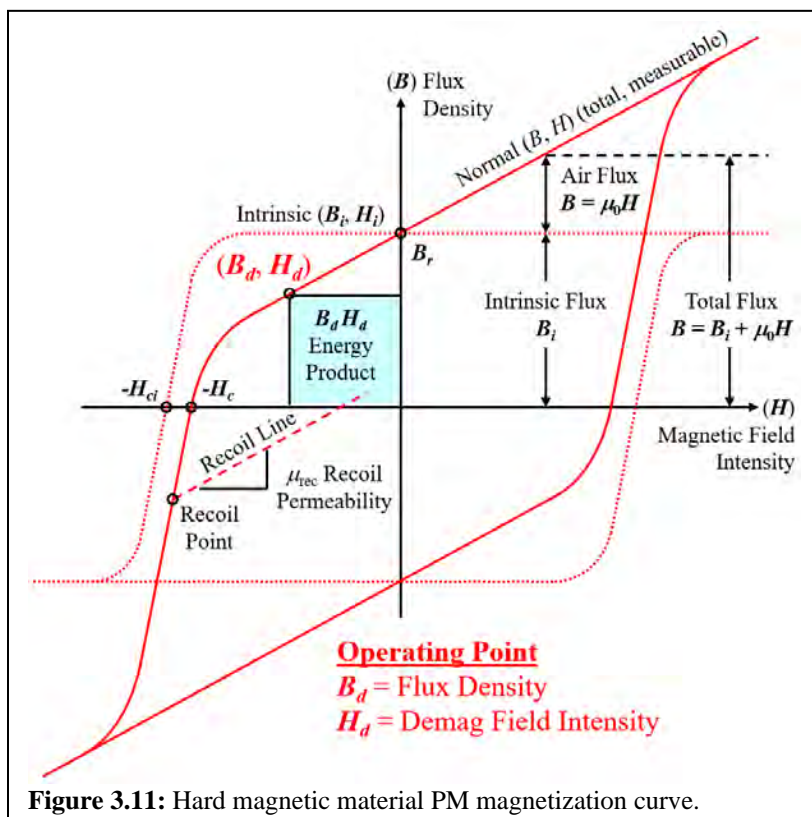


Figure 3.10: Magnetics Supermalloy with a rounded saturation knee. The RMS Error of the curve fit is 2.6%. Both graphs show the same data. The bottom graph has a log scale on the horizontal axis (H -values).

37 of the 40 materials in **Appendix-E** are also listed in Brauer's book [9]. Three additional materials include AK Steel M-4, Hitachi Finemet-3TL, and Magnetics Kool Mu 26u. Many of the k -values reported by Brauer [9] (as provided by this author) have been slightly modified to improve the curve fit accuracy. Note that these values are approximate because the material properties are highly dependent on manufacturing methods. Therefore, it's equally valid to use the values reported by Brauer [9]. It should be noted that the k -values for Magnetics Supermendur have been corrected here (the values provided to Brauer by this author were from data with a typographical error).

f. Hard Magnetic Materials

Hard magnetic materials (also known as permanent magnets) have a wide hysteresis loop (Fig. 3.11). The width of the hysteresis loop (coercivity, H_c) is large and the area (energy, BH) inside the hysteresis loop is large which results in a low magnetic permeability, high stored energy, and high losses during cyclic magnetizing and demagnetizing. A material with a larger coercivity requires a larger magnetic field to achieve complete saturation magnetization. Permanent magnets are typically magnetized once and the system is designed so that they are never demagnetized, therefore they are generally not used in cyclic magnetizing and demagnetizing applications.



The hysteresis loop characteristics listed below are generally used in most permanent magnet performance calculations.

Hysteresis Loop Characteristics

- B_r = Residual Flux Density (T)
- B_i = Intrinsic Magnetic Flux Density (T)
- H_c = Coercivity (A/m)
- H_{ci} = Intrinsic Coercivity (A/m)
- $B_d H_d$ = Energy Product (T-A/m, J/m³, MGOe)
- μ_{rec} = Recoil permeability (H/m)

Full (or permanent) magnetization occurs in the 1st quadrant (upper right) of **Fig. 3.11**. Full (or permanent) magnetization in the opposite polarity occurs in the 3rd quadrant (lower left). The operating region is the 2nd quadrant (upper left), where partial demagnetization occurs. The permanent magnet operating point lies on a recoil line (2nd quadrant *B-H* property curve), and moves up to the right or down to the left as the coil *NI* and air gap vary. A permanent magnet structure is typically designed to keep the operating point on the linear reversible part of the recoil line. If the operating point moves too far to the left, it enters the nonlinear region of the recoil line where the recoil line moves down and the permanent magnet permanently loses magnetization.

A recoil line (2nd quadrant *B-H* property curve) can be visualized as similar to the spring curve for a mechanical spring. A permanent magnet can be partially demagnetized by increasing the air gap in the flux path or by forcing magnetic flux in opposition to the permanent magnet with ampere-turns from a coil or with another permanent magnet. When the air gap is restored to the original small size or when the opposing magnetic flux is removed, the permanent magnet magnetization will increase (or rebound) along a curve called the recoil line. This is similar to compressing a spring by applying a force. When the force is removed the spring will rebound (or recoil) along the spring curve. Recoil line characteristics are discussed in detail in the following sections of this chapter (**Ch. 3.f, 3.g, and 3.k**).

Examples of permanent magnet material properties for some of the most common materials (AlNiCo, SmCo, NdFeB, and Ceramic) are shown as demagnetization curves in the 2nd quadrant of **Fig. 3.12**. The area under the curves represents energy density. NdFeB and SmCo both have much more area under their curves and they are known as high energy permanent magnet materials. Typical units for the area under the curve are MGOe or J/m³. Permanent magnet material properties are commonly presented with units of kG and kOe, as shown in **Fig. 3.12**. Permanent magnet grades are usually specified in the energy units of MGOe.

- $B \times H = \text{kG} \times \text{kOe} = \text{MGOe}$ (Mega-Gauss-Oersteds)
- $B \times H = \text{T} \times \text{A/m} = \text{T-A/m} = \text{J/m}^3$

High energy permanent magnet materials (NdFeB, SmCo) have a very large region where the recoil line is linear, compared to the other materials. The AlNiCo material curves (**Fig. 3.12**) have no obvious linear recoil region and require careful design with partial demagnetization to establish a linear recoil line on a minor hysteresis loop.

The curves in **Fig. 3.13**, give the magnetic properties and temperature sensitivity effects for the NdFeB-35 material (note that the number 35 is the permanent magnet material grade in units of MGOe). The normal curves (solid lines) are used directly as recoil lines in the system performance calculations. At 24°C and 60°C the recoil lines are linear. At 100°C and 140°C the recoil lines have a distinct nonlinear region toward the lower-left, which becomes larger with increasing temperature. Therefore, a permanent magnet with an operating point too far to the left (on the nonlinear portion of the recoil line) can be partially demagnetized due to high temperature.

Permanent Magnet Normal
De-Magnetization Curves at 20°C

Quadrant 2

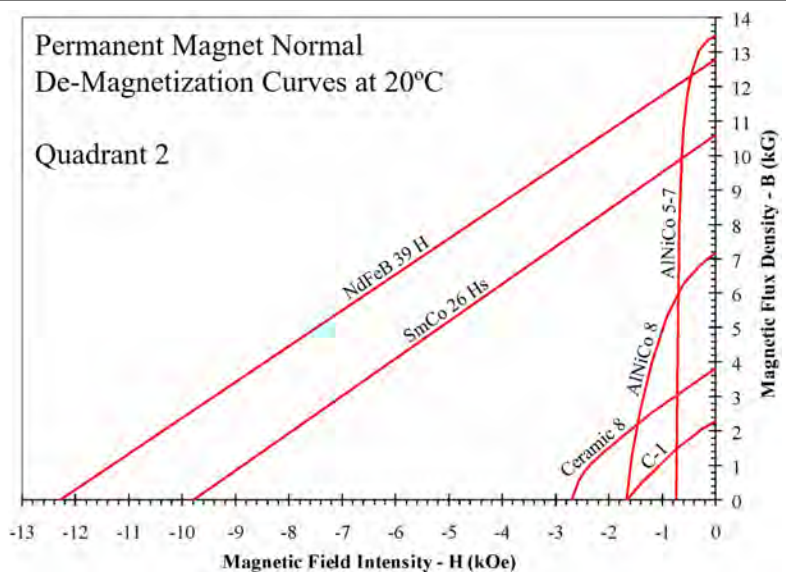


Figure 3.12: Permanent magnet 2nd quadrant demagnetization curves.

The dashed lines (**Fig. 3.13**) show the intrinsic (or internal) magnetic flux of a permanent magnet. The total flux emanating from the permanent magnet is represented by the normal curves. The total flux is the useful magnetic flux that is seen by the rest of the magnetic structure. Most permanent magnet data sheets show both the normal and the intrinsic curves. Temperature coefficients are generally given only for the intrinsic curves at the axis intercepts (H_{ci} and B_r).

The intrinsic magnetic flux (B_i) represents the magnetic flux produced only by the material (the electron spin and orbit). It describes the internal magnetic

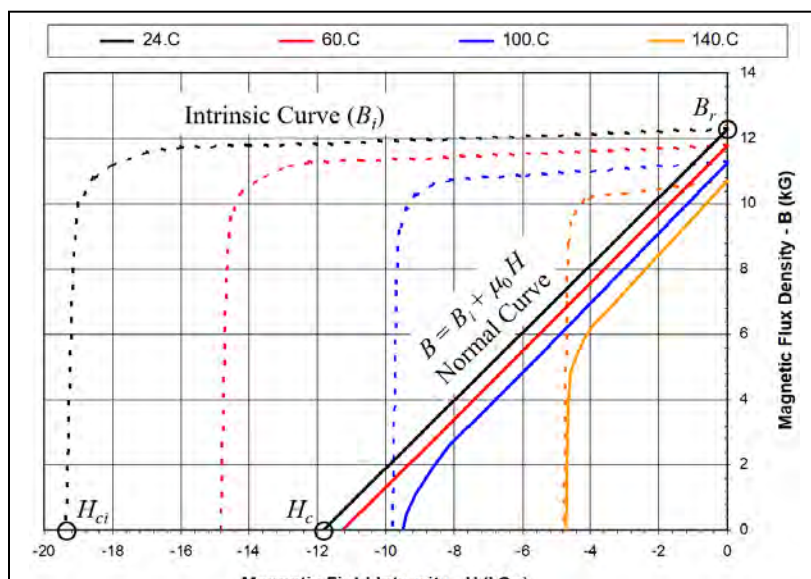


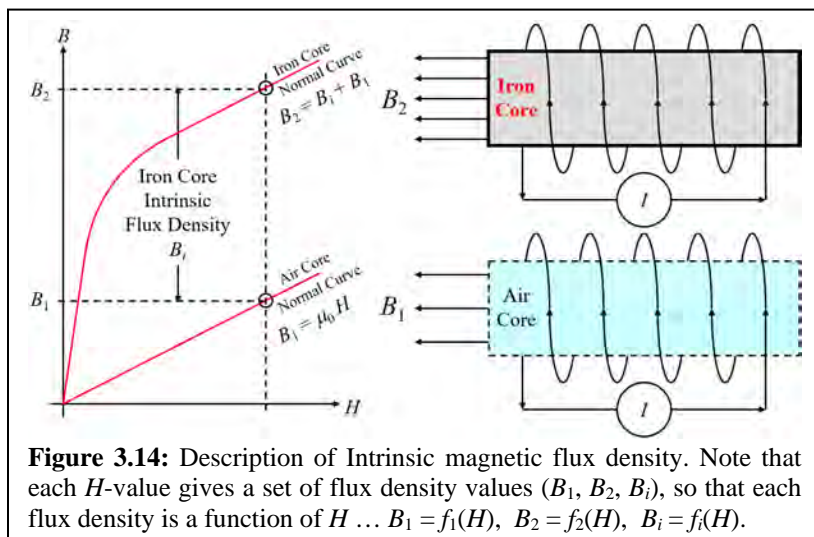
Figure 3.13: Permanent magnet temperature sensitivity for NdFeB-35.

property of the permanent magnet material. The intrinsic and normal (or total) magnetic flux are visually described in **Fig. 3.14**. The normal magnetic flux (B_2) is the total externally measurable or usable magnetic flux. The normal curve is used to determine the system performance. The normal curve can be calculated from the intrinsic curve by adding the air magnetic flux (B_1).

$$B_1 = \mu_0 H \quad \text{Air magnetic flux} \quad (3.4)$$

$$B_2 = B_i + B_1 \quad B_2 = B_i + \mu_0 H \quad \text{Total magnetic flux} \quad (3.5)$$

In **Fig. 3.14**, a coil is shown with an air core, or with an iron core. When the air core coil is energized it produces a magnetic flux density (B_1) as described by **Eq. 3.4**. When an iron core is inserted into the air-core space while the coil is energized, the magnetic flux density increases to the total magnetic flux density (B_2) described by **Eq. 3.5**. The amount of increase is the intrinsic magnetic flux density (B_i), the magnetic flux density due to the iron alone.



g. Permanent Magnet Performance

The permanent magnet operating point (B_d, H_d) and energy product ($B_d \times H_d$) are shown in **Fig. 3.15**. “ B_d ” is the demagnetizing magnetic flux density and “ H_d ” is the demagnetizing magnetic field intensity. The energy product is the rectangular area between the operating point and the origin, and is the product $B_d \times H_d$. The maximum value for the energy product in high energy permanent magnets occurs at an operating point halfway between B_r and H_c , ($(B_r/2, H_c/2)$). Operating at the maximum energy product results in the smallest possible permanent magnet size. The maximum energy product can be calculated from **Eq. 3.7**. It can be approximated fairly accurately by assuming the relative recoil permeability (μ_{r-rec}) is 1.00, a reasonable approximation for high energy permanent magnet materials, where $\mu_{r-rec} = 1.10$ (**Eq. 3.6**). The exact maximum energy product for the material in **Fig. 3.15** is 27.5 MGoe. The approximate maximum energy product is based on **Eq. 3.8** is 30.2 MGoe (10% error).

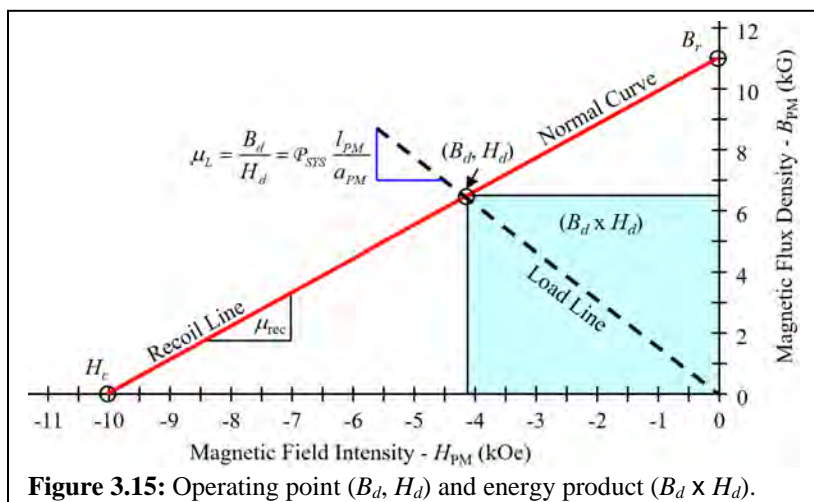


Figure 3.15: Operating point (B_d, H_d) and energy product ($B_d \times H_d$).

$$\mu_{r-rec} = \frac{\mu_{rec}}{\mu_0} = \frac{B_r}{\mu_0 H_c} = 1.10 \quad \text{Recoil Permeability} \quad (3.6)$$

$$BH_{MAX} = \left(\frac{B_r}{2} \right) \left(\frac{H_c}{2} \right) = \left(\frac{B_r}{2} \right) \left(\frac{H_c}{2} \frac{B_r}{\mu_{rec} H_c} \right) = \frac{B_r^2}{4\mu_{rec}} \quad (3.7)$$

$$BH_{MAX} \approx \frac{B_r^2}{4} = \left(\frac{B_r}{2} \right)^2 \quad \text{Approximate Max. Energy Product} \quad (3.8)$$

The load line in **Fig. 3.15** represents the permeance of the entire magnetic structure around the permanent magnet, as observed from the permanent magnet. The slope of the load line (μ_L) has units of permeability, as shown in **Eq. 3.9**.

$$\mu_L = \frac{B_d}{H_d} = \mathcal{P}_{\text{SYS}} \frac{l_{PM}}{a_{PM}} \quad (3.9)$$

Parker [5] presents a graph showing the historical increase in the maximum energy product (BH) of permanent magnet materials from 1890 to 1988. It includes notations when significant permanent magnet materials were introduced and became dominant. Brauer [9] gives a similar historical list. A curve fit (Fig. 3.16) of the maximum energy product from 1890 to 1988 shows a very constant incremental improvement rate of 5.6% per year.

Parker [5]		Fit 5.6%/yr		
		Energy Product	Energy Product	Fit
<u>Year</u>	<u>MGOe</u>	<u>MGOe</u>	<u>Error</u>	<u>PM Material</u>
1890	0.25	0.25	0.0%	High Carbon Steel
1919	1.20	1.21	1.2%	Introduction of AlNiCo
1939	3.50	3.61	3.1%	AlNiCo became dominant
1950	6.20	6.57	6.0%	AlNiCo
1961	11.7	12.0	2.3%	AlNiCo stopped improving
1967	16.3	16.6	1.8%	Rare Earth SmCo, NdFeB
1975	25.0	25.7	2.7%	SmCo
1980	33.5	33.7	0.6%	SmCo, NdFeB
1988	50.0	52.1	4.2%	NdFeB

Figure 3.16: Maximum Energy Product (BH) for permanent magnets [5] showing an incremental increase of 5.6% per year. The conversion factor from MGOe to J/m^3 (or T-A/m) is ... $7,958 (J/m^3) = 1.0 \text{ MGOe}$.

Since 1988 there has been very little improvement in the energy product of permanent magnet materials. The highest energy permanent magnet materials offered today have a maximum energy product of 52 MGOe (416 kJ/m^3) (Hitachi Metals NMX-S52) (Arnold Magnetic Tech. N55, N52, N52M).

A reasonable estimate for the maximum achievable energy product of potential new materials can be calculated from Eq. 3.8, as follows. At a remanent magnetic flux density of 1.6 T (16 kG) (approximately the knee of an iron magnetization curve), the maximum energy product would be about 64 MGOe (512 kJ/m^3). At a remanent magnetic flux density of 2.0 T (20 kG) (approximately the saturation flux density of iron), the maximum energy product would be about 100 MGOe (800 kJ/m^3).

The permanent magnet operating point moves up and down the recoil line as the coil- NI is increased or decreased (Fig. 3.17). Positive coil- NI moves the load line to the right on the H -axis, which causes the operating point to move up to the right on the recoil line. The recoil line represents the permanent magnet properties, therefore the coil- NI is applied as observed from the permanent magnet, dividing the coil- NI by the permanent magnet length (l_{PM}).

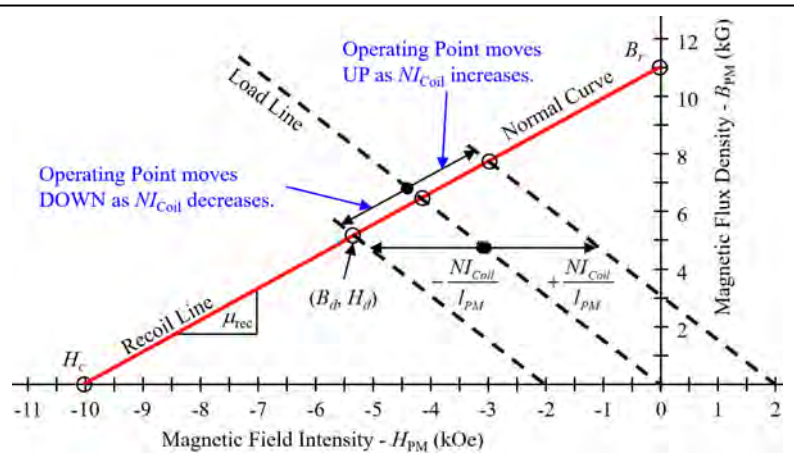


Figure 3.17: The operating point moves up and down the recoil line as the coil- NI varies.

The permanent magnet operating point moves up and down the recoil line as the air gap is increased or decreased (**Fig. 3.18**). A smaller air gap tilts the load line upward to the right, which causes the operating point to move up to the right. A larger air gap tilts the load line down to the left, which causes the operating point to move down to the left. The recoil line represents the permanent magnet properties, therefore the air gap is applied in the system permeance (\mathcal{P}_{SYS}) as observed from the permanent magnet, and multiplying by the permanent magnet length (l_{PM}) and dividing by the permanent magnet cross-sectional area (a_{PM}). The slope of the load line (μ_L) is proportional to the system permeance Eq. 3.8. Approximating the system permeance with the permeance of the main air gap ($\mathcal{P}_1 = \mu_0 a/g$) shows that a small air gap results in a larger permeance and a steeper slope for the load line.

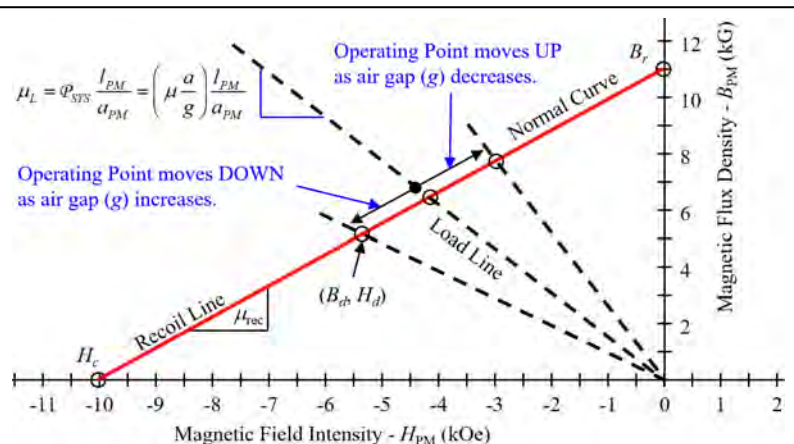
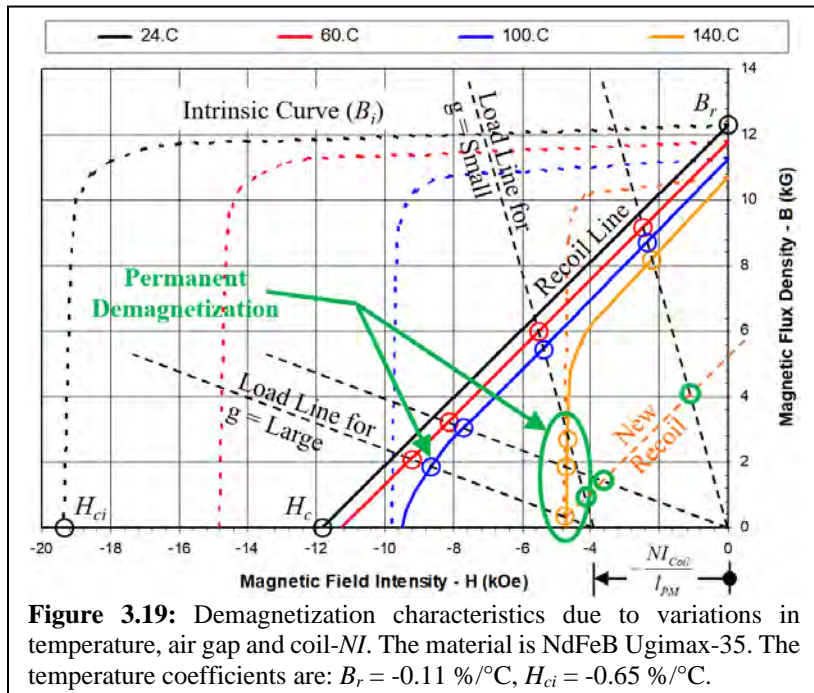


Figure 3.18: The operating point moves up and down the recoil line as the air gap varies.

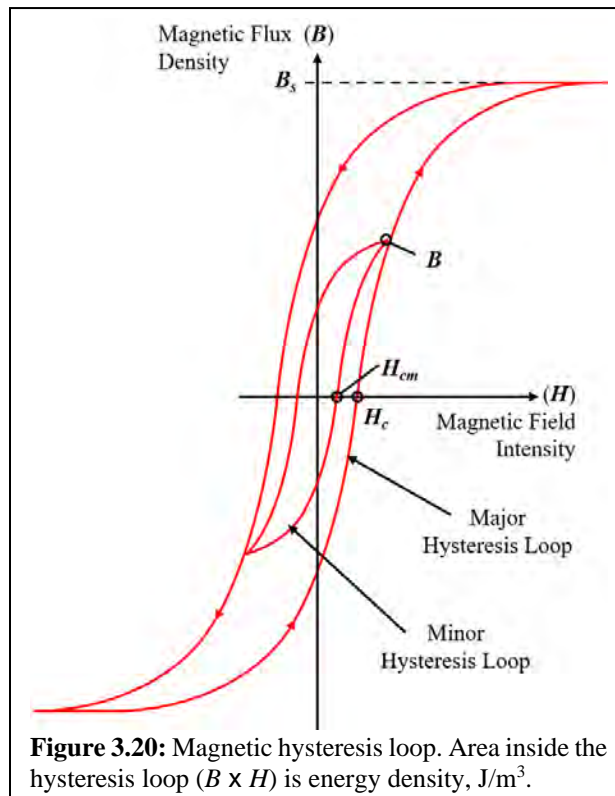
Permanent demagnetization is shown in **Fig. 3.19**, where some of the operating points lie on the non-linear lower-left region of the recoil lines. The operating points are defined at the intersection of the load lines and the recoil lines. The recoil line can move and change shape as a function of temperature, the load lines can move and change slope as a function of the coil- NI and air gap.



Four load lines and 4 recoil lines are shown in **Fig. 3.19**. The recoil line at 60°C (red line) is linear and the system can move between the 4 operating points (red circles) reversibly without permanent demagnetization. At 140°C the recoil line (orange line) becomes significantly nonlinear at the lower-left. When the system moves to any of the three lower-left operating points (orange circles) the permanent magnet experiences a permanent demagnetization, and a new recoil line (dashed orange line) is established from the lowest operating point. The new operating points are then defined at the intersection of the load lines and the new recoil line (green circles). It is important to note that the system can move between the 4 new operating points (green circles) reversibly without further permanent demagnetization. The loss in magnetic flux density between the solid orange and dashed orange recoil lines for the operating points at the upper-right load line is 50% (8.2 to 4.1 kG) (0.82 to 0.41 T). This is a permanent loss of magnetic flux density and it can only be restored by remagnetizing the permanent magnet.

h. Losses, Eddy Currents, Skin Effect

Losses in a magnetic material are due to hysteresis and eddy currents. The area inside a hysteresis loop represents energy that is dissipated during cyclic magnetizing and demagnetizing, such as in a motor or transformer or inductor. The hysteresis loop area ($B \times H$) has units of T-A/m or energy density J/m^3 . Dividing by the material density (ρ , kg/m^3) gives the loss in units of J/kg .



Hysteresis Core Loss:

The hysteresis power loss is the energy loss per cycle around the hysteresis loop multiplied by the cyclic frequency (f , Hz). The area inside the major hysteresis loop (Fig. 3.20) can be accurately estimated as a parallelogram of total height $2B_s$, and total width $2H_c$. The hysteresis power loss (P_h) is defined as follows.

$$P_h = \frac{4B_s H_c f}{\rho} \quad (3.10)$$

The minor hysteresis loop peak magnetic flux density and peak coercivity can be estimated as proportional to the major hysteresis loop values (B_s, H_c). Generally, the flux density can be easily measured or calculated. The minor loop coercivity and the hysteresis power loss (P_h) can be estimated as follows.

$$\frac{H_{cm}}{H_c} \approx \frac{B}{B_s} \quad H_{cm} \approx H_c \frac{B}{B_s} \quad (3.11)$$

$$P_h = 4BH_{cm} \frac{f}{\rho} = 4B \left(H_c \frac{B}{B_s} \right) \frac{f}{\rho} \quad (3.12)$$

$$P_h = 4B^2 f \frac{H_c}{B_s \rho} \quad \text{Hysteresis core loss (W/kg)} \quad (3.13)$$

Eddy Current Core Loss:

The eddy current power loss is a result of the Joule heating due to eddy currents flowing through a resistive path. According to Lenz's law, eddy currents oppose an applied change in the magnetic field. **Fig. 3.21** shows a uniform magnetic flux density (B) in a thin magnetic core material (such as a motor lamination), where $T \ll W$ and $T < 2s$ (s is the skin thickness discussed later in this section). The resistance of the eddy current path can be calculated with a small differential path thickness (dx), as follows.

$$l_e = 2W \quad da_e = Ddx \quad (3.14)$$

$$R_e = \frac{l_e}{\sigma da_e} = \frac{2W}{\sigma D dx} \quad \text{Eddy current path resistance} \quad (3.15)$$

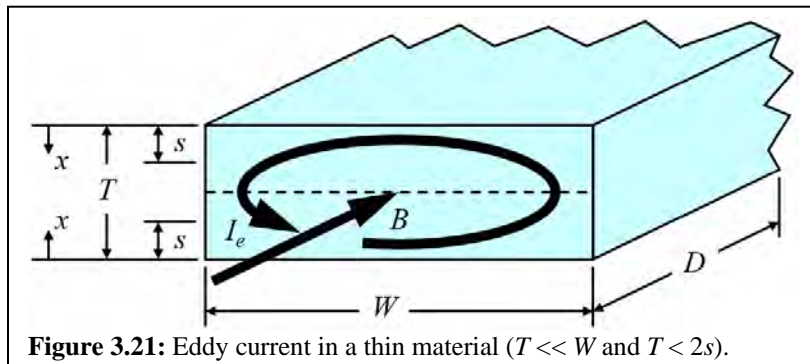


Figure 3.21: Eddy current in a thin material ($T \ll W$ and $T < 2s$).

The eddy current can be calculated from Faraday's law, where the induced voltage (V_e) drives an eddy current through the resistance (R_e) ($N = 1$). The voltage (V_e) is induced by the magnetic flux enclosed by the eddy current.

$$V_e = \frac{d(N\phi)}{dt} = B \omega W(T - 2x) \quad a = W(T - 2x) \quad B = B \sin(\omega t) \quad (3.16)$$

$$I_e = \frac{V_e}{R_e} \quad (3.17)$$

The eddy current power loss can be calculated using the peak current from **Eq. 3.17**. The power loss is divided by the magnetic material mass (m) to obtain the loss per unit mass, where $m = \rho v = \rho DWT$.

$$dP_e = \frac{1}{2} \frac{I_e^2 R_e}{m} = \frac{1}{2} \left(\frac{V_e}{R_e} \right)^2 \frac{R_e}{m} = \frac{1}{4} \frac{B^2 \omega^2 \sigma D W (T - 2x)^2 dx}{m} \quad (3.18)$$

$$P_e = \int_0^{T/2} dP_e = \frac{1}{4} \frac{B^2 \omega^2 \sigma}{\rho T} \int_0^{T/2} (T - 2x)^2 dx \quad P_e = \frac{B^2 \omega^2 T^2 \sigma}{24 \rho} \frac{W}{kg} \quad (3.19)$$

$$\boxed{P_e = 1.64 T^2 B^2 f^2 \frac{\sigma}{\rho} \frac{W}{kg}} \quad \text{Eddy current core loss} \quad (3.20)$$

Anomalous Core Loss:

The measured core loss is typically larger than the sum of the hysteresis and eddy current losses. The extra loss is called anomalous core loss. It's significant in some cases, depending on the magnetization process. The physical mechanisms include eddy-currents near moving domain walls.

The hysteresis power loss density (**Eq. 3.13**) and the eddy current power loss density (**Eq. 3.20**) together define most of the core loss in magnetic materials. The ratio for the hysteresis (P_h/P_c) and eddy current core loss (P_e/P_c) relative to the published core loss is fairly constant for motor lamination materials at 60 Hz. The ratios for 26 gage M47 motor lamination at $f=60$ Hz are listed below. Note that the proportion of eddy current loss increases with frequency.

- P_c = Published Core Loss Total core loss
- $P_e / P_c = 37\%$ Eddy current core loss, 60 Hz (3.21)
- $P_h / P_c = 63\%$ Hysteresis core loss, 60 Hz (3.22)

The following proportionalities are obtained from **Eq. 3.13** and **Eq. 3.20**.

- Hysteresis core loss (P_h) (**Eq. 3.13**):
 - $P_h \propto B^2$
 - $P_h \propto f$
 - $P_h \propto H_c$
- Eddy current core loss (P_e) (**Eq. 3.20**):
 - $P_e \propto B^2$
 - $P_e \propto f^2$
 - $P_e \propto T^2$
 - $P_e \propto \sigma$

This shows why high-frequency core materials are thin (small- T), with silicon content to reduce conductivity (small- σ), and low carbon content to reduce coercivity (small- H_c). The Steinmetz equation (**Eq. 3.23**) gives the total core loss, combining the hysteresis, eddy current, and anomalous losses.

$$\boxed{P_c = k f^a B^b} \quad (f = \text{Hz}, B = \text{T}, P_c = \text{W/kg}) \quad \text{Steinmetz Core Loss Eq. (3.23)}$$

Appendix-G gives the core loss for 84 low loss materials, including the Steinmetz coefficients (k, a, b). The values for coefficient- b are close to 2, and the values for coefficient- a are between 1 and 2 (closer to 1 for nonconductive materials). The Steinmetz coefficient values match the

exponent values in **Eq. 3.13** and **Eq. 3.20**, and verify the general form of the core loss relationships. Note that eddy currents in DC pulse actuator applications don't contribute losses. However, they work against the rising magnetic flux and can significantly delay achieving the desired mechanical force and displacement.

Skin Effect:

At high frequencies in electrically conductive materials, the eddy currents (I_e) and magnetic flux (B) become confined to a layer near the surface (skin) of the material (**Fig. 3.21**). Highly conductive materials slow the diffusion of the fields into the material, and thicker materials require more time for the fields to diffuse to the center. Higher frequencies reduce the time available for the fields to diffuse into the material. The skin depth (s , **Eq. 3.24**) and the depth of penetration (d , **Eq. 3.25**) provide a measure of the diffusion distance as a function of material properties and frequency. The skin depth (s) is defined as the depth (**Fig. 3.21**) at which the magnetic flux density falls to about 37% of the surface flux density. The depth of penetration (d) is defined as the depth over which all the magnetic flux is contained, at the value of the surface flux density.

$$s = \frac{1}{\sqrt{\pi f \mu \sigma}} \text{ m} \quad \text{Skin Depth [9]} \quad (3.24)$$

$$d = \frac{1}{\sqrt{2\pi f \mu \sigma}} \text{ m} \quad \text{Depth of Penetration [1]} \quad (3.25)$$

(μ & σ values are from **Appendix-D**)

	<u>Copper</u>	<u>M22 Steel</u>
• f = Frequency	60 Hz	60 Hz
• μ = Magnetic Permeability	$1.26E-6$ H/m	$9.84E-3$ H/m
• σ = Conductivity	$5.80E+7$ S/m	$2.00E+6$ S/m
• s = Skin Depth	8.51 mm	0.508 mm
• d = Depth of Penetration	6.02 mm	0.356 mm

The magnetic permeability of M22 steel is 7,800 times larger than copper, which results in a skin depth that is 16 times smaller than copper. Therefore, steels for AC applications such as motors and transformers are thin (on the order of the skin depth). Layers of steel laminations are stacked to attain a sufficient steel cross section. The skin depth and depth of penetration occur from both sides through the thickness. If the skin depth is small compared to the thickness, the center of a magnetic core plate will not carry magnetic flux, and the center of a bus bar or cable conductor will not carry current. Therefore, to effectively use the entire thickness of a plate, the plate thickness should be no more than twice the skin depth. For example, a copper bus bar at 60 Hz should be no thicker than 17 mm (0.670 inches), and an M-22 steel lamination at 60 Hz should be no thicker than 1.0 mm (0.040 inches). Losses in AC coil windings are produced by both the skin effect and the proximity effect. The proximity effect causes eddy currents in adjacent coil windings due to the small space between turns. Correlations for both effects in an AC Coil winding are available in technical papers, such as Jimenez [26] and Barrios [27].

i. Imaginary Permeability and Loss Tangent

The total magnetic flux density for a non-saturating hysteresis loop can be represented as a rotating vector system of real and imaginary permeability (**Eq. 3.26**). The core loss of a magnetic material is equal to the area inside the hysteresis loop, and can be characterized with imaginary permeability. The loss tangent is the ratio of the imaginary permeability to the real permeability.

$$B = \mu H = (\mu_R - j\mu_i)H \quad \text{Total flux density} \quad (3.26)$$

$$B = (\mu \cos(\delta) - j\mu \sin(\delta))H \quad (3.27)$$

$$\mu = \sqrt{\mu_R^2 + \mu_i^2} \quad \text{Total permeability} \quad (3.28)$$

$$\mu_R = \mu \cos(\delta) \quad \boxed{\mu_R = \mu_0 \mu_{rR}} \quad \text{Real permeability (BH curve)} \quad (3.29)$$

$$\mu_i = \mu \sin(\delta) \quad \text{Imaginary permeability} \quad (3.30)$$

The system inductance and impedance for a coil of resistance R surrounding a magnetic core can be written as follows with the real and imaginary permeabilities to show that the imaginary permeability becomes part of the power dissipating real impedance (**Eq. 3.33**).

$$L = N^2 \mathcal{P} = N^2 \mu \frac{a}{l} = N^2 (\mu_R - j\mu_i) \frac{a}{l} \quad \text{Inductance} \quad (3.31)$$

$$Z = R + j\omega L = R + j\omega N^2 (\mu_R - j\mu_i) \frac{a}{l} \quad \text{Impedance} \quad (3.32)$$

$$\boxed{Z = \left(R + \omega N^2 \mu_i \frac{a}{l} \right) + j \left(\omega N^2 \mu_R \frac{a}{l} \right)} \quad (3.33)$$

The 1st term of the impedance equation (**Eq. 3.33**) represents the real impedance and the 2nd term represents the imaginary impedance. Only the 1st term contributes to the power loss. The 1st part of the power loss (**Eq. 3.34**) represents the power loss in the coil resistance (P_R), and the 2nd part of the power loss (**Eq. 3.36**) represents the power loss in the core (P_c), or core loss.

$$P = \frac{I^2 Z}{m} = \frac{I^2}{m} \left(R + \omega N^2 \mu_i \frac{a}{l} \right) \quad \text{Power Loss per unit mass (W/kg)} \quad (3.34)$$

$$P = P_R + P_c \quad (3.35)$$

$$P_c = \omega \frac{N^2 I^2}{m} \mu_i \frac{a}{l} \quad \text{Core loss per unit mass (W/kg)} \quad (3.36)$$

The coil NI and the core mass relationships ($NI = H l$) ($m = \rho v = \rho la$) can be included to simplify the core loss equation (**Eq. 3.36**). The imaginary permeability (μ_i), core loss (P_c), loss angle (δ), and loss tangent ($\tan(\delta)$) are written as a function of the real flux density ($B_R = \mu_R H$), frequency (ω) and mass density (ρ), as follows.

$$\mu_i = \frac{P_c ml}{\omega N^2 I^2 a} = \frac{P_c \rho l^2 a}{\omega H^2 l^2 a} \quad \boxed{\mu_i = \mu_R^2 \frac{P_c \rho}{\omega B_R^2}} \quad \text{Imaginary Permeability} \quad (3.37)$$

$$P_c = \frac{\mu_i \omega B_R^2}{\mu_R^2 \rho} \quad \boxed{P_c} \quad \text{Core Loss} \quad (3.38)$$

$$\tan(\delta) = \frac{\mu_i}{\mu_R} \quad \boxed{\tan(\delta) = \mu_R \frac{P_c \rho}{\omega B_R^2}} \quad \text{Loss Tangent} \quad (3.39)$$

$$\delta = \tan^{-1} \left(\mu_R \frac{P_c \rho}{\omega B_R^2} \right) \quad \text{Loss Angle} \quad (3.40)$$

$$\tan(\delta) \approx \delta \approx \frac{\mu_i}{\mu_R} \quad \boxed{\delta \approx \mu_R \frac{P_c \rho}{\omega B_R^2}} \quad \text{Loss Tangent } (\delta < 0.3) \quad (3.41)$$

Example calculations are shown in **Fig. 3.22** for 4 materials based on property and core loss data from **Appendix-G** (table of low loss magnetic materials). The excitation frequency (f) is 60 Hz for the 1st material and 10 kHz for the others. The resulting loss characteristics are highlighted in yellow (core loss, imaginary permeability, loss tangent, loss angle).

Peak Real Flux Density $B_R = 0.20$ T		Material	Armco M2 - 3% Si				
Material ID			1	17	33	41	69
Density	ρ kg/m ³	7,600	7,300	7,290	5,790	4,800	
Frequency	f Hz	60	10,000	10,000	10,000	10,000	
Frequency	ω rad/s	377	62,832	62,832	62,832	62,832	
Core Loss	P_c W/kg	0.015	0.352	3.32	19.73	0.491	
Rel. Real Perm.	μ_{rR}	---	43,860	20,000	35,000	125	5,000
Real Perm.	μ_R H/m	5.51E-02	2.51E-02	4.40E-02	1.57E-04	6.28E-03	
Imaginary Perm.	μ_i H/m	2.29E-02	6.45E-04	1.86E-02	1.12E-06	3.70E-05	
Loss Tangent	$\tan(\delta)$	---	0.41512	0.02566	0.42403	0.00714	0.00589
Loss Angle	δ rad	0.39347	0.02566	0.40105	0.00714	0.00589	
Steinmetz	k	---	1.06E-03	8.15E-07	5.52E-05	1.96E-02	2.02E-07
Loss Coeffs. (see App. G)	a	---	1.433	1.780	1.550	1.086	2.079
	b	---	2.002	2.125	2.032	1.917	2.762

Figure 3.22: Core loss, imaginary permeability and loss tangent. Note that the Steinmetz core loss coefficients (k, a, b) are listed for 84 low loss materials in **Appendix-G**.

j. Permanent Magnet Model – Magnetic Moment

The magnetic moment (or magnetic dipole moment) [2, 3, 25] is based on a current loop (Fig. 3.23). It is used in determining the properties of magnetic materials and can be used to model the field around a permanent magnet. The magnitude of the magnetic moment (m) for a current loop is equal to the loop area (πa^2) multiplied by the current (I) (Eq. 3.42). The direction of the Magnetic Moment (m) can be visualized with the right-hand rule, where the fingers of the right hand follow the current (I) and the thumb points in the direction of the magnetic moment.

$$m = \pi a^2 I \quad \text{A-m}^2 \quad \text{Magnetic Moment} \quad (3.42)$$

The magnetic moment (m) for a permanent magnet is equal to the magnetization or magnetic polarization (M) multiplied by the volume (v), where the direction is normal and out of the north pole face (Fig. 3.24).

The magnetization or magnetic polarization (M) of a permanent magnet is the product of the operating point intrinsic flux density (B_{di}) divided by the permeability of free space (μ_0) (Eq. 3.43).

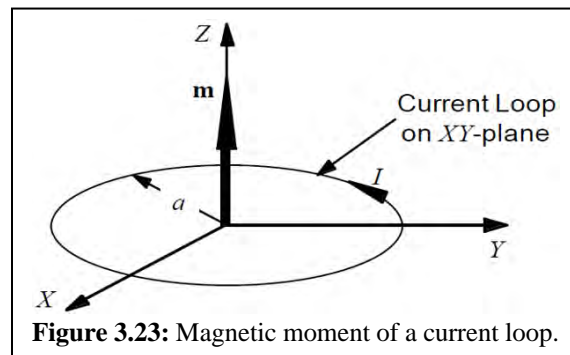


Figure 3.23: Magnetic moment of a current loop.

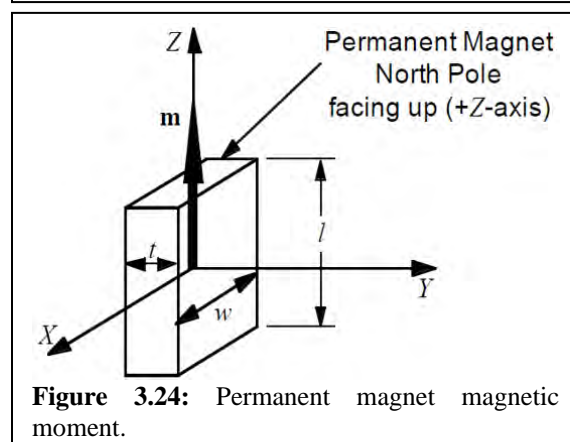


Figure 3.24: Permanent magnet magnetic moment.

$$m = Mv = \left(\frac{B_{di}}{\mu_0} \right) (wtl) \quad \left(T \frac{A}{T \cdot m} \right) (m^3) = A \cdot m^2 \quad (3.43)$$

High energy permanent magnets (such as NdFeB and SmCo) have a very small recoil permeability that is only slightly larger than the permeability of free space (μ_0). Therefore, the magnetization (M) and the magnetic moment (m) can be approximated based on the coercivity of the permanent magnet (H_c) (Fig. 3.25), as follows.

$$M = \frac{m}{v} = \frac{B_{di}}{\mu_0} \quad \text{Magnetization based on } B \quad (3.44)$$

$$B_{di} = B_R - (B_R - B_{di}) = \mu_{rec} H_c - (\mu_{rec} - \mu_0) H_d \quad (3.45)$$

$$M = \frac{\mu_{rec}}{\mu_0} H_c - \left(\frac{\mu_{rec}}{\mu_0} - 1 \right) H_d \quad \text{Magnetization based on } H \quad (3.46)$$

$$M \approx H_c \quad \text{Magnetization for } \mu_{rec} \approx \mu_0 \quad (3.47)$$

$$m = Mv \approx H_c (wtl) \quad \text{Magnetic moment for } \mu_{rec} \approx \mu_0 \quad (3.48)$$

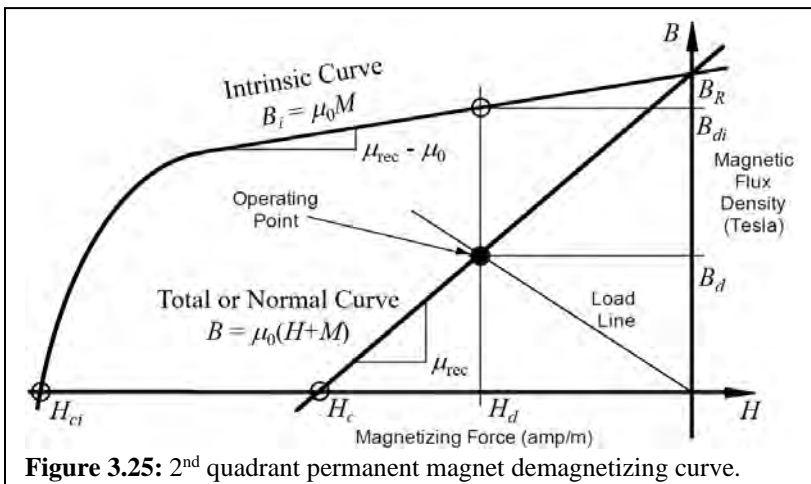


Figure 3.25: 2nd quadrant permanent magnet demagnetizing curve.

A high energy permanent magnet can be modeled as a current loop based on the magnetic moment, where H_c is the permanent magnet coercivity. This approximation (**Eq. 3.47**) is 95% accurate ($\mu_{rec}/\mu_0 = 1.1$, $H_d/H_c = 0.5$ at maximum energy product) for short permanent magnets with a high coercivity (such as NdFeB or SmCo). This also results in a conservative solution, where a prototype should perform slightly better. Long permanent magnets can be modeled as an assembly of short permanent magnets, each with a magnetic moment and a current loop. This becomes equivalent to a current sheet wrapped around a long permanent magnet over the entire length, where the total current represents the total magnetic moment (**Eq. 3.51**).

$$m = aI = H_c (wtl) \quad \text{A-m}^2 \quad \text{PM magnetic moment} \quad (3.49)$$

$$a = wt \quad \text{m}^2 \quad \text{PM current loop area} \quad (3.50)$$

$$I = H_c l \quad \text{amperes} \quad \text{PM loop current} \quad (3.51)$$

The permanent magnet coercivity used for the magnetic moment and current loop calculations is based on the recoil line for the worst-case conditions (maximum coil demagnetizing NI and maximum air gap). When the recoil line does not reach the H -axis, it is extended to define the recoil line coercivity (H_{cR}) (**Fig. 3.26**).

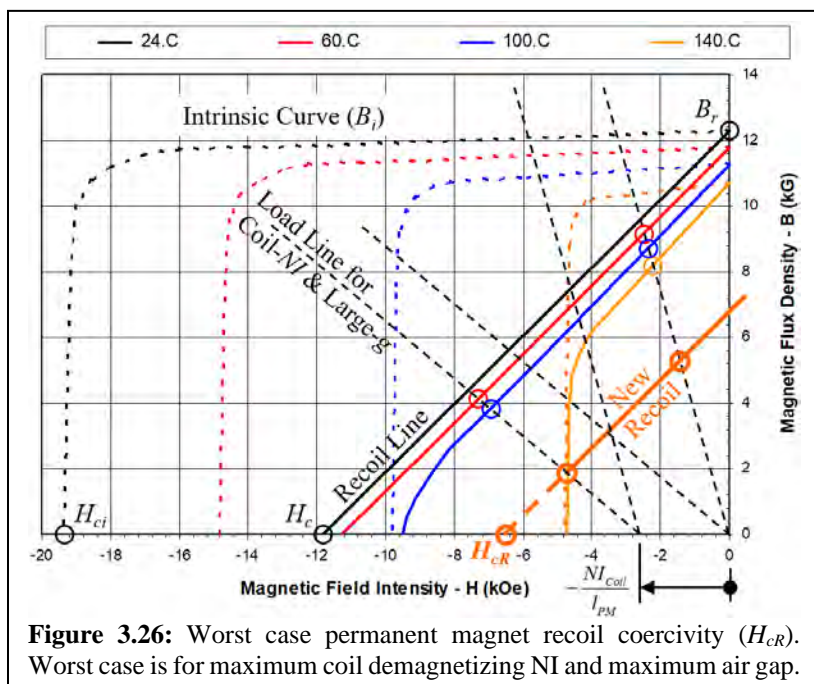
$$m = H_{cR} (wtl) \quad A\text{-m}^2 \quad \text{PM magnetic moment} \quad (3.52)$$

$$I = H_{cR} l \quad \text{ampères} \quad \text{PM loop current} \quad (3.53)$$

A permanent magnet can be accurately modeled as a magnetic material with a permeance (or reluctance) and a surface sheet current equal to the loop current (**Eq. 3.54**, **Eq. 3.55**). The permeance (or reluctance) is calculated with the recoil permeability (μ_{rec}).

$$NI_{PM} = H_{cR} l \quad \text{ampere-turns} \quad \text{PM NI} \quad (3.54)$$

$$\mathcal{P}_{PM} = \mu_{rec} \frac{wt}{l} \quad \text{Wb/ampere-turn} \quad \text{PM permeance} \quad (3.55)$$



The Magnetic Moment (m) can also be written as the product of the magnetic pole strength (p) and the distance (l) between the poles (**Eq. 3.56**). The magnetic pole strength (p) of a high energy permanent magnet can be approximated by the product of the coercivity (H_c) and the pole face area (wt) (**Eq. 3.57**).

$$m = pl = H_c wt l \quad A\text{-m}^2 \quad \text{PM magnetic moment} \quad (3.56)$$

$$p = H_c wt \quad A\text{-m} \quad \text{PM pole strength} \quad (3.57)$$

k. Example-4 – PM Model

A permanent magnet structure (Fig. 3.27) has steel pole pieces with an air gap and a DC coil (the Coil NI opposes the permanent magnet).

$$\begin{aligned}
 D &= 0.20 & \text{m} \\
 d &= 0.01 & \text{m} \\
 t &= 0.01 & \text{m} \\
 l_{PM} &= 0.02 & \text{m} \\
 NI &= 0 \text{ & } 6,000 & \text{A-t} \\
 g &= 0.01 \text{ & } 0.10 & \text{m} \\
 \mu_{Fe} &= 5,000. & \text{---} \\
 \mu_0 &= 4\pi E-7 & \text{H/m}
 \end{aligned}$$

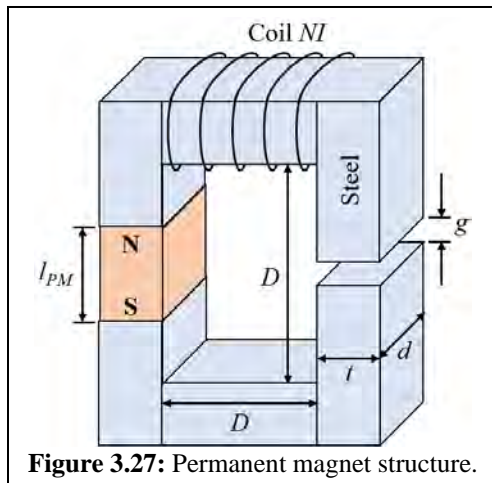


Figure 3.27: Permanent magnet structure.

Find: Operating points and the New Recoil line.

This data gives two air gap (g) dimensions and two Coil NI values, resulting in 4 operating points that define the entire operating region. The permanent magnet demagnetization curve (Fig. 3.28) is the 140°C curve for Ugimag-35 (also Fig. 3.26). The demagnetization curve starts to drop at about $H = -4$ kOe

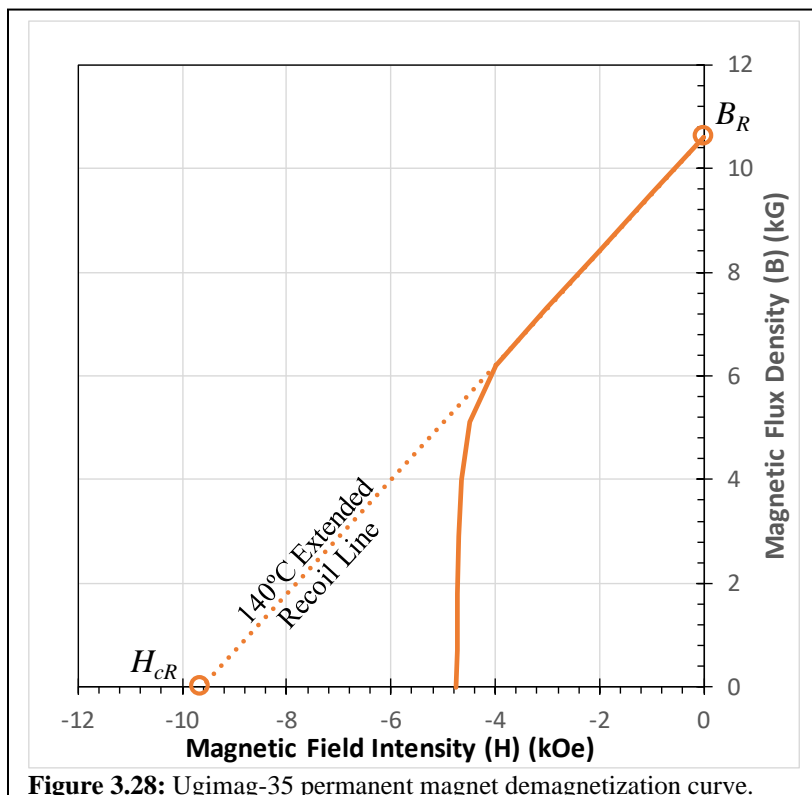


Figure 3.28: Ugimag-35 permanent magnet demagnetization curve.

(318 kA/m). Therefore, the recoil line needs to be extended to determine the recoil coercivity (H_{cR}). The permanent magnet properties from the recoil line are listed below. Note that the value for BH_{max} at 140°C is much less than 35 MGOe (279 kJ/m³) for Ugimag-35 at room temperature.

- $H_{cR} = -9.64 \text{ kOe} = 767 \text{ kA/m}$
- $B_R = 10.6 \text{ kG} = 1.06 \text{ T}$
- $\mu_{rec}/\mu_0 = 1.10$
- $BH_{max} = 25.5 \text{ MGOe} = 203 \text{ kJ/m}^3$

The following permeance analysis will ignore the leakage flux paths to simplify the calculations. The analysis process is as follows.

- Calculate the permeance of the steel path
- Calculate the permeance of the permanent magnet path
- Calculate the permeance of the air gap paths (P_1, P_2, P_4)
- Calculate the total reluctance of the flux path
- Calculate the permanent magnet ampere-turns
- Calculate the magnetic flux using the total NI (Coil & PM)
- Calculate the permanent magnet operating point (B_d, H_d)
- Draw the new recoil line through the lowest operating point
- Determine the pm properties from the new recoil line
- Re-calculate the operating points

Permeance and Reluctance of the steel path:

$$l_{Fe} = 4D + 2t - l_{PM} - g \quad (3.58)$$

$$l_{Fe} = 4(0.20) + 2(0.01) - 0.02 - 0.01 = 0.790 \text{ m} \quad (3.59)$$

$$\mathcal{P}_{Fe} = \mu_{Fe} \mu_0 \frac{a_{Fe}}{l_{Fe}} = (5000)(\mu_0) \frac{(0.01)(0.01)}{0.790} = 7.95E-7 \frac{\text{Wb}}{\text{A}} \quad (3.60)$$

$$\mathcal{R}_{Fe} = \frac{1}{\mathcal{P}_{Fe}} = 1.26E+6 \frac{\text{A}}{\text{Wb}}$$

(3.61)

Permeance and Reluctance of the PM path:

$$\mathcal{P}_{PM} = \mu_{rec} \frac{a_{PM}}{l_{PM}} = (1.10)(4\pi E - 6) \frac{(0.0001)}{0.02} = 6.91E-9 \frac{\text{Wb}}{\text{A}} \quad (3.62)$$

$$\mathcal{R}_{PM} = \frac{1}{\mathcal{P}_{PM}} = 1.45E+8 \frac{\text{A}}{\text{Wb}}$$

(3.63)

Permeance and Reluctance of the Air Gap at g-max:

$$\mathcal{P}_1 = \mu_0 \frac{a_{Fe}}{g} = (4\pi E - 6) \frac{(0.0001)}{0.10} = 1.26E-9 \frac{\text{Wb}}{\text{A}} \quad (3.64)$$

$$w = 2d + 2t = 2(0.01) + 2(0.01) = 0.04 \text{ m} \quad (3.65)$$

$$\mathcal{P}_2 = 0.24 \mu_0 w = 0.24(4\pi E - 6)0.04 = 1.21E-8 \frac{\text{Wb}}{\text{A}} \quad (3.66)$$

$$\mathcal{P}_4 = \mu_0 \frac{w}{\pi} \ln \left(1 + 2 \frac{h}{g} \right) \quad (3.67)$$

$$\mathcal{P}_4 = (4\pi E - 6) \frac{(0.04)}{\pi} \ln \left(1 + 2 \frac{0.01}{0.01} \right) = 2.92E - 9 \frac{\text{Wb}}{\text{A}} \quad (3.68)$$

$$\mathcal{P}_{gap} = \mathcal{P}_1 + \mathcal{P}_2 + \mathcal{P}_4 = 1.62E - 8 \frac{\text{Wb}}{\text{A}} \quad (3.69)$$

$\mathcal{R}_{gap} = \frac{1}{\mathcal{P}_{gap}} = 6.16E + 7 \frac{\text{A}}{\text{Wb}}$	(3.70)
--	--------

Total Reluctance:

$\mathcal{R}_{Tot} = \mathcal{R}_{Fe} + \mathcal{R}_{PM} + \mathcal{R}_{Gap} = 2.07E + 8 \frac{\text{A}}{\text{Wb}}$	(3.71)
--	--------

Permanent magnet NI:

$$NI_{PM} = H_{cR} I_{PM} = (767E + 3)(0.02) = 15,300 \text{ A-t} \quad (3.72)$$

Magnetic Flux and operating point:

$$\phi = \frac{NI_{PM} - NI_{Coil}}{\mathcal{R}_{Tot}} = \frac{15300 - 6000}{6.16E + 7} = 4.50E - 5 \text{ Wb} \quad (3.73)$$

$B_d = \frac{\phi}{a_{PM}} = \frac{4.50E - 5}{0.0001} = 0.45 \text{ T} = 4.50 \text{ kG}$	(3.74)
---	--------

$H_d = \frac{B_b - B_R}{\mu_{rec}} = \frac{0.45 - 1.06}{(1.10)(4\pi E - 7)} = -4.41E + 5 \frac{\text{A}}{\text{m}} = -5.54 \text{ kOe}$	(3.75)
---	--------

These calculations are for the 4th operating point at the worst-case conditions of maximum air gap and maximum Coil-NI (resulting in the lowest flux density and therefore the highest chance of demagnetization). Calculations can be done in the same way for the other 3 operating conditions to obtain the first 3 operating points (Fig. 3.29). Note that the reluctance of the steel

		Operating Point			
		1	2	3	4
Air Gap	g	0.01	0.01	0.10	0.10
Coil-NI	Nic	0	0	6000	6000
140°C Recoil Line					
PM Flux Density	<i>Bd</i>	0.90	0.74	0.55	0.45
PM Operating Point	<i>Hd</i>	-1.13E+05	-2.32E+05	-3.69E+05	-4.41E+05
PM Operating Point	<i>Hd</i>	kOe	-1.42	-2.91	-4.63
PM Flux Density	<i>Bd</i>	kG	9.04	7.40	5.50
New Recoil Line					
PM Flux Density	<i>Bd</i>	T	0.64	0.52	0.28
PM Operating Point	<i>Hd</i>	A/m	-7.96E+04	-1.64E+05	-3.35E+05
PM Operating Point	<i>Hd</i>	kOe	-1.00	-2.06	-4.22
PM Flux Density	<i>Bd</i>	kG	6.38	5.22	2.84

Figure 3.29: Results for 4 operating points and both recoil lines.

path can be ignored because it is 2 orders of magnitude smaller than the total reluctance. The resulting flux density error when ignoring the steel path is 0.4% at the 4th operating point, and 4.3% at the 1st operating point (0 Coil-NI, small air gap).

The 4 operating points for the 140°C recoil line are plotted on the demagnetization curve in **Fig. 3.30**. Also, shown are the load lines for the 4 operating points. Operating points #3 and #4 lie on the extended portion of the recoil line. The actual operating points are obtained by following the load line down to the demagnetization curve. The new recoil line is then drawn through the lowest operating point as done in **Fig. 3.30**. The permanent magnet properties from the new recoil line are listed below.

- $H_{cR} = -6.80 \text{ kOe} = 541 \text{ kA/m}$
- $B_R = 7.48 \text{ kG} = 0.75 \text{ T}$
- $\mu_{rec}/\mu_0 = 1.10$
- $BH_{max} = 12.7 \text{ MGOe} = 101 \text{ kJ/m}^3$

The calculated values for the 4 new operating points on the new recoil line are listed in **Fig. 3.29** and plotted on the graph in **Fig. 3.30**.

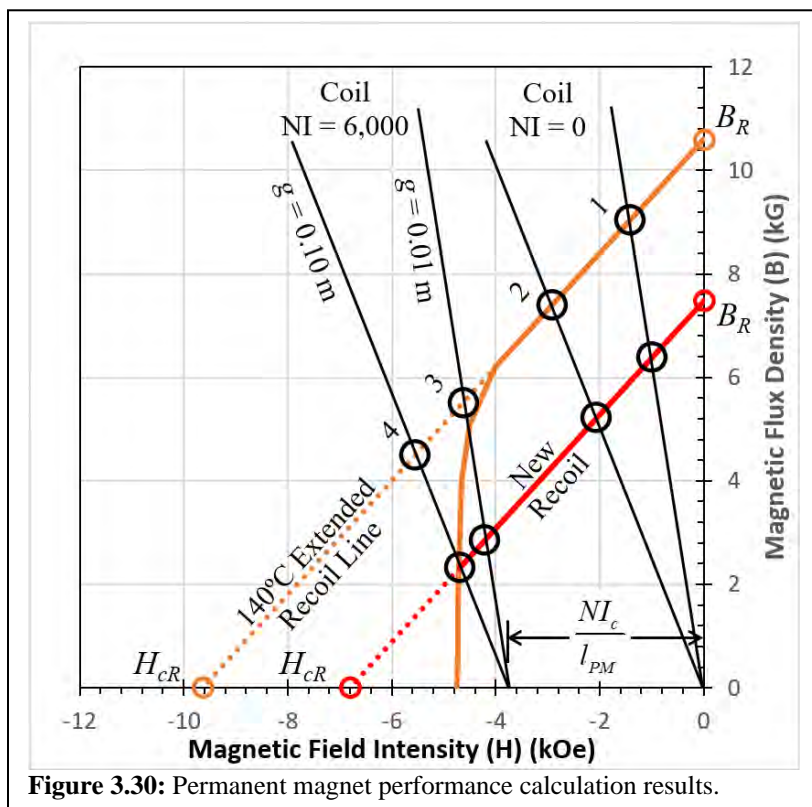


Figure 3.30: Permanent magnet performance calculation results.

4. Coil Design

a. Wire Resistivity and Size

The electrical conductivity of metal conductors is a function of temperature (**Eq. 4.1**). Values for the temperature coefficient of resistance (α) and the electrical conductivity at 20°C (σ_{20}) are listed in **Appendix-C**. The electrical conductivity of a wire should be calculated at the maximum expected operating temperature (σ_T), as follows. The copper temperature coefficient of resistance for copper (α_{cu}) is 0.393%/°C.

$$\boxed{\sigma_T = \frac{\sigma_{20}}{1 + \alpha(T - 20^\circ\text{C})}} \quad \text{Electrical Conductivity of a metal at } T^\circ\text{C} \quad (4.1)$$

$$\sigma_{cu-20} = 5.8E + 7 \text{ S/m} \quad \text{Copper electrical conductivity at } 20^\circ\text{C} \quad (4.2)$$

The bare wire diameter (d_B) (**Eq. 4.3**) is a function of the American Wire Gage (AWG). Wire sizes are typically available in integer values from 0 to 60 AWG. Half gage increments are available, but they are 2 to 3 times more expensive. The 1/0, 2/0, 3/0 and 4/0 wire sizes correspond to AWG values of 0, -1, -2 and -3, respectively. Increasing the wire gage by 3 (as from 2 to 5 AWG) reduces the bare wire cross-sectional area by a factor of 2.

$$\boxed{d_B = 0.008255(1.123)^{-\text{AWG}} \text{ m}} \quad \text{Bare wire diameter – Exact} \quad (4.3)$$

$$\boxed{d_B = 0.3250(1.123)^{-\text{AWG}} \text{ inch}} \quad \text{Bare wire diameter – Exact} \quad (4.4)$$

The maximum current density (J) for long wires (**Eq. 4.5**, 10.5% RMS Error) (from UL or IEC standards) is between $3E+6 \text{ A/m}^2$ ($2,000 \text{ A/in}^2$) for 1 AWG and $11E+6 \text{ A/m}^2$ ($7,000 \text{ A/in}^2$) for 18 AWG. Continuous operating coils typically have a current density of about $1,000 \text{ A/in}^2$ to $3,000 \text{ A/in}^2$, and higher values are possible with good cooling or a short operating time.

$$J < 111,711/d_B^{2/3} \text{ A/m}^2 \quad \text{IEC, UL Rated Current Density } (d_B = \text{m}) \quad (4.5)$$

Wire insulation is typically a varnish coating as described in **Appendix-H**. Temperature ratings for the various insulation materials vary from 105°C to 220°C. Coils should be designed to operate at or below the insulation temperature rating. This is discussed in detail in **Ch. 5**. The thickness (t) of a varnish coating can be accurately estimated with the following equations. Additional wire insulation details are provided in **Appendix-I**.

Single Build Insulation Thickness: (RMS Error = 10.5%)

$$t = 0.03924(1.0397)^{-\text{AWG}} \text{ mm} \quad (\text{for } 6 < \text{AWG} < 32) \quad (4.6)$$

$$t = 0.33361(1.1115)^{-\text{AWG}} \text{ mm} \quad (\text{for } 30 < \text{AWG} < 55) \quad (4.7)$$

Heavy Build Insulation Thickness: (RMS Error = 7.9%)

$$t = 0.06329(1.0360)^{-AWG} \text{ mm} \quad (\text{for } 6 < AWG < 32) \quad (4.8)$$

$$t = 0.40265(1.0992)^{-AWG} \text{ mm} \quad (\text{for } 30 < AWG < 55) \quad (4.9)$$

The overall wire diameter (d) including the insulation can be obtained with 2 methods, 1) from the bare wire diameter plus twice the insulation thickness, 2) from the curve fit correlations (Eq. 4.11 through Eq. 4.14).

$$d = d_B + 2t \quad \text{Overall wire diameter} \quad (4.10)$$

Single Build RMS Error = 1.2%
Heavy or Double Build RMS Error = 1.4%

Curve fit correlations for the overall wire diameter (d) including the insulation are listed below.

Single Build Insulation Overall Diameter: (for $6 < AWG < 55$)

$$d = 0.008172(1.1197)^{-AWG} \text{ m} \quad \text{RMS Error} = 1.3\% \quad (4.11)$$

$$d = 0.32174(1.1197)^{-AWG} \text{ inch} \quad (4.12)$$

Heavy Build Insulation Overall Diameter: (for $6 < AWG < 55$)

$$d = 0.007998(1.1165)^{-AWG} \text{ m} \quad \text{RMS Error} = 1.5\% \quad (4.13)$$

$$d = 0.31489(1.1165)^{-AWG} \text{ inch} \quad (4.14)$$

A typical coil and bobbin are shown in Fig. 4.1, where the dimensions represent the winding size. These are basic dimensions for all DC and AC coil.

l = Length of winding

D_I = Inside winding diameter

D_O = Outside winding diameter

A winding density factor (C) is used to account for non-precision winding, or the inclusion of terminations, which results in fewer turns. Typically, the values for C are between 0.70 and 0.95, where the higher value represents a precision winding. The winding mean turn length (l_M) and the winding cross-sectional area (A_W) can be calculated from the bobbin geometry, as follows.

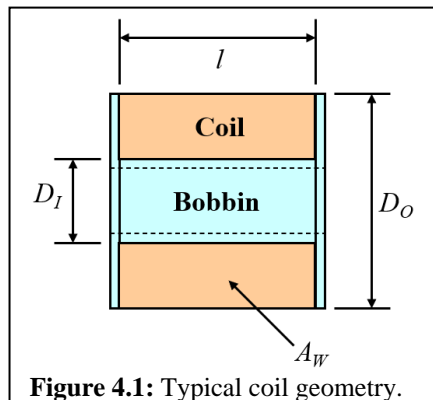


Figure 4.1: Typical coil geometry.

$$l_M = \pi \frac{D_O + D_I}{2} \quad \text{Mean Turn Length} \quad (4.15)$$

$$A_W = l \frac{D_O - D_I}{2} \quad \text{Winding Area} \quad (4.16)$$

b. DC Coil

A DC coil design is based on the source voltage (V) and required ampere-turns (NI). The required ampere-turns (NI) can be calculated from existing coil data, or it can be based on magnetic calculations for the NI needed to achieve a required flux density of force.

The minimum bare wire diameter ($d_{B\min}$) (**Eq. 4.21**) can be calculated with the required ampere-turns (NI), coil voltage (V), mean turn length (l_M), and the wire conductivity (σ_T) at the maximum coil temperature (T).

$$l = N l_M \quad \text{Wire length} \quad (4.17)$$

$$a = \pi \frac{d_B^2}{4} \quad \text{Wire cross-sectional area} \quad (4.18)$$

$$R = \frac{l}{\sigma_T a} = 4 \frac{N l_M}{\pi \sigma_T d_B^2} \quad \text{Winding resistance} \quad (4.19)$$

$$NI = N \left(\frac{V}{R} \right) = NV \left(\frac{\pi \sigma_T d_B^2}{4N l_M} \right) = \frac{\pi}{4} \left(\frac{V \sigma_T d_B^2}{l_M} \right) \quad (4.20)$$

$$d_{B\min} \geq \sqrt{\frac{4l_M NI}{\pi \sigma_T V}} \quad \text{Minimum bare wire diameter (m)} \quad (4.21)$$

Eq. 4.3 can be solved for the wire size (AWG), as follows. This is shown as an integer calculation because wire size is an integer AWG number. Also, the integer truncation (rounding down) gives a slightly larger bare wire diameter and gives a slightly larger NI . Rounding up will give a slightly small NI , which does not meet the NI requirement.

$$AWG = \text{int} \left(\frac{\ln(0.00826/d_{B\min})}{\ln(1.123)} \right) \quad \text{Wire AWG} \quad (4.22)$$

The turns (N) to achieve a full winding can be calculated as follows, given the wire size (AWG) (**Eq. 4.22**) and the overall wire diameter (d) (**Eq. 4.11** or **Eq. 4.13**). The 1st integer term represents the number of turns per winding layer. The 2nd integer term represents the number of winding layers.

$$N = \text{int} \left(\frac{l}{d} \sqrt{C} \right) \text{int} \left(\frac{(D_o - D_i)}{2d} \sqrt{C} \right) \quad \text{Turns for a full winding} \quad (4.23)$$

This always results in a coil design that produces the required NI . However, the overall size might need to be increased to reduce the current (to match the power supply) or to reduce the heat dissipation or temperature rise.

The DC coil performance characteristics, resistance (R), current (I), ampere-turns (NI), and heat dissipation (Q) are shown in **Fig. 4.2**.

Temperature = 20°C

$$R_{20} = 4 \frac{N l_M}{\pi \sigma_{20} d_B^2} \quad \text{Resistance (ohm)} \quad R_T = 4 \frac{N l_M}{\pi \sigma_T d_B^2} \quad (4.24)$$

$$I_{20} = \frac{V}{R_{20}} \quad \text{Current (A)} \quad I_T = \frac{V}{R_T} \quad (4.25)$$

$$NI_{20} = (N)(I_{20}) \quad \text{NI (ampere-turns)} \quad NI_T = (N)(I_T) \quad (4.26)$$

$$Q_{20} = \frac{V^2}{R_{20}} \quad \text{Heat (W)} \quad Q_T = \frac{V^2}{R_T} \quad (4.27)$$

Figure 4.2: DC coil performance characteristics, resistance (R), current (I), ampere-turns (NI) and heat dissipation (Q).

c. AC Coil

An AC coil design is based on the required peak magnetic flux (ϕ_P), the source peak voltage (V_P), and AC frequency (ω , rad/sec). The required magnetic flux can be calculated in 3 ways; 1) from existing coil data, 2) from the saturation flux density (B_{sat}), and the steel core cross-sectional area (a), 3) from magnetic calculations to achieve the desired magnetic flux or force.

Only the AC resistance loss is discussed in this section. Losses in AC coil windings are also produced by the skin effect and the proximity effect. The proximity effect causes eddy currents in adjacent coil windings due to the small space between turns. Correlations for both effects are available in technical papers, such as Jimenez [26] and Barrios [27].

$$\phi_P = \left(\frac{V_P}{N\omega} \right)_E \quad \text{Peak flux based on values from an existing coil} \quad (4.28)$$

$$\phi_P = B_{sat} a \quad \text{Peak flux based on } B_{sat}, \text{ see Appendix-D} \quad (4.29)$$

The number of turns (N) can be calculated based on Faraday's law. It is assumed that the inductive impedance is much larger than the coil resistance ($L\omega \gg R$), which is typical of AC Coils (a low resistance increases the magnetic flux and reduces the heat dissipation).

$$V = N \frac{d\phi}{dt} \quad \phi = \phi_P \sin(\omega t) \quad V_P = N\phi_P\omega \quad (4.30)$$

$$N = \text{int} \left(\frac{V_P}{\phi_P\omega} \right) \quad (4.31)$$

The max overall wire diameter (d_{MAX}) (Eq. 4.32) that can fit on the bobbin is calculated from the required turns (N) (Eq. 4.31) and the bobbin winding area (A_W) (Eq. 4.16). The wire size (AWG) corresponding to the overall wire diameter (d_{MAX}) is calculated from Eq. 4.33, where the AWG is rounded up. If it's rounded down the winding of N turns won't fit in the winding area.

$$d_{MAX} \leq \sqrt{\frac{CA_w}{N}} \quad (4.32)$$

$$AWG = \text{int} \left(\frac{\ln(0.00817/d_{MAX})}{\ln(1.1197)} \right) \quad (\text{single build insulation, round up}) \quad (4.33)$$

The bare wire diameter (d_B) can be obtained from **Eq. 4.3** and the coil resistance (R_{20} , R_T) can be obtained from **Eq. 4.24**. The coil inductance (L) can be calculated based on the permeance (\mathcal{P}), or from existing coil data (the E -subscripts refer to data from an existing coil).

$$L = N^2 \mathcal{P} \quad \text{from Permeance} \quad (4.34)$$

$$L = \left(\frac{N}{N_E} \right)^2 \left(\frac{V_p}{I_p \omega} \right)_E \quad \text{from an Existing coil data} \quad (4.35)$$

The actual flux (ϕ_A) will be smaller than the desired flux (ϕ_p) if the coil resistance is more than 5% of the inductive impedance ($L\omega$). The magnetic flux can be increased by decreasing the number of turns. The actual magnetic flux can be calculated as follows, based on the definition of inductance.

$$L = \frac{N\phi_A}{I_p} = \frac{N\phi_A}{V_p/Z} \quad \text{Inductance} \quad (4.36)$$

$$\phi_A = \frac{V_p}{N\omega} \frac{1}{\sqrt{(R/L\omega)^2 + 1}} \quad \text{Actual magnetic flux} \quad (4.37)$$

If the actual flux (ϕ_A) is less than the desired flux (ϕ_p), then the number of turns (N) in (Eq. 4.37) should be reduced until $\phi_A = \phi_p$ (within an acceptable tolerance). The initial estimate for the correct number of turns can be determined by multiplying the turns (N) by the flux ratio (ϕ_p/ϕ_A). The AC coil performance characteristics, resistance (R), impedance (Z), current (I), ampere-turns (NI), and heat dissipation (Q) are shown in **Fig. 4.3**.

Temperature = 20°C

$$R_{20} = 4 \frac{N l_M}{\pi \sigma_{20} d_B^2} \quad \text{Resistance (ohm)} \quad R_T = 4 \frac{N l_M}{\pi \sigma_T d_B^2} \quad (4.38)$$

$$Z_{20} = \sqrt{R_{20}^2 + (L\omega)^2} \quad \text{Impedance (ohm)} \quad Z_T = \sqrt{R_T^2 + (L\omega)^2} \quad (4.39)$$

$$I_{20} = \frac{V}{Z_{20}} \quad \text{Current (A)} \quad I_T = \frac{V}{Z_T} \quad (4.40)$$

$$Q_{20} = I_{20}^2 R_{20} \quad \text{Heat (Watts)} \quad Q_T = I_T^2 R_T \quad (4.41)$$

Figure 4.3: AC coil performance characteristics, resistance (R), current (I), ampere-turns (NI) and heat dissipation (Q). Note: “ Z ” and “ I ” are approximately constant with respect to temperature when $L\omega \gg R$.

d. Copper Area Ratio Method

The process of determining the wire diameter can be significantly simplified with the use of the copper area ratio ($K_A = A_C/A_W$) (Fig. 4.4), where the copper cross-sectional area (A_C) is based on the bare wire diameter (d_B), and A_W is winding cross-sectional area (Eq. 4.16).

$$A_C = N \frac{\pi d_B^2}{4} \quad \text{Total Copper cross-sectional area of a winding} \quad (4.42)$$

$K_A = A_C/A_W$		
<u>Copper Area Ratio</u>	<u>Insulation Layers</u>	
0.50 ± 0.04	Single Build	For C = 0.70
0.45 ± 0.07	Double Build	Best accuracy for
0.40 ± 0.10	Triple Build	$10 < \text{AWG} < 38$
0.35 ± 0.13	Quad Build	

Figure 4.4: Copper area ratio (K_A) for wires with various insulation build.

Fig. 4.4 illustrates that a coil wound with single build insulation wire, when cut in half, will show that 50% of the cross-sectional area is copper and 50% is air. This is very easy to remember and very easy to apply when, 1) needing to find the number of turns that will fit in the winding area for a given bare wire diameter (Eq. 4.43), or 2) needing to find the bare wire diameter that will fit the winding area for a given number of turns (Eq. 4.44).

The number of turns (N) for a DC Coil, or the bare wire diameter (d_B) for an AC Coil, can be estimated without needing to use the insulated wire diameter equations.

$$N = \text{int} \left(\frac{2 A_W}{\pi d_B^2} \right) \quad \text{DC Coil – replaces (Eq. 4.23)} \quad (4.43)$$

$$d_B \leq \sqrt{\frac{2 A_W}{\pi N}} \quad \text{AC Coil – replaces (Eq. 4.32)} \quad (4.44)$$

e. Coil Design Trade-Offs

The tables below show the design trade-offs and the resulting performance change for a given design variation. Each column shows the % change in performance for a variation in one of the 5 design variables. For example, in the DC chart below, the resulting change in performance for a +10% change in the length of the winding (l), is as follows.

- Resistance (R) Increases by 9.8%
- Inductance (L) Increases by 20.5%
- Temperature Rise (ΔT) Decreases by 13.5%
- Current (I) Decreases by 8.9%
- Ampere-Turns (NI) No change
- Flux (ϕ_A) No change

This chart can also be used from the bottom up. If a change in Coil- NI is desired the design variable with the largest effect is the wire gage (AWG).

<u>DC Coil Design Trade-Offs</u>					
Performance versus Design Variation					
Design Variables	Design Variations				
	const.	5%	const.	const.	---
	10%	const.	const.	---	const.
	const.	const.	+1	+1	+1
	---	---	---	const.	const.
Performance					
a. Winding Out. Dia. (D_o) [$D_i = 0.5 D_o$]	0.0%	5.0%	0.0%	0.0%	-9.2%
	10.0%	0.0%	0.0%	-19.2%	0.0%
	8.2%	4.3%	-0.8%	-16.7%	-10.4%
	9.8%	8.8%	23.5%	0.0%	0.0%
	9.8%	12.4%	55.7%	25.6%	18.4%
	20.5%	18.3%	52.5%	0.0%	0.0%
	-8.9%	-11.0%	-35.8%	-20.4%	-15.5%
	-13.5%	-12.5%	-30.9%	-3.7%	-4.8%
	-8.9%	-11.0%	-35.8%	-20.4%	-15.5%
	0.0%	-3.2%	-20.7%	-20.4%	-15.5%
	0.0%	-3.2%	-20.7%	-20.4%	-15.5%

Figure 4.5: DC Coil performance and design trade-offs.

In the AC chart below, the resulting change in performance for a +10% change in the length of the winding (l), is as follows.

- Turns (N) Increases by 11.8%
- Resistance (R) Increases by 11.8%
- Inductance (L) Increases by 24.9%
- Temperature Rise (ΔT) Decreases by 36.6%
- Current (I) Decreases by 19.9%
- Ampere-Turns (NI) Decreases by 10.5%
- Flux (ϕ_A) Decreases by 10.5%

This chart can also be used from the bottom up. If a change in magnetic flux (ϕ_A) is desired the design variables with the largest effect are the wire gage (AWG), winding outside diameter (Do), and length (l).

Note that this AC coil chart is for highly inductive AC coils, ($L\omega > 10 R$). Highly resistive AC coils ($R > 10 L\omega$) have the same trade-offs as DC coils.

AC Coil Design Trade-Offs					
Performance versus Design Variation					
<u>Design Variables</u>	<u>Design Variations</u>				
1. Winding Out. Dia. (Do) [$Di = 0.5 Do$]	const.	5%	const.	const.	---
2. Axial Winding Length (l)	10%	const.	const.	---	const.
3. Wire Gage (AWG)	const.	const.	+1	+1	+1
4. Turns (N)	---	---	---	const.	const.
<u>Performance</u>	<u>Results</u>				
a. Winding Out. Dia. (Do)	0.0%	4.8%	0.0%	0.0%	-9.4%
b. Axial Winding Length (l)	10.0%	0.0%	0.0%	-20.5%	0.0%
c. Heat Transfer Area (A)	6.2%	9.3%	-0.1%	-11.2%	-13.6%
d. Turns (N)	11.8%	10.0%	26.2%	0.0%	0.0%
e. Resistance (R) at 20.C	11.8%	13.1%	59.1%	26.1%	18.1%
f. Inductance (L)	24.9%	21.0%	59.2%	0.0%	0.0%
g. Power Diss. (Q) at 20.C	-28.3%	-22.8%	-37.2%	25.6%	17.7%
h. Temp. Rise (ΔT) at 20.C	-36.6%	-32.7%	-41.5%	54.0%	46.7%
i. Current (I) at 20.C	-19.9%	-17.2%	-37.2%	-0.2%	-0.1%
j. Coil NI at 20.C	-10.5%	-9.1%	-20.7%	-0.2%	-0.1%
k. Flux (ϕ_A) at 20.C	-10.5%	-9.2%	-20.7%	-0.2%	-0.1%

Figure 4.6: AC Coil performance and design trade-offs.

f. Example-5 – DC Coil Design

This is an exercise in the design of a cylindrical DC coil (Fig. 4.7). The design and performance calculations will be compared against measurements from an existing ST/SR coil.

The dimensions and performance requirements are as follows.

$$D_I = 0.687 \text{ inch} = 0.0174 \text{ m}$$

$$D_O = 1.300 \text{ inch} = 0.0330 \text{ m}$$

$$l = 1.775 \text{ inch} = 0.0451 \text{ m}$$

$$C = 0.90 \text{ winding density factor}$$

$$T_A = 50^\circ\text{C} - \text{air temperature}$$

$$T_I = 155^\circ\text{C} - \text{maximum insulation temperature}$$

$$V = 16.8 \text{ } 70\% \text{ of } 24 \text{ V} - \text{minimum source voltage}$$

$$NI = 3889 \text{ ampere-turns (at } 25^\circ\text{C, } 16.8 \text{ V) Copper Wire}$$

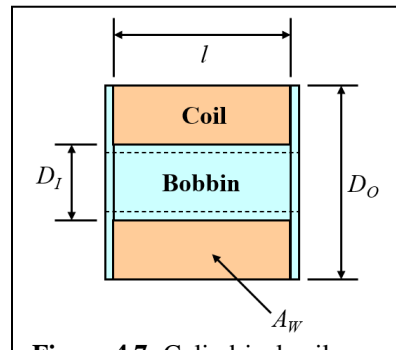


Figure 4.7: Cylindrical coil.

Calculate the mean turn length and the winding cross-sectional area:

$$l_M = \pi \frac{0.0330 + 0.0174}{2} = 0.0793 \text{ m} \quad (4.45)$$

$$A_W = 0.0451 \frac{0.0330 - 0.0174}{2} = 0.000351 \text{ m}^2 \quad (4.46)$$

Calculate the copper electrical conductivity, minimum bare wire diameter and the wire gage needed to achieve the required coil-*NI* at 25°C and 16.8 V:

$$\sigma_{25} = \frac{5.8E + 7}{1 + 0.00393(25 - 20)} = 5.69E + 7 \frac{\text{S}}{\text{m}} \quad (4.47)$$

$$d_{B,MIN} \geq \sqrt{\frac{4(0.0793)(3889)}{\pi(5.69E + 7)(16.8)}} = 0.000641 \text{ m} \quad (4.48)$$

$$AWG = \text{int}\left(\frac{\ln(0.00826/0.000641)}{\ln(1.123)}\right) = 22 \quad (4.49)$$

Calculate the bare wire diameter and the overall wire diameter from the wire size (*AWG*), and the number of turns.

$$d_B = 0.00826(1.123)^{-22} = 0.000644 \text{ m} \quad (4.50)$$

$$d = 0.00817(1.1197)^{-22} = 0.000679 \text{ m} \quad (4.51)$$

$$N = \text{int}\left(\frac{0.0451}{0.000679} \sqrt{0.9}\right) \text{int}\left(\frac{(0.0330 - 0.0174)}{2(0.000679)} \sqrt{0.9}\right) = 630 \text{ Turns} \quad (4.52)$$

Calculate the performance at 25°C and 16.8 V (resistance, current, NI).

$$R_{25} = 4 \frac{(630)(0.0793)}{\pi(5.69E+7)(0.000644)^2} = 2.70 \text{ ohms} \quad (4.53)$$

$$I_{25} = 16.8/2.70 = 6.22 \text{ amperes} \quad (4.54)$$

$$NI_{25} = (630)(6.22) = 3915 \text{ ampere-turns} \quad (4.55)$$

Calculate the performance at 50°C (air temperature) and 16.8 V (resistance, current, NI).

$$\sigma_{50} = \frac{5.8E+7}{1 + 0.00393(50 - 20)} = 5.19E+7 \frac{\text{S}}{\text{m}} \quad (4.56)$$

$$R_{50} = 4 \frac{(630)(0.0793)}{\pi(5.19E+7)(0.000644)^2} = 2.96 \text{ ohms} \quad (4.57)$$

$$I_{50} = 16.8/2.96 = 5.68 \text{ amperes} \quad (4.58)$$

$$NI_{50} = (630)(5.68) = 3579 \text{ ampere-turns} \quad (4.59)$$

Calculate the performance at 155°C (maximum insulation temperature) and 16.8 V (resistance, current, NI).

$$\sigma_{155} = \frac{5.8E+7}{1 + 0.00393(155 - 20)} = 3.79E+7 \frac{\text{S}}{\text{m}} \quad (4.60)$$

$$R_{155} = 4 \frac{(630)(0.0793)}{\pi(3.79E+7)(0.000644)^2} = 4.05 \text{ ohms} \quad (4.61)$$

$$I_{155} = 16.8/4.05 = 4.148 \text{ amps} \quad (4.62)$$

$$NI_{155} = (630)(4.14) = 2613 \text{ ampere-turns} \quad (4.63)$$

The comparison of the calculations to the measurements shows excellent agreement (**Fig. 4.8**).

Requirements				
	<i>D_I</i>	0.687	inch	
Inside Winding Dia.	<i>D_O</i>	1.300	inch	
Outside Winding Dia.	<i>l</i>	1.775	inch	
Winding Length	<i>V</i>	16.8	volts	
Voltage	<i>NI₂₅</i>	3,889	ampere-turns	
Ampere-Turns at 25°C				
Performance				
	Calculations		Measured	ST/SR Coil
Wire Size	AWG	22	22	AWG
Turns	<i>N</i>	630	625	turns
Resistance at 25°C	<i>R₂₅</i>	2.70	2.70	ohms
Current at 25°C	<i>I₂₅</i>	6.22	6.22	amperes
Ampere-Turns at 25°C	<i>NI₂₅</i>	3,915	3,889	ampere-turns
Ampere-Turns at 50°C	<i>NI₅₀</i>	3,579	---	ampere-turns
Ampere-Turns at 155°C	<i>NI₁₅₅</i>	2,613	---	ampere-turns

Figure 4.8: Coil performance calculations compared to measurements.

g. Example-6 – AC Coil Design

A sample AC coil design is shown below (Fig. 4.9) based on the procedures in **Section-c** (equation references are listed for each calculation). The AC coil has the same size and voltage as the DC coil in **Example-5**. The resulting design has 314 turns of 19 AWG wire and a resistance of 0.613 ohms.

- **Closed** air-gap: The coil has an inductance of 99.5 mH and a peak current of 0.633 amperes with a heat dissipation of 0.123 watts.
- **Open** air-gap: The coil has an inductance of 8.30 mH and a peak current of 7.45 amperes with a heat dissipation of 17.0 watts.
- AC actuators with an **open** air-gap have a low inductance, a high current, a high magnetic flux density, and can produce a high force.
- AC actuators with a **closed** air-gap have a high inductance, a low current, a high magnetic flux density, and a low heat dissipation. AC actuators have issues with alternating forces which can be addressed by rectification or with the use of shading rings (see **Ch. 8**).

Coil Geometry	Variable	Units	Value	Value	Units
Inside Winding Diameter	Di	in	0.687	1.74E-02	m
Outside Winding Diameter	Do	in	1.300	3.30E-02	m
Winding Length	l	in	1.775	4.51E-02	m
Winding Packing Factor	C	---	0.900	---	---
Core Diameter	Dc	in	0.600	1.52E-02	m
Required AC Performance	Variable	Units	Value	Value	Units
Peak Voltage (70% of 24 v-rms)	Vp	v-rms	16.80	2.38E+01	v-p
Frequency	f	Hz	60	3.77E+02	rad/s
Desired Pk. Mag. Flux Density	Bp	T	1.10	---	---
Material Properties	Variable	Units	Value		
Permeability of Air	μ_0	H/m	1.26E-06		
Conductivity of Copper at 25°C	σ	s/m	5.69E+07		
AC Calculation Results	Variable	Units	Value		Ref. Eq.
Desired Peak Magnetic Flux	ϕp	Wb	2.01E-04		Eq. 4.29
Number of Turns	N	turns	314		Eq. 4.31
Winding Cross Sectional Area	Aw	m^2	3.51E-04		Eq. 4.16
Max. Insulated Wire Diameter	d_{max}	m	1.00E-03		Eq. 4.32
Wire Size	AWG	awg	19		Eq. 4.33
Wire Insulated Diameter	d	m	9.53E-04		Eq. 4.11
Mean Turn Length of Winding	MTL	m	7.93E-02		Eq. 4.15
Resistance at 25°C	R	ohm	0.613		Eq. 4.19
AC Results with Various Gaps	Variable	Units	Closed	Open	Ref. Eq.
Core Air Gap	g	in	0.010	0.250	---
		m	2.54E-04	6.35E-03	---
Air Gap Permeance-1	P_1	Wb/NI	9.02E-07	3.61E-08	Eq. 1.47
Air Gap Permeance-2	P_2	Wb/NI	1.44E-08	1.44E-08	Eq. 1.52
Air Gap Permeance-4	P_4	Wb/NI	9.18E-08	3.37E-08	Eq. 1.63
Total Air Gap Permeance	$Pg = P_1 + P_2 + P_4$	Wb/NI	1.01E-06	8.42E-08	---
Inductance	L	H	9.95E-02	8.30E-03	Eq. 1.27
Pk. Magnetic Flux - Actual	ϕpa	Wb	2.01E-04	1.97E-04	Eq. 4.34
Pk. Mag. Flux Density - Actual	Bpa	T	1.10	1.08	Eq. 1.16
Impedance	Z	ohm	37.5	3.2	Eq. 4.39
Peak Current	I_p	amperes	0.633	7.448	Eq. 4.40
Heat Dissipation at 25°C	Q	watts	0.123	16.998	Eq. 4.41

Figure 4.9: AC coil design calculations for a closed and open air-gap.

5. Temperature Rise

a. Steady-State Heat Transfer

The smallest design usually has the highest temperature rise. The best design usually considers the trade-off between size and temperature rise. The heat dissipated (Q) and transferred from a hot object (such as a coil, T_C) to a cooler environment (such as the air, T_A) is proportional to the temperature difference between the coil and the air ($T_C - T_A$), the coil surface area (A_s) and the surface heat transfer coefficient (h) (Eq. 5.1). The coil surface temperature can be reduced by decreasing the heat dissipation (less resistance, less current), increasing the surface area (increasing the coil size or adding heat sink fins), or increasing the heat transfer coefficient (by using a fan to move the air).

$$Q = h A_s (T_C - T_A) = h A_s \Delta T \quad \text{Steady-State Heat Transfer} \quad (5.1)$$

$$h = 10 \frac{\text{W}}{\text{m}^2 \text{°K}} \quad \left[\begin{array}{l} \text{Combined Free Convection \& Radiation} \\ \text{Heat Transfer Coefficient} \end{array} \right] \quad (5.2)$$

$$A_s = \pi (D_o + D_l) l + \frac{\pi}{2} (D_o^2 - D_l^2) \quad \text{Coil Surface Area (Fig. 4.7)} \quad (5.3)$$

Measurements on coils by Roters [1] found the total heat transfer coefficient for coils to be $10 \text{ W/m}^2\text{°K}$. Also, the heat transfer coefficients for natural convection (h_c) and radiation (h_r) in electronic systems can be calculated from the correlations in Holman [18], as follows.

Listed below are the typical operating temperature values, the air properties (density, viscosity, thermal conductivity, Prandtl number), and the size and acceleration of gravity.

$$T_A = 30^\circ\text{C} = 303^\circ\text{K} \quad \Delta T = 60^\circ\text{K} \quad T_{ave} = 333^\circ\text{K} \quad \beta = \frac{1}{T_{ave}} = 0.003 \frac{1}{\text{°K}} \quad (5.4)$$

$$\rho = 1.06 \frac{\text{kg}}{\text{m}^3} \quad \nu = 1.89E - 5 \frac{\text{m}^2}{\text{s}} \quad k = 2.85E - 2 \frac{\text{W}}{\text{m}\cdot\text{°K}} \quad \text{Pr} = 0.707 \quad (5.5)$$

$$L = 0.25 \text{ m} \quad g = 9.8 \frac{\text{m}}{\text{s}^2} \quad (5.6)$$

The dimensionless Grashof number (Gr) and Nusselt number (Nu) define free convection heat transfer.

$$\text{Gr} = \frac{g \beta L^3 \Delta T \rho^2}{\nu^2} = 8.69E + 7 \quad (\text{Ratio of buoyancy to viscous forces}) \quad (5.7)$$

$$\text{Nu} = 0.520 \text{Pr}^{1/4} \text{Gr}^{1/4} = 46.0 \quad (\text{Ratio of convection to conduction}) \quad (5.8)$$

The free convection (no fan) heat transfer coefficient for electronic systems is defined from the Nusselt number, as follows.

$$h_c = \text{Nu} \frac{k}{L} = 5.25 \frac{\text{W}}{\text{m}^2 \cdot \text{°K}}$$

Free Convection heat transfer coefficient (5.9)

The radiation heat transfer coefficient for electronic systems is defined with the following radiation view factor ($F_{1,2}$), surface emissivity (ε), Stefan-Boltzmann constant (σ), and temperatures ($T_A = 303\text{°K}$, $T_C = 363\text{°K}$).

$$Q = h_r A_s \Delta T = F_{1,2} \sigma \varepsilon A_s (T_C^4 - T_A^4) \quad \text{Radiation Heat Transfer} \quad (5.10)$$

$$F_{1,2} = 0.8 \quad \varepsilon = 0.8 \quad \sigma = 5.669E-8 \frac{\text{W}}{\text{m}^2 \cdot \text{°K}^4} \quad (5.11)$$

$$h_r = F_{1,2} \sigma \varepsilon \frac{(T_C^4 - T_A^4)}{\Delta T} = 5.40 \frac{\text{W}}{\text{m}^2 \cdot \text{°K}} \quad \begin{bmatrix} \text{Radiation Heat} \\ \text{Transfer Coefficient} \end{bmatrix} \quad (5.12)$$

The heat transfer coefficient for combined heat transfer in electronic systems is the sum of the heat transfer coefficients for radiation and free convection. The value in **Eq. 5.13** matches up very well with the measured value from Roters [1]. This also shows that radiation heat transfer accounts for half of the total heat transfer in electronic systems with natural convection.

$$h = h_c + h_r = 10.65 \frac{\text{W}}{\text{m}^2 \cdot \text{°K}} \quad \begin{bmatrix} \text{Free Convection & Radiation} \\ \text{Heat Transfer Coefficient} \end{bmatrix} \quad (5.13)$$

The forced convection heat transfer coefficient with moving air from a fan ($h_c = 25 \text{ W/m}^2 \cdot \text{°K}$) can be more than 5x larger than the free convection heat transfer coefficient (**Eq. 5.9**). The total heat transfer coefficient becomes 3x larger than **Eq. 5.13** ($30 \text{ W/m}^2 \cdot \text{°K}$), which reduces the steady-state temperature rise by a factor of 3 (based on **Eq. 5.1**).

DC coils have a purely resistive impedance which changes with temperature. Therefore, the DC coil heat dissipation is calculated from constant voltage, ($Q = V^2 / R$). AC coils typically have a high inductive impedance which does not change with temperature. Therefore, the AC coil heat dissipation is calculated from constant current, ($Q = I^2 R$).

DC coil steady-state temperature rise:

The initial coil temperature is the ambient air temperature (T_A). The coil temperature eventually rises to the steady-state temperature ($T_C = T_A + \Delta T$). The initial heat dissipation (Q_A) can be calculated from the electrical resistance (R_A) when the coil temperature is at the ambient air temperature. The final heat dissipation (Q) can be calculated from the electrical resistance (R) when the coil is at the steady-state temperature ($T_C = T_A + \Delta T$), based on the temperature coefficient of resistance (α). The coil surface area (A_s) includes the outside and inside cylindrical circumference and both circular ends, as shown in **Fig. 4.7** and defined in **Eq. 5.3**.

$$Q_A = \frac{V^2}{R_A} = h A_s \Delta T_{0-A} \quad \text{Heat dissipation at } T_C = T_A \quad (5.14)$$

$$Q = \frac{V^2}{(1 + \alpha \Delta T) R_A} = \frac{Q_A}{1 + \alpha \Delta T} = h A_s \Delta T \quad \text{Heat at } T_C = T_A + \Delta T \quad (5.15)$$

The zero property temperature rise (ΔT_{0-A}) is based on a zero temperature coefficient of resistance ($\alpha = 0$) and properties at T_A , from **Eq. 5.14**.

$$\Delta T_{0-A} = \frac{Q_A}{h A_s} \quad \text{Zero property temperature rise, } \alpha = 0, T = T_A \quad (5.16)$$

The DC coil steady-state temperature rise (ΔT) can be defined as a function of the zero property temperature rise (ΔT_{0-A}) and the temperature coefficient of electrical resistance (α) by combining **Eq. 5.15** and **Eq. 5.16**, and solving the resulting quadratic equation.

$$\frac{\Delta T_{0-A}}{1 + \alpha \Delta T} = \Delta T \quad (5.17)$$

$$\Delta T = \frac{1}{2\alpha} \left(\sqrt{1 + 4\alpha \Delta T_{0-A}} - 1 \right) \quad \text{DC Steady-State temperature rise} \quad (5.18)$$

This equation (**Eq. 5.18**) gives a steady-state temperature rise (ΔT) that is smaller than zero property temperature rise (ΔT_{0-A}), as shown below.

- $\Delta T_{0-A} = 90^\circ\text{C}$ zero property temperature rise, $\alpha = 0, T = T_A$
- $\alpha = 0.393 \text{ \%}/^\circ\text{C}$ Temperature Coeff. of resistance for copper
- $\Delta T = 70^\circ\text{C}$ Steady-State temperature rise for a copper coil

AC coil steady-state temperature rise:

The initial coil temperature is the ambient air temperature (T_A). The coil temperature eventually rises to the steady-state temperature ($T_C = T_A + \Delta T$). The initial heat dissipation (Q_A) can be calculated from the electrical resistance (R_A) when the coil temperature is the ambient air temperature. The final heat dissipation (Q) can be calculated from the electrical resistance (R) when the coil is at the steady-state temperature ($T_C = T_A + \Delta T$), based on the temperature coefficient of resistance (α). These calculations do not include the high-frequency effects of skin effect and proximity effect. Correlations for both effects are available in technical papers, such as Jimenez [26] and Barrios [27].

$$Q_A = I^2 R_A = h A_s \Delta T_{0-A} \quad \text{Heat dissipation at } T_C = T_A \quad (5.19)$$

$$Q = I^2 (1 + \alpha \Delta T) R_A = (1 + \alpha \Delta T) Q_A = h A_s \Delta T \quad (\text{at } T_C = T_A + \Delta T) \quad (5.20)$$

The zero property temperature rise (ΔT_{0-A}) (**Eq. 5.16**) is based on a zero temperature coefficient of resistance ($\alpha = 0$) and properties at T_A . The AC coil steady-state temperature rise (ΔT) can be defined as a function of the zero property temperature rise (ΔT_{0-A}) and the temperature coefficient of electrical

resistance (α) by combining **Eq. 5.16** and **Eq. 5.20**, and solving the resulting equation.

$$\frac{Q_A}{h A_s} = \Delta T_{0-A} = \frac{\Delta T}{1 + \alpha \Delta T} \quad (5.21)$$

$\Delta T = \frac{\Delta T_{0-A}}{1 - \alpha \Delta T_{0-A}}$	AC Steady-State temperature rise	(5.22)
---	----------------------------------	--------

This equation (**Eq. 5.22**) gives a steady-state temperature rise (ΔT) that is larger than the zero property temperature rise (ΔT_{0-A}), as shown below.

- $\Delta T_{0-A} = 55^\circ\text{C}$ zero property temperature rise, $\alpha = 0$, $T = T_A$
- $\alpha = 0.393 \text{ \%}/^\circ\text{C}$ Temperature Coeff. of resistance for copper
- $\Delta T = 70^\circ\text{C}$ Steady-State temperature rise for a copper coil

Note that the steady-state temperature rise (ΔT) goes to infinity when $\Delta T_{0-A} = 1/\alpha = 254^\circ\text{C}$. This demonstrates thermal runaway (**Eq. 5.22**).

Summary of Steady State Heat Transfer	
$h = 10 \frac{\text{W}}{\text{m}^2 \text{K}}$	$\left[\begin{array}{l} \text{Combined Free Convection \&} \\ \text{Radiation Heat Transfer Coefficient} \end{array} \right]$ (5.2)
$\Delta T_{0-A} = \frac{Q_A}{h A_s}$	$\left[\begin{array}{l} \text{Zero property Temp. Rise } (\alpha = 0) \\ \text{Properties are based on } T = T_A \end{array} \right]$ (5.16)
$\Delta T = \frac{1}{2\alpha} \left(\sqrt{1 + 4\alpha \Delta T_{0-A}} - 1 \right)$	$\left[\begin{array}{l} \text{DC Steady State Temp. Rise} \\ \text{Temp. Coeff. of Resist. } \alpha > 0 \end{array} \right]$ (5.18)
$\Delta T = \frac{\Delta T_{0-A}}{1 - \alpha \Delta T_{0-A}}$	$\left[\begin{array}{l} \text{AC Steady State Temp. Rise} \\ \text{Temp. Coeff. of Resist. } \alpha > 0 \end{array} \right]$ (5.22)

Figure 5.1: Temperature rise including the temperature coefficient of resistance. Note that the difference between the DC and AC temperature rise is due to the impedance of the coil (the high-frequency skin effect and proximity effect are not included).

The current in a **DC coil** (or in a high resistance AC coil, $R \gg L\omega$) is inversely proportional to the coil resistance. Therefore, as the DC coil temperature increases, the resistance increases, the current decreases, and the heat dissipation decreases.

The current in a high inductance **AC coil** ($L\omega \gg R$) is inversely proportional to the coil inductance, which is constant relative to temperature. Therefore, as the AC coil temperature increases, the resistance increases, the current remains constant, and the heat dissipation increases.

Correlations for the high-frequency skin effect and proximity effect are available in technical papers, such as Jimenez [26] and Barrios [27].

b. Transient Heat Transfer

The purpose of this section is to estimate the maximum time duration that a coil can be energized (turned ON) before the wire temperature exceeds either the insulation temperature rating or the melting temperature.

If the coil temperature exceeds the wire insulation temperature rating (T_i), the life of the insulation decreases. If the temperature rating is exceeded by a larger margin the insulation will begin to smoke. Therefore, the time to reach T_i is called the **Smoke Time** (Δt_s).

If the coil temperature exceeds the wire melting temperature (T_M), the wire will begin to melt, which is what a fuse is designed to do. Therefore, the time to reach T_M is called the **Fusing Time** (Δt_f).

Generally, the ON-time is critical in pulsed coils, such as in an actuator that only needs to be energized for enough time to release a mechanical latch. Coils in these actuators can be very small, which would make them very hot in steady-state, but they can survive if the ON-time of the pulse is short. During short periods there is very little heat transfer away from a coil. Therefore, it can be assumed that all of the heat dissipation is absorbed by the wire (zero heat transfer coefficient, $h = 0$). The energy absorbed by the wire is proportional to the wire mass (m), the wire specific heat (c_p), and the temperature rise (ΔT), as follows.

$$Q \Delta t = m c_p \Delta T \quad \text{Energy absorbed by the wire} \quad (5.23)$$

$$m = N \rho l_M \frac{\pi}{4} d_B^2 \quad \text{Mass of the wire (\rho is the density)} \quad (5.24)$$

Typical wire materials are copper and aluminum. Silver is an interesting conductor only because it is 17% more conductive than copper. The electrical conductivity (σ) and specific heat (c_p) change as a function of temperature for copper and aluminum (Fig. 5.2) (material properties are listed in Appendix-C). Temperature dependant material properties cause the time versus temperature characteristic to be nonlinear, which is evaluated by integrating the properties over the temperature rise.

	<u>Copper</u>	<u>Aluminum</u>
Electrical Conductivity (σ), 20°C:	$5.80E+7$ S/m	$3.54E+6$ S/m
Electrical Resistivity, 20°C:	0.0172 $\mu\text{-ohm}\cdot\text{m}$	0.282 $\mu\text{-ohm}\cdot\text{m}$
Temp. Coeff. - Resistance (α):	0.393 %/°C	0.403 %/°C
Specific Heat (c_p), 20°C:	384 J/kg·°K	961 J/kg·°K
Temp. Coeff. - Specific Heat (α_{cp}):	0.025 %/°C	0.049 %/°C

Figure 5.2: Temperature dependant properties for copper & aluminum.

The smoke time (Δt_s) and fusing time (Δt_f) equations (Fig. 5.3) were curve-fit to the temperature rise data that was obtained by integrating Eq. 5.23 over the temperature rise with changing properties. The zero property time (Δt_0) is based on a zero temperature coefficient ($\alpha = 0$) and 20°C properties. Smoke

time is evaluated relative to the insulation temperature rating (T_I) and fusing time is evaluated relative to the wire melting temperature (T_M).

Eq. 5.30 shows the constant voltage fusing time is 3.37 times longer than the zero property fusing time, and **Eq. 5.33** shows the constant current fusing time is only 43% of the zero property fusing time. Both results are primarily due to the increase in resistance with temperature.

Summary of Transient Heat Transfer (in Still Air, or with a Fan)	
Smoke Time (Δt_S):	$\Delta t_S = \text{Time to reach } \Delta T_I$
Fusing Time (Δt_F):	$\Delta t_F = \text{Time to reach } \Delta T_M$
Insulation Temp. Rise Limit:	$\Delta T_I = T_I - T_A \quad (5.25)$
Melting Temp. Rise Limit:	$\Delta T_M = T_M - T_A \quad (5.26)$
Zero Property Time ($\alpha = 0, h = 0$, Properties are for $T = 20^\circ\text{C}$):	
$\Delta t_{0,I} = \frac{mc_p \Delta T_I}{Q_{20}}$	$\Delta t_{0,M} = \frac{mc_p \Delta T_M}{Q_{20}} \quad (5.27)$
DC Coil Time (Constant Voltage, $\alpha > 0$): (Fit Error < 2.3%)	
$\Delta t_{DC} = \Delta t_0 (0.00217 \Delta T + 0.00414 T_A + 0.922) \quad (5.28)$	
Example: $\Delta t_{S-DC} = 1.36 \Delta t_{0,I}$	$(T_A = 50^\circ\text{C}, T_I = 155^\circ\text{C}) \quad (5.29)$
Example: $\Delta t_{F-DC} = 3.37 \Delta t_{0,M}$	$(T_A = 50^\circ\text{C}, T_M = 1083^\circ\text{C}) \quad (5.30)$
AC Coil Time (Constant Current, $\alpha > 0$): (Fit Error < 2.9%)	
$\Delta t_{AC} = \frac{\Delta t_0}{\sqrt{[(1.09E-5)T_A + 0.00347]\Delta T + (0.00372T_A + 0.921)^2}} \quad (5.31)$	
Example: $\Delta t_{S-AC} = 0.779 \Delta t_{0,I}$	$(T_A = 50^\circ\text{C}, T_I = 155^\circ\text{C}) \quad (5.32)$
Example: $\Delta t_{F-AC} = 0.431 \Delta t_{0,M}$	$(T_A = 50^\circ\text{C}, T_M = 1083^\circ\text{C}) \quad (5.33)$
Figure 5.3: Smoke Time and Fusing Time for copper wire, including the temperature coefficient of resistance. Temperatures are in $^\circ\text{C}$. It is assumed that all of the heat dissipation is absorbed by the wire (no heat transfer to the air) (zero heat transfer coefficient, $h = 0$).	

The current in a **DC coil** (or in a high resistance AC coil, $R \gg L\omega$) is inversely proportional to the coil resistance. Therefore, as the DC coil temperature increases, the resistance increases, the current decreases, and the heat dissipation decreases.

The current in a high inductance **AC coil** ($L\omega \gg R$) is inversely proportional to the coil inductance, which is constant relative to temperature. Therefore, as the AC coil temperature increases, the resistance increases, the current remains constant, and the heat dissipation increases.

The difference between DC and AC coil temperature rise is due to the impedance, as described above. Correlations for the high-frequency skin

effect and proximity effect are available in technical papers, such as Jimenez [26] and Barrios [27], and used in calculations in **Ch. 9**.

Transient Time Constant:

The steady-state (**Eq. 5.1**) and transient (**Eq. 5.23**) heat transfer equations can be combined in an energy balance (heat in = heat out to air + heat stored) to give the thermal time constant (τ) and transient temperature solution.

$$Q = h A_s (T - T_A) + m c_p \frac{dT}{dt} \quad \text{Energy balance} \quad (5.34)$$

$$T = Be^{st} + C \quad \text{Exponential solution} \quad (5.35)$$

$$0 = h A_s + m c_p s \quad s = -\frac{h A_s}{m c_p} = -\frac{1}{\tau} \quad \text{Characteristic Eq.} \quad (5.36)$$

$$@ t = \infty : C = \frac{Q}{h A_s} + T_A \quad @ t = 0 : B = -\frac{Q}{h A_s} \quad \text{Constants} \quad (5.37)$$

$$T = \frac{Q}{h A_s} \left(1 - e^{-t/\tau} \right) + T_A \quad \text{Linear Transient solution} \quad (5.38)$$

$$\tau = \frac{m c_p}{h A_s} \quad \text{Thermal Time Constant} \quad (5.39)$$

An old joke states that wire is made of smoke, and you should never let the smoke out, because it's very difficult to get it back inside. This is comical, but smoke coming from a coil almost always means that the coil insulation has been damaged severely. Coil turns can become shorted if the insulation is hot enough to smoke, or if the coil experiences a voltage pulse high enough to exceed the insulation breakdown strength.

c. Magnet Wire Insulation Life

The magnet wire standard ANSI/NEMA MW 1000-2003 [17] gives the following requirements.

- Life must be $\geq 20,000$ hours at or above the thermal class rating.
- Life must be $\geq 5,000$ hours at least 20°C above the thermal class rating. Life is reduced by Half for each 10°C above the rating.

A listing of magnet wire insulation is provided in **Appendix-H**, where temperature ratings range from 105°C to 220°C . Also, both Essex and MWS Wire Industries offer a 240°C rated insulation.

Above 200°C , Copper oxidizes, pits, and becomes brittle, the insulation loses adhesion, becomes damaged, and the winding will fail. Oxidation can be prevented with a silver or nickel coating, or by using an aluminum conductor.

The Arrhenius Equation can be used to calculate Insulation Life (L):

$$L = A e^{(B/T)} \quad \text{Arrhenius Equation (Temperature is in } ^\circ\text{K}) \quad (5.40)$$

$$B = \ln\left(\frac{L_1}{L_2}\right) \left/ \left(\frac{1}{T_1} - \frac{1}{T_2} \right) \right. \quad \text{Solution for coefficient-}B \quad (5.41)$$

$$A = \frac{L_1}{e^{(B/T_1)}} \quad \text{Solution for coefficient-}A \quad (5.42)$$

The following temperature and life data combines the temperature rating for 155°C class insulation with the life requirements from ANSI/NEMA MW 1000-2003. These data points can be used to determine the coefficients A and B for the Arrhenius equation from **Eq. 5.41** and **Eq. 5.42**.

	Insulation	
	<u>Rated Temperature</u>	<u>20°C above Rating</u>
Temperature	$T_1 = 155^{\circ}\text{C} = 428^{\circ}\text{K}$	$T_2 = 175^{\circ}\text{C} = 448^{\circ}\text{K}$
Life	$L_1 = 20,000 \text{ hr}$	$L_2 = 5,000 \text{ hr}$

The Arrhenius coefficients for this data are, $A = 6.53E-10 \text{ hr}$, $B = 13,291 \text{ } ^\circ\text{K}$.

d. Example-7 – DC Coil Temperature

This example uses the coil design requirements and the performance calculations from **Example-5**. The objective is to calculate the steady-state temperature rise and the smoke time. The coil was designed to give the required coil-*NI* at 16.8 V (70% of the 24 V rating). But the voltage source can go up to 26.4 V (110% of the 24 V rating).

The dimensions and performance calculations are listed below.

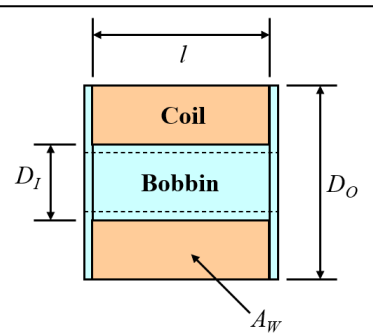


Figure 5.4: Cylindrical coil.

$$D_I = 0.687 \text{ inch} = 0.0174 \text{ m}$$

$$D_o = 1.300 \text{ inch} = 0.0330 \text{ m}$$

$$l = 1.775 \text{ inch} = 0.0451 \text{ m}$$

$$T_A = 50^\circ\text{C} - \text{Air temperature}$$

$$T_I = 155^\circ\text{C} - \text{Insulation temperature rating}$$

$$V = 26.4 \text{ } 100\% \text{ of } 24 \text{ V} - \text{Minimum source voltage}$$

$$N = 630 \text{ Turns}$$

$$R = 2.96 \text{ Ohms at } 50^\circ\text{C}$$

$$l_M = 0.0793 \text{ m} - \text{Winding mean turn length}$$

$$d_B = 0.000644 \text{ m} - \text{Bare wire diameter}$$

$$\rho = 8941 \text{ kg/m}^3 - \text{Density}$$

$$c_p = 385 \text{ J/kg} \cdot ^\circ\text{C} - \text{Specific Heat}$$

$$\alpha = 0.00393 \text{ } ^\circ\text{C}/\text{C} - \text{Temperature Coefficient of Resistance}$$

$$A_s = \pi(D_o + D_I)l + 2\frac{\pi}{4}(D_o^2 - D_I^2) \quad \text{Coil heat transfer surface area} \quad (5.43)$$

$$A_s = \pi(0.033 + 0.0174)0.0451 + \frac{\pi}{2}(0.033^2 - 0.0174^2) = 0.00838 \text{ m}^2 \quad (5.44)$$

- Still Air (No Fan) (natural or free convection)

Calculate the zero property temperature rise and heat dissipation at $T_A = 50^\circ\text{C}$:

$$h_c = 5 \text{ W/m}^2 \cdot ^\circ\text{K} - \text{Heat Trans. Coefficient} - \text{Natural Convection}$$

$$h_r = 5 \text{ W/m}^2 \cdot ^\circ\text{K} - \text{Heat Trans. Coefficient} - \text{Radiation}$$

$$h = 10 \text{ W/m}^2 \cdot ^\circ\text{K} - \text{Heat Trans. Coefficient} - \text{Total}$$

$$Q_{50} = \frac{26.4^2}{2.96} = 235 \text{ watts} \quad (5.45)$$

$$\Delta T_{0-A} = \frac{Q_{50}}{h A_s} = \frac{235}{(10)(0.00838)} = 2804^\circ\text{C} \quad (5.46)$$

Calculate the steady-state temperature rise from **Eq. 5.18**.

$$\Delta T = \frac{1}{2(0.00393)} \left(\sqrt{1+4(0.00393)(2804)} - 1 \right) = 726 \text{ } ^\circ\text{C} \quad (5.47)$$

$$T_{MAX} = T_A + \Delta T = 50 + 726 = 776 \text{ } ^\circ\text{C} \quad \text{Steady-State Temperature} \quad (5.48)$$

The steady-state temperature ($T_{MAX} = 776^\circ\text{C}$) is less than the melting temperature of copper ($T_M = 1083^\circ\text{C}$). Therefore, the wire won't melt and the fusing time calculation is not needed.

The steady-state temperature ($T_{MAX} = 776^\circ\text{C}$) is more than the insulation temperature rating ($T_i = 155^\circ\text{C}$). Therefore, we need to calculate the smoke time to determine how long the coil can remain "ON" before the wire temperature exceeds the insulation temperature rating.

Calculate the wire mass, the zero property smoke time, and the coil resistance at $T = 20^\circ\text{C}$.

$$R_{20} = \frac{(630)(0.0793)(4)}{(5.8E+7)(\pi)(0.000644)^2} = 2.64 \text{ ohm} \quad (5.49)$$

$$Q_{20} = \frac{26.4^2}{2.64} = 264 \text{ watts} \quad (5.50)$$

$$m = (630)(8941)(0.0793) \frac{\pi}{4} (0.000644)^2 = 0.145 \text{ kg} \quad (5.51)$$

$$\Delta T_i = 155 - 50 = 105 \text{ } ^\circ\text{C} \quad (5.52)$$

$$\Delta t_{0,I} = \frac{mc_p \Delta T_i}{Q_{20}} = \frac{(0.145)(385)(105)}{264} = 22.2 \text{ sec} \quad (5.53)$$

Calculate the Smoke Time from **Eq. 5.28**.

$$\Delta t_s = 22.2 \left((0.00217)(105) + (0.00414)(50) + 0.922 \right) = 30.1 \text{ sec} \quad (5.54)$$

The coil can stay on for 30.1 seconds before the insulation temperature rating is exceeded. In the actual application, the ST/SR coil is energized for only 0.400 seconds. Therefore, the coil will survive.

Calculate the thermal time-constant from **Eq. 5.39**:

$$\tau = \frac{mc_p}{h A_s} = \frac{(0.145)(385)}{(10)(0.00838)} = 666 \text{ sec} = 11.1 \text{ min} \quad (5.55)$$

The thermal time-constant is 11.1 minutes. The steady-state temperature rise (726°C) will be achieved after approximately 5 time-constants (55.5 minutes). Note that these calculations are for heat transfer in still air (no fan) (natural convection).

- Moving Air (With a Fan) (forced convection)

Using a fan can increase the convection heat transfer coefficient by 5x, to 25 W/m²·°K. The combined heat transfer coefficient becomes 30 W/m²·°K.

$h_c = 25 \text{ W/m}^2\cdot\text{°K}$ – Heat Trans. Coefficient – Forced Convection

$h_r = 5 \text{ W/m}^2\cdot\text{°K}$ – Heat Trans. Coefficient – Radiation

$h = 30 \text{ W/m}^2\cdot\text{°K}$ – Heat Trans. Coefficient – Total

$$\Delta T_{0-A} = \frac{Q_{50}}{h A_s} = \frac{235}{(30)(0.00838)} = 935 \text{ °C} \quad (5.56)$$

Calculate the steady-state temperature rise from **Eq. 5.18**.

$$\Delta T = \frac{1}{2(0.00393)} \left(\sqrt{1 + 4(0.00393)(935)} - 1 \right) = 377 \text{ °C} \quad (5.57)$$

$$T_{MAX} = T_A + \Delta T = 50 + 377 = 427 \text{ °C} \quad \text{Steady-State Temperature} \quad (5.58)$$

Calculate the thermal time-constant from **Eq. 5.39**:

$$\tau = \frac{mc_p}{h A_s} = \frac{(0.145)(385)}{(30)(0.00838)} = 222 \text{ sec} = 3.7 \text{ min} \quad (5.59)$$

The thermal time-constant is 3.7 minutes. The steady-state temperature rise (377°C) will be achieved after approximately 5 time-constants (18.5 minutes).

The calculations for still air and fan-forced air calculations are listed below in **Fig. 5.5**. The smoke time calculations are the same for both conditions (without a Fan and with a Fan) because the smoke time assumes no heat transfer to the air ($h = 0$). The smoke time (30.1 sec) is 7.4 times faster than the thermal time constant with a fan, and 22 times faster than the thermal time constant without a fan, which verifies the assumption of $h = 0$. The temperature rise (ΔT , $\alpha > 0$) is less than for zero properties (ΔT_{0-A}) because resistance increases and the current decreases with temperature.

		Units	No Fan	Fan
Heat Dissipation at 50°C	Q_{50}	W	235	
Temperature Rise ($\alpha = 0$)	ΔT_{0-A}	°C	2804	935
Temperature Rise ($\alpha > 0$)	ΔT	°C	726	377
Max. Steady State Temp.	T_{max}	°C	776	427
Heat Dissipation at 20°C	Q_{20}	W	264	
Temperature Rise to Smoke	ΔT_I	°C	105	
Smoke Time ($\alpha = 0, h = 0$)	Δt_{0-I}	sec	22.2	
Smoke Time ($\alpha > 0, h = 0$)	Δt_s	sec	30.1	
Thermal Time Constant	τ	min	11.1	3.7
Time to reach Steady State	5τ	min	55.5	18.5

Figure 5.5: DC Coil temperature rise and smoke time calculations for the conditions without Fan (still air), and with a Fan (moving air).

e. Example-8 – AC Coil Temperature

The AC coil design and the performance calculations are based on the design from **Example-6**. The same ambient air temperature (50°C) and wire insulation temperature rating (155°C) are used as in **Example-7**. The AC coil resistance, inductance, impedance, current, and heat dissipation are calculated for the open and closed core air-gap and baseline temperatures (**Fig. 5.6**). The impedance is relatively unaffected by the temperature and therefore the current is relatively constant with respect to temperature.

Coil & Wire Characteristics		Units	Values		Ref. Eq.
Peak Source Voltage	V_{pk}	volts-pk	23.8		Example-6
Frequency	f	Hz	60		Example-6
Frequency	ω	1/s	377.0		Example-6
Turns	N	turns	314		Example-6
Wire Size	AWG	awg	19		Example-6
Bare Wire Diameter	d_B	m	9.11E-04		Eq. 4.5
Mean Turn Length	Mtl	m	0.0793		Example-6
Length of Wire ($N \times Mtl$)	lw	m	24.9		---
Mass of Wire	m	kg	0.145		Eq. 5.51
Coil Surface area	As	m^2	0.00838		Eq. 5.44
Copper conductivity at 20°C	σ_{20}	s/m	5.80E+07		Eq. 4.3
Copper conductivity at 25°C	σ_{25}	s/m	5.69E+07		Eq. 4.47
Copper conductivity at 50°C	σ_{50}	s/m	5.19E+07		Eq. 4.56
Specific Heat of Copper	cp	J/kg·°C	384		App-C
Coil Resistance at 25°C	R_{25}	ohm	0.613		Example-6
Air Temperature	T_A	°C	50		Example-7
Insulation Temp. Rating	T_I	°C	155		Example-7
Temperature Rise to Smoke	ΔT_I	°C	105		Eq. 5.26
Copper Melting Temperature	T_M	°C	1083		App-C
Temperature Rise to Melt	ΔT_M	°C	1033		Eq. 5.27
		Air-Gap			
Current & Heat Dissipation		Units	Open	Closed	Ref. Eq.
Inductance	L	H	8.30E-03	9.95E-02	Example-6
Coil Resistance at 50°C	R_{50}	ohm		6.72E-01	Eq. 4.57
Coil Resistance at 20°C	R_{20}	ohm		6.01E-01	Eq. 5.49
Impedance at 50°C	Z_{50}	ohm	3.20	37.5	Eq. 4.39
Impedance at 20°C	Z_{20}	ohm	3.19	37.5	Eq. 4.39
Peak Current	I_{pk}	A-pk	7.44	0.634	Eq. 4.40
Heat Dissipation at 50°C	Q_{50}	w	18.58	0.135	Eq. 4.41
Heat Dissipation at 20°C	Q_{20}	w	16.63	0.121	Eq. 4.41

Figure 5.6: AC coil design characteristics, and calculations for current and heat dissipation as a function of temperature and core air-gap. Core diameter = 0.600 in., air-gap = 0.010 & 0.250 in. (see **Example-6**).

- **Still Air (No Fan) (natural or free convection)**

The steady-state and transient thermal performance results for operation without a fan (still air) are listed in **Fig. 5.7**.

Calculations Results - Still Air		Units	No Fan		Ref.
			Open	Closed	
Heat Transfer Coefficient					
– Natural Convection	h_c	w/m ² ·°K	5		Eq. 5.9
– Radiation	hr	w/m ² ·°K	5		Eq. 5.12
– Total	h	w/m ² ·°K	10		Eq. 5.13
Steady-State Heat Transfer		Units	No Fan		Ref.
			Open	Closed	
Temperature Rise ($\alpha = 0$)	$\Delta T_{0,A}$	°C	222	1.61	Eq. 5.16
Temperature Rise ($\alpha > 0$)	ΔT	°C	1726	1.62	Eq. 5.22
Max. Steady State Temp.	T_{max}	°C	1776	51.6	Eq. 5.48
Transient Heat Transfer		Units	No Fan		Ref.
			Open	Closed	
Smoke Time ($\alpha = 0, h = 0$)	$\Delta t_{0,I}$	min	5.85	-na-	Eq. 5.27
Smoke Time ($\alpha > 0, h = 0$)	Δt_s	min	4.56	-na-	Eq. 5.31
Fusing Time ($\alpha = 0, h = 0$)	$\Delta t_{0,F}$	min	57.6	-na-	Eq. 5.27
Fusing Time ($\alpha > 0, h = 0$)	Δt_F	min	48.2	-na-	Eq. 5.31
Thermal Time Constant	τ	min	11.1	11.1	Eq. 5.39
Time to reach Steady State	5τ	min	55.3	55.3	---

Figure 5.7: AC coil thermal performance without a fan.

- **Moving Air (With a Fan) (forced convection)**

The steady-state and transient thermal performance results for operation with a fan (moving air) are listed in **Fig. 5.8**.

Calculations Results - Moving Air		Units	with a Fan		Ref.
			Open	Closed	
Heat Transfer Coefficient					
– Forced Convection	h_c	w/m ² ·°K	25		Eq. 5.9
– Radiation	hr	w/m ² ·°K	5		Eq. 5.12
– Total	h	w/m ² ·°K	30		Eq. 5.13
Steady-State Heat Transfer		Units	with a Fan		Ref.
			Open	Closed	
Temperature Rise ($\alpha = 0$)	$\Delta T_{0,A}$	°C	73.9	0.54	Eq. 5.16
Temperature Rise ($\alpha > 0$)	ΔT	°C	104	0.54	Eq. 5.22
Max. Steady State Temp.	T_{max}	°C	154	50.5	Eq. 5.48
Transient Heat Transfer		Units	with a Fan		Ref.
			Open	Closed	
Thermal Time Constant	τ	min	3.7	3.7	Eq. 5.39
Time to reach Steady State	5τ	min	18.4	18.4	---

Figure 5.8: AC coil thermal performance with a fan.

The AC coil steady-state and transient calculation results (**Fig. 5.7**, **Fig. 5.8**) show the following characteristics.

- No Fan: (**Fig. 5.7**)
 - Open air-gap:
 - The Maximum Steady-State Temperature ($T_{max} = 1776^\circ\text{C}$) is greater than the melting temperature ($T_m = 1083^\circ\text{C}$). The temperature rise is very high because the current is relatively constant and the coil resistance increases with temperature. This calculation shows that the AC coil has entered the slippery slope of “Thermal Runaway”.
 - Thermal Time Constant is: $\tau = 11.1$ minutes.
 - Steady-State temperature rise time is: $5\tau = 55.3$ minutes.
 - The Smoke Time ($\Delta t_s = 4.56$ minutes) (time to exceed the insulation temperature rating) is less than the thermal time constant. Therefore, the assumption of zero heat transfer to the air is valid, and this is a good estimate of the Smoke Time.
 - The Fusing Time ($\Delta t_F = 48.2$ minutes) (time to exceed the copper melting temperature) is much larger than the thermal time constant. Therefore, the assumption of zero heat transfer to the air is not valid, and the Fusing Time will be longer, up to the time to reach the Steady-State temperature rise ($5\tau = 55.3$ minutes). However, realistically, the maximum coil operating time should be less than the Smoke Time (4.5 min.) to prevent damage to the insulation.
 - Closed air-gap:
 - Heat dissipation is reduced by more than 2 orders of magnitude due to the increased inductive impedance.
 - The Maximum Steady-State Temperature ($T_{max} = 51.6^\circ\text{C}$) is less than the insulation temperature rating ($T_I = 155^\circ\text{C}$). Therefore, there is no Smoke Time and no Fusing Time.
- With a Fan: (**Fig. 5.8**)
 - Open air-gap:
 - The Maximum Steady-State Temperature ($T_{max} = 154^\circ\text{C}$) is less than the insulation temperature rating ($T_I = 155^\circ\text{C}$). Therefore, there is no Smoke Time and no Fusing Time.
 - Thermal Time Constant is: $\tau = 3.7$ minutes.
 - Steady-State temperature rise time is: $5\tau = 18.4$ minutes.
 - The Fan increases the heat transfer coefficient by a factor of 3 and reduces the temperature rise by a factor of 16.6. This very large temperature reduction is a result of staying away from “Thermal Runaway”.
 - Closed air-gap:
 - Heat dissipation is reduced by more than 2 orders of magnitude due to the increased inductive impedance.
 - The Maximum Steady-State Temperature ($T_{max} = 50.5^\circ\text{C}$) is much lower than the insulation temperature rating. Therefore, there is no Smoke Time and no Fusing Time.

6. Solenoid Design and Pole Shaping

a. Simplified Solenoid Geometry

A flat face pole face configuration (rather than a tapered cup-cone shape) is used in this example to simplify the calculations. The dimensions for the existing solenoid parts are shown below (**Fig. 6.1**) with the armature in the open position.

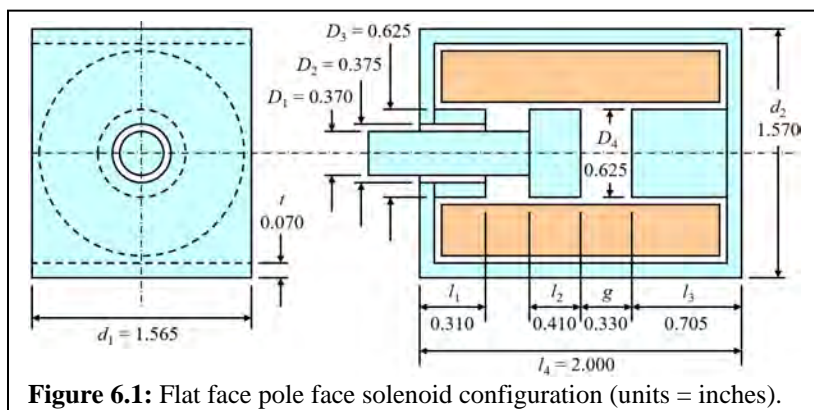


Figure 6.1: Flat face pole face solenoid configuration (units = inches).

The spring force characteristic is shown in **Fig. 6.2**, where a low spring force ($F_{s1} = 0.6 \text{ lbf}$) holds the solenoid open. The armature begins to push on a trip latch when the gap (g) is 0.175 inches and the combined spring and latch force (F_{s2}) is 2.70 lbf.

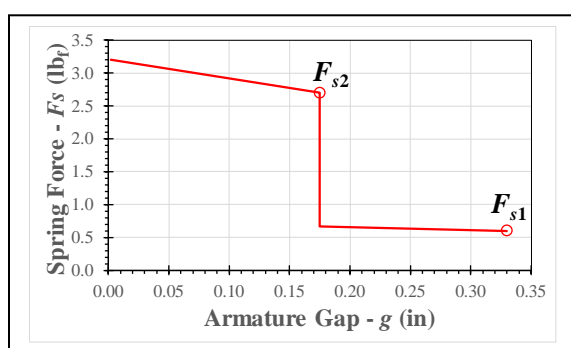


Figure 6.2: Spring force versus air gap size.

Spring Force Curve:

Open Position	$g_1 = 0.330 \text{ in}$	Spring Force	$F_{s1} = 0.60 \text{ lbf}$
Trip Latch Contact	$g_2 = 0.175 \text{ in}$	Total Force	$F_{s2} = 2.70 \text{ lbf}$
Closed Position	$g_3 = 0 \text{ in}$	Total Force	$F_{s3} = 3.20 \text{ lbf}$

The critical positions are the open position (g_1) and the trip latch contact position (g_2). The design must produce more force than 0.60 lbf to start the armature moving and more force than 2.70 lbf to move the trip latch.

b. Solenoid Flux Paths

The magnetic flux paths are shown in **Fig. 6.3**. The magnetic flux is shown in the steel parts (red arrows) and the air gaps (blue arrows with fringing). The air gap permeances are indicated as P_{g1} , P_{g2} , P_{g3} , P_{g4} , P_{s1} , P_{s3} , and P_{s5} , as defined in **Ch. 1.g.**

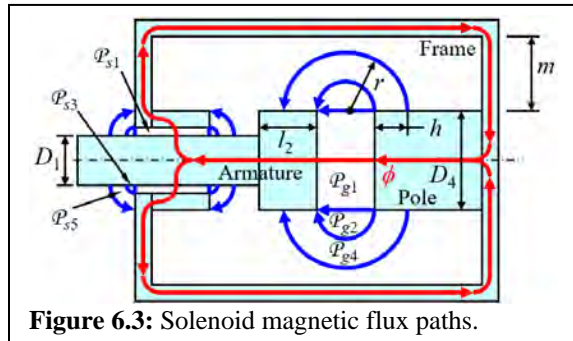


Figure 6.3: Solenoid magnetic flux paths.

The height (h) of the outer flux path (P_{g4}) is equal to D_4 (**Ch. 1.g.**). However, in this case, it is limited by the space (m) from the pole to the magnetic frame.

$$m = \frac{d_2 - 2t - D_4}{2} \quad \text{Space between pole and magnetic frame} \quad (6.1)$$

$$h = m - \frac{g}{2} < D_4 \quad \text{Height of fringing flux path} \quad (6.2)$$

A large radius ($r > m$) for flux path P_{g4} (**Fig. 6.3**) causes the fringing flux to flow to the magnetic frame (as leakage flux), where it leaks away from the armature. However, the magnetic frame is rectangular with open sides (**Fig. 6.1**). Therefore, the leakage is small and can be ignored to simplify the calculations. Leakage can be minimized in a cylindrical frame by increasing the space (m).

c. Reluctance Network

The magnetic flux paths are shown in **Fig. 6.4**. A single frame reluctance is shown due to symmetry. One magnetic frame reluctance covers both sides of the magnetic frame by using twice the cross-sectional area of the frame. The

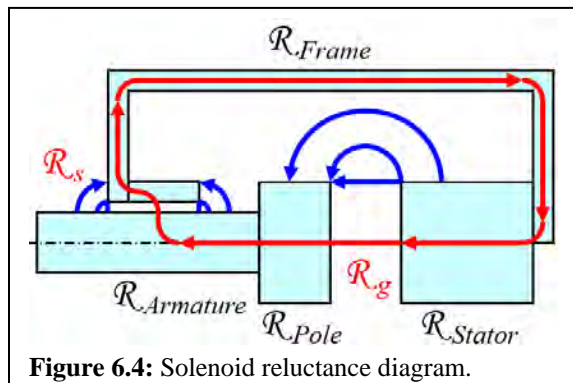


Figure 6.4: Solenoid reluctance diagram.

armature with the enlarged pole face moves toward the stator pole across an air gap (g) and slides through the frame in a clearance air gap (s).

The reluctance network (**Fig. 6.5**) shows the coil- NI , the linear constant reluctance of the air gap flux path (\mathcal{R}_g), and the clearance air gap flux path (\mathcal{R}_s) in red. The steel nonlinear reluctance flux paths for the armature, pole, and stator are shown in black.

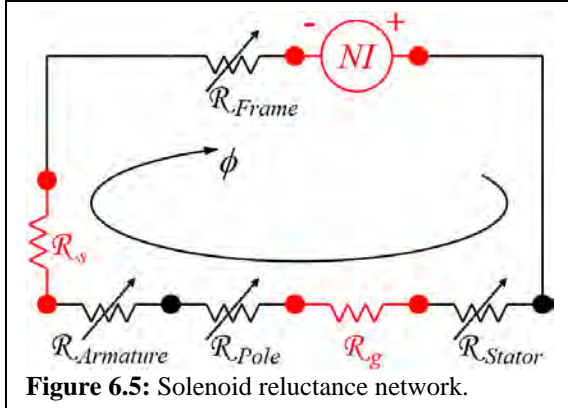


Figure 6.5: Solenoid reluctance network.

The nonlinear permeability for annealed 1010 steel is obtained from **Appendix-E** with the k -values, $k_1 = 4.847$, $k_2 = 1.908$, $k_3 = 227.3$. The maximum relative permeability is 3,429 and the saturation flux density (B_{sat}) is 1.79 T.

$$\mu_{Steel} = \mu_{r-Steel} \mu_0 \quad \text{Steel permeability} \quad (6.3)$$

$$\mu_{r-Steel} = \frac{1}{\mu_0 \left(k_1 e^{(k_2 B^2)} + k_3 \right)} + 1 \quad \text{Steel relative permeability} \quad (6.4)$$

A simplified approach is used here, in which the nonlinear reluctance of the steel is assumed to be zero ($\mathcal{R}_{steel} = 0$). This is valid when the steel permeability is large and the flux density in the steel remains below the saturation level ($B < B_{sat} = 1.8$ T). The high relative permeability of the steel ($\mu_{r-Steel} = 3,429$) results in steel reluctance values that are 3 orders of magnitude smaller than the air gap reluctance. Therefore, only the air-gap permeance (P_g and P_s) and reluctance (\mathcal{R}_g and \mathcal{R}_s) values need to be calculated.

The resulting linear reluctance network with only the air gap reluctances and the coil- NI is shown below (**Fig. 6.6**) (nonlinear steel reluctance is assumed equal to zero).

Assumptions:

$$B < B_{sat}$$

$$\mathcal{R}_{Air} \gg \mathcal{R}_{Steel}$$

$$\mathcal{R}_{Frame} = 0$$

$$\mathcal{R}_{Armature} = 0$$

$$\mathcal{R}_{Pole} = 0$$

$$\mathcal{R}_{Stator} = 0$$

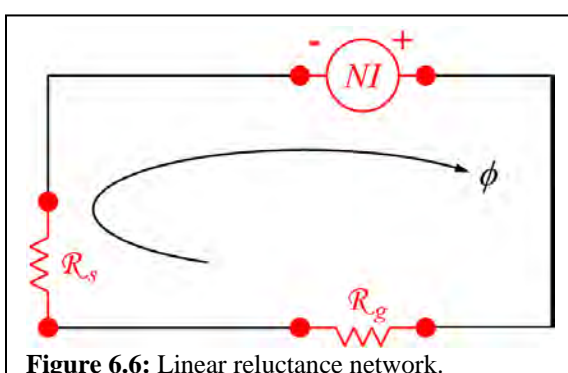


Figure 6.6: Linear reluctance network.

d. Estimated Armature Cross Section

The 1st step in designing a solenoid is to estimate the pole diameter from the chart in **Fig. 2.6** or from **Eq. 2.24** based on the highest critical spring force ($F_{s2} = 2.70 \text{ lbf}$) and corresponding air gap ($g_2 = 0.175 \text{ in}$) at the saturation magnetic flux density ($B = B_{sat} = 1.8 \text{ T}$).

$$\text{Eq. 2.24 for reference: } p_{\max} = \frac{1.02 \left(\frac{B}{1.6} \right)^2}{\left(1 + 4.96 \left(\frac{g}{D} \right)^{0.724} + 0.264 \left(\frac{g}{D} \right)^2 \right)} \text{ MPa}$$

The initial estimate for the diameter (D_4) of the pole and stator:

- $F_{s2} = 2.70 \text{ lbf}$
- Assume the air gap (g_2) and diameter (D_4) are similar for $g/D = 1$
- For **Eq. 2.24**, $B = 1.8 \text{ T}$, $p_{\max} = 0.218 \text{ MPa} = 31.8 \text{ lbf/in}^2$
- $a_4 = \frac{\pi D^2}{4} = \frac{F_{s2}}{p_{\max}} = \frac{2.70}{31.8} = 0.0849 \text{ in}^2 \quad D_4 = 0.329 \text{ in}$

This result ($D_4 = 0.329 \text{ in}$) is a reasonable initial estimate for the pole diameter. But it results in a g/D ratio that is closer to 0.53. Iteration could be done on this to get a value that converges to a consistent solution. However, there are additional characteristics that need to be considered, such as adjusting the pole and stator diameter to minimize the coil- NI while achieving the required forces.

The force at $g = 0.175 \text{ in}$, and $B = 1.8 \text{ T}$ is calculated for a wide range of pole face diameters and is shown in the graph in **Fig. 6.7**. The solid red line is calculated with **Eq. 2.24**. The dashed red line uses the permeance calculations (P_{g1} , P_{g2} , P_{g4} , P_{s1} , P_{s3} , P_{s5}) and the permeance rate of change (dP/dg) calculations as detailed in the next section (**Ch. 1.e**).

The results plotted in **Fig. 6.7** for **Eq. 2.24** are summarized below. These calculations are based on an armature shaft diameter of $D_1 = 0.370 \text{ inches}$ and an armature air gap of $g = 0.175 \text{ inches}$. The total magnetic flux is calculated by saturating the smallest diameter (D_1 or D_4) at $B = 1.8 \text{ T}$.

- $0.480 < D_4 < 0.580 \text{ inches}$ = the recommended range for the pole face diameter.
- The force exceeds 2.70 lbf over the recommended range for D_4 , and the required ampere-turns are relatively low (52% lower compared to the coil- NI for $D_4 = 0.329 \text{ in.}$).
- **Eq. 2.24** uses the largest value for the height of the fringing flux path (h) rather than the reduced value from **Eq. 6.2**. This results in a 20% lower force for large values of D_4 .

The permeance calculations in the next section (**Ch. 1.e**) allow for the use of the smaller h -value (**Eq. 6.2**), which gives a 20% increase in the force at large values of D_4 . The coil- NI and force are calculated from the air gap permeance (\mathcal{P}) and the permeance rate of change ($d\mathcal{P}/dg$) in the next section. The coil- NI is calculated by multiplying the total magnetic flux by the total reluctance. The results from **Fig. 6.7** for the permeance rate of change ($d\mathcal{P}/dg$) calculations are summarized below.

- $0.550 < D_4 < 0.650$ inches = the recommended range for the pole face diameter.
- This range validates the design of the existing armature and pole, where $D_4 = 0.625$ in.
- The force is proportional to the square of the magnetic flux density (**Eq. 2.16**, **Eq. 2.24**). Therefore, a 5% increase in the magnetic flux density gives a 10% increase in the force.
- The magnetic flux density in the pole and stator (diameter D_4) is equal to 1.8 T when $D_4 < D_1$. When $D_4 > D_1$, the magnetic flux density in the armature (diameter D_1) is 1.8 T, and the magnetic flux density in the pole and stator is less than 1.8 T based on the area ratio, $B = 1.8 (D_1/D_4)^2$ T.

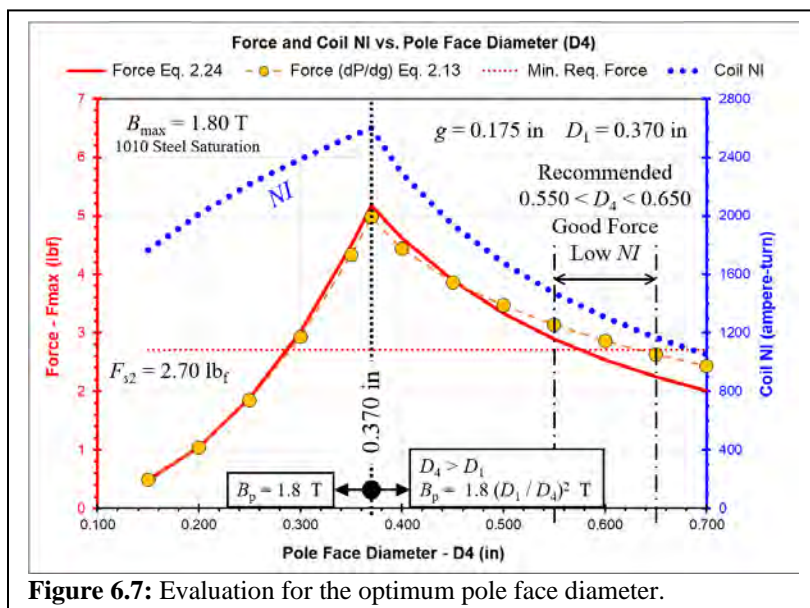


Figure 6.7: Evaluation for the optimum pole face diameter.

e. Magnetic Calculations, Linear Model

This analysis corresponds to the linear reluctance network in **Fig. 6.6**. Only the air-gap permeances (\mathcal{P}_g and \mathcal{P}_s) are calculated. All calculations use the critical operating point ($g_2 = 0.175$ in., $F_{s2} = 2.70$ lb_f) and the pole and stator diameter from the physical solenoid, $D_4 = 0.625$ inches.

Permeance (\mathcal{P}_g) and reluctance (\mathcal{R}_g) for the pole to stator air-gap (g):

Clearance from pole to frame:

$$m = \frac{d_2 - 2t - D_4}{2} = \frac{1.570 - 0.140 - 0.625}{2} = 0.4025 \text{ in} = 0.0102 \text{ m} \quad (6.5)$$

Height of fringing flux path:

$$h = m - \frac{g}{2} < D_4 = 0.4025 - \frac{0.175}{2} = 0.315 \text{ in} = 0.00800 \text{ m} \quad (6.6)$$

Pole to stator air-gap permeance:

$$\mathcal{P}_{g1} = \mu_0 \frac{\pi D_4^2 / 4}{g} = (4\pi E - 7) \frac{0.000198}{0.00445} = 5.596E - 8 \frac{\text{Wb}}{\text{A}} \quad (6.7)$$

$$\mathcal{P}_{g2} = 0.24\mu_0(\pi D_4) = 0.24(4\pi E - 7)0.2953 = 1.504E - 8 \frac{\text{Wb}}{\text{A}} \quad (6.8)$$

$$\mathcal{P}_{g4} = \mu_0 \frac{\pi D_4}{\pi} \ln\left(1 + 2 \frac{h}{g}\right) = 3.044E - 8 \frac{\text{Wb}}{\text{A}} \quad (6.9)$$

$$\mathcal{P}_g = \mathcal{P}_{g1} + \mathcal{P}_{g2} + \mathcal{P}_{g4} = 1.014E - 7 \frac{\text{Wb}}{\text{A}} \quad (6.10)$$

$$\boxed{\mathcal{R}_g = 1/\mathcal{P}_g = 9.858E + 6 \frac{\text{A}}{\text{Wb}}} \quad (6.11)$$

Sliding air-gap (l_2) permeance (\mathcal{P}_s) and reluctance (\mathcal{R}_s):

$$\mathcal{P}_{s1} = \mu_0 \frac{\pi D_1 l_1}{(D_2 - D_1)/2} = (4\pi E - 7) \frac{0.000232}{0.000064} = 4.601E - 6 \frac{\text{Wb}}{\text{A}} \quad (6.12)$$

$$\mathcal{P}_{s3} = 0.48\mu_0\pi D_2 = 0.48(4\pi E - 7)\pi(0.00953) = 1.805E - 8 \frac{\text{Wb}}{\text{A}} \quad (6.13)$$

$$\mathcal{P}_{s5} = 2\mu_0 \frac{\pi D_2}{\pi} \ln\left(1 + \frac{(D_3 - D_2)/2}{(D_2 - D_1)/2}\right) = 9.412E - 8 \frac{\text{Wb}}{\text{A}} \quad (6.14)$$

$$\mathcal{P}_s = \mathcal{P}_{s1} + 2(\mathcal{P}_{s3} + \mathcal{P}_{s5}) = 4.825E - 6 \frac{\text{Wb}}{\text{A}} \quad (6.15)$$

$$\boxed{\mathcal{R}_s = 1/\mathcal{P}_s = 2.073E + 5 \frac{\text{A}}{\text{Wb}}} \quad (6.16)$$

The reluctance of the sliding air gap (\mathcal{R}_s) is nearly two orders of magnitude smaller than the reluctance of the pole to stator air-gap (\mathcal{R}_g). Therefore, sliding air gap reluctance (\mathcal{R}_s) could be assumed to be zero ($\mathcal{R}_s = 0$) to provide a quicker estimate. This analysis uses both reluctances (\mathcal{R}_g and \mathcal{R}_s).

Total Reluctance (\mathcal{R}) and Permeance (\mathcal{P}):

$$\boxed{\mathcal{R} = \mathcal{R}_s + \mathcal{R}_g = 1.007E + 7 \frac{\text{A}}{\text{Wb}}} \quad (6.17)$$

$$\mathcal{P} = 1/\mathcal{R} = 9.935E - 8 \frac{\text{Wb}}{\text{A}} \quad (6.18)$$

Permeance rate of change ($d\mathcal{P}/dg$) at the pole to stator air-gap (g):

$$\frac{d\mathcal{P}_{g1}}{dg} = \frac{\mathcal{P}_{g1}}{g} = \frac{5.596E - 8}{0.00445} = 1.259E - 5 \frac{\text{Wb}}{\text{A-m}} \quad (6.19)$$

$$\frac{d\mathcal{P}_{g4}}{dg} = \mu_0 \frac{w}{\pi} \left(\frac{2h/g}{1 + 2h/g} \right) \frac{1}{g} = 3.512E - 6 \frac{\text{Wb}}{\text{A-m}} \quad (6.20)$$

$$\boxed{\frac{d\mathcal{P}_g}{dg} = \frac{d\mathcal{P}_{g1}}{dg} + \frac{d\mathcal{P}_{g4}}{dg} = 1.610E - 5 \frac{\text{Wb}}{\text{A-m}}} \quad (6.21)$$

The DC coil design (**Ch. 4.f**) shows the minimum Coil-NI at 155°C is 2613 ampere-turns. The linear solution (assuming no saturation) gives the following magnetic flux and flux density.

Total Flux:

$$\phi = NI\mathcal{P} = (2613)(1.007E - 7) = 2.63E - 4 \text{ Wb} \quad (6.22)$$

The maximum flux density is calculated on the flux path with the smallest diameter (D_1):

$$B = \frac{\phi}{\pi D_1^2 / 4} = \frac{2.63E - 4}{\pi (0.370 / 39.37)^2 / 4} \quad \boxed{B = 3.79 \text{ T} \gg 1.8 \text{ T}} \quad (6.23)$$

NI drop across the pole to stator air-gap (g):

$$NI_g = \phi \mathcal{R}_g = (2.63E - 4)(9.858E + 6) = 2592 \text{ ampere-turns} \quad (6.24)$$

Force across the pole to stator air-gap:

$$F_g = 0.5(NI_g^2) \frac{d\mathcal{P}_g}{dg} = 0.5(2592^2)(1.610E - 5) \quad \boxed{= 54.1 \text{ N} = 12.2 \text{ lb}_f} \quad (6.25)$$

The flux density (**Eq. 6.23**) is far above the saturation point for 1010 steel, which is not consistent with the assumption of no saturation ($B < 1.8 \text{ T}$). Therefore, this is not a physically reasonable solution, and a non-linear saturating calculation or flux limiting calculation is needed.

Flux limiting calculation:

It is very difficult to get more magnetic flux at saturation. The smallest cross-section flux path will act as a flux limiter. The maximum force (F_{max}) on the pole can be estimated by limiting the flux density in the smallest flux path (D_1) to saturation ($B_{a-sat} = 1.8 \text{ T}$) and reducing the flux density in the pole (D_4) proportionally to $B_p = B_{a-sat} (D_1/D_4)^2$. Saturation is not a perfect flux limiter, and this coil produces a lot of ampere-turns. Therefore, the actual flux density in the armature can be a little higher than 1.8 T, and the actual force on the pole can be higher than F_{max} . As mentioned earlier, force is proportional to the square of the magnetic flux density (**Eq. 2.16**, **Eq. 2.24**), therefore 5% more magnetic flux produces 10% more force.

The force in a linear (non-saturating) system can be estimated using the proportionality to the square of the magnetic flux density (with dimensions held constant). In this case, the Armature flux density is limited to saturation at $B_{a-sat} = 1.8$ T (rather than 3.79 T as calculated in **Eq. 6.23**).

$$\frac{F_{\max}}{F} = \frac{B_{a-sat}^2}{B_a^2} \quad F_{\max} = F \frac{B_{a-sat}^2}{B_a^2} = 12.2 \left(\frac{1.8}{3.79} \right)^2 \quad \boxed{F_{\max} = 2.74 \text{ lb}_f} \quad (6.26)$$

The maximum force (F_{\max}) exceeds the required force (2.70 lb_f). Therefore, the solenoid should pull-in and trip the latch mechanism.

f. Comparison of Analysis Methods

The results are compared (**Fig. 6.8**) for five analysis methods (listed below), including the results from a 3D finite element simulation.

1. Linear reluctance, no flux limit, using $d\Phi/dg$, **Ch. 6.e.**
2. Linear reluctance, flux-limited to 1.8 T, using $d\Phi/dg$, **Ch. 6.e.**
3. Linear reluctance, flux-limited to 1.8 T, using **Eq. 2.24**
4. Nonlinear reluctance with a nonlinear BH curve, using $d\Phi/dg$
5. 3D finite element simulation with a nonlinear BH curve.

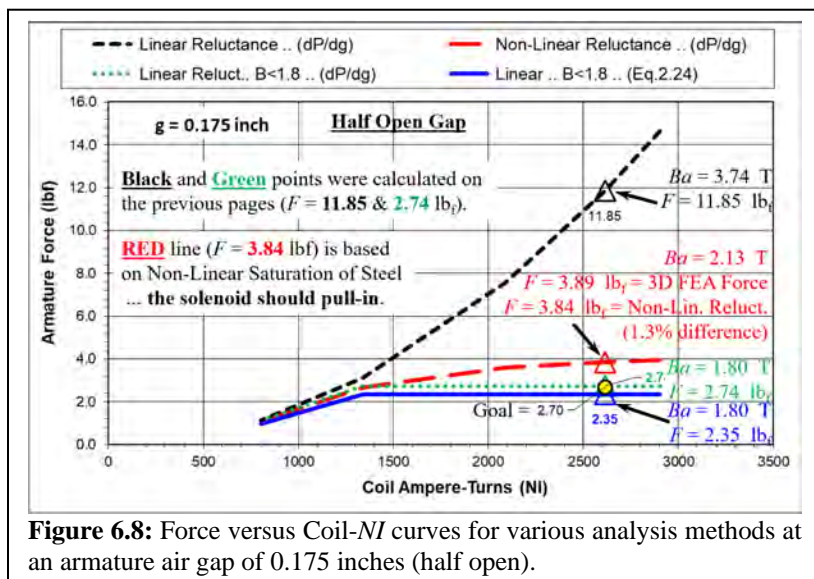


Figure 6.8: Force versus Coil-NI curves for various analysis methods at an armature air gap of 0.175 inches (half open).

Summary of results from **Fig. 6.8**, at $g = 0.175$ in. (half-open).

- Linear reluctance method #1, no flux limit, (**black** dashed line), gives a much higher force and flux density than any other method.
- Linear reluctance methods with flux limiting, #2 (**green** dashed line), and #3 (**blue** solid line), give a force difference of 17%, due to the reduced h -value used in the $d\Phi/dg$ calculation.
- Calculations details for methods #1 and #2 are shown in **Ch. 6.e.**

- The nonlinear reluctance (red dashed line) and 3D FEA methods give very similar force results (within 1.3%). This validates the nonlinear reluctance model. The flux density is 18.3% higher and the force is 40% higher than the linear flux limiting methods.
- Only method #3 gives a force lower than the goal ($F = 2.70 \text{ lbf}_f$). This is due to the more conservative calculation with [Eq. 2.24](#).
- 1300 ampere-turns are needed to achieve saturation at a flux density of 1.8 T. At double the coil- NI (2613 ampere-turns) the nonlinear reluctance model gives 18% more flux density (2.13 T).

The same analysis methods were used for the fully open gap ($g = 0.330 \text{ in.}$), as plotted in [Fig. 6.9](#). A summary of the results is listed below.

- Linear reluctance method #1, no flux limit, (black dashed line), gives a much higher force and flux density than any other method.
- Linear reluctance methods with flux limiting, #2 (green dashed line), and #3 (blue solid line), give a force difference of 32%, due to the significantly reduced h -value used in the dP/dg calculation.
- The nonlinear reluctance method (red dashed line) has a flux density that is 10.6% higher and a force that is 22% higher than the linear flux limiting methods.
- All of the analysis methods produce force results that are much higher than the goal ($F = 0.60 \text{ lbf}_f$).
- 2100 ampere-turns are needed to achieve saturation at a flux density of 1.8 T. At 24% more coil- NI (2613 ampere-turns) the nonlinear reluctance model gives 10% more flux density (1.99 T).

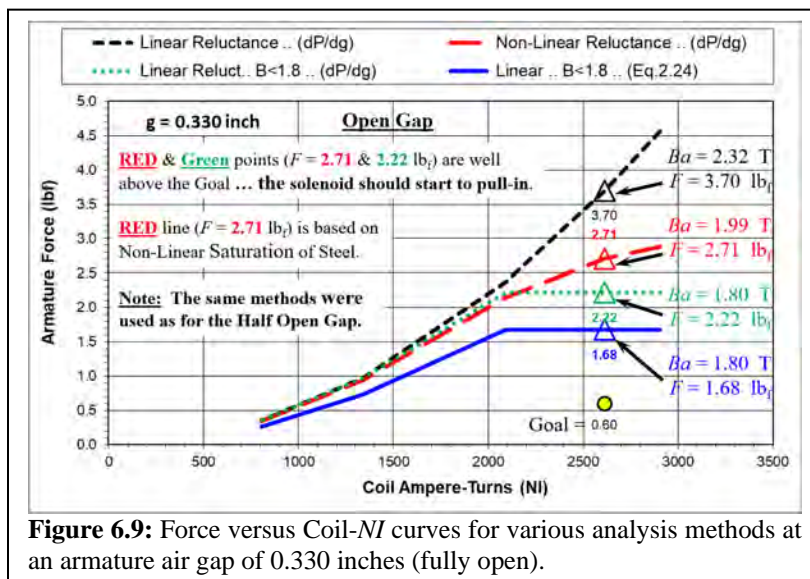
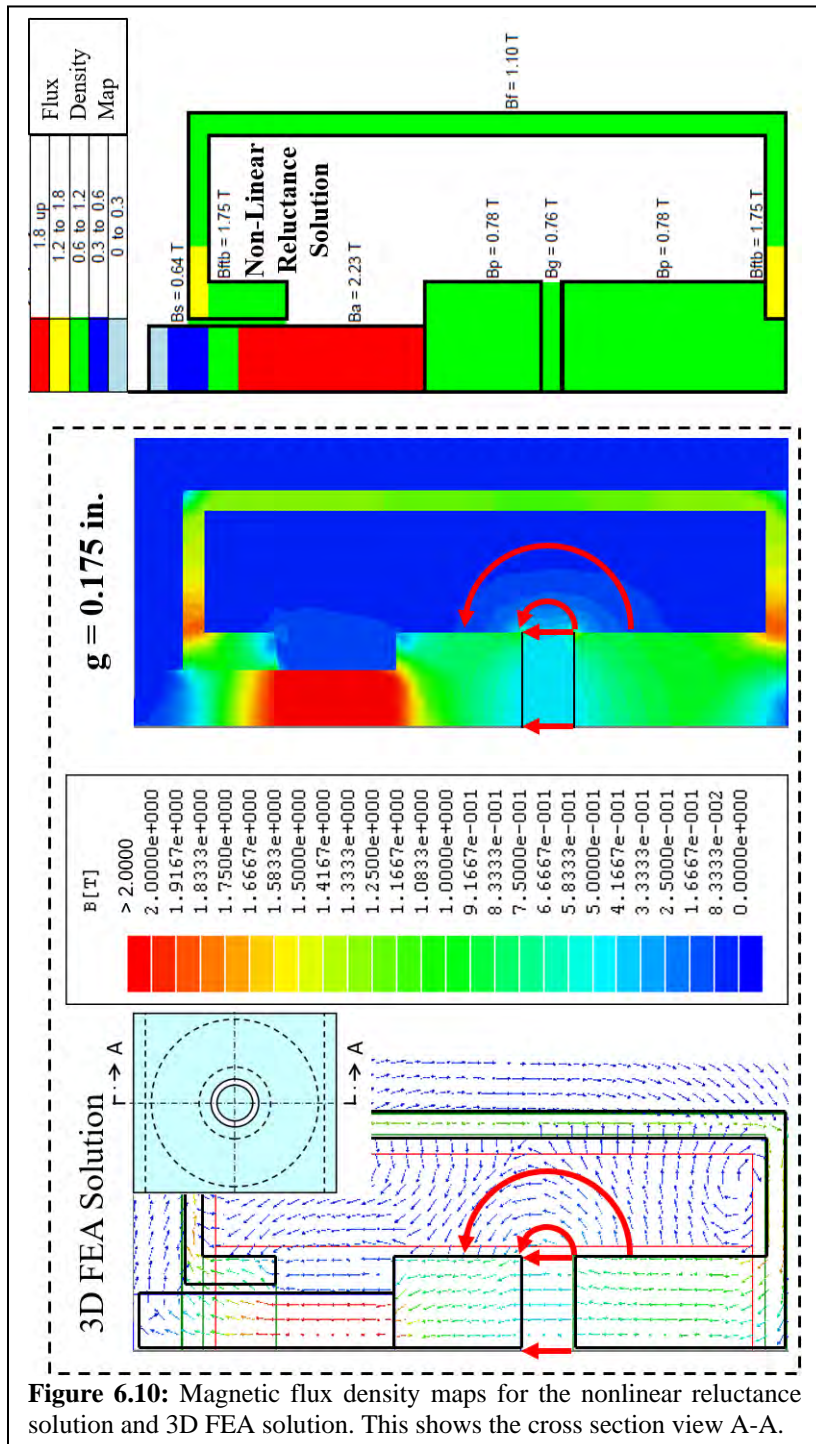


Figure 6.9: Force versus Coil- NI curves for various analysis methods at an armature air gap of 0.330 inches (fully open).

Flux density maps for the 3D finite element simulation and the nonlinear reluctance model are shown in [Fig. 6.10](#) for the half-open gap ($g = 0.175 \text{ in.}$) and 2613 ampere-turns. The flux density distributions are essentially the same for both models, which gives additional validation for the nonlinear

reluctance model. This also demonstrates that the linear flux limiting reluctance methods can provide quick and useful performance estimates.



g. Pole Shaping

Pole Shaping was briefly discussed in Ch. 2.d. Performance details are shown here based on a nonlinear reluctance model for a tapered cup-cone pole configuration, developed similarly to the previous flat face pole configuration.

Fig. 6.11 shows the typical geometry for a tapered pole. The air gap flux paths are drawn in red with perpendicular lines where possible, as indicated by the perpendicularity symbols. Permeances P_{g3} , P_{g5} , and P_{g7} are drawn as triangular regions to fill in between the rectangular and circular regions. The flux path permeances for P_{g1} , P_{g2} , and P_{g4} can be calculated from the equations for the same permeances in Ch. 1.g. The permeances for P_{g3} , P_{g5} , P_{g6} , and P_{g7} can be calculated using the same techniques as those in Ch. 1.g, by defining the volume (v) of the path and the average length of the flux in the path (l), where

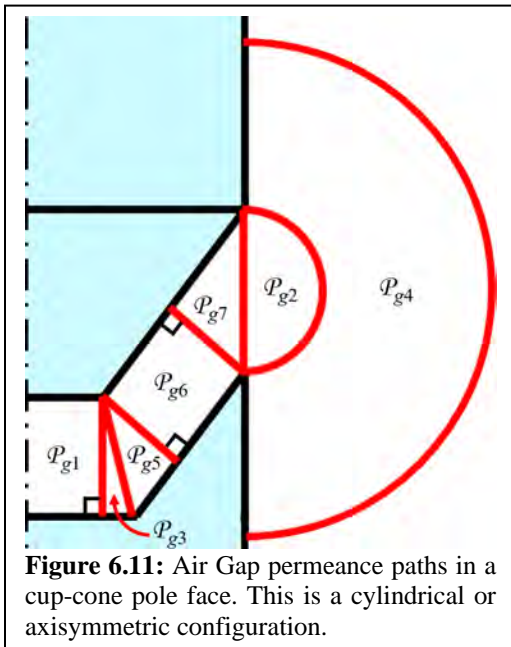


Figure 6.11: Air Gap permeance paths in a cup-cone pole face. This is a cylindrical or axisymmetric configuration.

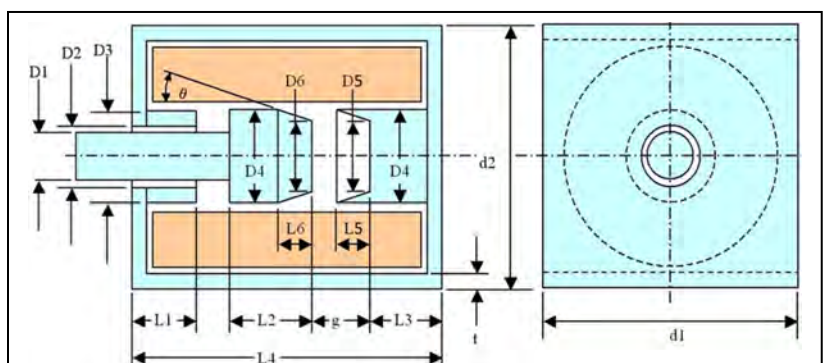


Figure 6.12: Tapered pole cup-cone dimensional variables.

A drawing for the tapered pole cup-cone configuration is shown with the dimensional variable names in **Fig. 6.12**. A nonlinear reluctance model was developed in a spreadsheet. The baseline dimensions used in the calculations are listed in **Fig. 6.13**. Several simulations were completed to determine the performance curve for force versus armature position, and the effect of

changing the coil-*NI* (2613, 1307, 653 ampere-turns), cone angle (θ) (0° , 30°) and the length of the cone ($L5$) (0, 0.10, 0.15, 0.20, 0.30, 0.40 in.).

Geometry & Properties		Input Values		Calculated Values	
Armature Shaft Diameter	D1	in	0.370	D2 = 0.375 in	
Clearance - Bushing to Armature	(D2 - D1)/2	in	0.0025	D3 = 0.625 in	
Bushing Thickness	(D3 - D2)/2	in	0.1250	D5 = 0.394 in	
Cone Outer Diameter	D4	in	0.625	D6 = 0.374 in	
Clearance - Cup to Cone	(D5 - D6)/2	in	0.010	L6 = 0.217 in	
Cone Angle	θ	deg.	30.0	L2 = 0.417 in	
Depth of Frame	d1	in	1.565		
Width of Frame	d2	in	1.570		
Thickness of Frame	t	in	0.070		
Length of Bushing	L1	in	0.310		
Length of Stationary Pole	L3	in	0.705		
Length of Frame	L4	in	2.000		
Length of Cone	L5	in	0.200		
Additional Length behind the Cone	(L2 - L6)	in	0.200		
Working Air Gap	g	in	0.330		

Figure 6.13: Tapered pole cup-cone baseline dimension values.

The graph in **Fig. 6.14** shows the effect on the force curve due to changing the coil-*NI* for the baseline dimensions. The performance curves (**Fig. 6.14**) show the following.

- Increased coil-*NI* increases the force more at a large air gap. This is due to saturation at small air gaps. When the steel pole saturates it limits the flux in the air gap and therefore limits the force.
- A Conical pole shape increases the armature force at large gaps.
- A Conical pole shape decreases the armature force at small gaps.

Fig. 6.15 shows the flux density distribution plots for the baseline dimensions at 2613 ampere-turns and 3 air gap sizes ($g = 0.002, 0.175, 0.330$ in). All of the flux density plots are from the spreadsheet nonlinear reluctance model.

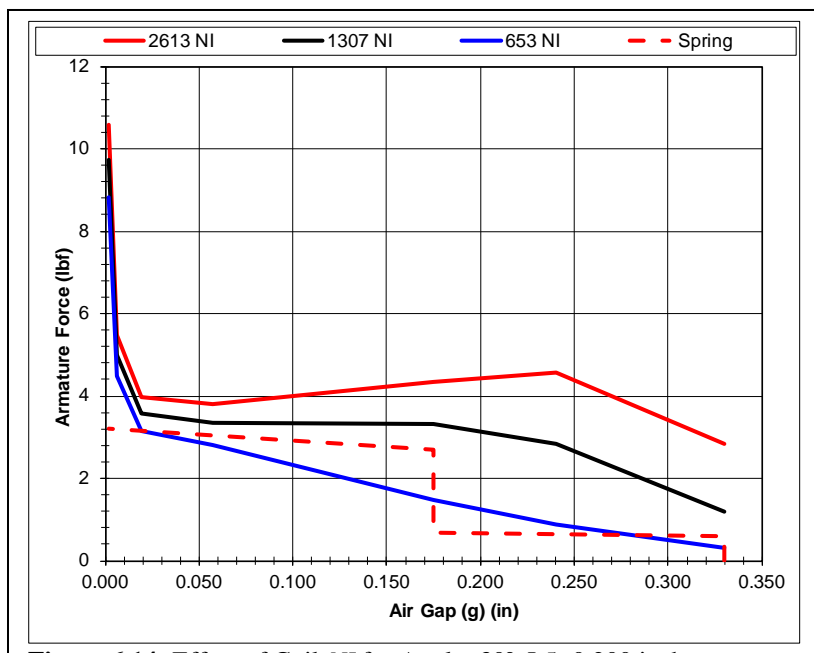


Figure 6.14: Effect of Coil-*NI* for Angle=30°, L5=0.200 inches.

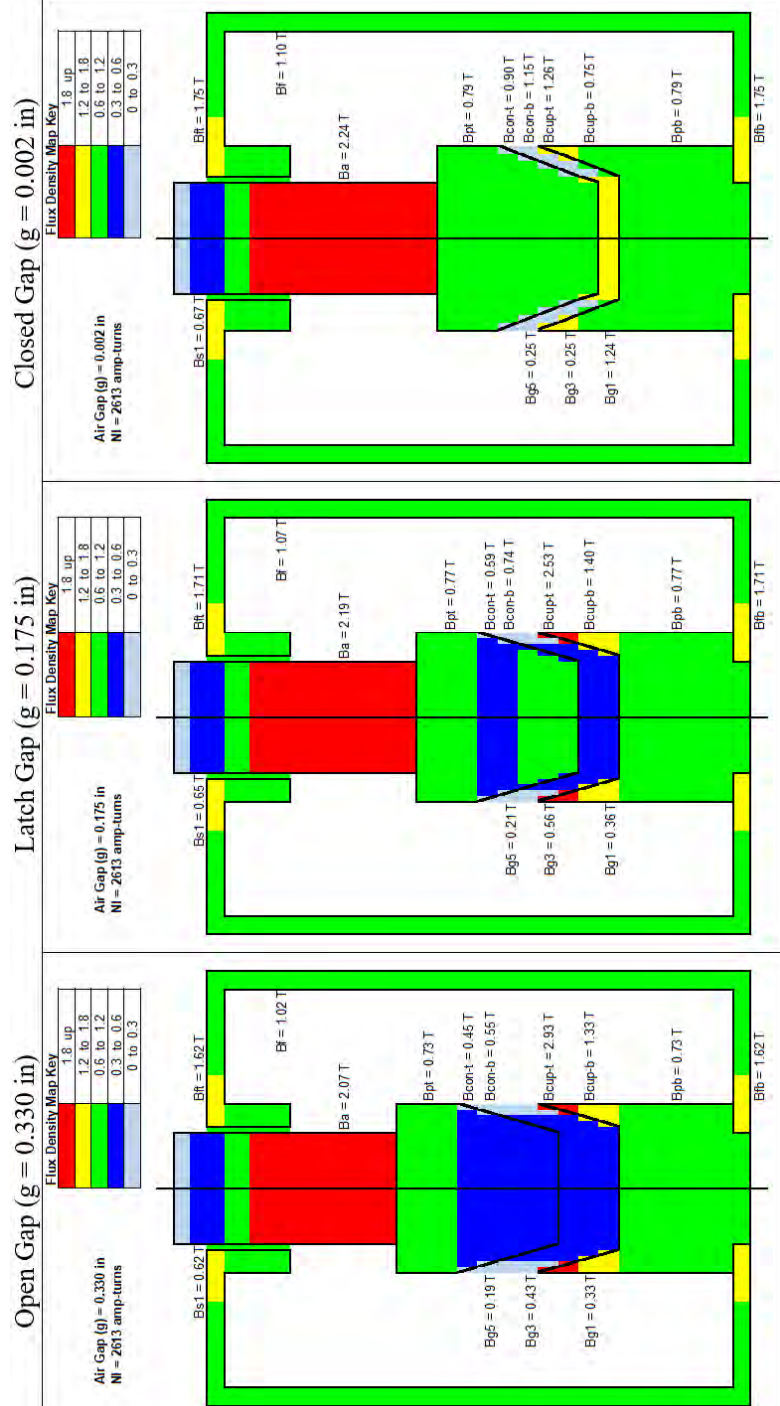


Figure 6.15: Flux density maps for the tapered pole cup-cone baseline dimensions ($\theta = 30^\circ$, $L5 = 0.200$ in) at 2613 ampere-turns, from the spreadsheet nonlinear reluctance model.

The flux density distribution (**Fig. 6.15**) shows the following.

- The armature is saturated at all air gap sizes.
- The tips of the cup are saturated at large air gaps.
- The cup tips bring magnetic flux into the air gap, which increases the force at larger air gaps.
- With a small air gap, the air flux density is concentrated at the small flat region at the pole face.

The graph in **Fig. 6.16** shows the detailed effects of pole shaping.

- A tapered pole increases the force at large gaps and decreases the force at small gaps, and a longer cone increases this effect.
- Pole shaping can adjust the force curve to match the load characteristic. A better match results in a smaller actuator or less coil current or improved force linearity and control characteristics.

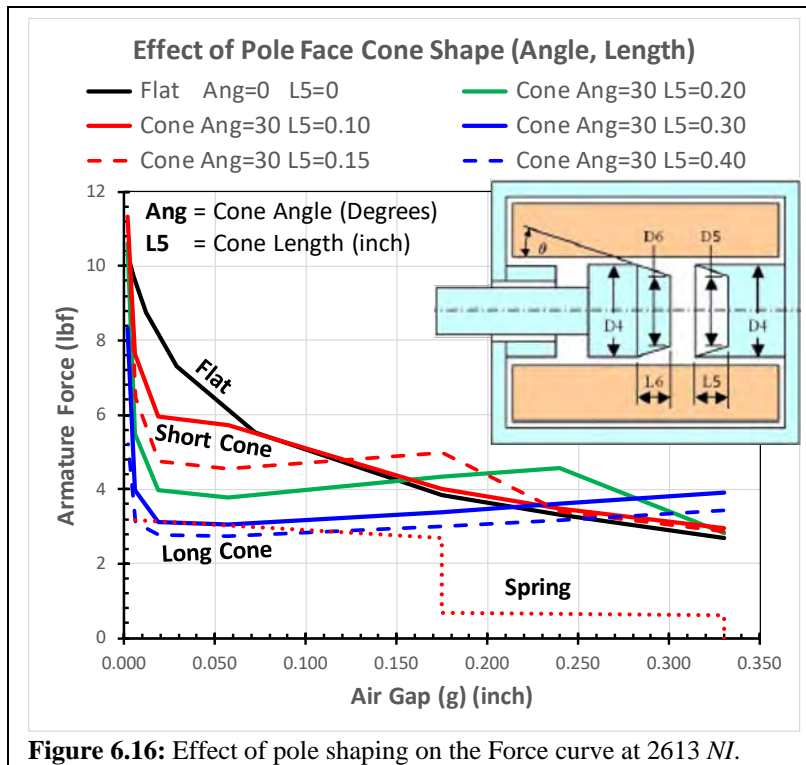


Figure 6.16: Effect of pole shaping on the Force curve at 2613 NI.

The tapered sides of the cup and cone must be prevented from touching. When the tapered sides touch, all of the magnetic flux will go through that spot, which results in a very large contact force and causes the armature motion to stop due to the resulting friction. Three strategies can prevent contact of the tapered sides.

- Make the diameter of the tapered pole smaller than the internal diameter of the tapered cup.
- Add a spacer at the face of the cup to prevent complete engagement of the tapered pole and tapered cup.
- Guide the tapered pole to minimize the assembly tolerance.

7. Solenoid Pull-In Dynamics

a. Mechanical Dynamics

The mechanical dynamics of a solenoid actuator is described with the mechanical spring and mass system in **Fig. 7.1** and the mechanical free body diagram in **Fig. 7.2**. During the solenoid operation, the armature mass (m) is accelerated by the magnetic force (F_M) against the spring force (F_s). The variables (x , v , and a) represent the armature position, velocity, and acceleration.

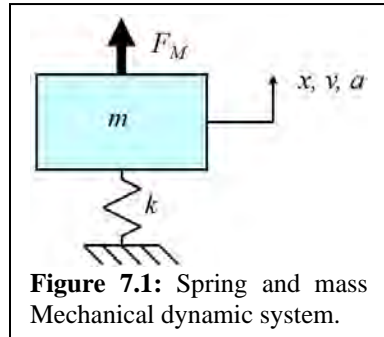


Figure 7.1: Spring and mass Mechanical dynamic system.

The free-body diagram shows that the inertia force (ma) and the spring force (F_s) oppose the magnetic force (F_M). The spring force is shown (Eq. 7.1) as a function of the spring constant (k) the position (x) and the initial spring force (F_{s0}). The resulting mechanical dynamic equations are as follows.

$$F_s = k x + F_{s0} \quad \text{Spring force} \quad (7.1)$$

$$\sum F = 0 = F_M - ma - F_s \quad \text{Force balance} \quad (7.2)$$

$$ma = F_M - F_s \quad \boxed{\text{Inertia force balance}} \quad (7.3)$$

$$a = \frac{F_M - F_s}{m} \quad \text{Acceleration} \quad (7.4)$$

$$\Delta v = a \Delta t \quad \text{Change in velocity} \quad (7.5)$$

$$\Delta x = v_{ave} \Delta t \quad \text{Change in position} \quad (7.6)$$

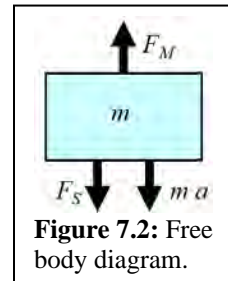


Figure 7.2: Free body diagram.

These equations are discretized for small time intervals (Δt) as follows.

$$a_i = \frac{F_{Mi} - F_{si}}{m} \quad \text{Discretized acceleration} \quad (7.7)$$

$$\Delta v_i = a_i \Delta t \quad v_i = v_{i-1} + a_i \Delta t \quad \text{Discretized velocity} \quad (7.8)$$

$$\Delta x_i = v_{avei} \Delta t \quad x_i = x_{i-1} + \frac{(v_i + v_{i-1})}{2} \Delta t \quad \text{Discretized position} \quad (7.9)$$

The spring force curve is shown in **Fig. 6.2** with the following data.

Open Position	$g_1 = 0.330$ in	Spring Force	$F_{s1} = 0.60$ lbf
Trip Latch Contact	$g_2 = 0.175$ in	Total Force	$F_{s2} = 2.70$ lbf
Closed Position	$g_3 = 0$ in	Total Force	$F_{s3} = 3.20$ lbf

b. DC Circuit and Motion Dynamics

The typical power source for a solenoid actuator is a DC voltage source, as shown in **Fig. 7.3**. The system variables are defined as follows.

V_{DC} = DC Voltage

R = Coil Resistance

L = Coil Inductance

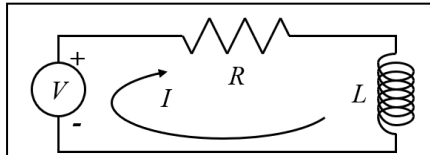


Figure 7.3: DC Voltage source with coil resistance and inductance.

The solenoid inductance (L) changes with the armature position (or air gap) (x), as shown in **Eq. 1.27**. The electrical performance is defined by summing the voltages around the current loop. The source voltage is equal to the voltage drop across the resistance and the across the inductance. The resulting transient dynamic equations (motion and DC circuit) are as follows.

$$\sum V = 0 = V_{DC} - IR - \frac{d(LI)}{dt} \quad \text{Voltage balance} \quad (7.10)$$

$$V_{DC} = IR + L \frac{dI}{dt} + I \frac{dL}{dt} \quad \text{Expansion of terms} \quad (7.11)$$

$$V_{DC} = IR + L \frac{dI}{dt} + I \frac{dL}{dx} \frac{dx}{dt} \quad \text{Chain rule} \quad (7.12)$$

$$V_{DC} = IR + L \frac{dI}{dt} + v I \frac{dL}{dx} \quad v = \frac{dx}{dt} \quad v I \frac{dL}{dx} = \text{Back EMF} \quad (7.13)$$

The Back *EMF* is a result of the moving armature and the changing air gap which causes a change of inductance relative to position (dL/dx). When the velocity (v) increases, the Back *EMF* increases, and the other voltage drops decrease to maintain the voltage balance. Therefore, the current is reduced as the velocity increases.

This equation is discretized for small time intervals (Δt) as follows.

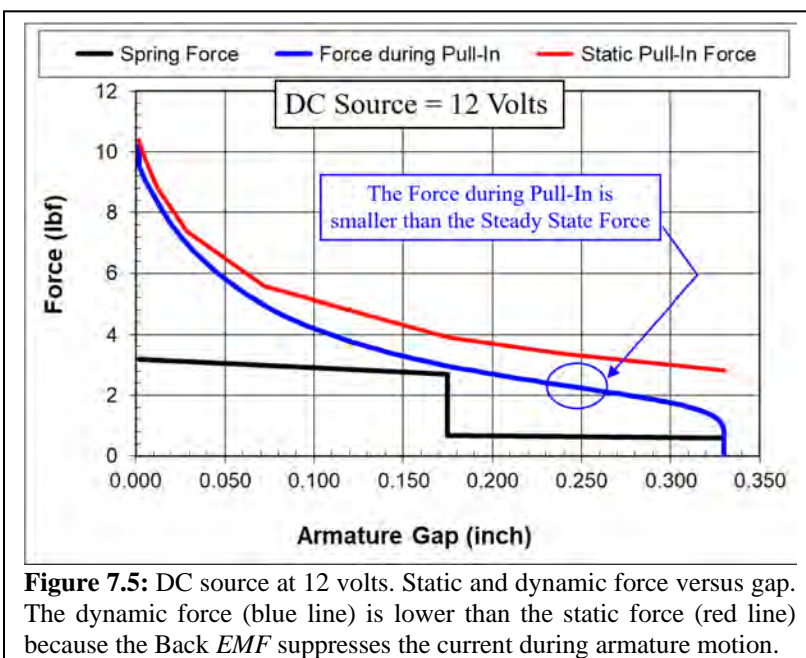
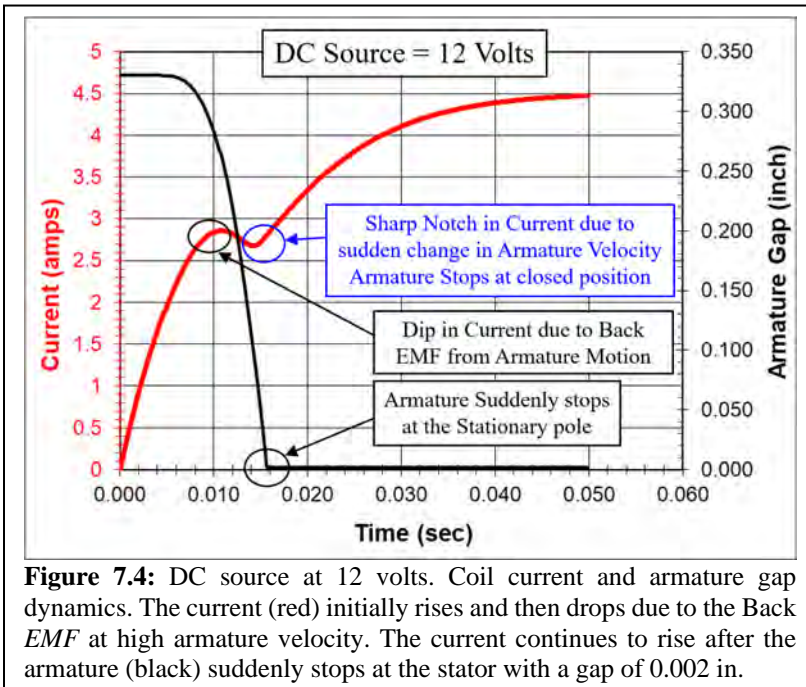
$$\frac{dI}{dt} = \frac{1}{L} \left(V_{DC} - IR - v I \frac{dL}{dx} \right) \quad \text{Solving Eq. 7.13 for } \frac{dI}{dt} \quad (7.14)$$

$$\Delta I_i = \frac{\Delta t}{L_i} \left[V_{DC} - I_i R - v_i I_i \frac{\Delta L}{\Delta x} \right] \quad \text{Discretized} \quad (7.15)$$

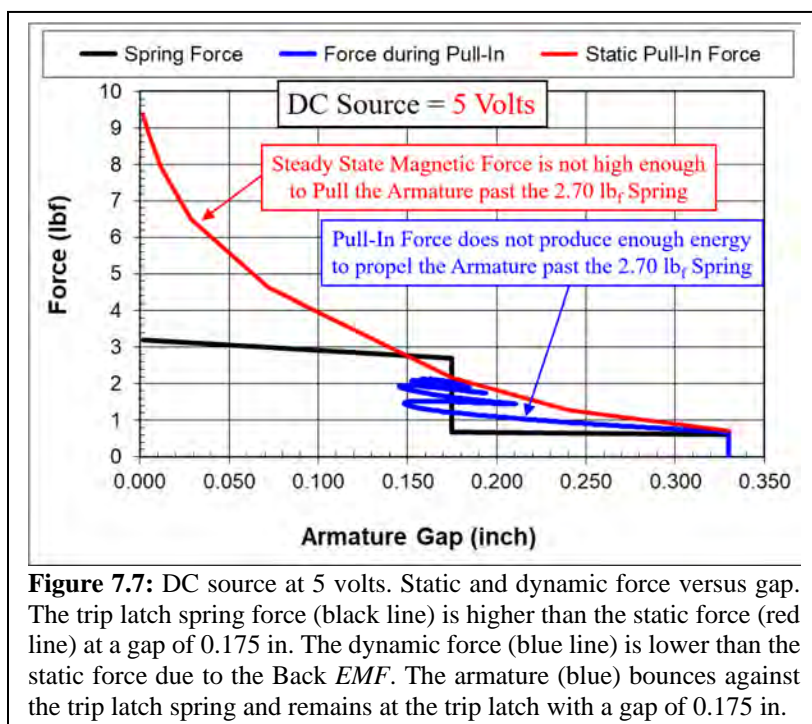
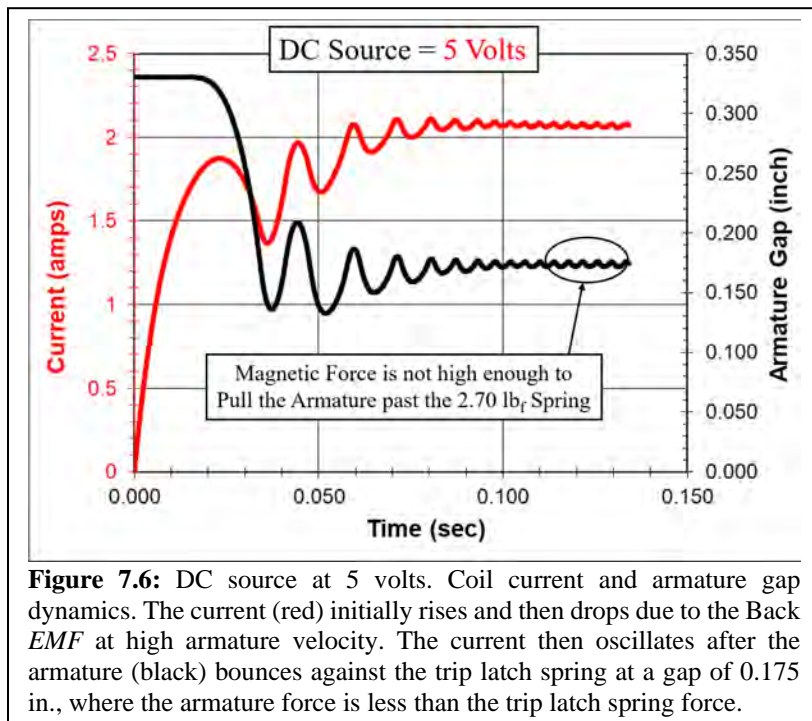
$$I_{i+1} = I_i + \Delta I_i \quad \text{Next step current} \quad (7.16)$$

The incremental magnetic force ($F_{M,i}$) can be calculated from the current (I_i) and position (air gap) (x_i) with the methods shown in **Ch. 2** and **Ch. 6.e**. The incremental position (x_i) can be determined from **Eq. 7.7, 7.8, 7.9**. The time step dynamic analysis was implemented in a spreadsheet and completed for the solenoid design developed in **Ch. 6.e**. Eddy currents were ignored, but

they can significantly delay the rise in magnetic flux and delay reaching the desired mechanical force and displacement. High-speed actuators typically have larger effects due to eddy currents. Brauer [9, Ch. 9, etc.] discusses the eddy current effects in detail. Eddy current effects can also be modeled by a single secondary turn with the techniques in **Ch. 8**, **Ch. 9** and **Ch. 14**. The results below show a successful pull-in at a DC voltage source of 12 volts.



These results show an unsuccessful pull-in at a DC voltage source of 5.0 volts.



c. Capacitor and Motion Dynamics

Another power source for a solenoid actuator is a discharging capacitor, as shown in **Fig. 7.8**. The system variables are defined as follows.

V_C = Initial Capacitor Voltage

R = Coil Resistance

L = Coil Inductance

C = Capacitance

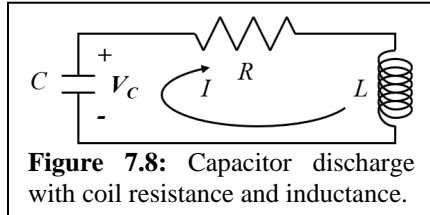


Figure 7.8: Capacitor discharge with coil resistance and inductance.

The solenoid inductance (L) changes with the armature position (or air gap) (x), as shown in **Eq. 1.27**. The electrical performance is defined by summing the voltages around the current loop. When the velocity (v) increases, the Back EMF increases, and the other voltage drops decrease to maintain the voltage balance. The capacitor voltage is determined from the initial voltage and the integrated current (**Eq. 7.19**). The resulting transient dynamic equations (motion and capacitor circuit) are as follows.

$$\sum V = 0 = V_{Cap} - IR - \frac{d(LI)}{dt} \quad \text{Voltage balance} \quad (7.17)$$

$$V_{Cap} = IR + L \frac{dI}{dt} + v I \frac{dL}{dx} \quad \text{Expansion & chain rule} \quad (7.18)$$

$$V_{Cap} = V_C - \frac{1}{C} \int Idt \quad \text{Capacitor voltage} \quad (7.19)$$

$$V_C = IR + L \frac{dI}{dt} + v I \frac{dL}{dx} + \frac{1}{C} \int Idt \quad \text{System equation} \quad (7.20)$$

This equation is discretized for small time intervals (Δt) as follows.

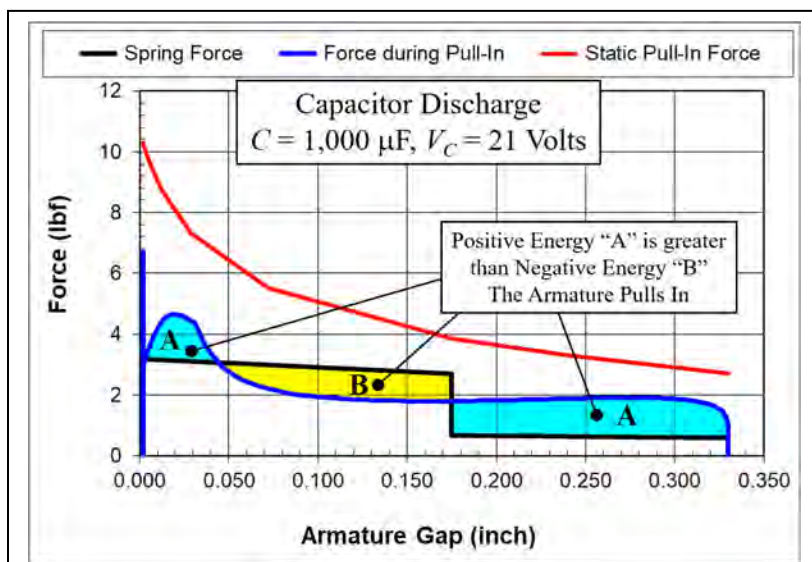
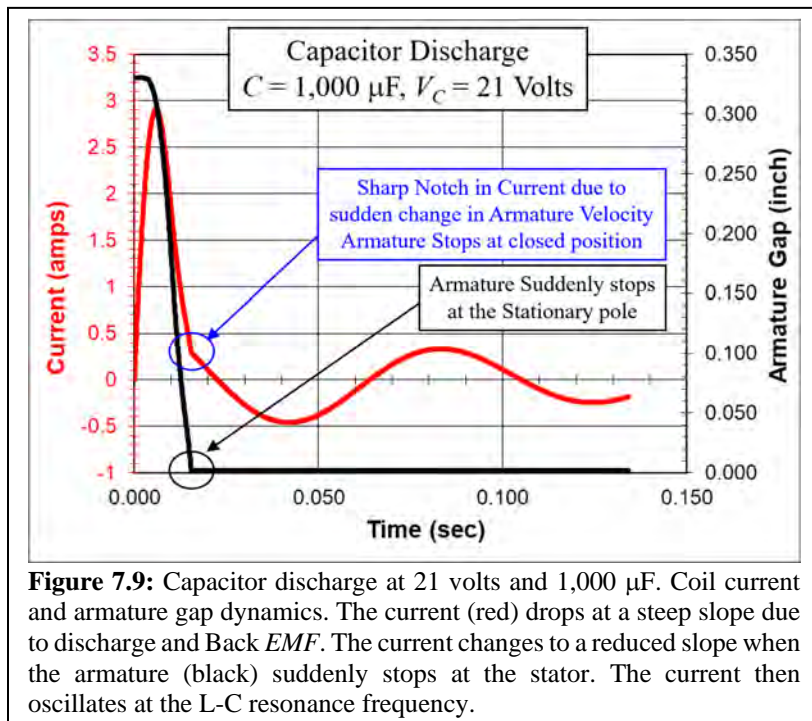
$$\frac{dI}{dt} = \frac{1}{L} \left(V_C - IR - v I \frac{dL}{dx} - \frac{1}{C} \int Idt \right) \quad \text{Solving Eq. 7.20 for } \frac{dI}{dt} \quad (7.21)$$

$$\Delta I_i = \frac{\Delta t}{L_i} \left(V_C - I_i R - v_i I_i \frac{dL}{dx} \Big|_i - \frac{1}{C} \sum I_i \Delta t \right) \quad \text{Discretized} \quad (7.22)$$

$$I_{i+1} = I_i + \Delta I_i \quad \text{Next step current} \quad (7.23)$$

The incremental magnetic force ($F_{M,i+1}$) can be calculated from the incremental current (I_{i+1}) and the incremental position (or air gap) (x_i) with the methods shown in **Ch. 2** and applied in **Ch. 6.e**. The incremental position (or air gap) (x_i) can be determined from **Eq. 7.7**, **Eq. 7.8** and **Eq. 7.9**. Calculations were completed for the solenoid design developed in **Ch. 6.e**. The time step dynamic analysis was implemented in a spreadsheet. Eddy currents were ignored, but they can significantly delay the rise in magnetic flux. This can cause significant delays in achieving the desired mechanical

force and displacement. These results show a successful pull-in with a 1,000 μF capacitor at 21 volts.



These results show an unsuccessful pull-in with a 1,000 μF capacitor at 20 volts.

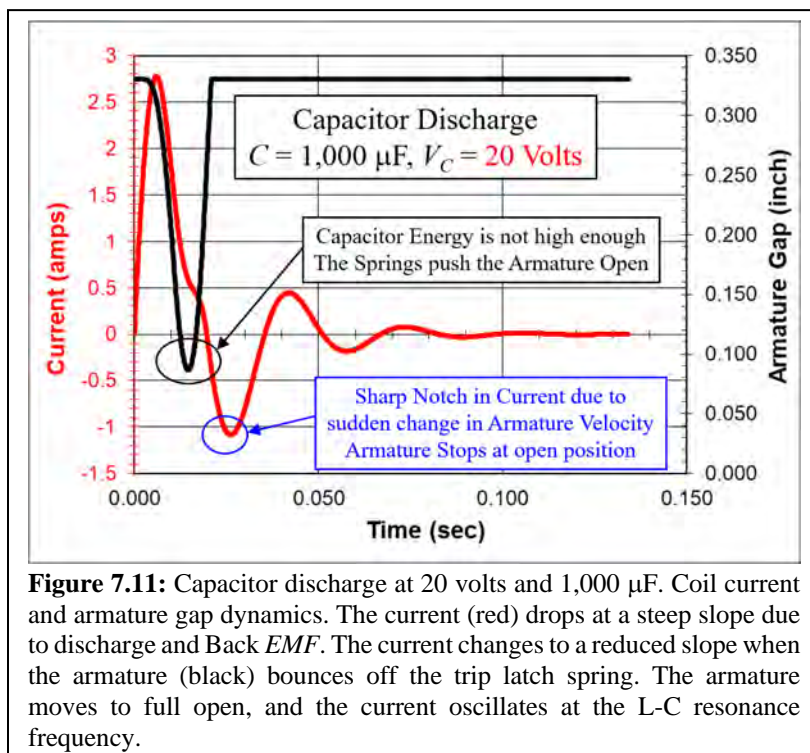


Figure 7.11: Capacitor discharge at 20 volts and 1,000 μF . Coil current and armature gap dynamics. The current (red) drops at a steep slope due to discharge and Back *EMF*. The current changes to a reduced slope when the armature (black) bounces off the trip latch spring. The armature moves to full open, and the current oscillates at the L-C resonance frequency.

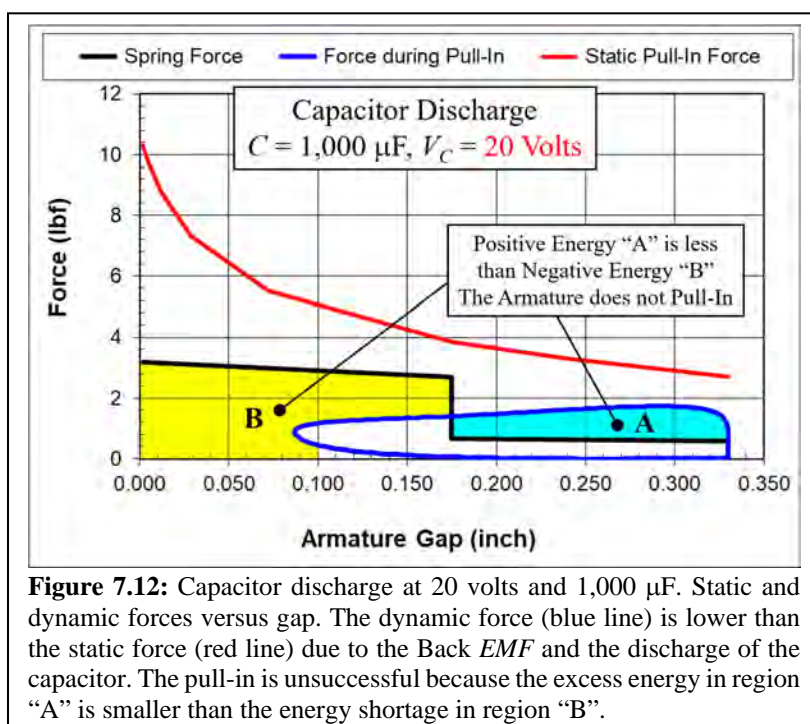


Figure 7.12: Capacitor discharge at 20 volts and 1,000 μF . Static and dynamic forces versus gap. The dynamic force (blue line) is lower than the static force (red line) due to the Back *EMF* and the discharge of the capacitor. The pull-in is unsuccessful because the excess energy in region "A" is smaller than the energy shortage in region "B".

8. Rectification and Shading

AC electromagnets are used in many applications, such as contactors for control and power switching, to close electrical contacts against a system of springs. The magnetic flux in an AC electromagnetic actuator follows the current, which passes through zero twice per cycle. Therefore, the magnetic flux and the magnetic force also pass through zero twice per cycle.

When the magnetic holding force becomes momentarily smaller than the opposing spring force, the magnet poles move slightly apart. The poles slam back together when the magnetic flux rises again after passing through the zero point. This magnet pole motion causes undesirable vibration and noise. Rectification and shading are two methods that prevent the cyclic zero force in AC electromagnets.

a. Rectified AC Electromagnets

Rectification is one of the methods used in AC electromagnets to prevent the magnetic holding force falling below the spring force when the magnetic flux crosses zero.

Rectification (**Fig. 8.1**) causes a coil to behave as if it was supplied with a DC voltage. The rectifier permits the coil current to keep flowing and circulating through the rectifier when the AC voltage source goes to zero. This system can be analyzed with the following system equations.

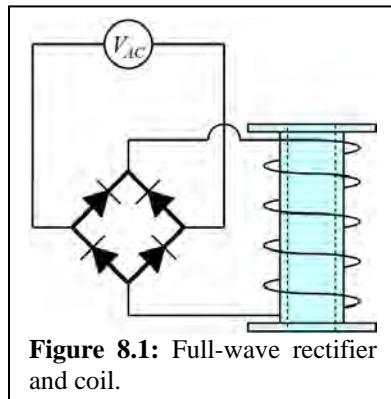


Figure 8.1: Full-wave rectifier and coil.

$$V_{AC} = IR + L \frac{dI}{dt} \quad \text{System equation} \quad (8.1)$$

$$\frac{dI}{dt} = \frac{1}{L} (V_{AC} - IR) \quad \text{Solved for } \frac{dI}{dt} \quad (8.2)$$

$$\Delta I_i = \frac{\Delta t}{L} (V_{ACi} - I_i R) \quad \text{Discretized} \quad (8.3)$$

Full-wave rectification uses the absolute value of the AC voltage (\$V_{AC}\$). Half-wave rectification uses the positive value of the AC voltage (\$V_{AC}\$) when it is positive, and uses a value of zero when it is negative. This analysis was done in a spreadsheet, and the time increment was adjusted smaller until the solution remained constant. The results are summarized in **Fig. 8.2**. Model details and results are listed in **Fig. 8.3**, and the current waveforms are shown in **Fig. 8.4** (full-wave) and **Fig. 8.5** (half-wave).

The equivalent DC voltage (V_{DC}) depends mainly on the type of rectifier (full or half-wave) and only weakly on the coil impedance ratio ($L\omega/R$) (Fig. 8.2). The magnitude of the ripple current is significantly larger for half-wave rectification compared to full-wave rectification.

- Full-wave:
 - The equivalent DC voltage (V_{DC}) is $90\% \pm 1\%$ of the RMS AC voltage (V_{RMS}) regardless of the impedance ratio ($L\omega/R$).
 - The peak ripple current increases by 10x (from 3.0% to 30.9% of I_{Ave}) when the impedance ratio decreases by 10x.
- Half-wave:
 - The equivalent DC voltage (V_{DC}) is $50\% \pm 6\%$ of the RMS AC voltage (V_{RMS}). (44% at a high impedance ratio, and 56% at a low impedance ratio).
 - The peak ripple current increases by 6x when the impedance ratio decreases by 10x.
 - Changing to half-wave from full-wave rectification increases the peak ripple current by 5x at a high impedance ratio, and increases the peak ripple current by 3x at a low impedance ratio.

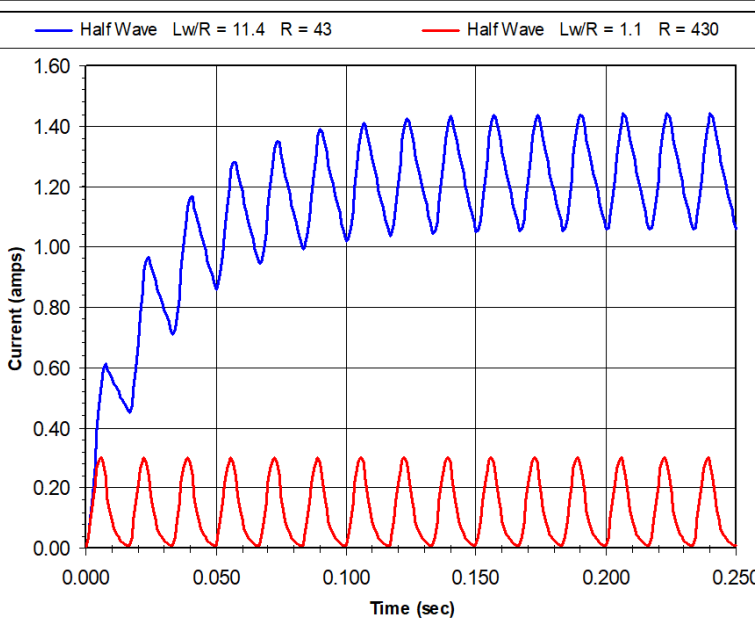
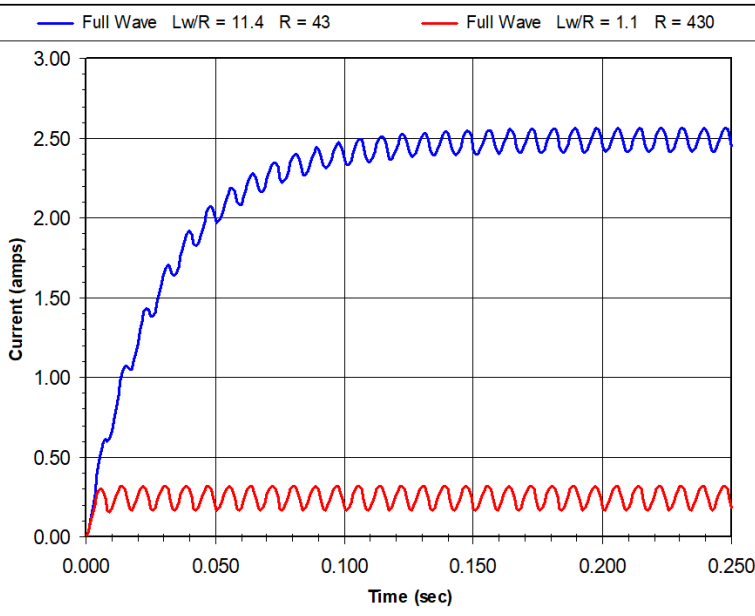
Rectifier	DC Equivalent Voltage Ratio		Current Ripple Ratio	
	V_{DC} / V_{RMS}	V_{DC} / V_{RMS}	I_{Rip} / I_{Ave}	I_{Rip} / I_{Ave}
	<u>$L\omega/R = 11.4$</u>	<u>$L\omega/R = 1.14$</u>	<u>$L\omega/R = 11.4$</u>	<u>$L\omega/R = 1.14$</u>
Full Wave	0.892	0.905	3.0%	30.9%
Half Wave	0.445	0.568	15.5%	92.9%

Figure 8.2: Summary of full-wave and half-wave rectifier performance.

The details for the full-wave and half-wave rectifier models and results are listed below in Fig. 8.3 and plotted in Fig. 8.4 and Fig. 8.5.

<u>Model Details</u>		<u>Full-Wave</u>		<u>Half-Wave</u>	
$L\omega/R$	---	11.4	1.14	11.4	1.14
V_{RMS}	volt	120	120	120	120
f	Hz	60	60	60	60
R	ohm	43	430	43	430
L	H	1.31	1.31	1.31	1.31
<u>Results Details</u>					
I_{RMS}	ampere	2.49	0.252	1.24	0.158
I_{Rip}	ampere	0.075	0.078	0.192	0.147
I_{Rip} / I_{RMS}	%	3.0%	30.9%	15.5%	92.9%
<u>Equivalent DC Voltage</u>					
$V_{DC} = I_{Ave} R$	volt	107.0	108.5	53.5	68.1
V_{DC} / V_{RMS}	---	0.892	0.905	0.445	0.568

Figure 8.3: Full-wave and half-wave rectifier model and results details.



b. Shaded Pole AC Electromagnets

AC electromagnets are typically composed of two magnet poles (of which one may be stationary). They are typically made of thin steel laminations, a drive coil, and shading rings are embedded into the pole faces on one or both magnet poles.

A shading ring (**Fig. 8.6**) is a shorted turn of electrically conductive material, that encloses a portion of a magnetic pole face (usually greater than 50% of the pole face). The purpose of a shading ring is to delay the magnetic flux within the shading ring so that the time of zero crossing for the magnet flux waveform is different inside and outside of the shading ring, and different on the center pole. The resistance of the shading ring and the size of the pole face inside the shading ring can be adjusted to maximize the minimum holding force and minimize the heat dissipation of the induced shading ring current.

Shading rings are used in AC electromagnets to prevent the magnetic holding force falling below the spring force when the AC magnetic flux crosses zero. This work was presented at the International Relay Conference in 1994 [19].

A nonlinear reluctance network is used to calculate the saturation of the lamination steel, resistive loss in the drive coil, resistive loss in the shading rings, the induced current in the shading rings, and the core loss in the lamination steel. Steady-state operation is evaluated in the closed position for a small air gap.

The geometry of the electromagnet core is divided into small regions (**Fig. 8.7**) so that the

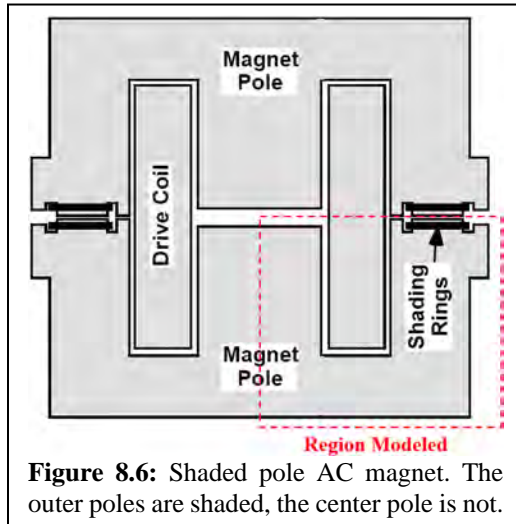


Figure 8.6: Shaded pole AC magnet. The outer poles are shaded, the center pole is not.

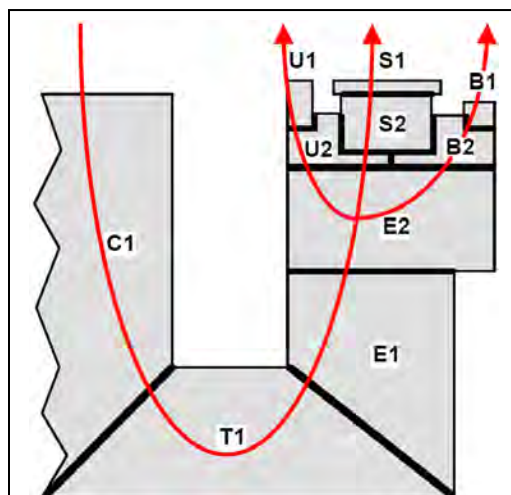


Figure 8.7: Core Sub-Regions and Flux Paths.

resulting flux paths are valid for both the drive coil flux and for the shading ring flux. Also, these regions were selected so that each region would not contain any significant flux density gradients.

The drive coil is mounted on the center pole (C1), the shading ring is mounted on the shaded pole (S1), the unshaded pole (U1) does not have a shading ring and it is equal in height to the shaded pole, and the backstop pole (B1) does not have a shading ring and it mainly serves as a method for retaining the shading ring.

The reluctance for each steel flux path region is calculated with [Eq. 1.22](#). The air gap flux paths at the pole faces ([Fig. 8.8](#)) can be calculated as described in [Ch. 1.g](#). Leakage across the drive coil is assumed to be insignificant in the closed position because the pole face air gap is very small in comparison to the coil leakage path.

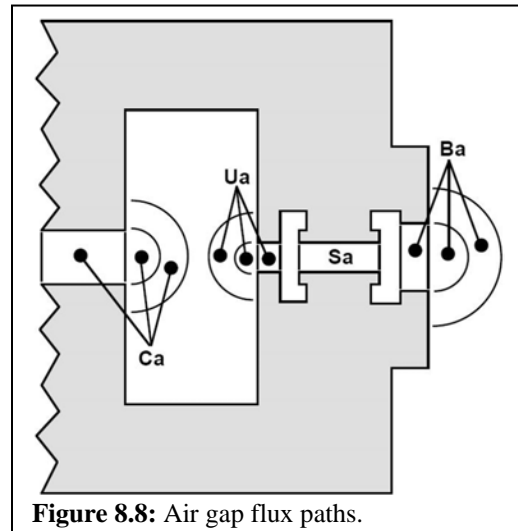


Figure 8.8: Air gap flux paths.

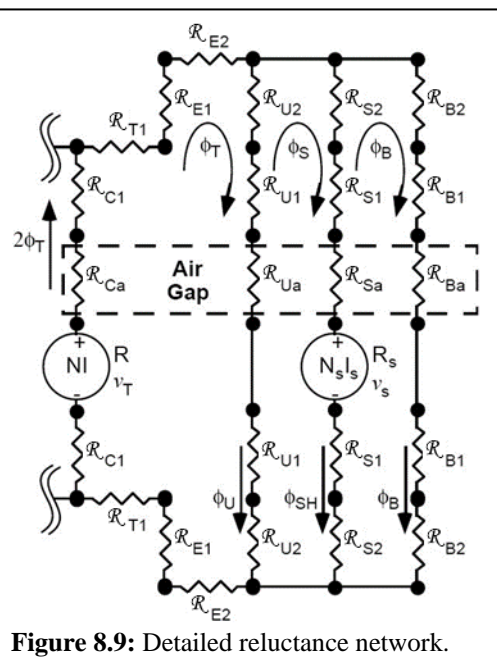


Figure 8.9: Detailed reluctance network.

The detailed reluctance network ([Fig. 8.9](#)) shows only the right-hand side of the electromagnet due to symmetry about the center pole ([Fig. 8.6](#)).

Three flux loops and the flux in each leg of the detailed network are shown in [Fig. 8.9](#). Half of the total flux (ϕ_T) is supplied to both sides of the symmetric reluctance network by the induction of the

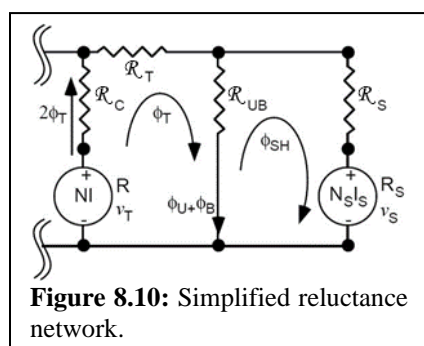


Figure 8.10: Simplified reluctance network.

drive coil on the center pole. Therefore, the center pole carries twice that flux ($2\phi_T$). The reluctances in **Fig. 8.9** can be combined to form the simplified reluctance network in **Fig. 8.10**. Two simultaneous loop equations can be defined based on an MMF balance around each loop in the simplified reluctance network (**Eq. 8.4** and **Eq. 8.5**). The current (I) in the drive coil is a function of the drive coil voltage (v_T), the magnetic flux through the drive coil ($2\phi_T$), and the drive coil resistance (R) as shown in **Eq. 8.6** and **Eq. 8.7**.

$$2\phi_T \mathcal{R}_C + \phi_T \mathcal{R}_T + (\phi_T - \phi_{SH}) \mathcal{R}_{UB} - NI = 0 \quad \text{MMF balance in } \phi_T \text{ loop} \quad (8.4)$$

$$(\phi_{SH} - \phi_T) \mathcal{R}_{UB} + \phi_{SH} \mathcal{R}_S + N_S I_S = 0 \quad \text{MMF balance in } \phi_{SH} \text{ loop} \quad (8.5)$$

$$v_T = IR + 2N \frac{d\phi_T}{dt} \quad \text{Drive coil voltage} \quad (8.6)$$

$$I = \frac{1}{R} \left(v_T - 2N \frac{d\phi_T}{dt} \right) \quad \text{Drive coil current} \quad (8.7)$$

The current in the shading ring (I_S) is a function of the magnetic flux through the shading ring (ϕ_{SH}), and the shading ring resistance (R_S), as follows.

$$v_S = \frac{d\phi_{SH}}{dt} \quad \text{Voltage around shading ring} \quad (8.8)$$

$$I_S = \frac{v_S}{R_S} = \frac{1}{R_S} \frac{d\phi_{SH}}{dt} \quad \text{Current in shading ring} \quad (8.9)$$

Eq. 8.4 and **Eq. 8.7** can be combined into a differential equation (**Eq. 8.10**), and **Eq. 8.5** and **Eq. 8.9** can be combined into a differential equation (**Eq. 8.11**), to produce 2 equations with 2 unknowns (ϕ_T and ϕ_{SH}).

$$2 \frac{N^2}{R} \frac{d\phi_T}{dt} + (2\mathcal{R}_C + \mathcal{R}_T + \mathcal{R}_{UB}) \phi_T - \mathcal{R}_{UB} \phi_{SH} = \frac{N}{R} v_T \quad (8.10)$$

$$\frac{N_S}{R_S} \frac{d\phi_{SH}}{dt} + (\mathcal{R}_{UB} + \mathcal{R}_S) \phi_{SH} - \mathcal{R}_{UB} \phi_T = 0 \quad (8.11)$$

Eq. 8.10 through **Eq. 8.11** can be combined into a single second-order differential equation in ϕ_{SH} as a function of drive coil voltage v_T .

$$A \frac{d^2 \phi_{SH}}{dt^2} + B \frac{d\phi_{SH}}{dt} + C \phi_{SH} = \frac{N}{R} v_T$$

(8.12)

$$A = 2 \frac{1}{\mathcal{R}_{UB}} \frac{N^2}{R} \frac{N_S}{R_S} \quad (8.13)$$

$$B = 2 \left(\frac{\mathcal{R}_S + \mathcal{R}_{UB}}{\mathcal{R}_{UB}} \right) \frac{N^2}{R} + \left(\frac{2\mathcal{R}_C + \mathcal{R}_T + \mathcal{R}_{UB}}{\mathcal{R}_{UB}} \right) \frac{N_S}{R_S} \quad (8.14)$$

$$C = (2\mathcal{R}_C + \mathcal{R}_T + \mathcal{R}_{UB}) \left(\frac{\mathcal{R}_S + \mathcal{R}_{UB}}{\mathcal{R}_{UB}} \right) \quad (8.15)$$

The total power loss for the electromagnet includes steel lamination core losses in addition to the resistive losses in the drive coil and the shading rings. The steel lamination core loss and the magnetizing curve (BH curve) were obtained by cutting ring samples from the electromagnet laminations, and measuring their properties (**Fig. 8.11**).

The core loss can be included in the differential equations with an equivalent core loss resistance (R_{CD} and R_{CS}) added to the drive coil resistance ($R + R_{CD}$) and the shading ring resistance ($R_S + R_{CS}$).

The ratio of the ampere-turns in the drive coil and the shading rings can be used to distribute the core loss (P_C) between the 2 coils, as follows. This model has 2 shading rings ($N_S = 2$) and the total shading- NI is twice the value of the shading current (I_S).

$$NI_R = \frac{NI_S}{NI_S + NI_{DR}} \quad \text{Ratio of shading-}NI \text{ to total-}NI \quad (8.16)$$

$$P_{CS} = P_C NI_R \quad \text{Core loss applied to the shading rings} \quad (8.17)$$

$$P_{CD} = P_C (1 - NI_R) \quad \text{Core loss applied to the drive coil} \quad (8.18)$$

The shading ring core loss (P_{CS}) is divided by 2 (the number of shading rings in the electromagnet model) to obtain the added resistance per shading ring. The added core loss resistances (R_{CD} and R_{CS}) (**Eq. 8.19**, **Eq. 8.20**), use initial values for the currents (I and I_S) from a linear phasor solution for the differential equation (**Eq. 8.12**). Iteration on the nonlinear solution is needed to obtain the final resistance values.

The drive coil and shading ring resistances with the added core loss resistance are shown below, (**Eq. 8.21**, **Eq. 8.22**).

$$R_{CD} = \frac{P_{CD}}{I^2} \quad \text{Drive coil added core loss resistance} \quad (8.19)$$

$$R_{CS} = \frac{P_{CS}}{2N_S I_S^2} \quad \text{Shading ring added core loss resistance} \quad (8.20)$$

$$R = R + R_{CD} \quad \text{Drive coil total resistance} \quad (8.21)$$

$$R_S = R_S + R_{CS} \quad \text{Shading ring total resistance} \quad (8.22)$$

A Runge-Kutta 4th order (RK-4) difference approximation was used to obtain the nonlinear solution for the simultaneous differential equations (**Eq. 8.10** and **Eq. 8.11**). These equations are rearranged as shown below to apply the

B Flux Density Tesla	H Magnetizing Force ampere/m	P_C Core Loss 60 Hz watt/kg
0.10	80	0.29
0.20	160	0.57
0.50	400	1.43
1.06	800	2.86
1.29	1,600	6.95
1.55	4,000	13.64
1.68	8,000	15.62
1.88	16,000	17.20
2.10	40,000	20.13
2.30	80,000	23.10
2.50	160,000	26.18
2.80	400,000	31.24

Figure 8.11: Measured steel lamination properties.

RK-4 difference approximation. An additional variable (\mathcal{R}_{CTUB}) is defined to reduce the size of the equations.

$$\mathcal{R}_{CTUB} = (2\mathcal{R}_C + \mathcal{R}_T + \mathcal{R}_{UB}) \quad (8.23)$$

$$\frac{d\phi_T}{dt} = \frac{R}{2N^2} \left(\frac{N}{R} v_T - \mathcal{R}_{CTUB} \phi_T + \mathcal{R}_{UB} \phi_{SH} \right) \quad (8.24)$$

$$\frac{d\phi_{SH}}{dt} = \frac{R_s}{N_s} (\mathcal{R}_{UB} \phi_T - (\mathcal{R}_{UB} + \mathcal{R}_S) \phi_{SH}) \quad (8.25)$$

The RK-4 difference solution for the magnetic flux (ϕ_T and ϕ_{SH}) at the $(i+1)$ time step is based on the previous values at the (i) time step as shown.

$$\phi_T|_{i+1} = \phi_T|_i + \frac{1}{6} (k_0 + 2k_1 + 2k_2 + k_3) \quad (8.26)$$

$$\phi_{SH}|_{i+1} = \phi_{SH}|_i + \frac{1}{6} (m_0 + 2m_1 + 2m_2 + m_3) \quad (8.27)$$

The constants k and m are defined below at intermediate positions between the (i) and the $(i+1)$ time step.

$$k_0 = \Delta t \frac{R}{2N^2} \left(\frac{N}{R} v_T - \mathcal{R}_{CTUB} \phi_T + \mathcal{R}_{UB} \phi_{SH} \right)_i \quad (8.28)$$

$$k_1 = \Delta t \frac{R}{2N^2} \left(\frac{N}{R} v_T - \mathcal{R}_{CTUB} \phi_T + \mathcal{R}_{UB} \phi_{SH} \right)_0 \quad \phi_T|_0 = \phi_T|_i + \frac{k_0}{2} \quad (8.29)$$

$$k_2 = \Delta t \frac{R}{2N^2} \left(\frac{N}{R} v_T - \mathcal{R}_{CTUB} \phi_T + \mathcal{R}_{UB} \phi_{SH} \right)_1 \quad \phi_T|_1 = \phi_T|_i + \frac{k_1}{2} \quad (8.30)$$

$$k_3 = \Delta t \frac{R}{2N^2} \left(\frac{N}{R} v_T - \mathcal{R}_{CTUB} \phi_T + \mathcal{R}_{UB} \phi_{SH} \right)_2 \quad \phi_T|_2 = \phi_T|_i + k_2 \quad (8.31)$$

$$m_0 = \Delta t \frac{R_s}{N_s} (\mathcal{R}_{UB} \phi_T - (\mathcal{R}_{UB} + \mathcal{R}_S) \phi_{SH})_i \quad (8.32)$$

$$m_1 = \Delta t \frac{R_s}{N_s} (\mathcal{R}_{UB} \phi_T - (\mathcal{R}_{UB} + \mathcal{R}_S) \phi_{SH})_0 \quad \phi_{SH}|_0 = \phi_{SH}|_i + \frac{m_0}{2} \quad (8.33)$$

$$m_2 = \Delta t \frac{R_s}{N_s} (\mathcal{R}_{UB} \phi_T - (\mathcal{R}_{UB} + \mathcal{R}_S) \phi_{SH})_1 \quad (8.34)$$

$$m_3 = \Delta t \frac{R_s}{N_s} (\mathcal{R}_{UB} \phi_T - (\mathcal{R}_{UB} + \mathcal{R}_S) \phi_{SH})_2 \quad \phi_{SH}|_2 = \phi_{SH}|_i + m_2 \quad (8.35)$$

The drive coil voltage is defined for each of these intermediate states as follows, where ω is the radian frequency and V_p is the peak voltage on the drive coil.

$$v_T|_i = V_p \cos(\omega t_i) \quad (8.36)$$

$$v_T|_0 = v_T|_1 = V_p \cos\left(\omega\left(t_i + \frac{\Delta t}{2}\right)\right) \quad (8.37)$$

$$v_T|_2 = V_p \cos(\omega(t_i + \Delta t)) \quad (8.38)$$

The Runge-Kutta 4th order (RK-4) solution was verified by using a linear nonsaturating magnetization curve and comparing the results with the linear phasor solution. The RK-4 solution was also verified against magnetic flux measurements at full magnetic saturation. This was done by placing a loop of fine wire around each pole face (C1, U1, S1, B1) and integrating the open-circuit voltage to obtain the magnetic flux from Faraday's law ($\phi = \frac{1}{N} \int V dt$).

The calculated and measured magnetic flux density waveforms are plotted in **Fig. 8.12**. The maximum phase angle error at zero crossing is less than 2 degrees (5%) and the maximum peak magnitude error is less than 0.07 Tesla (4%). The small error verifies the accuracy of this numerical formulation. The 2nd graph in **Fig. 8.12** shows the calculated force waveforms, where the minimum total force is 34 lb_f.

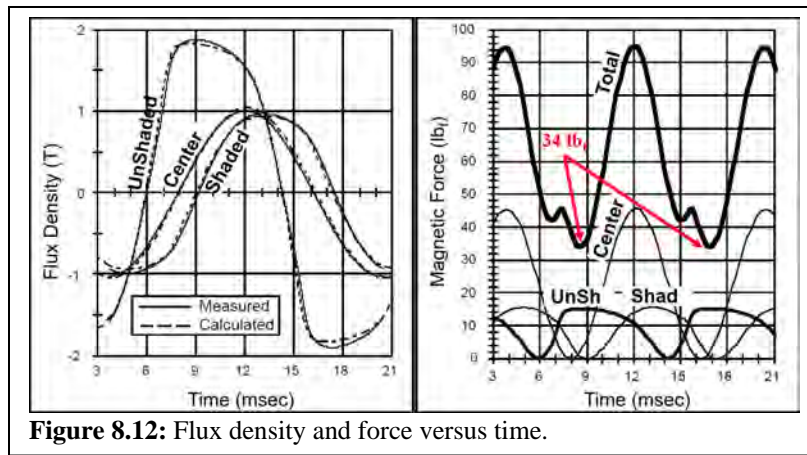


Figure 8.12: Flux density and force versus time.

The charts (**Fig. 8.13**) show tradeoffs with opportunities to reduce weight or improve performance. The following tradeoffs are presented.

- “A” 10% larger unshaded pole and 25% less shading ring resistance gives 18% more force and 25% more heat dissipation.
- “B” 10% larger unshaded pole and 5% less shading ring resistance gives 9% more force and no change in the heat dissipation.
- “C” 10% larger unshaded pole and 33% more shading ring resistance gives no change in force and 25% less heat dissipation.

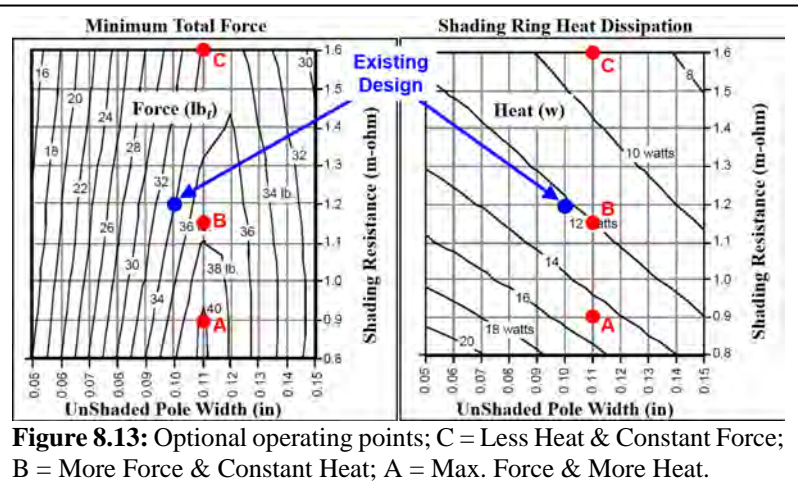


Figure 8.13: Optional operating points; C = Less Heat & Constant Force; B = More Force & Constant Heat; A = Max. Force & More Heat.

9. Transformer, Inductors

Transformers can be evaluated in the same way as the actuators were evaluated in the previous chapters. In particular, the shaded pole AC electromagnet in **Ch. 8** is a transformer with high leakage and saturation that induces a current in a secondary coil (shading ring). The key to setting up the system of equations is to consider what the magnetic flux is doing.

Understanding the magnetic flux in a transformer (or any magnetic device) is critical to determining the performance characteristics relative to saturation, leakage flux, and core loss. The first approach (sections a and b) makes the simple assumption that all of the magnetic flux remains inside the core, which means there is no flux leakage. The second approach (sections c through f) includes flux leakage and core loss.

a. Transformer (No Leakage)

The general configuration of a transformer without flux leakage is shown in **Fig. 9.1**, in which a primary winding drives magnetic flux through a core and a secondary winding, inducing a secondary current into a load. It is assumed that there is no leakage flux between the primary and secondary windings.

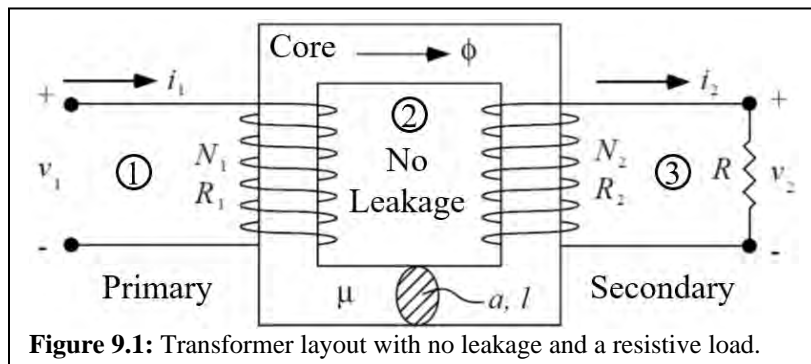


Figure 9.1: Transformer layout with no leakage and a resistive load.

The following dimensions, components, and parameters are defined for the transformer in **Fig. 9.1**.

- Primary:
 v_1 = primary voltage
 i_1 = primary current
 N_1 = primary coil winding turns
 R_1 = primary coil resistance
- Core:
 ϕ = magnetic flux in the core
 a = core cross-sectional area
 l = length of the core flux path
 μ = core magnetic permeability

- Secondary:
 - v_2 = secondary voltage across the load
 - i_2 = secondary current
 - N_2 = secondary coil winding turns
 - R_2 = secondary coil resistance
 - R = load resistance

The following characteristic constants and dimensionless ratios are defined for the transformer in **Fig. 9.1**.

$$\mathcal{R} = \frac{l}{\mu a} \quad \text{Reluctance of the core} \quad (9.1)$$

$$L_1 = \frac{N_1^2}{\mathcal{R}} \quad \text{Inductance - Primary coil} \quad (9.2)$$

$$L_2 = \frac{N_2^2}{\mathcal{R}} \quad \text{Inductance - Secondary coil} \quad (9.3)$$

$$g = \frac{\omega L_1}{R_1} \quad \text{Impedance ratio - Primary coil} \quad (9.4)$$

$$h = \frac{\omega L_2}{R + R_2} \quad \text{Impedance ratio - Secondary coil} \quad (9.5)$$

$$k = g + h \quad \text{Sum of impedance ratios} \quad (9.6)$$

A loop equation can be written for each of the 3 sections of the transformer (**Eq. 9.7**, **Eq. 9.8**, **Eq. 9.9**), and combined into a single 1st order differential equation of the system for the magnetic flux (**Eq. 9.10**).

$$\text{Loop #1 - Sum of voltages} \quad (9.7)$$

$$N_1 i_1 = \phi \mathcal{R} + N_2 i_2 \quad \text{Loop #2 - Sum of ampere-turns} \quad (9.8)$$

$$N_2 \frac{d\phi}{dt} = i_2 (R_2 + R) \quad \text{Loop #3 - Sum of voltages} \quad (9.9)$$

$$\boxed{\left(\frac{N_1^2}{R_1} + \frac{N_2^2}{R + R_2} \right) \frac{d\phi}{dt} + \phi \mathcal{R} = N_1 \frac{v_1}{R_1}} \quad \text{Combined system equation} \quad (9.10)$$

Transformers generally operate in the linear range of magnetic flux (not saturating). Therefore, this system can be evaluated with a linear phasor solution based on magnitudes and phase angles, as follows.

$$e^{(j\omega t)} = \cos(\omega t) + j \sin(\omega t) \quad \text{Euler Identity} \quad (9.11)$$

$$v_1 = V_1 e^{(j\omega t)} \quad i_1 = I_1 e^{(j\omega t + \beta)} \quad \text{Phasor - primary} \quad (9.12)$$

$$\phi_1 = \phi_1 e^{(j\omega t + \alpha)} \quad \text{Phasor - magnetic flux} \quad (9.13)$$

$$i_2 = I_2 e^{(j\omega t + \gamma)} \quad v_2 = V_2 e^{(j\omega t + \psi)} \quad \text{Phasor - secondary} \quad (9.14)$$

Substituting the individual phasor equations into the combined system equation and loop equations gives solutions for the magnitude and phase angle variables.

- Transformer (No Leakage)

These equations assume a stiff (ideal) primary voltage source that supplies as much current as the load needs to draw. The phase angles are relative to V_1 .

$$\phi = \frac{N_1 V_1}{\mathcal{R} R_1} \sqrt{\frac{1}{1+k^2}} \quad \alpha = -\tan^{-1} k \quad \text{Magnetic flux} \quad (9.15)$$

$$I_2 = \frac{N_1 V_1}{N_2 R_1} h \sqrt{\frac{1}{1+k^2}} \quad \beta = \alpha + \frac{\pi}{2} \quad \text{Secondary current} \quad (9.16)$$

$$I_1 = \frac{V_1}{R_1} g \sqrt{\frac{1}{1+k^2}} \sqrt{\left(\frac{\sqrt{1+k^2}}{g} + \sin \alpha \right)^2 + \cos^2 \alpha} \quad \text{Primary current} \quad (9.17)$$

$$\gamma = \tan^{-1} \frac{-g \cos \alpha}{\sqrt{1+k^2} + g \sin \alpha} \quad I_1 \text{ Phase angle} \quad (9.18)$$

$$V_2 = \frac{N_1}{N_2} V_1 \frac{R}{R_1} h \sqrt{\frac{1}{1+k^2}} \quad \psi = \beta \quad \text{Secondary voltage} \quad (9.19)$$

$$P_{out} = \frac{1}{2} \frac{V_1^2}{R} \left(\frac{N_1}{N_2} \right)^2 \left(\frac{R}{R_1} \right)^2 \left(\frac{h^2}{1+k^2} \right) \quad \text{Power output} \quad (9.20)$$

$$P_{out_{max}} = \frac{1}{2} \frac{(N_2 \omega B_{sat} a)^2}{R} \left(\frac{R}{R+R_2} \right)^2 \quad \text{Max. power output} \quad (9.21)$$

$$P_{out_{max}} = \frac{1}{2} \frac{(N_2 \omega B_{sat} a)^2}{R} \quad \text{Max. Power output for } R_2 \ll R \quad (9.22)$$

The power output is $I_2^2 R / 2$, where the secondary current (I_2) is a peak value. The maximum power output occurs at the maximum core flux density (saturation, $B = B_{Sat}$). The secondary winding resistance is typically small compared to the resistance of the load ($R_2 < R$). Otherwise, the secondary coil will become hot and it will quickly exceed the insulation temperature rating of the wire.

b. Special Cases (No Leakage)

Special cases can be defined based on the general transformer formulation, by assuming a primary current source (rather than voltage source) and an open or shorted secondary coil.

- Inductor, Rogowski Coil
- Current Transformer (CT), Ideal Current Transformer

- Inductor

The load resistance is infinite or the secondary coil is open ($R = \infty$). These equations assume a stiff (ideal) primary current source that supplies as much voltage as needed across the inductor. The phase angles are relative to I_1 .

$$\phi = \frac{N_1 I_1}{\mathcal{R}} = \frac{L_1 I_1}{N_1} \quad \text{Magnetic flux} \quad (9.23)$$

$$B = \mu_r \mu_0 \frac{N_1 I_1}{l} = \frac{L_1 I_1}{N_1 a} \quad \text{Core flux density} \quad (9.24)$$

$$V_1 = I_1 \sqrt{R_1^2 + (\omega L_1)^2} \quad \alpha = \tan^{-1} \frac{\omega L_1}{R_1} \quad \text{Voltage drop} \quad (9.25)$$

$$W = \frac{1}{2} \phi^2 \mathcal{R} \quad \text{Stored Energy} \quad (9.26)$$

$$W_{\max} = \frac{1}{2} \frac{B_{sat}^2 a l}{\mu} \quad \text{Max. Stored Energy} \quad (9.27)$$

The smallest size inductor will have the highest core flux density (B). However, high frequency and high flux density produce high core losses (see **Eq. 3.13**, **Eq. 3.20**, **Eq. 3.23**) which will require either enhanced heat transfer (fan-forced airflow or liquid immersion) or lower core loss (lower flux density or lower core loss material). **Eq. 9.24** gives the design tradeoffs for inductance, current, core flux density, core size, and core relative permeability. See **Example-9** at the end of this chapter.

- Current Transformer (CT)

These equations assume a stiff (ideal) primary current source that supplies as much voltage as the load needs to draw. Typically the CT is used for current sensing, where the secondary current is a fraction of the primary current and the secondary load and output voltage are small. Also, a CT can be used to transform low current to high current at low voltage when a high current source is needed in laboratory testing. The phase angles are relative to I_1 .

$$\phi = \frac{N_1 I_1}{\mathcal{R}} \sqrt{\frac{1}{1+h^2}} \quad \alpha = -\tan^{-1} \frac{\omega L_2}{R+R_2} \quad \text{Magnetic flux} \quad (9.28)$$

$$I_2 = \frac{N_1}{N_2} I_1 \sqrt{\frac{h^2}{1+h^2}} \quad \beta = \alpha + \frac{\pi}{2} \quad \text{Secondary current} \quad (9.29)$$

$$V_2 = \frac{N_1}{N_2} I_1 R \sqrt{\frac{h^2}{1+h^2}} \quad \psi = \beta \quad \text{Secondary voltage} \quad (9.30)$$

$$P_{out} = \frac{1}{2} I_1^2 R \left(\frac{N_1}{N_2} \right)^2 \left(\frac{h^2}{1+h^2} \right) \quad \text{Power output} \quad (9.31)$$

$$P_{out_{\max}} = \frac{1}{2} \left(\frac{N_2 \omega B_{sat} a}{R} \right)^2 \left(\frac{R}{R+R_2} \right)^2 \quad \text{Max. power output} \quad (9.32)$$

- Rogowski Coil

This is a current rate-of-change sensor. The secondary coil is open ($R = \infty$, $I_2 = 0$, $P_{out} = 0$) and the primary coil typically has a low number of turns (such as 1). This sensor is typically used to measure very high current in large conductors. As such, this sensor can have a flexible core or a split core that allows it to be wrapped around the high current conductor. The output signal is the open secondary voltage (V_2). It is proportional to the rate of change of the primary current (dI_1/dt), which also makes it proportional to the frequency (ω) or harmonic distortion of the primary current. The phase angles (Eq. 9.33 and Eq. 9.34) are relative to I_1 . A detailed discussion is provided in Ch. 15 and a typical Rogowski coil configuration is shown in Fig. 15.1.

A magnetic core increases the core flux and allows the secondary turns to be reduced for the same output voltage. However, the maximum detectable current is limited by the core saturation. Also, the minimum detectable current is limited by the coercivity of the magnetic core.

A nonmagnetic core eliminates the sensing limits due to saturation and coercivity. There is no upper sensing limit other than the ability to measure high voltage, and there is no lower sensing limit other than the ability to measure low voltage. The main design and performance tradeoff is the number of secondary turns to achieve the desired output voltage range. Also, a uniform winding will significantly reduce the sensitivity of the output voltage to the location of the primary conductor inside the Rogowski loop.

Rogowski Coil:

$$\phi = \frac{N_1 I_1}{\mathcal{R}} \quad \alpha = 0 \quad \text{Magnetic flux} \quad (9.33)$$

$$V_2 = \frac{N_1 N_2}{\mathcal{R}} \omega I_1 = \frac{N_1 N_2}{\mathcal{R}} \left(\frac{dI_1}{dt} \right) \quad \psi = \frac{\pi}{2} \quad \text{Secondary voltage} \quad (9.34)$$

- Ideal Current Transformer (Ideal CT)

The secondary resistance and load resistance are very small ($R = R_2 = 0$), which means that the secondary voltage and power output are small ($V_2 = 0$, $P_{out} = 0$). The phase angle between the primary and secondary current is very small ($\beta = 0$) due to the zero resistance values. Therefore the magnetic flux is very small ($\phi = 0$), which means that the core will not saturate. However, if the resistance is not exactly zero, the phase angle will not be exactly zero, and there will be a magnetic flux that can saturate the core at a high current according to Eq. 9.28.

$$I_2 = \frac{N_1}{N_2} I_1 \quad \beta = 0 \quad \text{Secondary current} \quad (9.35)$$

The performance of a CT can be evaluated for a wide range of secondary impedance ratios, $h = \omega L_2/(R+R_2)$, with Eq. 9.28, Eq. 9.29. The calculation results in Fig. 9.2 are based on the configuration in Example-1 and Fig. 1.23, with the following additional characteristics ($N_2 = 5$ turns, $f = 60$ Hz). The

secondary inductance is calculated similarly to **Eq. 1.108**, as $L_2 = 8.0 \mu\text{H}$ (with $N_2 = 5$). The calculation results show the following trends.

- Good CT performance is attained with a high impedance ratio ($h > 30$).
- The Current Error increases as the impedance ratio decreases.
- The Phase Angle Error increases as the impedance ratio decreases.
- The Core Saturation Current decreases as the impedance ratio decreases.

CT Performance	Poor	Good	Ideal
Impedance Ratio (h)	3.02	30.2	30,200
Current Error	5.08 %	0.055 %	5.5E-8 %
Phase Angle Error	18.3 deg	1.90 deg	0.0019 deg
Saturation Current	28.6 A	272 A	272,000 A

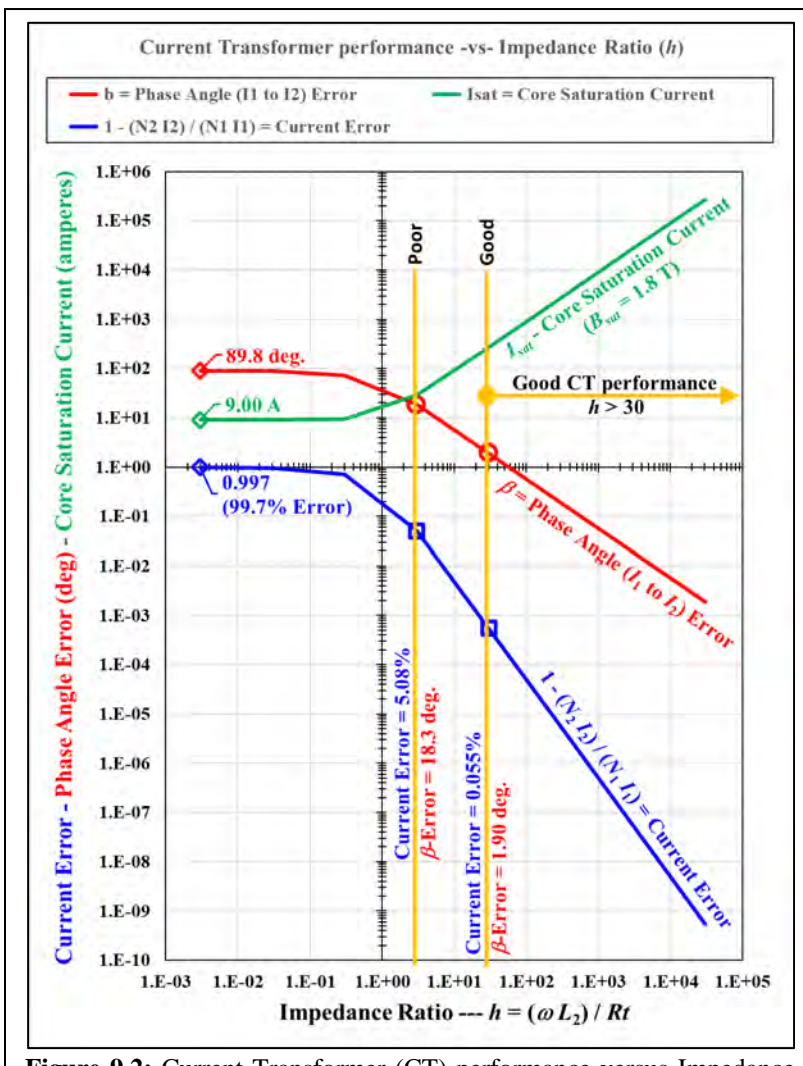


Figure 9.2: Current Transformer (CT) performance versus Impedance Ratio. A high impedance ratio ($h > 30$) give good CT performance. An Ideal CT has an infinite impedance ratio ($h = \infty$, or $R_t = 0$).

c. Transformer (with Leakage)

The general configuration of a transformer with flux leakage is shown in **Fig. 9.3**, in which a primary winding drives magnetic flux through a core and a secondary winding, inducing a secondary current into a load. The leakage flux is shown across the core between the primary and secondary windings.

Four loop equations can be written as done in the previous section. The magnetizing flux path in the core can be defined from the core dimensions. Defining the leakage flux path outside the core is presented in the next section, and is critical to developing an accurate magnetic model.

The following characteristic constants and dimensionless ratios are defined for the transformer in **Fig. 9.3**. Note that k and q (**Eq. 9.45**, **Eq. 9.46**) are impedance ratio combinations that reduce the size of the solution equations.

$$R_T = R_2 + R \quad \text{Total secondary resistance} \quad (9.36)$$

$$\mathcal{R} = \frac{l}{\mu a} \quad \text{Reluctance - Core flux path} \quad (9.37)$$

$$\mathcal{R}_H = \frac{l_H}{\mu a} = 0.5 \mathcal{R} \quad \text{Reluctance - Half of core } (l_H = 0.5l) \quad (9.38)$$

$$\mathcal{R}_L = \frac{l_L}{\mu_0 a} \quad \text{Reluctance - Leakage flux path} \quad (9.39)$$

$$L_1 = \frac{N_1^2}{\mathcal{R}} \quad \text{Inductance - Primary coil} \quad (9.40)$$

$$L_2 = \frac{N_2^2}{\mathcal{R}} \quad \text{Inductance - Secondary coil} \quad (9.41)$$

$$g = \frac{\omega L_1}{R_1} \quad \text{Impedance ratio - Primary coil} \quad (9.42)$$

$$h = \frac{\omega L_2}{R + R_2} \quad \text{Impedance ratio - secondary coil} \quad (9.43)$$

$$m = \frac{\mathcal{R}}{\mathcal{R}_L} \quad \text{Reluctance ratio - core to leakage} \quad (9.44)$$

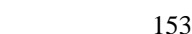


Figure 9.3: Transformer layout with leakage and a resistive load.

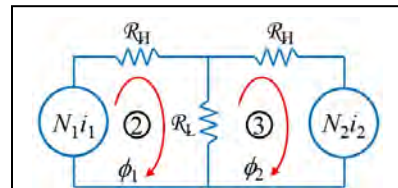


Figure 9.4: Reluctance network with leakage.

$$k = \sqrt{\left(\frac{m}{2} + 1\right)^2 + (mh)^2} \quad (9.45)$$

$$q = \sqrt{\left(1 + \frac{m}{4} - ghm\right)^2 + \left(\left(1 + \frac{m}{2}\right)(g+h)\right)^2} \quad (9.46)$$

A loop equation can be written for each of the 4 sections of the transformer (**Fig. 9.4**, **Eq. 9.47**, **Eq. 9.48**, **Eq. 9.49**, **Eq. 9.50**), and combined into a single 2nd order differential equation of the system for the magnetic flux (**Eq. 9.51**).

$$v_1 = i_1 R_1 + N_1 \frac{d\phi_1}{dt} \quad \text{Loop #1 - Sum of voltages} \quad (9.47)$$

$$N_1 i_1 = \phi_1 (\mathcal{R}_H + \mathcal{R}_L) - \phi_2 \mathcal{R}_L \quad \text{Loop #2 - Sum of ampere-turns} \quad (9.48)$$

$$i_2 R_T = N_2 \frac{d\phi_2}{dt} \quad \text{Loop #3 - Sum of ampere-turns} \quad (9.49)$$

$$0 = -\phi_2 \mathcal{R}_L + \phi_2 (\mathcal{R}_H + \mathcal{R}_L) + N_2 i_2 \quad \text{Loop #4 - Sum of voltages} \quad (9.50)$$

$$\boxed{\left(\frac{N_1^2 N_2^2}{R_1 R_T \mathcal{R}_L}\right) \frac{d^2 \phi_2}{dt^2} + \left(\frac{\mathcal{R}_H + \mathcal{R}_L}{\mathcal{R}_L}\right) \left(\frac{N_1^2}{R_1} + \frac{N_2^2}{R_T}\right) \frac{d\phi_2}{dt} + \left(\frac{\mathcal{R}_H + 2\mathcal{R}_L}{\mathcal{R}_L}\right) \mathcal{R}_H \phi_2 = \frac{N_1 v_1}{R_1}} \quad (9.51)$$

Transformers generally operate in the linear range of magnetic flux (not saturating). Therefore, this system can be evaluated with a linear phasor solution based on magnitudes and phase angles, as follows.

$$e^{(j\omega t)} = \cos(\omega t) + j \sin(\omega t) \quad \text{Phasor exponential form} \quad (9.52)$$

$$v_1 = V_1 e^{(j\omega t)} \quad i_1 = I_1 e^{(j\omega t + \gamma)} \quad \text{Phasor - primary} \quad (9.53)$$

$$\phi_1 = \phi_1 e^{(j\omega t + \alpha)} \quad \phi_2 = \phi_2 e^{(j\omega t + \beta)} \quad \phi_L = \phi_L e^{(j\omega t + \lambda)} \quad \text{Phasor - flux} \quad (9.54)$$

$$i_2 = I_2 e^{(j\omega t + \sigma)} \quad v_2 = i_2 R e^{(j\omega t + \sigma)} \quad \text{Phasor - secondary} \quad (9.55)$$

Substituting the individual phasor equations into the combined system equation and loop equations gives solutions for the magnitude and phase angle variables. These equations assume a stiff primary voltage source that can supply as much current as the load needs to draw. The phase angles are relative to V_1 .

$$\phi_2 = \frac{N_1 V_1}{\mathcal{R} R_1 q} \quad \beta = -\tan^{-1} \left(\frac{\left(1 + \frac{m}{2}\right)(g+h)}{1 + \frac{m}{4} - ghm} \right) \quad \text{Secondary flux} \quad (9.56)$$

$$I_2 = \frac{N_1}{N_2} \frac{V_1}{R_1} \frac{h}{q} = \frac{N_1 N_2}{\mathcal{R}} \frac{\omega}{R_T} \frac{V_1}{R_1} \frac{1}{q} \quad \sigma = \beta + \frac{\pi}{2} \quad \text{Secondary current} \quad (9.57)$$

$$\phi_1 = \frac{N_1 V_1}{\mathcal{R} R_1 q} k \quad \alpha = \tan^{-1} \left(\frac{2mh}{m+2} \right) + \beta \quad \text{Primary flux} \quad (9.58)$$

$$\phi_L = \phi_1 - \phi_2$$

Leakage flux (9.59)

$$I_1 = \frac{V_1}{R_1 q} \sqrt{\left[\left(\frac{1}{2} + \frac{1}{m} \right) k \cos \alpha - \frac{1}{m} \cos \beta \right]^2 + \left[\left(\frac{1}{2} + \frac{1}{m} \right) k \sin \alpha - \frac{1}{m} \sin \beta \right]^2} \quad (9.60)$$

$$\gamma = \tan^{-1} \left(\frac{\left(\frac{1}{2} + \frac{1}{m} \right) k \sin \alpha - \frac{1}{m} \sin \beta}{\left(\frac{1}{2} + \frac{1}{m} \right) k \cos \alpha - \frac{1}{m} \cos \beta} \right) \quad \text{Primary Current, Phase} \quad (9.61)$$

d. Core-Type, Shell-Type, and Leakage

The addition of leakage flux in the formulation adds a single reluctance term and one more flux loop, which seems fairly simple. However, the system equation (**Eq. 9.51**) becomes a 2nd order differential equation and the leakage flux paths are in the air, which makes them complex to define.

The configurations that will be considered include core-type and shell-type transformers, as shown in **Fig. 9.5**. The emphasis in this section is on the identification of the leakage flux paths, and on the performance differences for core-type and shell-type transformers that result from leakage.

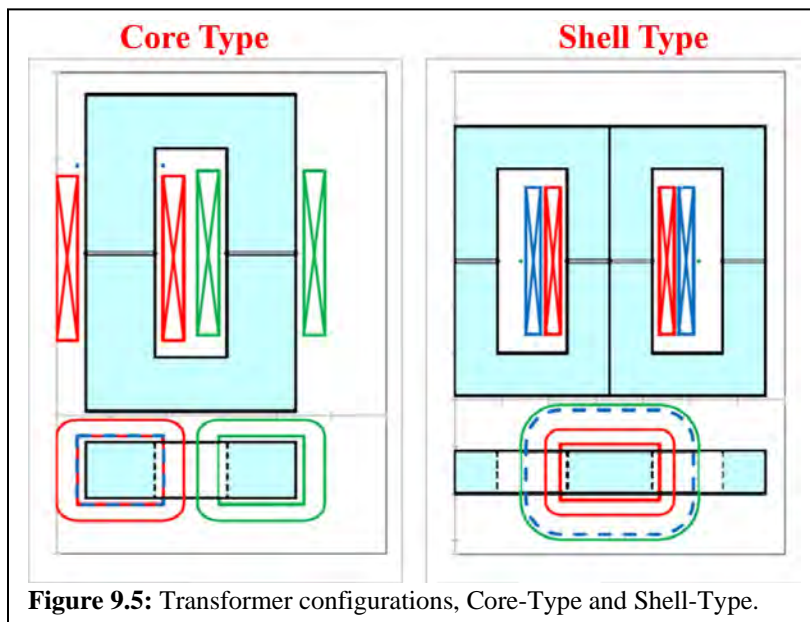


Figure 9.5: Transformer configurations, Core-Type and Shell-Type.

The core-type transformer has separate coils on the opposite sides of a rectangular or circular core. The shell-type transformer uses two rectangular cores side-by-side and the coils are wound concentrically on the center of the core assembly (the core appears to be a shell around the coils).

The leakage flux paths for the core-type and shell-type transformers are very different. However, in both cases, the leakage flux paths can be defined by visualizing where the magnetic flux can go to avoid passing through the secondary coil. Therefore, the leakage flux passes through the primary coil in the core and then exits the core above the primary and secondary coils and

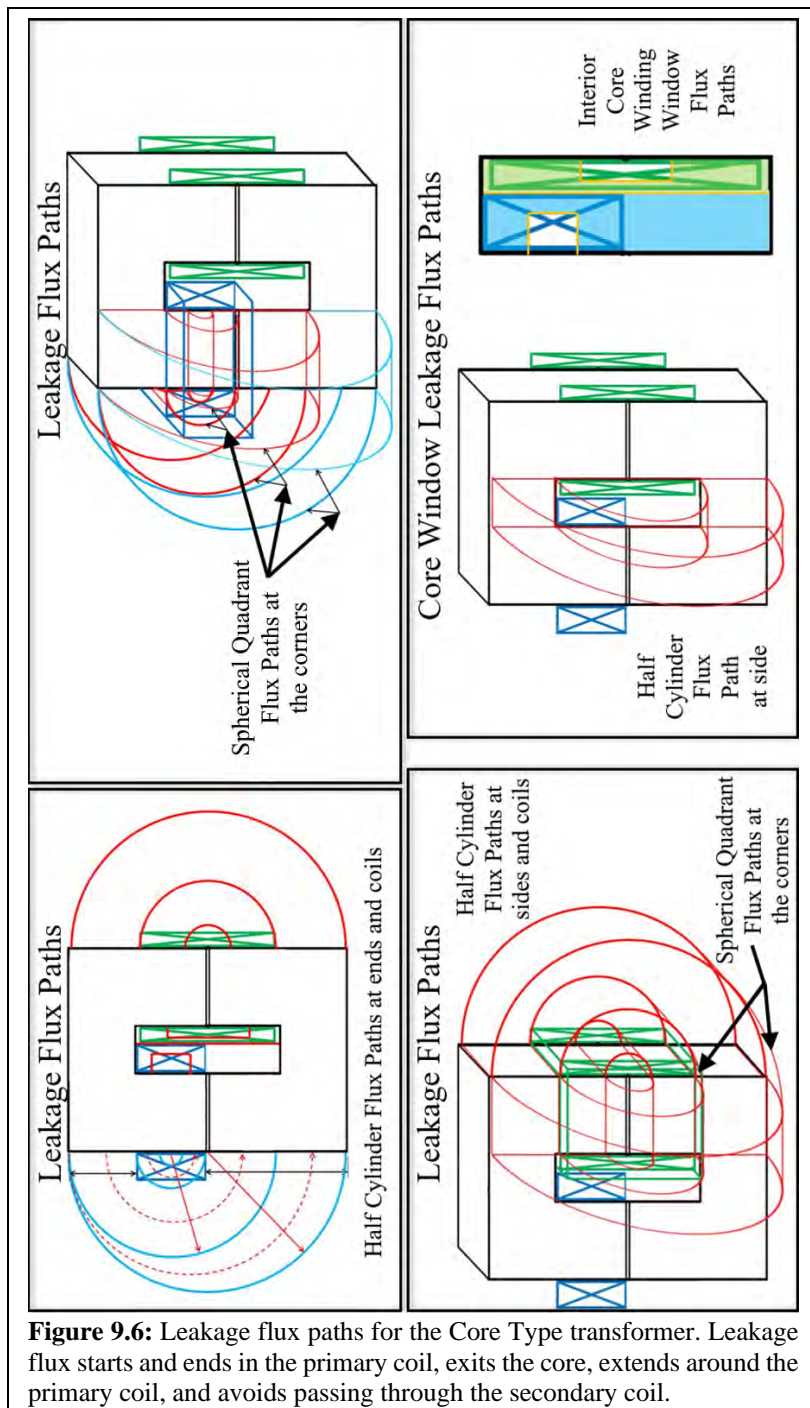


Figure 9.6: Leakage flux paths for the Core Type transformer. Leakage flux starts and ends in the primary coil, exits the core, extends around the primary coil, and avoids passing through the secondary coil.

re-enters the core below the primary and secondary coils and closes the flux loop by passing through the primary coil.

The leakage flux paths for the core-type transformer are shown in **Fig. 9.6**. All of the leakage flux paths on the outside surfaces of the core are drawn as half-cylinders and shells on the sides, and as spherical quadrants and shells at the corners, as defined for the air flux paths in **Ch. 1.g**. The leakage flux paths in the core winding window are shown as rectangular regions where the volume (v) and the average length (l) of the flux path can be determined to obtain the permeance ($\mathcal{P} = \mu_0 v / l^2$).

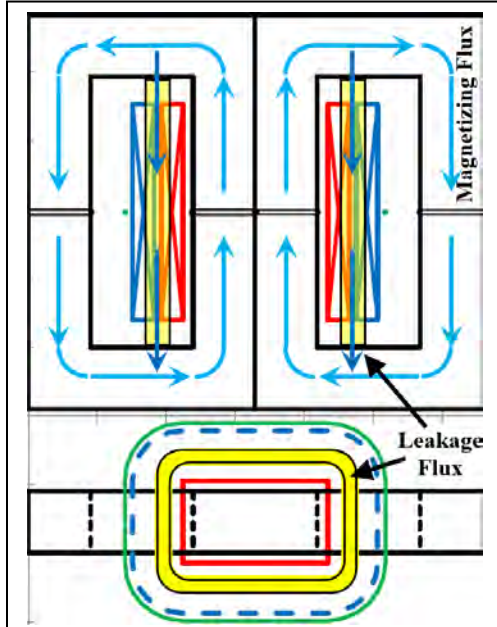


Figure 9.7: Magnetizing flux and Leakage flux paths for the Shell-Type transformer.

The leakage flux path for a shell-type transformer (**Fig. 9.7**) is very simple. The only path available for flux to link the primary coil and avoid linking the secondary coil is the small air space (highlighted in yellow) between the primary and secondary coils. A finite element analysis (**Fig. 9.8**) shows the

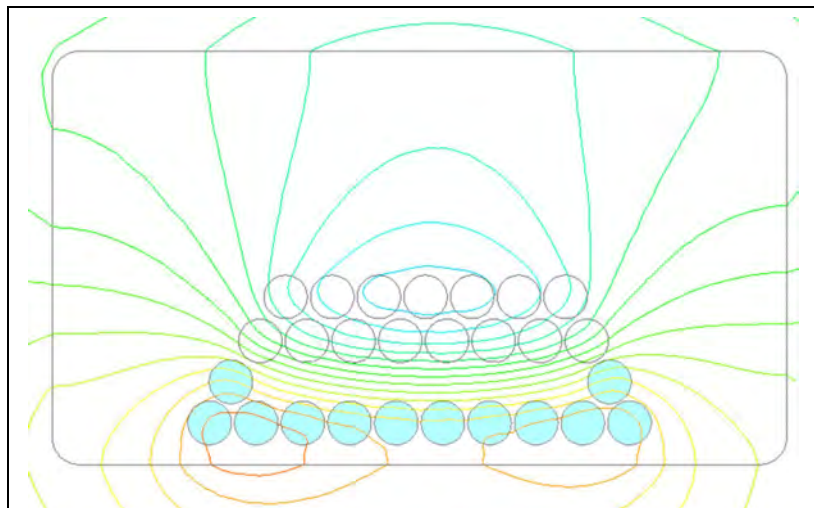


Figure 9.8: FEA flux line plot of leakage in a shell-type transformer, showing the windings in the core window. The primary coil is blue with +900 NI. The secondary coil is white with -900 NI. The leakage flux lines lie between the primary and secondary coils.

leakage flux lines in the space between the primary and secondary windings, as portrayed in **Fig. 9.7**.

Design and performance calculations were completed for a 50 kW transformer at 10 kHz using a nanocrystalline core material (Finemet), with 3 windings, 600 V-RMS, 800 V-RMS (main primary), and 1,000 V-RMS. The number of turns was determined by minimizing both the core size and the leakage. The core-type transformer coils have 10 turns, 12 turns, and 18 turns. The shell-type transformer coils have 9 turns, 12 turns, and 15 turns. The turns ratios for the core-type transformer are slightly different to achieve the correct secondary voltage with the high leakage. The transformer magnetic design calculations (**Eq. 9.56** through **Eq. 9.61**) were completed for each pair of coils for all conditions with a single primary and a single secondary. Testing included the case of 1 primary and 2 secondaries, and the case of 2 primaries and 1 secondary.

A rectangular core was selected from the Hitachi catalog (Finemet FT-3TL, area = 2.30 in², mass = 5.5 kg). Two cores are required for this transformer. The core-type transformer uses the 2 cores stacked, and the shell-type transformer uses the 2 cores side-by-side. The skin effect and proximity effect were evaluated for 4 AWG solid wire and 4 AWG Litz wire based on the correlations published by Jimenez [26] and Barrios [27]. The calculations show that the AC to DC resistance ratio is 8.00 for solid wire and 1.07 for Litz wire. The primary coil was designed with 12 turns of 4 AWG Litz wire. A core-type transformer and a shell-type transformer were constructed and tested (**Fig. 9.9**).

This work was presented at the 2019 MMM-Intermag Joint Conference [28]. Funding for this work was provided by the DOE SunShot program as part of the SuNLaMP project. This material is based upon work supported by the Department of Energy, Office of Energy Efficiency and Renewable Energy (EERE), under Award Number DE-EE0007506.



Figure 9.9: Core-type (left) and shell-type (right) transformer prototypes.

Calculations for the leakage permeance and inductance were completed for both the core-type and shell-type transformers. The leakage inductance was measured by driving the primary winding while the secondary winding was shorted. A shorted low resistance secondary winding causes the magnetic flux to go around the secondary winding (not through, not linking).

The error is fairly small (< 7.5%) for the calculated leakage results as compared to the measurements (**Fig. 9.10**). The leakage permeance for the core-type transformer was calculated as shown in **Fig. 9.6**. The shell-type transformer leakage permeance is based on the insulation thickness between the windings plus half of the space for each winding, as shown in **Fig. 9.7**. The results show that the core-type transformer has 5.8x the leakage permeance and leakage inductance of the shell-type transformer. This shows that the core-type transformer is a high leakage configuration.

Core-Type	Leakage		Inductance (H)
	Permeance (Wb/NI)	Leakage	
Calculated	6.60E-7		9.50E-5
Measured	6.14E-7		8.97E-5
Error	+7.5%		+5.9%

Shell-Type	Leakage		Inductance (H)
	Permeance (Wb/NI)	Leakage	
Calculated	1.00E-7		1.45E-5
Measured	1.06E-7		1.53E-5
Error	-5.7%		-5.2%

Figure 9.10: Comparison of calculated and measured leakage inductance and leakage permeance for the core-type and shell-type transformers.

A comparison of additional performance calculations and measurements is shown in **Fig. 9.11** for the core-type transformer, and in **Fig. 9.12** for the shell-type transformer. In general, the performance measurements correlate very well with the calculations. Both the calculated core loss due to the magnetizing flux and the calculated relative permeability are from the datasheet provided by Hitachi. The measured core loss and permeability were obtained by measurements on the transformer and by measurements on the core alone.

Core-Type	Calculated	Measured	Error
Primary Current	109.1 A-pk	103.3 A-pk	5.3%
Leakage Inductance	95.3 μ H	89.7 μ H	5.9%
Primary Flux Density	0.631 T	0.631 T	0.0%
Leakage Flux Density	0.365 T	0.320 T	12.3%
Core Loss – Magnetizing	6.51 W/kg	6.51 W/kg	0.0%
Core Rel. Permeability	26,500	26,526	0.1%

Figure 9.11: Core-type transformer performance compared to calculations at 50 kW and 10 kHz.

The leakage flux density reported in **Fig. 9.11**, **Fig. 9.12** and **Fig. 9.13** is calculated by dividing the leakage flux by the cross-sectional area of the core inside the primary winding. The performance for both the core type transformer and the shell-type transformers are listed in **Fig. 9.13**. The shell-type transformer offers significant performance improvements. The primary

current is reduced by 13.9% as a result of less leakage flux. The leakage inductance is reduced by 82.9%, the leakage flux is reduced by 85.0%, and the core loss due to leakage flux is reduced by 95.5%. The core loss due to leakage flux is addressed in the next section.

Shell-Type	Calculated	Measured	Error
Primary Current	88.9 A-pk	88.9 A-pk	0.0%
Leakage Inductance	14.5 μ H	15.3 μ H	5.2%
Primary Flux Density	0.629 T	0.631 T	0.3%
Leakage Flux Density	0.045 T	0.048 T	6.3%
Core Loss – Magnetizing	6.51 W/kg	6.51 W/kg	0.0%

Figure 9.12: Shell-type transformer performance compared to calculations at 50 kW and 10 kHz. Core mass = 11.3 kg.

Measurements	Core-Type	Shell-Type	Change
Primary Current	103.3 A-pk	88.9 A-pk	-13.9%
Winding Loss	33.2 W	28.3 W	-14.8%
Leakage Inductance	89.7 μ H	15.5 μ H	-82.9%
Primary Flux Density	0.631 T	0.631 T	0
Leakage Flux Density	0.320 T	0.048 T	-85.0%
Core Loss – Magnetizing	6.51 W/kg	6.51 W/kg	0
Core Loss – Leakage	123.0 W/kg	5.53 W/kg	-95.5%
Total Loss (Coil & Core)	1,497 W	164 W	-89.0%
Temperature Rise	1,047 °C	78 °C	-92.6%
Power Density @ 50 kW	156 W/in ³	84.5 W/in ³	
Efficiency @ 50 kW	97.01%	99.67%	

Figure 9.13: Core-type versus shell-type transformer performance at 50 kW and 10 kHz. Core mass = 11.3 kg. Estimated temperature rise uses a heat transfer coefficient of 10 W/m²·°K (no fan), and a transformer surface area of 0.143 m² (Core-Type) and 0.210 m² (Shell-Type).

The power density in **Fig. 9.13** is calculated by dividing the power delivered to the load (50 kW) by the volume of a rectangular box around the transformer. The box for the core-type transformer contains less air space because the coils cover more of the core. This gives the core-type transformer a higher power density.

e. Core Loss (with Leakage)

The core loss and magnetic permeability were measured at 10 kHz with the secondary coil open to determine the magnetizing characteristics, and with the secondary coil shorted to determine the leakage characteristics.

Core-Type Transformer

The top chart in **Fig. 9.14** shows the measured voltage and current on the 10-turn coil with all other coils open. The voltage is 1,000 V-DC oscillated at 10

kHz with an H-bridge. The current is a triangular waveform with a peak of approximately 1.5 amperes. The core magnetic flux density (B) was obtained by integrating the voltage and correcting for integration drift (Eq. 9.62). The magnetic field intensity (H) was obtained by dividing the coil ampere-turns by the magnetic flux path length through the entire core (Eq. 9.63).

$$B = \frac{1}{N} \int V dt \quad \text{Magnetic flux density} \quad (9.62)$$

$$H = \frac{NI}{l} \quad \text{Magnetic field intensity} \quad (9.63)$$

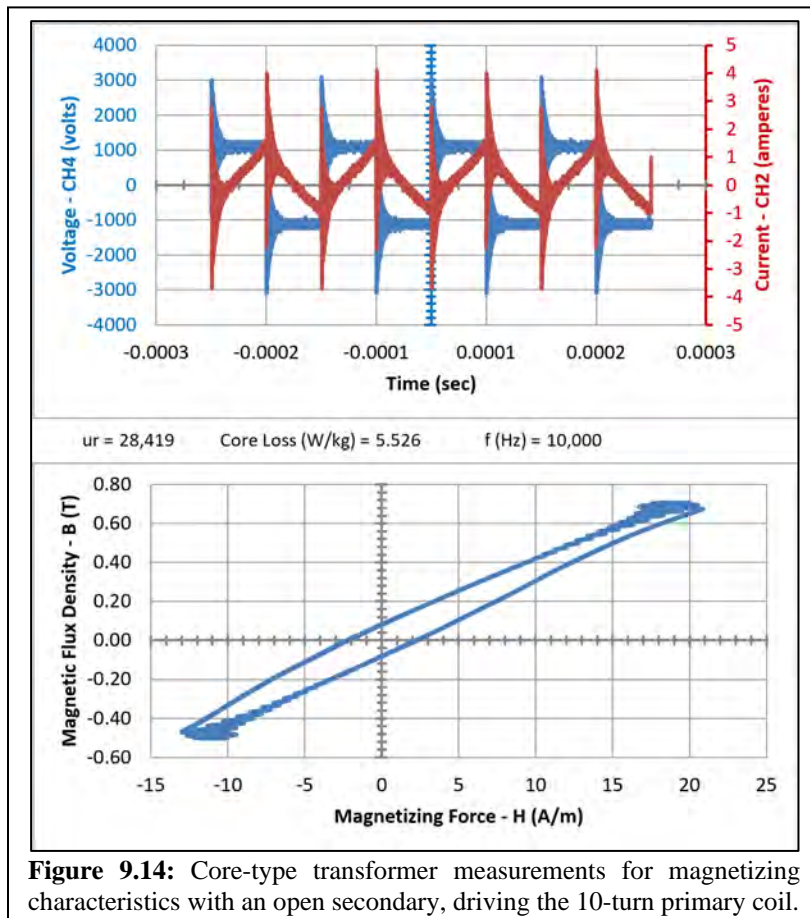


Figure 9.14: Core-type transformer measurements for magnetizing characteristics with an open secondary, driving the 10-turn primary coil.

The B and H values give the magnetic hysteresis loop as shown in the bottom chart of Fig. 9.14. The relative permeability of the core ($\mu_r = 28,419$) is the slope of the hysteresis loop relative to the permeability of free space (μ_0). This is 7% higher than the published value from Hitachi ($\mu_r = 26,500$). Integrating the area inside the hysteresis loop gives 4.0 TA/m (or $\text{J/m}^3\text{-Cycle}$). Multiplying by the cyclic frequency (10 kHz) and the core density (7300 kg/m^3) gives a core loss of 5.526 W/kg . The core loss can also be measured by integrating the coil voltage and current to get the power delivered into the system, and subtracting the resistive power loss in the coil. This produces a

core loss of 5.561 W/kg, which is within 0.6% of the hysteresis loop measurement.

The current and voltage waveforms in **Fig. 9.14** have significant ringing, and the waveforms in **Fig. 9.15** have no ringing. The damping ratio (**Eq. 14.55**) for the 2 tests can be compared as follows. In the short-circuit test, the coil resistance and the coil capacitance (turn to turn) are 2x the values for the open-circuit test (there are 2 coils carrying current in the short-circuit test). Also, the inductance for the open-circuit test is 220x the inductance for the short-circuit test. The result is a damping ratio for the short-circuit test that is 42x the damping ratio for the open-circuit test. Therefore, the short circuit test has much more damping and should have much less ringing.

The top chart in **Fig. 9.15** shows the measured voltage and current on the 12-turn coil with a shorted secondary coil. The voltage is 350 V-DC oscillated at 10 kHz with an H-bridge. The current is a triangular waveform with a peak of approximately 100 amperes. The core magnetic flux density (B) was obtained by integrating the voltage and correcting for integration drift. The magnetic field intensity (H) was obtained by dividing the coil ampere-turns by the magnetic flux path length through the entire core.

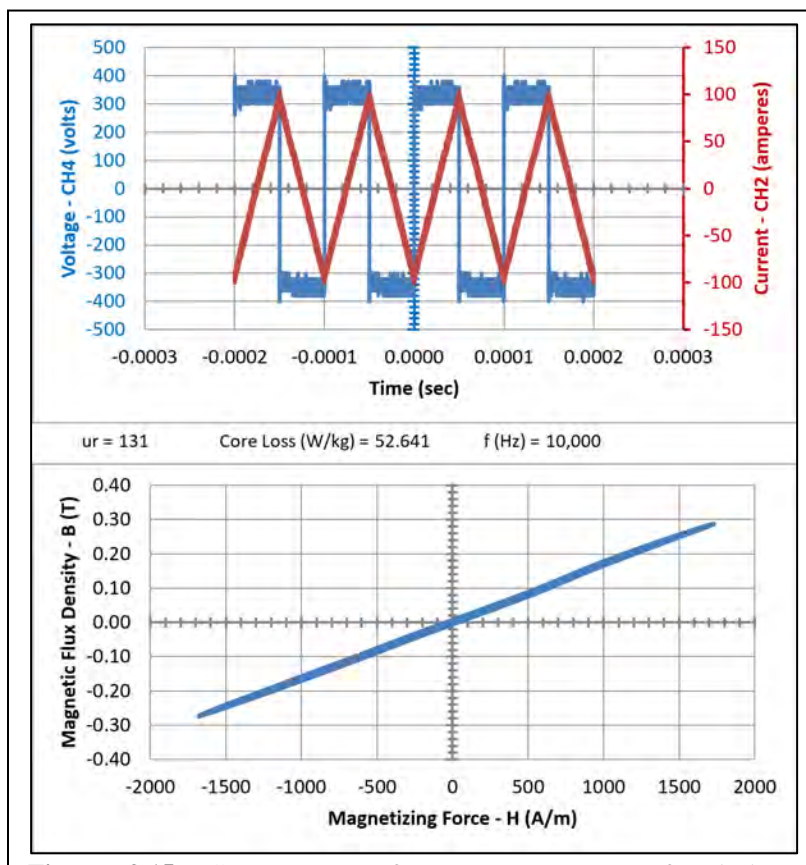


Figure 9.15: Core-type transformer measurements for leakage characteristics with a shorted secondary, driving the 12-turn primary coil.

The B and H values give the magnetic hysteresis loop as shown in the bottom chart of **Fig. 9.15**. The relative permeability ($\mu_r = 131$) is the slope of the hysteresis loop relative to the permeability of free space (μ_0). This is a very small value that represents the leakage air flux paths. Integrating the area inside the hysteresis loop gives 38.4 TA/m (or J/m³-Cycle). Multiplying by the cyclic frequency (10 kHz) and the core density (7300 kg/m³) gives a core loss of 52.6 W/kg. The core loss can also be measured by integrating the coil voltage and current to get the power delivered into the system, and subtracting the resistive power loss in both coils. This produces a core loss of 49.6 W/kg, which is within 6.0% of the hysteresis loop measurement.

The core-type transformer has a core loss due to leakage flux that is 9.5 times the core loss due to magnetizing flux. These losses were measured at many operating conditions as shown in **Fig. 9.16**. The measurements of the loss due to magnetizing flux with open secondary (blue circle data points) match the measurements done at Carnegie Mellon University (CMU) by Kevin Byerly, and it matches the published core loss for Finemet by Hitachi. At the rated power level of 50 kW, **Fig. 9.13** shows the magnetizing flux is 0.631 T and the core loss due to magnetizing flux is 6.51 W/kg (71.6 W for an 11 kg core), the leakage flux is 0.32 T and the core loss due to leakage flux is 123 W/kg (1,353 W for an 11 kg core).

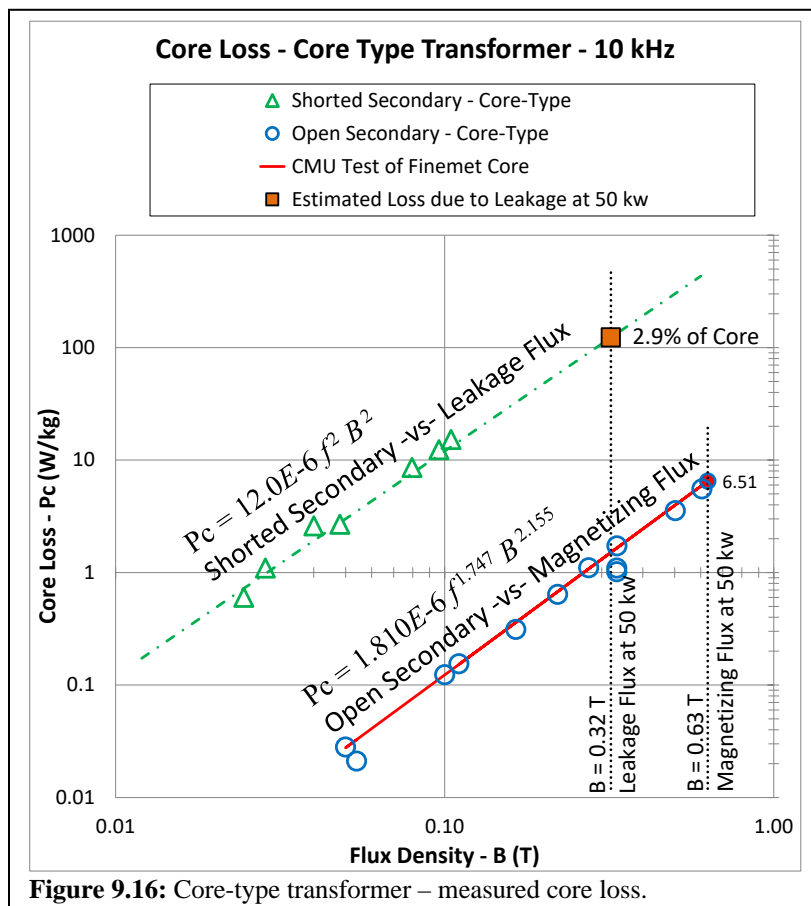


Figure 9.16: Core-type transformer – measured core loss.

The loss due to leakage flux is surprisingly large because it is generally insignificant at 60 Hz. In this case, it increases the total heat dissipation from 72 W to 1,424 W, which increases the temperature rise by a factor of 19.8 (for example, a temperature rise of 60°C at 72 W, becomes a temperature rise of 1,188°C at 1,424 W). The loss due to leakage flux can be shown to be a result of surface eddy currents in the first few layers of the core ribbon. The leakage that is normal to the ribbon surface produces eddy currents in the ribbon. An estimate of this effect is shown in **Fig. 9.17**. This calculation is for the 50 kW rating in which the leakage flux density is 0.32 T (**Fig. 9.13**).

The eddy current loss estimate is calculated as follows. Each coil has 2 leakage flux paths, outside the core at the end, and inside the core winding window. There are 2 stacked cores, therefore there are 4 leakage flux paths per coil. There are 2 coils, with 8 total leakage flux paths normal to the ribbon surface. Each flux path has a ribbon surface at each end, for a total of 16 ribbon surfaces. The ribbon surface area exposed to the leakage flux is

Measured peak leakage flux at 50 kW (Fig. 9.11)	0.320	T
Frequency	10000	Hz
Total layers in core	2054	Layers
Core Window Height	5.509	in
Core Window Width	3.153	in
Core Thickness	2	in
Coil-1 Height	1.91	in
Coil-3 Height	2.86	in
Ribbon Width	1.15	in
Ribbon Thickness	20	um
Ribbon Resistivity	0.0000011	ohm-m
Core cross-sectional area	4.6	in ²
Total leakage flux area of ribbon	72.6	in ²
Leakage flux paths for a coil with 2 cores	4	paths
Leakage flux paths for 2 coils	8	paths
Ribbon surfaces for 8 flux paths	16	surfaces
Portion of leakage flux normal to ribbon	53.5%	
Ribbon area at each end of each leakage path	4.54	in ²
Ribbon leakage flux area width	1.15	in
Ribbon leakage flux area height	3.95	in
Eddy current path – width		0.00974 m
Eddy current path – thickness		0.00002 m
Eddy current path – length		0.21996 m
Eddy current path – resistance	1.242	ohm
Total Leakage flux	9.50E-04	Wb
Leakage flux in each of 8 path	1.19E-04	Wb
Eddy current peak voltage	3.99	volts
Eddy current power - each area	6.41	watt
Eddy current power - total of 16 areas	102.5	watt
Core Loss in 1 layer	9.32	W/kg
Layers for 80% of loss at 96.2% flux pass through	21	1.0% of core
Layers for 99% of loss at 96.2% flux pass through	60	2.9% of core
Total core loss of 60 layers	123.8	W/kg

Figure 9.17: Estimated eddy current layers and loss due to leakage flux.

divided into 16 equal small areas. Each small area is assumed to have an eddy current path around the outer edge equal in width to 1/3 of the ribbon width, which defines an eddy current path resistance (R_e). The leakage flux normal to each small area produces a voltage (V_p) on the eddy current path based on Faraday's law, which defines an eddy current loss (P_c).

$$V = N \frac{d\phi}{dt} \quad V_p = \phi_p \omega \quad N = 1 \quad \text{Voltage driving the eddy current} \quad (9.64)$$

$$P_c = \frac{1}{2} \frac{V_p^2}{R_e} \quad \text{Eddy current loss} \quad (9.65)$$

The estimated loss (**Fig. 9.17**) shows 99% of the loss due to leakage flux is produced in the first 60 ribbon layers (2.9% of 2054 ribbon layers, 1.2 mm thick), and 80% of the loss is produced in the first 21 layers (1.0% of 2054 ribbon layers, 0.4 mm thick). This assumes a flux pass-through of 96.2% from layer to layer. The 2.9% data point is shown in **Fig. 9.16**.

Thermal imaging was done on a transformer with a shorted secondary coil at North Carolina State University by R. B. Beddingfield [30]. The image (**Fig. 9.18**) shows a hot surface layer on the core due to leakage flux. This validates the surface eddy current heating model due to leakage flux. The loss due to leakage flux is an eddy current loss, therefore it is the same form as **Eq. 3.20**, in which the loss is proportional to the square of the flux density and the square of the frequency, as shown in **Fig. 9.16**.

At 60 Hz the loss due to leakage flux drops to 0.0044 W/kg from 123 W/kg, a factor of 28,000, and becomes insignificant. The loss due to leakage flux is a high-frequency issue that requires low leakage designs at frequencies above 1 kHz.

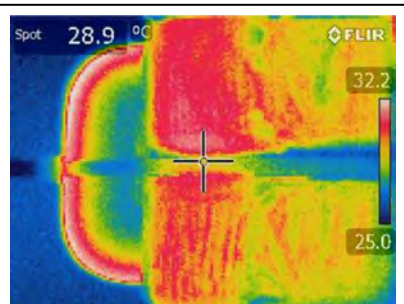


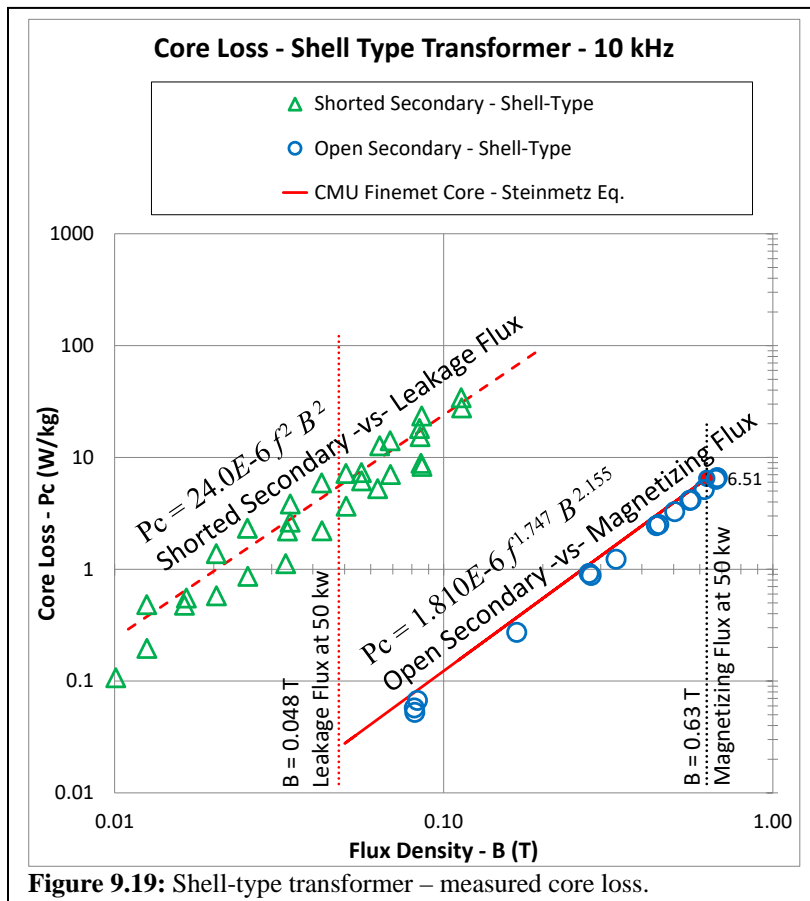
Figure 9.18: Thermal image of a transformer with shorted secondary showing heat due to leakage flux. From R. B. Beddingfield at North Carolina State University [30].

Ferrite magnetic materials have very high electrical resistivity, therefore the use of a ferrite core material can eliminate eddy current losses. However, the saturation magnetic flux density of ferrite is fairly low (0.20 to 0.35 T) (Finemet = 1.0 T), and the available size of ferrite cores is relatively small (28 blocks of ferrite would need to be assembled into a single core).

Shell-Type Transformer

Measurements were done in the same way for the shell-type transformer. Loss due to magnetizing flux was measured by driving the primary coil while the secondary coils are open, and the loss due to leakage flux was measured by driving the primary coil while a secondary coil is shorted. The test results are shown in **Fig. 9.19**. The measurements of the loss due to magnetizing flux with open secondary (blue circle data points) match the measurements done

at Carnegie Mellon University (CMU) by Kevin Byerly, and it matches the published core loss for Finemet by Hitachi. At the rated power level of 50 kW, **Fig. 9.13** shows the magnetizing flux is 0.631 T and the core loss due to magnetizing flux is 6.51 W/kg (71.6 W for an 11 kg core), the leakage flux is 0.048 T and the core loss due to leakage flux is 5.53 W/kg (60.8 W for an 11 kg core). The shell-type transformer is a low leakage design. The data in **Fig. 9.13** shows that the leakage flux is reduced by 85% and the loss due to leakage flux is reduced by 95.5% from the core-type transformer.



f. Performance Charts (with Leakage)

Design and performance calculations were done for both core-type and shell-type transformers over a wide range of frequencies (60 Hz to 20 kHz) and winding turns (10 to 1000) (primary = secondary). The winding aspect ratio was kept constant (turns-per-layer/number-of-layers = 10). The results are shown in the following graphs (**Fig. 9.20** – **Fig. 9.27**). The core size was chosen for operation near saturation flux density. A larger core was used to reduce the flux density and core loss if the temperature rise exceeded 70°C. The wire size was chosen to achieve a temperature rise near 70°C.

Leakage flux produces eddy currents in the surface of a core which causes losses in addition to the core loss. The loss due to leakage flux is significant (dominant) in core-type transformers, and it is highly dependant on the coil geometry. For example, a concentrated coil winding will produce more leakage flux and more losses due to leakage flux than a distributed coil winding. The use of a ferrite core material can eliminate all eddy current losses, including the loss due to leakage flux. However, the saturation magnetic flux density of ferrite is fairly low (0.20 to 0.35 T), which requires a larger core. Also, ferrite plates might be used to shield the core from exposure to leakage flux to reduce the loss due to leakage flux.

The loss due to leakage flux is highly dependant on coil and core geometry and core materials. Therefore, these calculations only consider the winding loss and the core loss in evaluating the basic design and performance trade-offs, and the loss due to leakage flux is not included. Faraday's law shows that increased winding turns and increased frequency both reduce the core magnetic flux and permit the use of a smaller core. The following charts show additional trade-off details and limits (**Fig. 9.20 – 9.29**).

- **Fig. 9.20-9.21:** Power Density (W/in³) increases as the frequency increases. The peak power density occurs at an intermediate value of coil turns, and it increases as the frequency increases. The power density decreases as leakage flux increases above 10%.
- **Fig. 9.22-9.25:** Leakage Flux (%) increases as the frequency and coil turns increase. Also, leakage flux increases (approximately linearly) with the phase angle between the primary and secondary currents, regardless of the frequency and regardless of the configuration (Core-Type or Shell-Type). When the phase angle gets large it becomes difficult to transfer power to the secondary, and more magnetic flux goes into leakage.

$$\text{Leakage Flux (\%)} = 1.60 \text{ Phase Angle (deg)} \dots \text{RMS Error} = 1.21\% \\ \text{for } \dots 0 < \text{Phase Angle} < 45 \text{ deg} \dots 60 \text{ Hz} < \text{Frequency} < 20 \text{ kHz}$$

The phase angle between the primary and secondary currents increases with the frequency and with the coil turns (approximately $f^{0.5}$ and $N^{1.4}$). This can be visualized as resulting from; 1) the inductive lag which becomes a larger part of the oscillation period as the frequency increases; and 2) the increased inductance due to increased turns.

- **Fig. 9.26-9.27:** Core Mass (kg) decreases with increased frequency and with increased coil turns (per Faraday's law). From 10 kHz to 20 kHz, the core mass is constant due to high core loss, which is reduced by decreasing the flux density to maintain a 70°C temperature rise.
- **Fig. 9.28-9.29:** Overall Transformer Volume (in³) decreases with increased frequency and with increased coil turns. From 10 kHz to 20 kHz, the overall transformer volume is constant due to high core loss, which is reduced by decreasing the flux density to maintain a 70°C temperature rise.

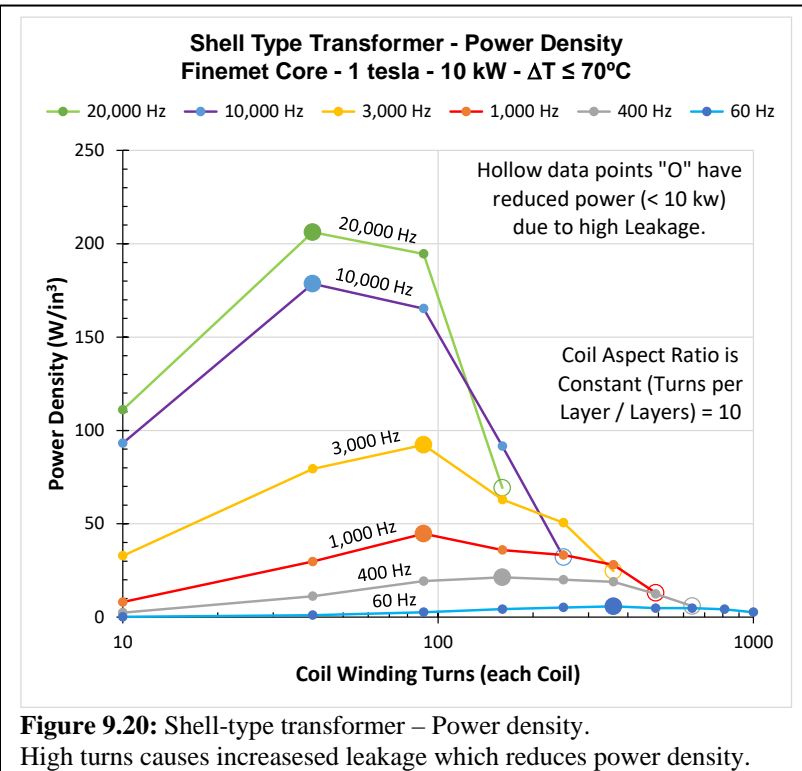


Figure 9.20: Shell-type transformer – Power density.
 High turns causes increased leakage which reduces power density.

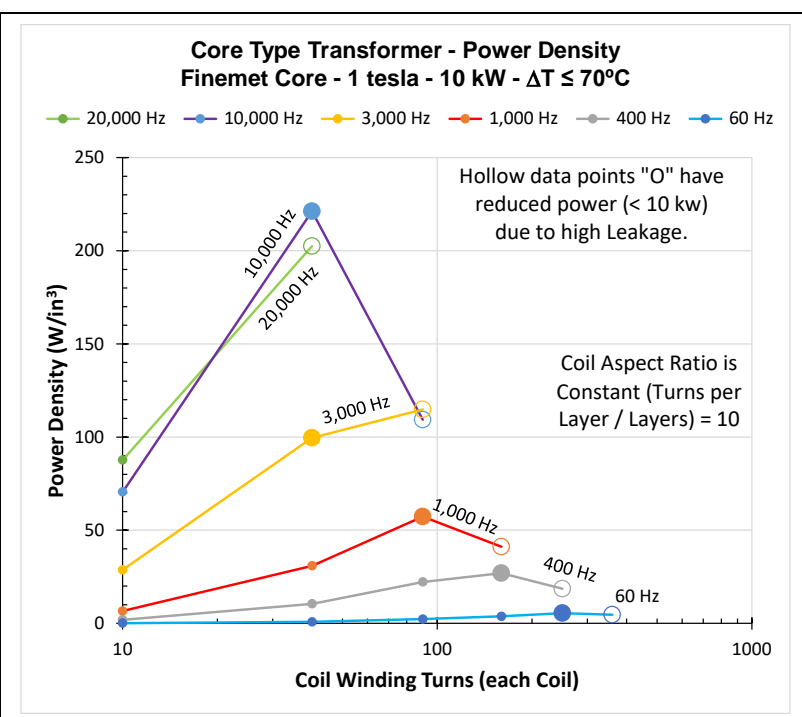


Figure 9.21: Core-type transformer – Power density.
 High turns causes increased leakage which reduces power density.
 Core-type transformers have more leakage than shell-type transformers.

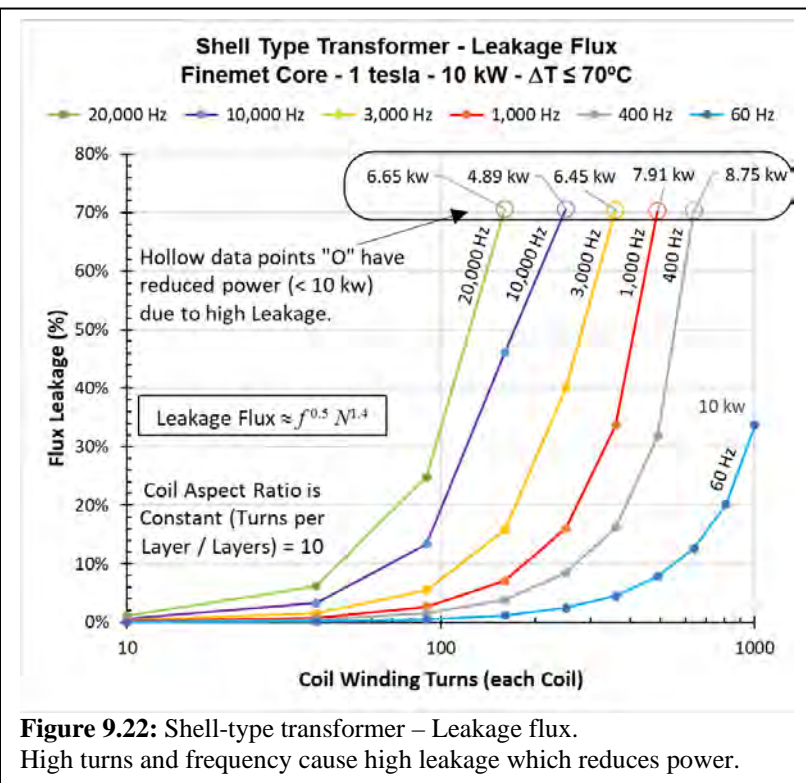


Figure 9.22: Shell-type transformer – Leakage flux.
 High turns and frequency cause high leakage which reduces power.

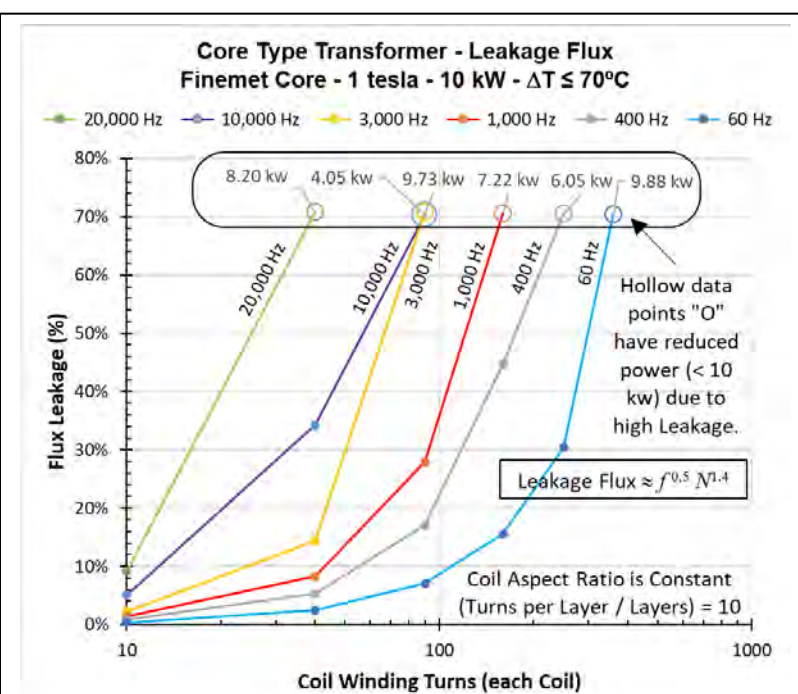


Figure 9.23: Core-type transformer – Leakage flux.
 High turns and frequency cause high leakage which reduces power.
 Core-type transformers have more leakage than shell-type transformers.

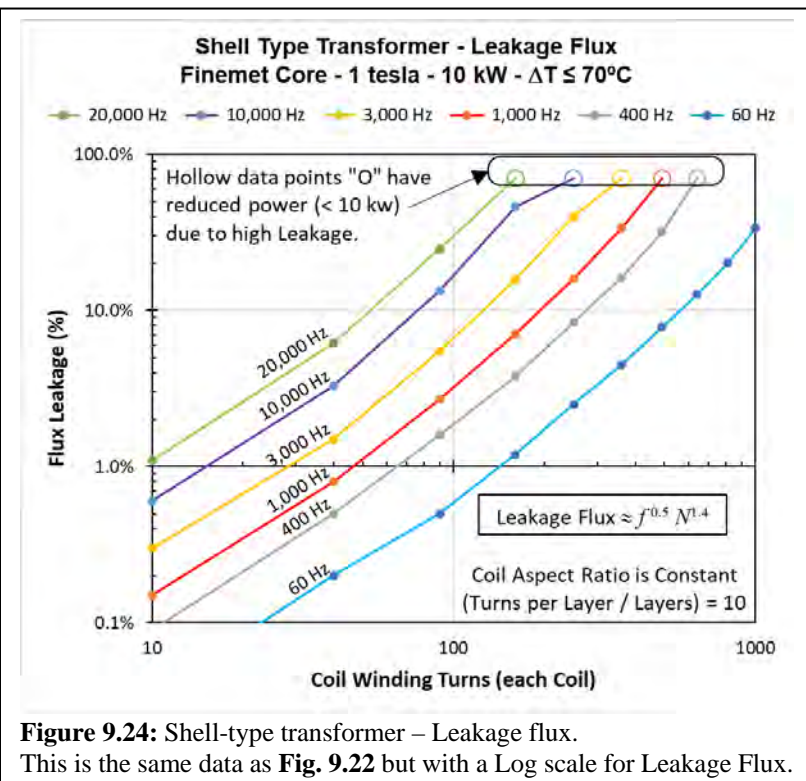


Figure 9.24: Shell-type transformer – Leakage flux.
 This is the same data as **Fig. 9.22** but with a Log scale for Leakage Flux.

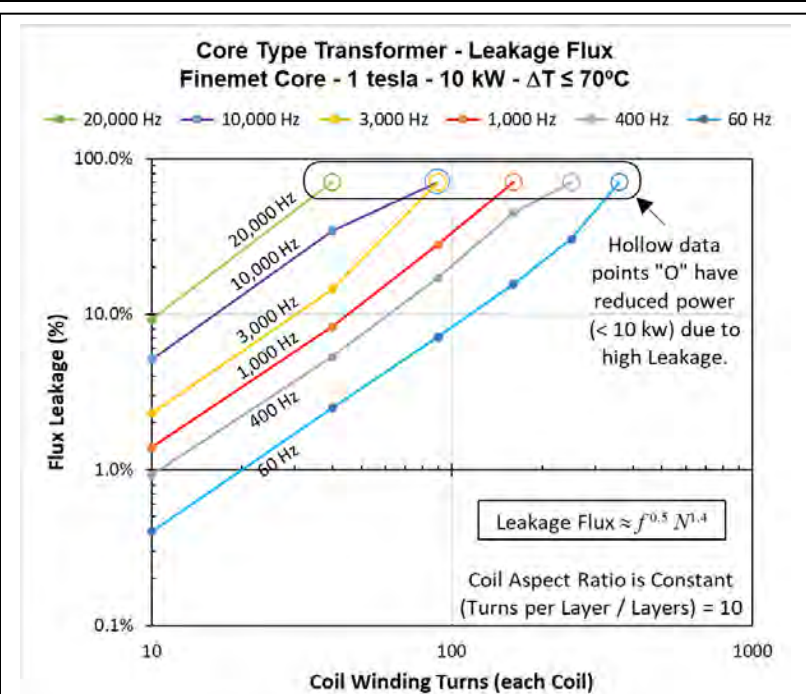


Figure 9.25: Core-type transformer – Leakage flux.
 This is the same data as **Fig. 9.23** but with a Log scale for Leakage Flux..
 Core-type transformers have more leakage than shell-type transformers.

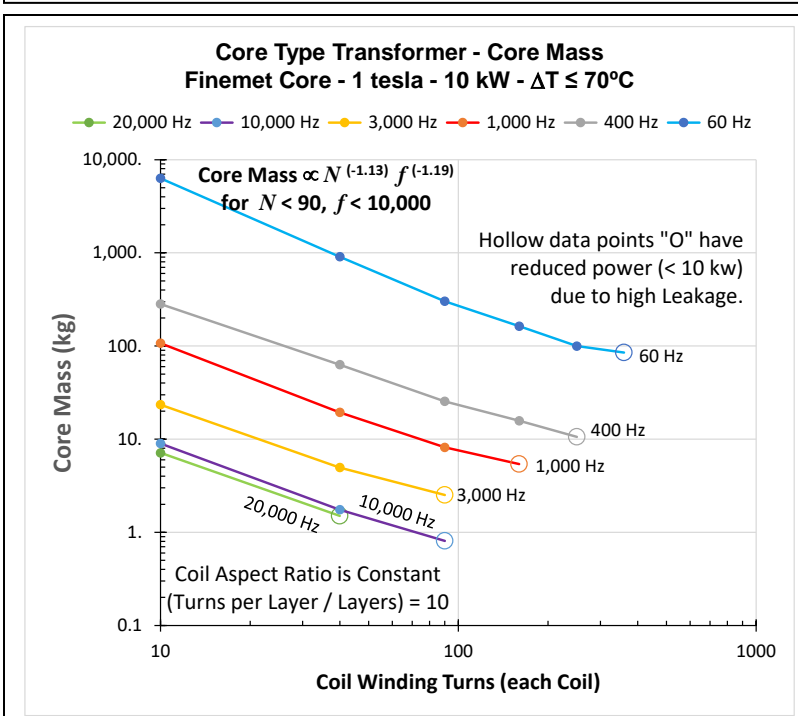
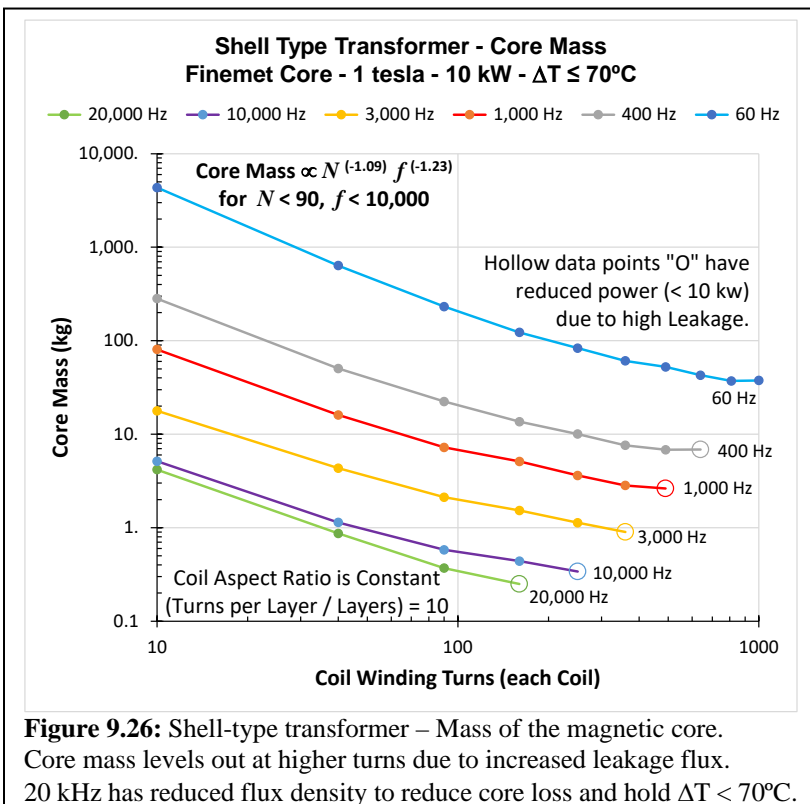


Figure 9.27: Core-type transformer – Mass of the magnetic core. 20 kHz has reduced flux density to reduce core loss and hold $\Delta T < 70^\circ\text{C}$.

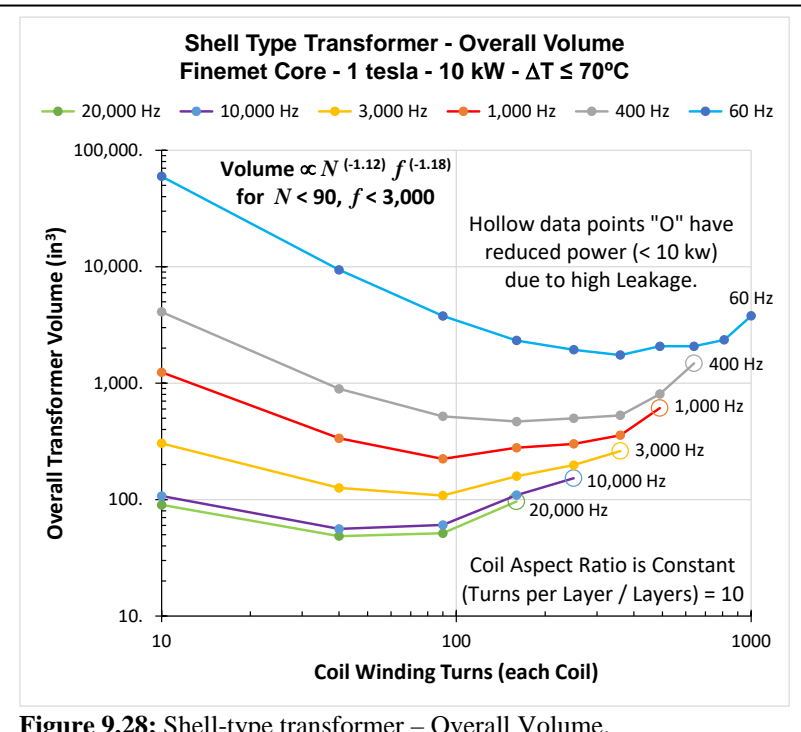


Figure 9.28: Shell-type transformer – Overall Volume.
Core volume levels out at higher turns due to increased Leakage Flux.
20 kHz has reduced flux density to reduce core loss and hold $\Delta T < 70^\circ\text{C}$.

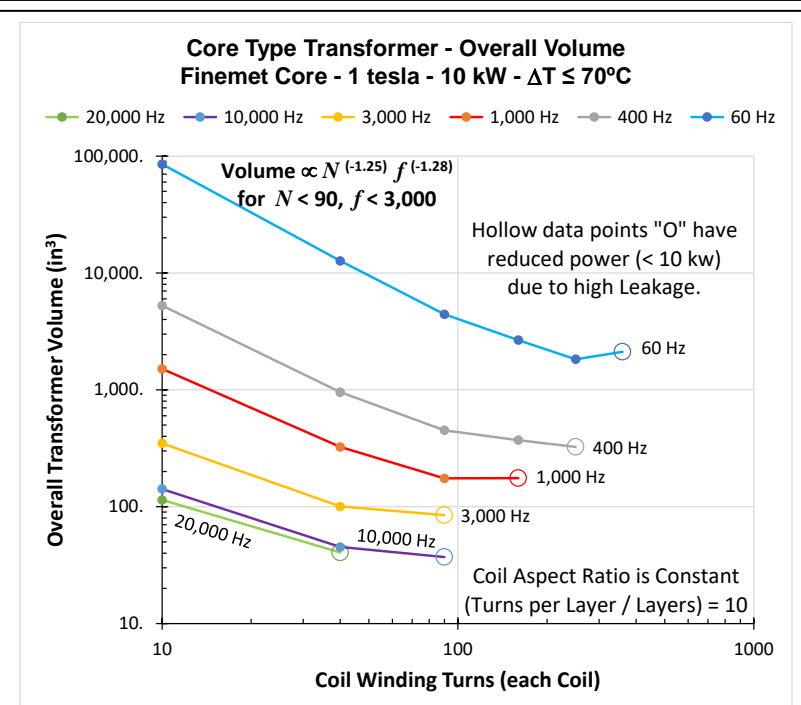


Figure 9.29: Core-type transformer – Overall Volume.
20 kHz has reduced flux density to reduce core loss and hold $\Delta T < 70^\circ\text{C}$.

g. Example-9 – Inductor Design

This inductor design example is based on a toroidal core geometry with a rectangular core cross-section, such as shown in **Fig. 9.30**.

The main objective for designing an inductor is to achieve the desired inductance at the maximum current without exceeding the core saturation flux density (note that some inductor requirements allow a lower inductance at the peak current). Additional goals include minimizing the weight and size, and operating at an acceptable temperature rise (such as the limits for the core material and wire insulation). These last two goals are typically in opposition, where a smaller size usually results in a higher temperature rise.

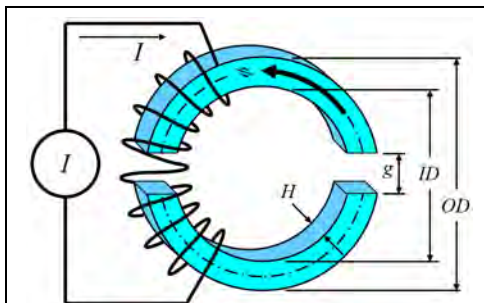


Figure 9.30: Toroidal core geometry with an air gap (g).

This design example is for a high frequency (10 kHz) inductor (50 μH) at a current of 100 amperes-pk. The high frequency is typical for variable frequency motor drives and power conversion systems (DC-DC, DC-AC) where the high frequency also reduces the size of the transformer (**Fig. 9.29**).

The maximum current density (J) of long wires (listed in UL or IEC standards) is given in **Eq. 4.5**. The initial wire size for a transformer or inductor can be estimated with **Eq. 4.4** based on a current density of 1,000 A/in^2 to 3,000 A/in^2 , or higher with good cooling.

$$a_{w-\min} = \frac{100}{3000} = 0.0333 \frac{\text{ampere}}{\text{inch}^2} \quad (9.66)$$

$$d_{B-\min} = \sqrt{\frac{4}{\pi} a_w} = \sqrt{\frac{4}{\pi} 0.0333} = 0.206 \text{ inch} \quad (9.67)$$

$$\text{AWG} = \frac{\ln(d_B/0.325)}{\ln(1.123)} = \frac{\ln(0.206/0.325)}{\ln(1.123)} = 3.93 \approx \boxed{4 \text{ AWG}} \quad (9.68)$$

$$d_B = 0.008255(1.123^{-4}) = 0.00519 \text{ m} \quad \text{From Eq. 4.3} \quad (9.69)$$

$$a_w = \frac{\pi}{4} 0.00519^2 = 2.12E-5 \text{ m}^2 \quad (9.70)$$

The bare wire diameter (d_B) for a solid 4 AWG wire is 5.19 mm (**Eq. 9.69**). The initial magnetic core selection is Kool Mu (Fe-Si-Al powder, $B_{sat} = 1 \text{ T}$) part number 77339A7, which has the following dimensions and properties.

Outside Diameter (OD)	= 134 mm	= 0.134 m
Inside Diameter (ID)	= 77.2 mm	= 0.0772 m
Height (H)	= 26.8 mm	= 0.0268 m

Relative Permeability (μ_r)	= 60
Core Cross Section (a_e)	= 678 mm ² = 6.78E-4 m ²
Core Flux Path Length (l_e)	= 324 mm = 0.324 m
Core Winding Window (W_a)	= 4710 mm ² = 4.71E-3 m ²
Core Mass (M_c)	= 1.20 kg

Eq. 9.24 can be used with the characteristics of the selected core and the desired peak current (I_1) to determine the maximum number of turns ($N_{1\text{-max}}$) to produce the saturation flux density (B_{sat}) and the number of turns (N_1) to achieve the desired inductance (L_1). Also, **Eq. 9.24** can be used to determine the operating inductance (L_1) and flux density (B), as follows.

$$N_{1\text{-max}} = \frac{B_{sat} l_e}{\mu_r \mu_0 I_1} = \frac{(1)(0.324)}{(60)(4\pi E - 7)(100)} = 42.9 \quad [N_1 < 42 \text{ turns}] \quad (9.71)$$

$$N_1 = \sqrt{\frac{L_1 l_e}{\mu_r \mu_0 a_e}} = \sqrt{\frac{(50E - 6)(0.324)}{(60)(4\pi E - 7)(6.78E - 4)}} = 17.8 \approx [18 \text{ turns}] \quad (9.72)$$

$$L_1 = N_1^2 \mu_r \mu_0 \frac{a_e}{l_e} = 18^2 (60)(4\pi E - 7) \frac{6.78E - 4}{0.324} = [51.1 \mu\text{H}] \quad (9.73)$$

$$B = \mu_r \mu_0 \frac{N_1 I_1}{l_e} = (60)(4\pi E - 7) \frac{(18)(100)}{(0.324)} = [0.419 \text{ T-peak}] \quad (9.74)$$

These calculations show that this inductor can be produced with the selected core without a gap (g) because the inductance can be achieved with 18 turns, which is fewer turns than is needed to saturate the core (42 turns). With 18 turns, the inductance is 51.1 μH and the maximum flux density is 0.419 T.

The high frequency of 10 kHz will require the use of Litz wire to minimize the winding resistance due to the skin effect and proximity effect. The 4 AWG Litz wire available from New England Wire for 10 kHz excitation has 850 insulated strands of 33 AWG wire. The overall diameter (d_i) of the Litz cable is 0.302 inches ($d_i = 0.00767 \text{ m}$). The total wire length (l_w) and the total winding area (W_w) can be calculated as follows.

$$l_w = N_1 \left(2(H + 2d_i) + 2 \left(\frac{OD - ID}{2} + 2d_i \right) \right) = 3.09 \text{ m} \quad (9.75)$$

$$W_w = N_1 d_i^2 = 18(0.00767^2) = 1.06E - 3 \text{ m}^2 \quad (9.76)$$

$$\frac{W_w}{W_a} = \frac{1.06E - 3}{4.71E - 3} = 0.22 \quad (9.77)$$

The 18 turns of 4 AWG Litz wire uses only 22% of the core winding area (**Eq. 9.77**). This verifies that the winding can be produced. It is difficult to produce a winding that uses more than 70% of the core winding area.

The winding mass (M_w) and DC resistance (R_{DC}) can be calculated from the wire length (l_w) and area (a_w), as follows. The density of copper is 8940 kg/m³ and the conductivity of copper is 5.80E+7 s/m.

$$M_w = \rho_{cu} a_w l_w = (8940)(2.12E-5)(3.09) = \boxed{0.585 \text{ kg}} \quad (9.78)$$

$$R_{DC} = \frac{l_w}{\sigma_{cu} a_w} = \frac{3.09}{(5.80E+7)(2.12E-5)} = \boxed{0.00251 \text{ ohm}} \quad (9.79)$$

The 10 kHz Litz wire resistance can be calculated from the correlations in Jimenez [26] and Barrios [27], which account for skin effect and proximity effect. The 10 kHz resistance multiplier for 4 AWG solid wire is 8.64, and it is 1.03 for 4 AWG Litz wire. This is based on a single winding layer.

$$R_{10kHz} = 1.03(0.00251) = \boxed{0.00259 \text{ ohm}} \quad \text{Resistance at 10 kHz} \quad (9.80)$$

The overall inductor dimensions (over the windings) (OD_I , ID_I , h_I) and the overall inductor surface area (A_I) are based on a single winding layer.

$$OD_I = OD + 2d_i = 0.134 + 2(0.00767) = 0.149 \text{ m} \quad (9.81)$$

$$ID_I = ID - 2d_i = 0.0772 - 2(0.00767) = 0.0619 \text{ m} \quad (9.82)$$

$$H_I = H + 2d_i = 0.0268 + 2(0.00767) = 0.0421 \text{ m} \quad (9.83)$$

$$A_I = 2 \frac{\pi}{4} (OD_I^2 - ID_I^2) + \pi (OD_I + ID_I) H_I = 0.0570 \text{ m}^2 \quad (9.84)$$

The core loss for the Kool Mu 60u material can be calculated from the Steinmetz coefficients listed in **Appendix-G**, based on the frequency (10 kHz), and the peak flux density ($B = 0.419 \text{ T}$), as follows.

$$P_c \left(\frac{\text{W}}{\text{kg}} \right) = k f(\text{Hz})^a B(\text{T})^b \quad \text{Steinmetz core loss Eq.} \quad (9.85)$$

$$k = 1.049E-2 \quad a = 1.103 \quad b = 1.771$$

$$P_c = (1.0492E-2)(10,000)^{1.103} (0.419)^{1.771} = 58.0 \frac{\text{W}}{\text{kg}} \quad (9.86)$$

The 10 kHz heat dissipation in the winding is calculated from the current and the winding resistance, the heat dissipation in the core is calculated from the core loss and core mass. The estimated steady-state temperature rise is calculated from the total heat dissipation, the overall surface area (A_I), and the total heat transfer coefficient (h) (**Ch. 5.a**).

$$Q_w = \frac{I_1^2 R_{10kHz}}{2} = \frac{100^2 (0.00259)}{2} = 12.95 \text{ W} \quad \text{Winding heat} \quad (9.87)$$

$$Q_c = P_c M_c = 58(1.2) = 69.6 \text{ W} \quad \text{Core Heat} \quad (9.88)$$

$$\Delta T = \frac{Q}{hA_I} = \frac{12.95 + 69.6}{10(0.057)} = 145 \text{ }^\circ\text{C} \quad \text{Still air} \quad (9.89)$$

$$\Delta T = \frac{Q}{hA_I} = \frac{12.95 + 69.6}{30(0.057)} = 48.3 \text{ }^\circ\text{C} \quad \text{Fan forced air} \quad (9.90)$$

The 20 kHz Litz wire resistance can be calculated from the correlations in Jimenez [26] and Barrios [27], which account for skin effect and proximity effect. The 20 kHz resistance multiplier for 4 AWG solid wire is 12.2, and it is 1.12 for 4 AWG Litz wire. This is based on a single winding layer.

$$R_{20kHz} = 1.12(0.00251) = \boxed{0.00282 \text{ ohm}} \quad \text{Resistance at 20 kHz} \quad (9.91)$$

The core loss for the Kool Mu 60u material at $f=20$ kHz, and at $B=0.419$ T, is calculated as follows.

$$P_c \left(\frac{\text{W}}{\text{kg}} \right) = k f(\text{Hz})^a B(\text{T})^b \quad \text{Steinmetz core loss Eq.} \quad (9.92)$$

$$k = 1.049E-2 \quad a = 1.103 \quad b = 1.771$$

$$P_c = (1.0492E-2)(20,000)^{1.103} (0.419)^{1.771} = 124.6 \frac{\text{W}}{\text{kg}} \quad (9.93)$$

The 20 kHz heat dissipation in the winding is calculated from the current and the winding resistance, the heat dissipation in the core is calculated from the core loss and core mass. The estimated steady-state temperature rise is calculated from the total heat dissipation, the overall surface area (A_I), and the total heat transfer coefficient (h) (Ch. 5.a).

$$Q_w = \frac{I_1^2 R_{20kHz}}{2} = \frac{100^2 (0.00282)}{2} = 14.12 \text{ W} \quad \text{Winding heat} \quad (9.94)$$

$$Q_c = P_c M_c = 124.6(1.2) = 149.59 \text{ W} \quad \text{Core Heat} \quad (9.95)$$

$$\Delta T = \frac{Q}{hA_I} = \frac{14.12 + 149.59}{10(0.057)} = 287.3 \text{ } ^\circ\text{C} \quad \text{Still air} \quad (9.96)$$

$$\Delta T = \frac{Q}{hA_I} = \frac{14.12 + 149.59}{30(0.057)} = 95.8 \text{ } ^\circ\text{C} \quad \text{Fan forced air} \quad (9.97)$$

All of these calculations for a Kool Mu core are summarized in **column-1** of the table shown in **Fig. 9.31**. Additional Kool Mu calculation results are listed in columns-2, 3, 4, and 5. The trends shown in the table are as follows.

1. Reducing the core size (OD and cross-section) or Increasing the core permeability (μ_r):
 - a. Decreases the total Mass (M-tot)
 - b. Increases the Flux Density (B)
 - c. Increases the Core Loss (Qc)
 - d. Increases the Temperature Rise (ΔT)
2. Increasing the Frequency (f):
 - a. Increases the Core Loss (Qc)
 - b. Increases the Temperature Rise (ΔT)

		1	2	3	4	5	6	7
Current Inductance	A-pk μH	100 50	100 50	100 50	100 50	100 50	100 50	100 50
Core Properties & Size								
Core Material	Kool Mu	Kool Mu	Kool Mu	Kool Mu	Kool Mu	Finemet	Finemet	
Core Part Number	77339A7	77337A7	77098A7	77099A7	77100A7	---	---	
μ_r	---	60	26	125	60	40	26,500	26,500
Bsat	T	1	1	1	1	1	1	1
OD	mm	134.0	134.0	103.0	103.0	103.0	65.0	80.0
ID	mm	77.2	77.2	55.8	55.8	55.8	40.0	50.0
H	mm	26.8	26.8	17.9	17.9	17.9	30.0	15.0
M _c	kg	1.20	1.20	0.47	0.45	0.47	0.45	0.34
Gap	mm	0	0	0	0	0	1.25	2.5
$\mu_r\text{-eff}$	---	60	26	125	60	40	91.3	69.4
B	T-pk	0.42	0.27	0.97	0.65	0.54	0.97	0.98
Winding								
Litz.	AWG	4	4	4	4	4	4	4
N	turns	18	27	15	21	26	14	23
M _w	kg	0.58	0.88	0.41	0.61	0.80	0.41	0.61
Overall Mass & Size								
M-tot	kg	1.78	2.08	0.88	1.06	1.27	0.86	0.94
Vol-tot	cm ³	940.5	940.5	572.8	572.8	572.9	341.7	345.5
f = 10 kHz - Heat & Temperature Rise								
Q _w	w	13.0	19.5	9.1	14.6	19.3	9.9	14.6
Q _c	w	69.6	35.1	191.3	57.1	45.3	7.5	5.7
Q _{tot}	w	82.6	54.5	200.4	71.7	64.5	17.4	20.3
ΔT still	°C	145.0	95.7	556.4	181.8	163.5	69.7	74.2
ΔT fan	°C	48.3	31.9	185.5	60.6	54.5	23.2	24.7
f = 20 kHz - Heat & Temperature Rise								
Q _w	w	14.1	21.2	9.9	19.1	25.1	12.9	19.1
Q _c	w	149.6	70.7	406.0	122.7	91.3	25.3	19.1
Q _{tot}	w	163.7	91.9	415.9	141.7	116.4	38.1	38.2
ΔT still	°C	287.3	161.2	1154.9	359.3	295.1	152.9	139.5
ΔT fan	°C	95.8	53.7	385.0	119.8	98.4	51.0	46.5

Figure 9.31: Inductor design calculations with various toroidal cores of Kool Mu material (columns-1, 2, 3, 4, 5) and Finemet (columns-6, 7) with a Litz wire winding at 10 kHz and 20 kHz. The RED colored cells indicate a temperature rise exceeding 75°C. The calculations for **column-1** (Kool Mu) are shown above. The calculations for **column-6** (Finemet) are shown below.

Calculations for a Finemet nano-crystalline core (Fe-Si-B-Cu-Nb alloy, 17 μm thick, $B_{sat} = 1 \text{ T}$) can be done in the same way as for the Kool Mu cores. However, the relative permeability of Finemet is very high ($\mu_r = 26,500$). The maximum core relative permeability that will prevent saturation can be calculated from Eq. 9.24, as follows.

$$OD = 65 \text{ mm} \quad ID = 40 \text{ mm} \quad H = 30 \text{ mm} \quad \text{Core size} \quad (9.98)$$

$$l_e = \pi \frac{65 + 40}{2} = 164.9 \text{ mm} = 0.1649 \text{ m} \quad (9.99)$$

$$a_e = \frac{65 - 40}{2} 30 = 375 \text{ mm}^2 = 3.75E - 4 \text{ m}^2 \quad (9.100)$$

$$\mu_r < \frac{B_{sat}^2 l_e a_e}{\mu_0 L_1 I_1^2} = \frac{(1^2)(0.1649)(3.75E - 4)}{(4\pi E - 7)(50E - 6)(100^2)} = 98.4 \quad \text{Max. } \mu_r \quad (9.101)$$

The relative permeability of a Finemet core can be reduced by cutting the core and inserting a non-magnetic insulator to produce a permanent air gap (g) (**Fig. 9.30**). The permeance across the air gap (\mathcal{P}_g) can be calculated as shown in **Ch. 1.g**. The permeances \mathcal{P}_6 , \mathcal{P}_7 , \mathcal{P}_8 , \mathcal{P}_9 , are small and not calculated for simplification.

$$g = 1.25 \text{ mm} = 0.00125 \text{ m} \quad \text{Air Gap thickness} \quad (9.102)$$

$$w = OD - ID + 2H = 65 - 40 + 2(30) = 85 \text{ mm} = 0.085 \text{ m} \quad (9.103)$$

$$h = \frac{w}{4} = 21.25 \text{ mm} = 0.02125 \text{ m} \quad (9.104)$$

$$\mathcal{P}_1 = \mu_0 \frac{a_e}{g} = 4\pi E - 7 \frac{3.75E - 4}{1.25E - 3} = 3.77E - 7 \frac{\text{Wb}}{\text{NI}} \quad (9.105)$$

$$\mathcal{P}_2 = 0.24 \mu_0 w = 0.24(4\pi E - 7)(0.085) = 2.56E - 8 \frac{\text{Wb}}{\text{NI}} \quad (9.106)$$

$$\mathcal{P}_4 = \mu_0 \frac{w}{\pi} \ln \left(1 + 2 \frac{h}{g} \right) \quad (9.107)$$

$$\mathcal{P}_4 = 4\pi E - 7 \frac{0.085}{\pi} \ln \left(1 + 2 \frac{0.02125}{0.00125} \right) = 1.21E - 7 \frac{\text{Wb}}{\text{NI}} \quad (9.108)$$

$$\mathcal{P}_g = \mathcal{P}_1 + \mathcal{P}_2 + \mathcal{P}_4 = 5.24E - 7 \frac{\text{Wb}}{\text{NI}} \quad \text{Air Gap permeance} \quad (9.109)$$

$$\mathcal{R}_g = \frac{1}{\mathcal{P}_g} = 1.91E + 6 \frac{\text{NI}}{\text{Wb}} \quad \text{Air Gap reluctance} \quad (9.110)$$

The total reluctance of the core (\mathcal{R}_{tot}) and the effective permeability of the core (μ_{r-eff}) can be calculated as follows.

$$\mathcal{P}_c = \mu_r \mu_0 \frac{a_e}{l_e} = 26500(4\pi E - 7) \frac{3.75E - 4}{0.1649} = 7.57E - 5 \frac{\text{Wb}}{\text{NI}} \quad (9.111)$$

$$\mathcal{R}_c = \frac{1}{\mathcal{P}_c} = 1.32E + 4 \frac{\text{NI}}{\text{Wb}} \quad \text{Core reluctance with no gap} \quad (9.112)$$

$$\mathcal{R}_{tot} = \mathcal{R}_c + 2\mathcal{R}_g = 3.83E + 6 \frac{\text{NI}}{\text{Wb}} \quad \text{Core reluctance with 2 gaps} \quad (9.113)$$

$$\mu_{r-eff} = \frac{l_e}{\mathcal{R}_{tot} \mu_0 a_e} = \frac{0.1649}{(3.83E + 6)(4\pi E - 7)(3.75E - 4)} = 91.3 \quad (9.114)$$

Two methods can be used to achieve a low relative permeability.

1. The first method, as discussed above, involves the cutting and gapping of the core. Cutting a Finemet core has the following issues.
 - a. The very thin Finemet layers must be contained. This can be done mechanically or by infusing the core with epoxy.
 - b. The cut ends of the very thin Finemet layers tend to have small burs that make electrical contact with the next layer. This makes a good path for eddy currents and significantly increases the core loss at the cut. This can be minimized by acid etching the cut Finemet surfaces.
 - c. The fringing flux interacts with the winding to produce additional eddy current losses.
2. The second method uses an uncut core with a low relative permeability.
 - a. Aronhime *et al.* [44] shows that strain annealing offers an effective method for tuning the permeability of Fe-Ni-based metal amorphous nanocomposite (MANC) alloys. The permeability increased from 4,000 to 16,000 for an Fe-rich alloy and decreased from 290 to 40 for a Ni-rich alloy.
 - b. Byerly *et al.* [45] shows that in-line strain annealing can achieve relative permeabilities in the range of 10 to 10,000 for the MANC alloy $\text{Co}_{80-x-y}\text{Fe}_x\text{Mn}_y\text{Nb}_4\text{Si}_2\text{B}_{14}$, depending on the x and y values.

The calculations (**Eq. 9.115 - Eq. 9.119**) show that a uniform magnetic flux density throughout this core can be achieved if the effective relative permeability varies from 69.6 at the core ID to 113.1 at the core OD.

Byerly *et al.* achieved a graded relative permeability inductor core with a variation of 27.8 at the ID and 44.5 at the OD (the desired ideal variation was 22.7 to 54.0). This was achieved experimentally by linearly increasing the tension during the strain annealing process. The resulting inductor performance testing showed reduced core loss and a more uniform temperature profile with a reduced peak temperature at the inner core diameter.

- c. This method of tuning the permeability by varying the strain annealing process and achieving a graded permeability magnetic core is also described in US patent 10,168,392.
- d. Alex Leary at NASA Glenn Research Center provided core loss data for a new cobalt-rich strain annealed MANC alloy with a relative permeability of $\mu_r = 41$, designated GRC133 and listed on line 24 in **Appendix-G**. It's a variation of the material in Byerly's 2018 paper [45] and uses a new process described in a patent filed in July 2020.

The range for the effective relative permeability ($69.6 < \mu_{r\text{-eff}} < 113.1$), from the ID to the OD, can be calculated as follows.

$$\mu_{r\text{-eff}} = \frac{l}{\mathcal{R}_{\text{tot}} \mu_0 a_e} \quad \text{Effective permeability from Eq. 9.111} \quad (9.115)$$

$$l_{\min} = 40\pi = 125.7 \text{ mm} = 0.1257 \text{ m} \quad \text{Flux path length at ID} \quad (9.116)$$

$$l_{\max} = 65\pi = 204.2 \text{ mm} = 0.2042 \text{ m} \quad \text{Flux path length at OD} \quad (9.117)$$

$$\mu_{r\text{-eff-min}} = \frac{l_{\min}}{\mathcal{R}_{\text{tot}} \mu_0 a_e} = \frac{0.1257}{(3.83E+6)(4\pi E-7)(3.75E-4)} = 69.6 \quad (9.118)$$

$$\mu_{r\text{-eff-max}} = \frac{l_{\max}}{\mathcal{R}_{\text{tot}} \mu_0 a_e} = \frac{0.2042}{(3.83E+6)(4\pi E-7)(3.75E-4)} = 113.1 \quad (9.119)$$

The number of turns (N_1), the inductance (L_1), and the peak flux density (B) can be calculated as follows.

$$N_1 = \sqrt{\frac{L_1 l_e}{\mu_r \mu_0 a_e}} = \sqrt{\frac{(50E-6)(0.1649)}{(91.3)(4\pi E-7)(3.75E-4)}} = 13.8 \approx [14 \text{ turns}] \quad (9.120)$$

$$L_1 = N_1^2 \mu_r \mu_0 \frac{a_e}{l_e} = 14^2 (91.3)(4\pi E-7) \frac{3.75E-4}{0.1649} = [51.1 \text{ } \mu\text{H}] \quad (9.121)$$

$$B = \mu_r \mu_0 \frac{N_1 I_1}{l_e} = (91.3)(4\pi E-7) \frac{(14)(100)}{(0.1649)} = [0.974 \text{ T-peak}] \quad (9.122)$$

The overall diameter (d_i) of the Litz cable is $d_i = 0.00767 \text{ m}$. The total wire length (l_w) and the total winding area (W_w) can be calculated as follows.

$$l_w = N_1 \left(2(H + 2d_i) + 2 \left(\frac{OD - ID}{2} + 2d_i \right) \right) = 2.17 \text{ m} \quad (9.123)$$

$$W_w = N_1 d_i^2 = 14(0.00767^2) = 8.24E-4 \text{ m}^2 \quad (9.124)$$

$$\frac{W_w}{W_a} = \frac{8.24E-4}{(\pi/4)0.04^2} = 0.66 \quad (9.125)$$

The 14 turns of 4 AWG Litz wire uses only 66% of the core winding area (Eq. 9.125). This verifies that the winding can be produced. It is difficult to produce a winding that uses more than 70% of the core winding area.

The winding mass (M_w) and DC resistance (R_{DC}) can be calculated from the wire length (l_w) and area (a_w), as follows. The density of copper is 8940 kg/m^3 and the conductivity of copper is $5.80E+7 \text{ s/m}$.

$$M_w = \rho_{cu} a_w l_w = (8940)(2.12E-5)(2.17) = [0.411 \text{ kg}] \quad (9.126)$$

$$R_{DC} = \frac{l_w}{\sigma_{cu} a_w} = \frac{2.17}{(5.80E+7)(2.12E-5)} = [0.00177 \text{ ohm}] \quad (9.127)$$

The Litz wire resistance at 10 kHz can be calculated from the correlations in Jimenez [26] and Barrios [27], which account for skin effect and proximity effect. The 10 kHz resistance multiplier for 4 AWG solid wire is 57.3, and it is 1.11 for 4 AWG Litz wire. This is based on two winding layers inside the core ID.

$$R_{10kHz} = 1.11(0.00177) = \boxed{0.00197 \text{ ohm}} \quad \text{Resistance at 10 kHz} \quad (9.128)$$

The overall inductor dimensions (over the windings) (OD_I , ID_I , h_I) and the overall inductor surface area (A_I) are calculated as follows. Note that there are 2 winding layers inside the core ID, therefore **Eq. 9.130** reduces ID_I by 4 Litz wire diameters (d_i). Also, there is only one winding layer on the core OD, therefore **Eq. 9.131** increases H_I by 3 Litz wire diameters (d_i) - the average of 1 turn above and below the core (2 Litz wires) at the OD, and 2 turns above and below the core (4 Litz wires) at the ID.

$$OD_I = OD + 2d_i = 0.065 + 2(0.00767) = 0.0803 \text{ m} \quad (9.129)$$

$$ID_I = ID - 4d_i = 0.040 - 4(0.00767) = 0.0093 \text{ m} \quad (9.130)$$

$$H_I = H + 3d_i = 0.030 + 3(0.00767) = 0.053 \text{ m} \quad (9.131)$$

$$A_I = 2\frac{\pi}{4}(OD_I^2 - ID_I^2) + \pi(OD_I + ID_I)H_I = 0.0249 \text{ m}^2 \quad (9.132)$$

The core loss for the Finemet material can be calculated from the Steinmetz coefficients listed in **Appendix-G**, from the frequency (10 kHz), and the peak flux density ($B = 0.974$ T). The core mass (M_c) is calculated from the density of Finemet (7300 kg/m³).

$$P_c \left(\frac{\text{W}}{\text{kg}} \right) = k f(\text{Hz})^a B(\text{T})^b \quad \text{Steinmetz core loss Eq.} \quad (9.133)$$

$$k = 1.814E-6 \quad a = 1.747 \quad b = 2.088$$

$$P_c = (1.814E-6)(10,000)^{1.747} (0.974)^{2.088} = 16.7 \frac{\text{W}}{\text{kg}} \quad (9.134)$$

$$M_c = \rho_c l_e a_e = (7300)(0.1649)(3.75E-4) = 0.452 \text{ kg} \quad (9.135)$$

The 10 kHz heat dissipation in the winding is calculated from the current and the winding resistance, the heat dissipation in the core is calculated from the core loss and core mass. The estimated steady-state temperature rise is calculated from the total heat dissipation, the overall surface area (A_I), and the total heat transfer coefficient (h) (**Ch. 5.a**).

$$Q_w = \frac{I_1^2 R_{10kHz}}{2} = \frac{100^2 (0.00197)}{2} = 9.85 \text{ W} \quad \text{Winding heat} \quad (9.136)$$

$$Q_c = P_c M_c = 16.7(0.452) = 7.52 \text{ W} \quad \text{Core Heat} \quad (9.137)$$

$$\Delta T = \frac{Q}{hA_I} = \frac{9.85 + 7.52}{10(0.0249)} = 69.7 \text{ }^\circ\text{C} \quad \text{Still air} \quad (9.138)$$

$$\Delta T = \frac{Q}{hA_I} = \frac{9.85 + 7.52}{30(0.0249)} = 23.2 \text{ } ^\circ\text{C} \quad \text{Fan forced air} \quad (9.139)$$

The Litz wire resistance at 20 kHz can be calculated from the correlations in Jimenez [26] and Barrios [27], which account for skin effect and proximity effect. The 20 kHz resistance multiplier for 4 AWG solid wire is 81.1, and it is 1.45 for 4 AWG Litz wire. This is based on two winding layers inside the core ID.

$$R_{20kHz} = 1.45(0.00177) = \boxed{0.00257 \text{ ohm}} \quad \text{Resistance at 20 kHz} \quad (9.140)$$

The core loss for the Finemet material at $f=20$ kHz, and $B=0.974$ T, is calculated as follows.

$$P_c \left(\frac{\text{W}}{\text{kg}} \right) = k f(\text{Hz})^a B(\text{T})^b \quad \text{Steinmetz core loss Eq.} \quad (9.141)$$

$$k = 1.814E-6 \quad a = 1.747 \quad b = 2.088$$

$$P_c = (1.814E-6)(20,000)^{1.747} (0.974)^{2.088} = 55.9 \frac{\text{W}}{\text{kg}} \quad (9.142)$$

The 20 kHz heat dissipation in the winding is calculated from the current and the winding resistance, the heat dissipation in the core is calculated from the core loss and core mass. The estimated steady-state temperature rise is calculated from the total heat dissipation, the overall surface area (A_I), and the total heat transfer coefficient (h) (**Ch. 5.a**).

$$Q_w = \frac{I_1^2 R_{20kHz}}{2} = \frac{100^2 (0.00257)}{2} = 12.86 \text{ w} \quad \text{Winding heat} \quad (9.143)$$

$$Q_c = P_c M_c = 55.9(0.452) = 25.26 \text{ w} \quad \text{Core Heat} \quad (9.144)$$

$$\Delta T = \frac{Q}{hA_I} = \frac{12.86 + 25.26}{10(0.0249)} = 152.9 \text{ } ^\circ\text{C} \quad \text{Still air} \quad (9.145)$$

$$\Delta T = \frac{Q}{hA_I} = \frac{12.86 + 25.26}{30(0.0249)} = 51.0 \text{ } ^\circ\text{C} \quad \text{Fan forced air} \quad (9.146)$$

All of these calculations with a Finemet core are summarized in **column-6** of the table shown in **Fig. 9.31**. Additional calculation results are listed in **column-7**. The trends for a Kool Mu core (listed preceding **Fig. 9.31**) also apply for the Finemet core designs. The core loss of the Finemet core is much lower than the Kool Mu core material. Therefore, the Finemet core material provides a smaller and much lower temperature inductor design than the Kool Mu core material.

10. BH Curve Measurement

Commercial test equipment is available that can measure the *BH* hysteresis loop in DC and AC excitation. The AC hysteresis loop is measured in the same way as the DC hysteresis loop, but the AC test induces additional losses due to eddy currents. Therefore, the AC hysteresis loop is wider than the DC loop. In both cases, the current is swept to a positive maximum and negative maximum several times. The DC sweep rate is very slow (such as 0.10 Hz). Many of the companies that make the test equipment also offer testing services.

Measuring the *BH* hysteresis curve can be very helpful in identifying magnetic materials issues that cause poor performance in products coming through manufacturing (such as low permeability, low saturation flux density, high coercivity, or high core loss). Also, using the measured magnetic properties rather than the datasheet properties in FEA simulations can result in significant improvements in the accuracy of the calculated performance.

This chapter covers the basics of *BH* curve measurement which can be done quickly with the power supplies and oscilloscopes that are available in most engineering labs. A DC *BH* curve can be produced by adjusting a DC power supply output by hand to produce a slow sweep of the current. As a practical matter, the accuracy of the *BH* curve and core loss data from these methods can be used to quickly identify issues with materials in manufacturing, to evaluate the effects from manufacturing processes, and to define the properties for input to simulations.

a. Basic Test Characteristics

The objective is to measure the magnetic properties including the magnetic permeability, the saturation magnetic flux density, coercivity, and the core loss. This can be done very easily with a circular or rectangular core and one or two windings. The basic configuration of the test setup is an inductor with a single coil or a transformer with two coils, as shown in **Fig. 10.1**.

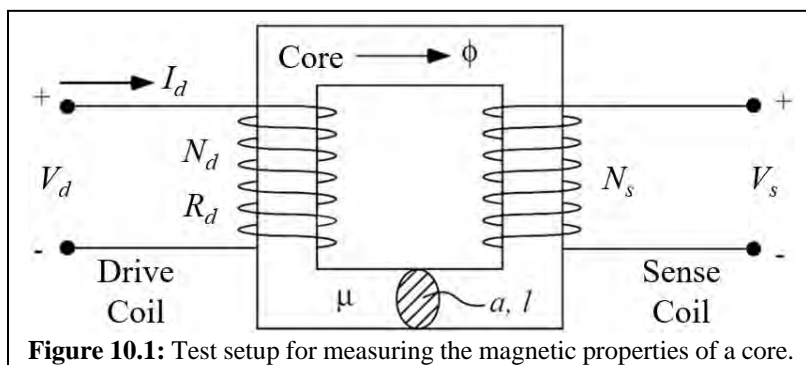


Figure 10.1: Test setup for measuring the magnetic properties of a core.

The drive coil has turns (N_d) and resistance (R_d), and carries the drive voltage (V_d) and drive current (I_d) from the power supply. The sense coil has turns (N_s) and produces an open circuit voltage (V_s), and it carries no current. The core dimensions include the cross-sectional area (a) and the average perimeter or average length of the flux path (l).

The system equations are as follows.

$$V_d = I_d R_d + \frac{d(N_d \phi)}{dt} = I_d R_d + N_d a \frac{dB}{dt} \quad \text{Drive coil} \quad (10.1)$$

$$V_s = \frac{d(N_s \phi)}{dt} = N_s a \frac{dB}{dt} \quad \text{Sense coil} \quad (10.2)$$

The magnetic field intensity (H) can be defined from the drive coil current (I_d), and the magnetic flux density (B) can be defined from the sense coil voltage (V_s).

$$H = \frac{N_d I_d}{l} \quad \text{Magnetic field intensity from drive coil} \quad (10.3)$$

$$B = \frac{1}{N_s a} \int V_s dt \quad \text{Magnetic flux density from sense coil} \quad (10.4)$$

Also, from **Eq. 10.1**, both the magnetic field intensity (H) and the magnetic flux density (B) can be obtained from the drive coil, as follows. A sense coil is not strictly required.

$$B = \frac{1}{N_d a} \int (V_d - I_d R_d) dt \quad \text{Magnetic flux density from drive coil} \quad (10.5)$$

The benefits of a sense coil (an open secondary) is that it can have more turns than the drive coil, which gives more voltage and more accuracy (increased signal/noise). It can also isolate the core loss from the primary winding losses, which is important for lower permeability cores where high primary currents are required.

The core loss (power loss in the core) can be determined in 2 ways.

- 1) The core power loss (**Eq. 10.6**) can be calculated from the difference between the input power and the coil resistive power loss.
- 2) The core power loss (**Eq. 10.7**) can be calculated from the area inside the BH hysteresis loop.

$$P_{CL} = f \left(\int_0^{\tau} V_d I_d dt - \int_0^{\tau} I_d^2 R_d dt \right) \quad \text{Core loss from drive coil } (\tau = 1/f) \quad (10.6)$$

$$P_{CL} = f a l \int_0^{\tau} B dH \quad \text{Core loss from } BH \text{ hysteresis loop} \quad (10.7)$$

b. Ring Sample

One of the most accurate methods for determining the magnetic properties of a core is to use a circular ring sample, as shown in **Fig. 10.2**. In a rectangular core, the magnetic flux crowds at the inside radius of the corners and results in small regions of saturation. A circular ring eliminates the corners and

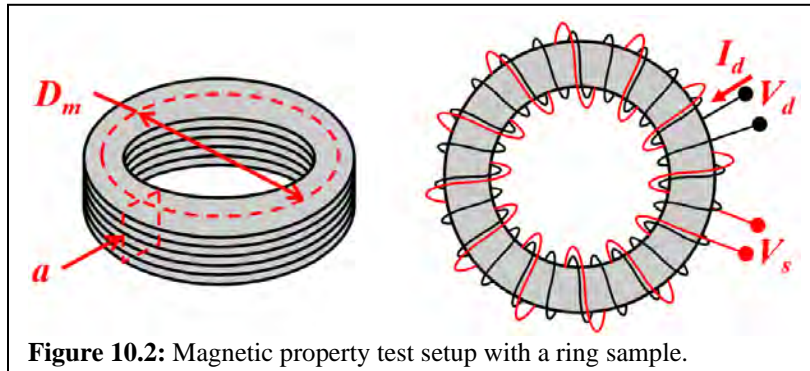


Figure 10.2: Magnetic property test setup with a ring sample.

produces a uniform magnetic flux density throughout the entire circumference. The flux density uniformity is improved when the inside diameter of the ring is larger than 80% of the outside diameter of the ring. This configuration also eliminates the leakage flux induced eddy current losses on the surface (as discussed in **Ch. 9**).

As discussed in **Ch. 3**, the introduction of mechanical strain into the ring sample by a machining or forming process significantly reduces the magnetic properties, resulting in less magnetic permeability, less saturation flux density, and more core loss. Therefore, care must be taken when obtaining the ring samples. The least severe cutting method is wire EDM or abrasive water jet.

Lamination steel materials are typically coated with a thin insulation (ASTM Type C-0, C-3, C-4, C-5). The cutting process (including wire EDM) tends to damage the insulation coating near the inside and outside edges of the rings, which leaves a path for interlaminar eddy currents. It might be necessary to add a layer of mylar tape between each ring to prevent interlaminar eddy currents.

The drive coil should use a large enough wire to carry the drive coil current without making the drive coil excessively hot. The drive coil turns and resistance should be chosen to achieve the maximum desired ampere-turns based on the power supply characteristics (available V_d and I_d). Increasing the number of rings and the number of sense turns (N_s) increases the sense coil open-circuit voltage (V_s), which increases the measurement accuracy. The sense winding carries no current, therefore the wire can be as small as desired (although very small wire breaks easily during winding).

The rings typically have sharp corners at the inside and outside edges, which can easily cut the wire insulation on the drive and sense windings and result

in continuity between the windings and the rings, which can damage the measurement instruments. This can be prevented by wrapping the stack of rings in an insulating tape. The windings and rings should be checked for continuity before connecting power and instruments.

A digital oscilloscope should be used to measure and record the drive current (I_d) and the sense voltage (V_s) waveforms over at least 3 cycles. The digital data can be exported as a CSV file containing (t, I_d, V_s) , where each time increment (t) includes the drive current (I_d) and the sense voltage (V_s). After importing the CSV file into MS-Excel, the data can be processed as follows, where C is the integration drift correction factor. The value for C can be determined by iteration until the difference is minimized between the maximum and minimum values of the magnetic flux density (B_i). **Eq. 10.3**, **Eq. 10.4**, **Eq. 10.5** can be discretized as follows. Note that the commercially available test equipment does all of these calculations automatically including the correction for integration drift.

$$H_i = \frac{NI}{l} = \frac{N_d I_{di}}{\pi D_m} \quad \text{Magnetic field intensity from drive coil} \quad (10.8)$$

$$B_i = \frac{1}{N_s a} \sum (V_{si} \Delta t + C) \quad \text{Flux density from sense coil} \quad (10.9)$$

$$B_i = \frac{1}{N_d a} \sum (V_{di} - I_{di} R_d + C) \Delta t \quad \text{Flux density from drive coil} \quad (10.10)$$

c. Examples – Core-Type Transformer

The core type transformer of **Ch. 9** was tested at 60 Hz with open secondary coils. The 18-turn winding was used as both the drive coil and the sense coil to measure B and H from **Eq. 10.8** and **Eq. 10.10**. The measured drive coil voltage (V_d) and drive coil current (I_d) are shown in the graph of **Fig. 10.3**. The resulting BH hysteresis loop is shown in the graph of **Fig. 10.4**. The saturation flux density and the relative permeability are consistent with published values. The calculated core loss is 0.0390 W/kg from the integral

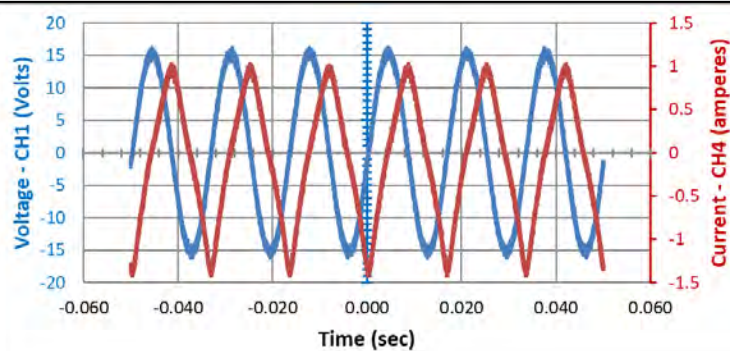


Figure 10.3: Drive coil (18-turn) current (I_d) and voltage (V_s).

of VI_{dt} (**Eq. 10.6**), and 0.0391 W/kg from the BH hysteresis loop area (**Eq. 10.7**), a difference of 0.25% (the 18-turn coil resistance is 4.32 m-ohm).

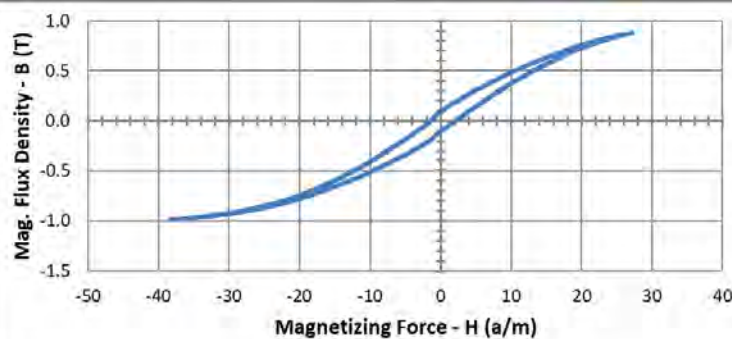


Figure 10.4: $B_i H_i$ values based on the I_d and V_s values (from **Fig. 10.3**). Tip to tip relative permeability is ... $\mu_r = 22,697$.

Tests were also conducted on the same core-type transformer by using only the peak values of drive coil current ($I_{d\ pk}$) and sense coil voltage ($V_{s\ pk}$) to obtain the peak values for magnetic field intensity (H_{pk}) and magnetic flux density (B_{pk}). This was done for a sequence of tests at successively increasing drive coil current. The following equations were used to obtain the peak magnetic field intensity (H_{pk}), the peak magnetic flux density (B_{pk}), and the relative permeability (μ_r).

$$B_{pk} = \frac{V_{s\ pk}}{N_s a \omega} \quad \text{Peak magnetic flux density} \quad (10.11)$$

$$H_{pk} = \frac{N_d I_{d\ pk}}{l} \quad \text{Magnetic field intensity} \quad (10.12)$$

$$\mu_r = \frac{B_{pk}}{\mu_0 H_{pk}} \quad \text{Relative magnetic permeability} \quad (10.13)$$

The peak B and H values are plotted in the graph of **Fig. 10.5**. The relative permeability values are plotted in the graph of **Fig. 10.6**. These measurements were replicated 4 times with 4 different combinations of drive and sense coils, as follows.

- 1) Sense coil-2 = 12-turns ... Drive coil-1 = 10-turns
- 2) Sense coil-3 = 18-turns ... Drive coil-1 = 10-turns
- 3) Sense coil-1 = 10-turns ... Drive coil-3 = 18-turns
- 4) Sense coil-2 = 12-turns ... Drive coil-3 = 18-turns

These measurements are validated in the following 2 ways.

- The magnetic flux density and the relative permeability are very consistent regardless of the coil combinations used to make the measurements.

- The magnetic saturation flux density (knee of the BH curve) and the peak relative permeability are consistent with published values.

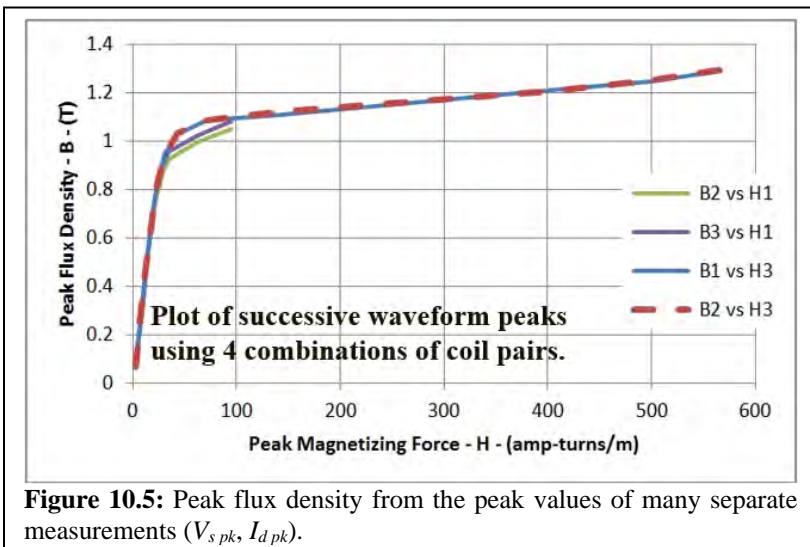


Figure 10.5: Peak flux density from the peak values of many separate measurements ($V_{s\ pk}$, $I_{d\ pk}$).

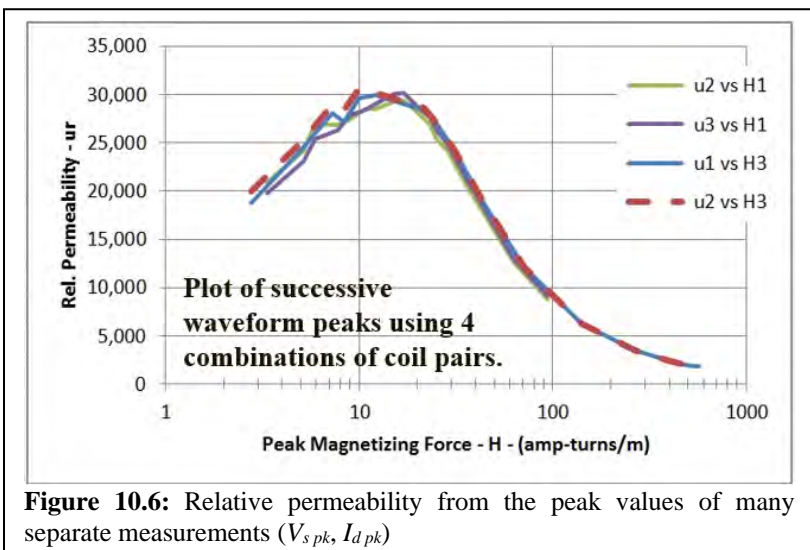


Figure 10.6: Relative permeability from the peak values of many separate measurements ($V_{s\ pk}$, $I_{d\ pk}$)

11. Air Core Inductor

a. Air Core Coil Geometry

The inductance of an air-core coil is difficult to calculate because the flux path in the air is challenging to define. The air flux path in a magnetic core with a small air gap is easy to characterize because the magnetic flux follows the magnetic core. The main advantage of an air-core inductor is that it does not saturate, and the inductance is constant regardless of the current.

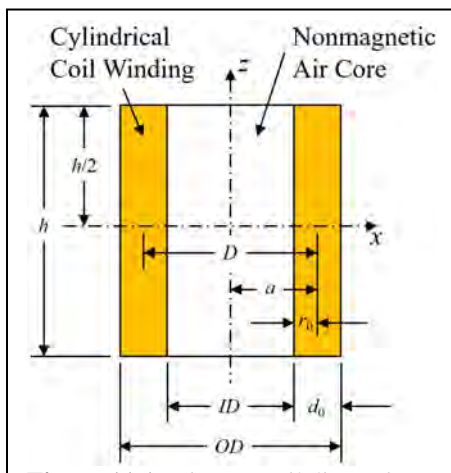


Figure 11.1: Air core coil dimensions.

The basic geometry of an air-core coil is shown in **Fig. 11.1**, and defined as follows (there is no magnetic material in the model).

h = Coil Winding Height

ID = Coil Winding Inside Diameter

OD = Coil Winding Outside Diameter

$$D = \frac{1}{2}(OD + ID) \quad \text{Winding mean diameter} \quad (11.1)$$

$$a = \frac{D}{2} \quad \text{Winding mean radius} \quad (11.2)$$

$$d_0 = \frac{1}{2}(OD - ID) \quad \text{Winding thickness (or 1-turn wire diameter)} \quad (11.3)$$

$$r_0 = \frac{d_0}{2} \quad \text{Half winding thickness (or 1-turn wire radius)} \quad (11.4)$$

b. Ansys Maxwell Simulation Results

Ansys-Maxwell FEA magnetic simulations were completed to evaluate the inductance of a cylindrical air core coil for 81 variations of the winding aspect ratios (OD/ID , h/ID). The results are listed in **Fig. 11.2**, where the Inductance has the units of micro-henries per square turn (L/N^2) ($\mu\text{H}/\text{turn}^2$).

α OD / ID	Ansys-Maxwell FEA							β h / ID
	0.01	0.03	0.10	0.32	1.00	3.16	10.00	
100.00	3.5258	3.5244	3.5199	3.5060	3.4627	3.3335	2.9811	2.2155
50.00	1.8300	1.8285	1.8238	1.8093	1.7650	1.6388	1.3336	0.8244
20.00	0.7827	0.7811	0.7762	0.7610	0.7168	0.6052	0.3998	0.1873
9.00	0.3993	0.3976	0.3920	0.3757	0.3319	0.2405	0.1251	0.0486
7.00	0.3315	0.3295	0.3237	0.3067	0.2628	0.1787	0.0863	0.0322
3.00	0.2079	0.2052	0.1969	0.1749	0.1286	0.0683	0.0269	0.0092
2.00	0.1908	0.1867	0.1752	0.1471	0.0973	0.0461	0.0170	0.0057
1.50	0.1968	0.1903	0.1732	0.1364	0.0826	0.0363	0.0130	0.0043
1.01	0.3264	0.2692	0.2019	0.1322	0.0693	0.0280	0.0097	0.0031
								0.0010

Figure 11.2: Ansys-Maxwell FEA inductance for an air core coil.

c. Accurate Wide Range Correlation

A correlation was developed for the inductance of a cylindrical air core coil with excellent accuracy over a very wide range of winding aspect ratios (OD/ID , h/ID). This correlation (Eq. 11.5) was established based on the magnetic flux in a coil as derived by Cullity [3] with additional factors obtained from curve fitting the deviations from the FEA inductance results (Fig. 11.2). The error for Eq. 11.5 is listed in Fig. 11.3, where the RMS Error over the entire range of aspect ratios is 6.7%.

- Winding diameter aspect ratio: $1.01 < OD/ID < 100$
- Winding height aspect ratio: $0.01 < h/ID < 100$

$$L_{a1} = K \mu_0 a N^2 \left(\frac{D}{\sqrt{D^2 + h^2}} \right) \quad \left[\begin{array}{l} \text{Air core coil Inductance for} \\ \text{wide range of aspect ratios} \end{array} \right] \quad (11.5)$$

$$K = A \left(\frac{ID}{OD} \right)^B + C \quad (11.6)$$

$$A = 1.61 \left(\frac{h}{ID} \right)^B \quad (11.7)$$

$$B = -0.232 e^{\left(-0.232 \frac{h}{ID} \right)} \quad (11.8)$$

$$C = -0.99 + 0.15 e^{\left(-\frac{h}{ID} \right)} \quad (11.9)$$

OD / ID	La1 / L - 1		Eq. 11.5 - La1 Error vs. Maxwell							Inductance Error	h / ID
	0.01	0.03	0.10	0.32	1.00	3.16	10.00	31.62	100.00		
100.00	-1.8%	-2.3%	-3.3%	-5.6%	-9.7%	-11.2%	-3.0%	12.8%	12.2%		
50.00	-3.1%	-3.8%	-4.9%	-7.0%	-10.2%	-9.0%	4.4%	14.0%	2.1%		
20.00	-2.5%	-3.8%	-5.3%	-7.0%	-7.9%	-1.0%	13.1%	5.3%	-5.0%		
9.00	-0.4%	-3.1%	-5.3%	-6.5%	-3.8%	7.2%	9.4%	-1.1%	-6.7%		
7.00	0.5%	-2.8%	-5.5%	-6.4%	-2.4%	8.4%	6.9%	-2.4%	-6.9%		
3.00	6.3%	-1.5%	-6.7%	-6.8%	1.0%	3.8%	-1.2%	-4.9%	-7.0%		
2.00	11.5%	-0.3%	-7.7%	-7.3%	1.1%	-1.4%	-4.4%	-5.7%	-7.1%		
1.50	15.8%	0.2%	-8.5%	-7.0%	1.1%	-4.9%	-5.7%	-5.4%	-6.5%		
1.01	-8.4%	-14.8%	-13.6%	-4.2%	2.9%	-7.8%	-5.0%	-1.9%	-2.9%		

Figure 11.3 Accuracy of Eq. 11.5 shown as error relative to the Ansys-Maxwell FEA Inductance results for an air core coil.

RMS Error = 6.7%, Average Error = 5.7%, Maximum Error = 15.8%.

d. Other Air-Core Correlations

Other published correlations (listed below) have been developed for the inductance of an air-core coil. These equations are very accurate for special geometries and a small range of aspect ratios. The accuracy of these inductance correlations is shown in **Fig. 11.4**, **Fig. 11.5**, and **Fig. 11.6**, where the inductance error for each cell is listed relative to the inductance calculated from the Ansys-Maxwell FEA simulations (**Fig. 11.2**).

- Plonsey [21] developed an equation (**Eq. 11.10**) for a single turn wire loop. This is also valid for the cases where the winding cross-section is much smaller than the coil *ID*.
 - Single wire loop ... $1 + h/ID = OD/ID$
Diagonal group of cells through **Fig. 11.4**
- Wheeler [22] developed several simple equations for a long thin solenoid coil (**Eq. 11.11**, **Eq. 11.13**) and a thin pancake coil (**Eq. 11.12**).
 - Long thin solenoid ... $OD/ID = 1.01$
Bottom row of cells in **Fig. 11.5** (top) (bottom)
 - Pancake winding ... $OD/ID > 10 (1 + h/ID)$
Upper left triangular group of cells in **Fig. 11.5** (middle)
- Wheeler [23] developed several complex equations for a long thin solenoid coil (**Eq. 11.14**, **Eq. 11.15**, **Eq. 11.16**).
 - Long thin solenoid ... $OD/ID = 1.01$
Bottom row of cells in **Fig. 11.6**
- Grover [24] gives many correlations for inductance and mutual inductance based on the use of the Taylor series. There are also many graphs and tables.

The Plonsey approximation (L_{a2}) [21] for the inductance of an air-core wire loop is very accurate for small wires ($a/r_0 > 10$) (where a is the radius of the loop, and r_0 is the radius of the solid wire). The classical solution (involving elliptic integrals) is required when the wire radius is large.

$$L_{a2} = \mu_0 a N^2 \left(\ln \left(\frac{8a}{r_0} \right) - 1.75 \right) \quad (\text{valid for } a/r_0 > 10) \quad (11.10)$$

The accuracy of the Plonsey inductance correlation (**Eq. 11.10**) (L_{a2}) is shown in **Fig. 11.4**, where the inductance error for each aspect ratio is listed relative to the inductance calculated from the Ansys-Maxwell FEA simulations. The best accuracy in **Fig. 11.4** is shown on a diagonal path through the table, which is consistent with the aspect ratios for a thin wire loop.

OD / ID	La2 / L - 1		Plonsey - La2 Error vs. Maxwell					Inductance Error		h / ID
	0.01	0.03	0.10	0.32	1.00	3.16	10.00	31.62	100.00	
100.00	-68.0%	-68.0%	-68.0%	-67.9%	-67.5%	-66.2%	-62.2%	-49.2%	-4.9%	
50.00	-67.1%	-67.1%	-67.0%	-66.8%	-65.9%	-63.3%	-54.9%	-27.0%	66.0%	
20.00	-63.2%	-63.1%	-62.9%	-62.2%	-59.8%	-52.4%	-28.0%	53.7%	318.5%	
9.00	-55.8%	-55.6%	-55.0%	-53.1%	-46.9%	-26.7%	41.0%	262.9%	970.4%	
7.00	-52.5%	-52.2%	-51.3%	-48.6%	-40.0%	-11.8%	82.7%	389.8%	1366.8%	
3.00	-37.2%	-36.4%	-33.7%	-25.4%	1.5%	91.1%	385%	1323%	4294%	
2.00	-28.3%	-26.8%	-21.9%	-7.0%	40.6%	196.9%	703%	2313%	7405%	
1.50	-21.4%	-18.7%	-10.7%	13.4%	87.4%	326.1%	1092%	3520%	11203%	
1.01	10.7%	34.3%	79.0%	173.4%	421.8%	1191.9%	3638%	11403%	35900%	

Figure 11.4: Accuracy for the Plonsey inductance correlation, Eq. 11.10.

Wheeler (1928) [22] developed some simple approximations for long thin solenoid windings and a flat pancake winding, listed below. The charts (Fig. 11.5) show good accuracy only for the small aspect ratio ranges that correspond to the thin solenoid or thin pancake coils.

$$L_{a3} = \mu_0 a N^2 \left(\frac{10}{\pi} R_4 \right) \quad R_3 = \frac{a}{0.9a + 1.0h} \quad \text{Long thin solenoid} \quad (11.11)$$

$$L_{a4} = \mu_0 a N^2 \left(\frac{10}{\pi} R_4 \right) \quad R_4 = \frac{a}{0.8a + 1.1d_0} \quad \text{Pancake winding} \quad (11.12)$$

$$L_{a5} = \mu_0 a N^2 \left(\frac{10}{\pi} R_5 \right) \quad R_5 = \frac{a}{0.8a + 1.1h} \quad \text{Long thin solenoid} \quad (11.13)$$

OD / ID	La3 / L - 1		Wheeler - La3					Inductance Error		h / ID
	0.01	0.03	0.10	0.32	1.00	3.16	10.00	31.62	100.00	
100.00	223.2%	223.1%	222.5%	220.7%	215.4%	200.2%	165.6%	115.2%	78.3%	
50.00	214.3%	214.0%	212.9%	209.7%	200.0%	175.4%	130.7%	85.9%	63.6%	
20.00	202.2%	201.5%	199.1%	192.0%	172.9%	134.7%	90.2%	64.5%	55.5%	
9.00	181.5%	180.0%	175.7%	163.5%	135.5%	95.1%	65.8%	54.3%	50.7%	
7.00	170.9%	169.3%	164.3%	150.4%	120.9%	83.3%	59.7%	51.2%	48.6%	
3.00	114.8%	112.6%	106.4%	91.0%	66.3%	46.4%	38.5%	36.2%	35.5%	
2.00	74.9%	73.3%	68.4%	56.8%	40.3%	29.3%	25.8%	24.9%	24.6%	
1.50	40.9%	40.4%	38.4%	32.5%	23.1%	17.4%	15.8%	15.4%	15.3%	
1.01	32.0%	21.2%	8.0%	1.0%	2.0%	1.5%	1.6%	1.8%	1.8%	

OD / ID	La4 / L - 1		Wheeler - La4					Inductance Error		h / ID
	0.01	0.03	0.10	0.32	1.00	3.16	10.00	31.62	100.00	
100.00	1.6%	1.5%	1.4%	1.0%	0.2%	4.1%	16.4%	56.7%	193.1%	
50.00	2.8%	2.7%	2.5%	1.7%	0.8%	8.5%	33.3%	115.7%	391.0%	
20.00	2.3%	2.1%	1.5%	0.5%	6.7%	26.3%	91.2%	308.1%	1011.5%	
9.00	0.6%	0.2%	1.2%	5.6%	19.6%	65.0%	217%	717%	2308%	
7.00	0.1%	0.7%	2.5%	8.2%	26.3%	85.6%	285%	931%	2988%	
3.00	2.9%	4.3%	8.6%	22.3%	66.3%	213.0%	695%	2232%	7098%	
2.00	4.2%	6.5%	13.5%	35.1%	104.3%	331.5%	1068%	3407%	10809%	
1.50	4.1%	7.6%	18.3%	50.2%	148.1%	464.1%	1478%	4693%	14864%	
1.01	22.9%	6.4%	24.7%	90.5%	263.6%	800.2%	2505%	7916%	24986%	

OD / ID	La5 / L - 1		Wheeler - La5					Inductance Error		h / ID
	0.01	0.03	0.10	0.32	1.00	3.16	10.00	31.62	100.00	
100.00	263.6%	263.3%	262.4%	259.7%	251.3%	228.3%	178.6%	112.7%	68.0%	
50.00	253.5%	253.0%	251.3%	246.2%	231.2%	194.7%	133.7%	78.1%	51.7%	
20.00	239.8%	238.6%	234.8%	223.7%	194.8%	141.1%	84.3%	53.4%	42.6%	
9.00	216.3%	214.0%	207.1%	188.0%	146.9%	92.8%	56.2%	42.1%	37.6%	
7.00	204.4%	201.7%	193.6%	172.1%	129.1%	79.1%	49.5%	38.9%	35.6%	
3.00	141.0%	137.3%	126.8%	102.4%	66.3%	39.0%	28.0%	24.5%	23.4%	
2.00	96.1%	92.9%	83.8%	64.0%	38.2%	21.7%	15.8%	14.0%	13.4%	
1.50	57.9%	56.0%	50.3%	37.3%	20.2%	9.9%	6.3%	5.3%	5.0%	
1.01	23.9%	12.7%	0.8%	3.5%	1.3%	5.5%	6.9%	7.2%	7.4%	

Figure 11.5: Wheeler simple inductance approximations for a long thin solenoid winding (Eq. 11.11) (top), a pacncake winding (Eq. 11.12) (middle), and a long thin solenoid winding (Eq. 11.13) (bottom).

Wheeler (1982) [23] developed some complex approximations for long thin solenoid windings, listed below. The charts (**Fig. 11.6**) show good accuracy only for the small aspect ratio ranges that correspond to the thin solenoid coils. These correlations significantly improve the accuracy for small values of the h/ID aspect ratio, compared to the simpler equations (**Eq. 11.11** and **Eq. 11.13**).

Long thin solenoid approximations.

$$L_{a6} = \mu_0 a N^2 R_6 \quad R_6 = 0.48 \ln \left(1 + \pi \frac{a}{h} \right) + 0.52 \operatorname{arcsinh} \left(\pi \frac{a}{h} \right) \quad (11.14)$$

$$L_{a7} = \mu_0 a N^2 R_7 \quad R_7 = \left(\frac{2.78}{1.1 + \frac{h}{a}} \right) + \ln \left(1 + 0.39 \frac{a}{h} \right) \quad (11.15)$$

$$L_{a8} = \mu_0 a N^2 R_8 \quad R_8 = \ln \left(1 + \pi \frac{a}{h} \right) + \frac{1}{2.3 + 1.6 \frac{h}{a} + 0.44 \left(\frac{h}{a} \right)^2} \quad (11.16)$$

OD / ID	La6 / L - 1					Wheeler - La6					Inductance Error			h / ID
	0.01	0.03	0.10	0.32	1.00	3.16	10.00	31.62	100.00					
100.00	753.9%	649.0%	544.5%	441.3%	341.3%	248.3%	169.3%	112.5%	79.3%					
50.00	670.0%	568.1%	467.2%	368.4%	274.7%	191.7%	127.4%	86.2%	63.9%					
20.00	565.3%	467.9%	372.3%	280.9%	198.5%	132.7%	89.5%	65.2%	54.6%					
9.00	461.7%	371.8%	285.2%	205.2%	138.6%	92.8%	66.7%	53.9%	49.3%					
7.00	424.1%	338.1%	255.6%	180.8%	120.8%	81.8%	60.5%	50.5%	47.1%					
3.00	275.3%	208.9%	147.9%	97.3%	63.8%	47.0%	38.5%	35.1%	34.0%					
2.00	192.4%	139.9%	93.5%	58.3%	38.7%	30.1%	25.4%	23.7%	23.1%					
1.50	128.8%	88.5%	54.9%	32.3%	22.1%	18.0%	15.2%	14.2%	13.9%					
1.01	6.6%	2.0%	0.1%	0.0%	1.7%	1.9%	1.0%	0.7%	0.5%					

OD / ID	La7 / L - 1					Wheeler - La7					Inductance Error			
	0.01	0.03	0.10	0.32	1.00	3.16	10.00	31.62	100.00					
100.00	761.3%	656.3%	551.9%	448.8%	349.1%	256.2%	175.1%	111.4%	75.1%					
50.00	677.1%	575.3%	474.4%	375.8%	282.4%	198.7%	129.4%	82.2%	61.5%					
20.00	572.2%	474.9%	379.4%	288.2%	205.6%	136.2%	86.3%	62.1%	54.2%					
9.00	468.2%	378.4%	291.9%	212.1%	143.7%	91.7%	62.8%	52.7%	49.8%					
7.00	430.4%	344.5%	262.2%	187.4%	124.9%	79.6%	57.1%	49.8%	47.8%					
3.00	280.3%	214.1%	153.2%	101.9%	64.1%	43.6%	37.0%	35.3%	34.9%					
2.00	196.5%	144.2%	98.0%	61.6%	37.7%	27.1%	24.6%	24.1%	24.0%					
1.50	132.2%	92.0%	58.6%	34.7%	20.6%	15.5%	14.7%	14.7%	14.8%					
1.01	8.3%	4.0%	2.5%	1.4%	0.1%	0.0%	0.7%	1.3%	1.3%					

OD / ID	La8 / L - 1					Wheeler - La8					Inductance Error			
	0.01	0.03	0.10	0.32	1.00	3.16	10.00	31.62	100.00					
100.00	760.7%	655.8%	551.3%	448.0%	347.7%	254.0%	172.8%	111.8%	76.5%					
50.00	676.6%	574.7%	473.7%	374.8%	280.6%	196.2%	128.5%	83.6%	62.1%					
20.00	571.7%	474.2%	378.5%	286.7%	203.3%	134.7%	87.5%	63.0%	53.8%					
9.00	467.6%	377.7%	290.8%	210.1%	141.7%	92.0%	64.1%	52.8%	49.0%					
7.00	429.8%	343.7%	261.0%	185.4%	123.2%	80.4%	58.2%	49.6%	46.8%					
3.00	279.7%	213.3%	151.8%	100.2%	63.9%	44.8%	37.2%	34.7%	33.9%					
2.00	196.0%	143.4%	96.7%	60.3%	38.0%	28.1%	24.5%	23.4%	23.0%					
1.50	131.8%	91.4%	57.4%	33.7%	21.2%	16.3%	14.6%	14.0%	13.9%					
1.01	8.0%	3.6%	1.7%	0.9%	0.6%	0.6%	0.5%	0.6%	0.5%					

Figure 11.6: Wheeler inductance approximations for a long thin solenoid winding from **Eq. 11.14** (top), **Eq. 11.15** (middle), **Eq. 11.16** (bottom).

12. Forces on Permanent Magnets and Coils

The torque and force on a magnetic moment in a magnetic field can be calculated as the Lorentz force due to the magnetic flux density (B) on the current loop (I) of the magnetic moment. A rectangular current loop is shown on the XY -plane (Fig. 12.1) with the associated magnetic moment (m_z) in the Z -direction. The magnetic moment for the current loop is given in Eq. 12.1.

As described in Ch. 3.j, a thin permanent magnet can be modeled as a magnetic moment with a surface current (I) encircling an area (wt). A thick permanent magnet of length (l) can be modeled as a stack of thin permanent magnets, with the current loops combined into a sheet current on the surface. In a spreadsheet calculation, the sheet current can be modeled as several discrete current loops distributed on the permanent magnet length. The total current for the magnetic moment of a permanent magnet is given in Eq. 12.2.

$$\vec{m}_z = IA_L = Iwt \quad \text{Magnetic moment} \quad (12.1)$$

$$I = H_c l \quad \text{Current for a permanent magnet magnetic moment} \quad (12.2)$$

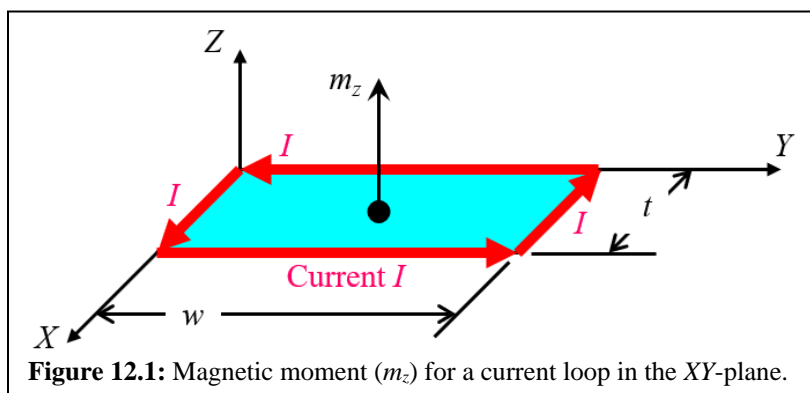


Figure 12.1: Magnetic moment (m_z) for a current loop in the XY -plane.

A uniform magnetic flux density produces only a torque on the magnetic moment, such as the earth's magnetic field (approximately uniform). This is the effect observed on a compass needle. The torque works to align the magnetic moment with the external magnetic field. The torque goes to zero when the permanent magnet is aligned with the external magnetic field.

A non-uniform magnetic flux density, such as from a 2nd magnetic moment (m_2), produces both a force and a torque on the 1st magnetic moment (m_1). The force and torque are equal and opposite on both magnetic moments. The 2 magnetic moments can represent 2 coils, 2 permanent magnets, or a coil and a permanent magnet. The non-uniform magnetic flux density distribution on the 1st magnetic moment from a 2nd magnetic moment of arbitrary shape and orientation can be calculated from the Biot-Savart law.

a. Biot-Savart Law

The Biot-Savart Law [25] gives the magnetic field distribution (in the absence of magnetic materials) for both the near and far-fields, for any current path, or current path segment. This is a very useful tool for determining the magnetic flux density distribution for an air-core coil or the magnetic flux density vector on a conductor due to the current in another conductor. The two conductors can also be different sections of the same conductor.

Defining the magnetic flux density vector on a conductor permits calculating the Lorentz force vector on the conductor. Note that the current in 2 conductors each produces a magnetic field on the other, and the resulting Lorentz force on each conductor is equal and opposite. Also, a permanent magnet can be modeled as a magnetic moment with a current loop (**Ch. 3.j**), which can be used to calculate the magnetic field around the permanent magnet. The force on a permanent magnet due to an external magnetic field can be calculated as the Lorentz force on the magnetic moment current loop of the permanent magnet. In a spreadsheet calculation, the sheet current for a thick permanent magnet can be modeled as several discrete current loops distributed along the permanent magnet length.

The Biot-Savart law (**Eq. 12.3**) gives the differential magnetic flux density vector ($d\vec{B}$) at a point $P(x,y,z)$ based on the cross product of the differential current path vector ($d\vec{l}$) and the radius vector (\vec{r}) from the current path to the point $P(x,y,z)$. This is also shown in **Fig. 12.2**, for a circular wire loop in the XY-plane.

$$d\vec{B} = \frac{\mu_0 I}{4\pi} \frac{d\vec{l} \times \vec{r}}{r^3} \text{ tesla} \quad \text{Biot-Savart Law} \quad (12.3)$$

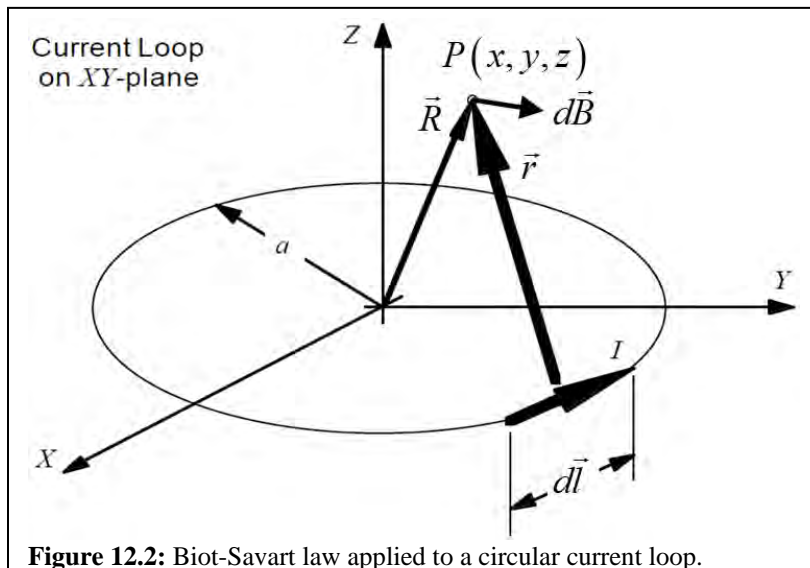


Figure 12.2: Biot-Savart law applied to a circular current loop.

- Circular Loop Flux Density

The Biot-Savart equation can be integrated around the circular loop to obtain the Z-direction magnetic flux density at the center (B_Z) on the vertical axis (Z-axis), as follows.

$$B_Z = \frac{\mu_0 I}{4\pi r^3} \frac{a^{2\pi a}}{r} \int_0^{2\pi a} r dl \quad r = \sqrt{a^2 + z^2} \quad (12.4)$$

$$B_Z = \frac{\mu_0 a^2 I}{2(a^2 + z^2)^{3/2}}$$

Magnetic flux density on the Z-axis
(12.5)

The Z-axis magnetic flux density at the center of the circle on the XY-plane, $P = (0, 0, 0)$, is obtained by setting $z = 0$.

$$B_Z|_{z=0} = \frac{\mu_0 I}{2a}$$

Magnetic flux density on the Z-axis at $z = 0$
(12.6)

- Air-Core Coil Inductance

The Biot-Savart law can be used to calculate the inductance of an air-core coil. The magnetic flux density distribution inside the circular loop can be calculated using the Biot-Savart law and integrated over the area of the circular loop to determine the magnetic flux linkage. The accuracy of the inductance calculation can be very good, with a sufficiently small differential current path vector ($d\vec{l}$) and a sufficiently small differential area inside the circular loop.

A Visual Basic macro was written in MS-Excel to solve a mesh with 5700 points over the 81 coil aspect ratio combinations (OD/ID , h/ID). The accuracy of the Biot-Savart inductance calculation (L_B) is shown in **Fig. 12.3**, where the inductance error for each aspect ratio is listed relative to the inductance from the Ansys-Maxwell FEA simulations (**Fig. 11.2**). The RMS Error is very good, at 3.0%. Increasing the number of mesh points reduces the error and increases the solution time.

OD / ID	LB / L - 1		Biot-Savart Error vs. Maxwell					Inductance Error		h / ID
	0.01	0.03	0.10	0.32	1.00	3.16	10.00	31.62	100.00	
100.00	6.4%	6.4%	6.3%	5.9%	5.4%	4.7%	4.4%	4.9%	6.2%	
50.00	4.2%	4.1%	3.8%	3.3%	2.9%	2.7%	2.9%	4.0%	3.8%	
20.00	3.5%	3.0%	2.3%	1.8%	1.7%	2.0%	3.1%	3.4%	0.9%	
9.00	3.4%	2.5%	1.6%	1.2%	1.3%	2.3%	3.3%	1.7%	-1.4%	
7.00	3.2%	2.3%	1.4%	1.0%	1.4%	2.6%	3.1%	0.9%	-2.2%	
3.00	2.0%	1.2%	0.5%	0.7%	1.7%	2.8%	1.5%	-1.8%	-3.0%	
2.00	0.9%	0.3%	0.1%	0.8%	2.0%	2.5%	0.4%	-2.3%	-3.2%	
1.50	-0.3%	-0.4%	0.0%	0.9%	2.1%	2.2%	-0.5%	-2.9%	-3.5%	
1.01	-7.0%	-3.3%	-1.2%	0.3%	1.3%	0.8%	-1.9%	-3.6%	-2.6%	

Figure 12.3: Accuracy of Biot-Savart air core coil inductance calculation relative to the Ansys-Maxwell FEA simulations (**Fig. 11.2**).

RMS Error = 3.0%, Average Error = 2.5%, Maximum Error = 7.0%.

b. Torque on a Magnetic Moment

The Lorentz force vector equations (**Eq. 12.10 – Eq. 12.12**) define the forces in X , Y , and Z -directions on each of the 4 edges of the current loop, as shown in **Fig. 12.4**. The current loop is in the XY -plane, the magnetic moment (m_z) is in the Z -direction, and the uniform magnetic flux density is in the YZ -plane.

$$\vec{B} = \vec{B}_x + \vec{B}_y + \vec{B}_z \quad \text{Magnetic flux density vector} \quad (12.7)$$

$$\vec{B}_x = 0 \quad \text{Zero } X\text{-direction flux density} \quad (12.8)$$

$$\vec{B} = \vec{B}_y + \vec{B}_z \quad \text{YZ-plane magnetic flux density vector} \quad (12.9)$$

	<u>Left Edge Force</u>	<u>Right Edge Force</u>	
Z-direction Force	$\vec{F}_{zL} = \vec{I}_x \times \vec{B}_y t$	$\vec{F}_{zR} = -\vec{I}_x \times \vec{B}_y t$	(12.10)
Y -direction Force	$\vec{F}_{yL} = -\vec{I}_x \times \vec{B}_z t$	$\vec{F}_{yR} = \vec{I}_x \times \vec{B}_z t$	(12.11)

	<u>Front Edge Force</u>	<u>Back Edge Force</u>	
X -direction Force	$\vec{F}_{xF} = \vec{I}_y \times \vec{B}_z w$	$\vec{F}_{xB} = -\vec{I}_y \times \vec{B}_z w$	(12.12)

The X , Y & Z -direction forces on opposite sides of the current loop are equal and opposite and produce no net force.

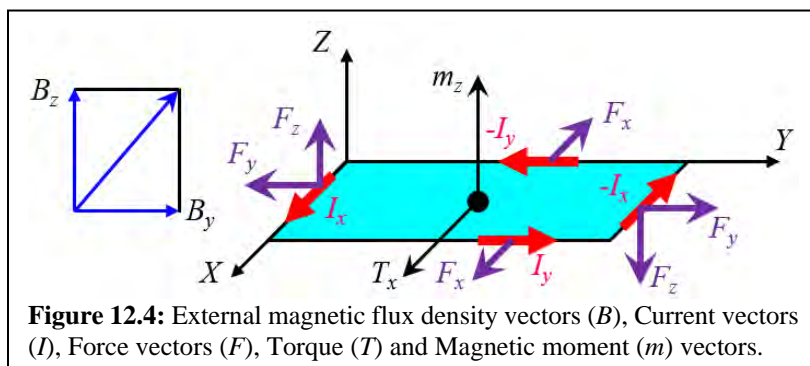
$$\vec{F}_{yL} + \vec{F}_{yR} = 0 \quad \vec{F}_{xF} + \vec{F}_{xB} = 0 \quad (12.13)$$

The X and Y -direction forces are perfectly in line, the perpendicular distance between the force lines is zero and they produce zero torque. The Z -direction forces are not in line, the perpendicular distance between the force lines is the width (w) of the current loop, and they produce a torque (T_x) in the negative X -direction. In general, the torque (T) is the vector cross product of the magnetic moment (m) and the magnetic flux density (B) (**Eq. 12.15**).

$$T_x = -\vec{F}_z w = -(\vec{I}_x \times \vec{B}_y t) w = -\vec{I}_x w t \times \vec{B}_y = \vec{m}_z \times \vec{B}_y \quad (12.14)$$

$\vec{T} = \vec{m} \times \vec{B}$

 Torque on magnetic moment due to the magnetic field (12.15)



c. Force on a Magnetic Moment

Both a torque and a force are produced on a magnetic moment (m) by a non-uniform magnetic flux density (B). In **Fig. 12.5**, a current loop of radius (r) and current (I_2) is positioned in a non-uniform magnetic field (B). The current loop is in the XY-plane, and the magnetic moment (m) is in the Z-direction. The magnetic flux density (B) is symmetric about the Z-axis and is non-uniform in the Z-direction. It could be produced by another circular coil on the Z-axis.

The magnetic flux density (B) has axial (B_z) and radial (B_r) components that interact with the current loop (**Fig. 12.5**). The force on the magnetic moment can be calculated as the Lorentz force (F) on the current (I) due to the magnetic flux density (B).

An outward radial Lorentz force (F_r) results from the axial magnetic flux density (B_z) on the current (I). There is zero net force and torque from the uniform radial force (F_r). A downward Z-axis Lorentz force (F_z) results from the outward radial magnetic flux density (B_r) on the current (I) (**Fig. 12.5**).

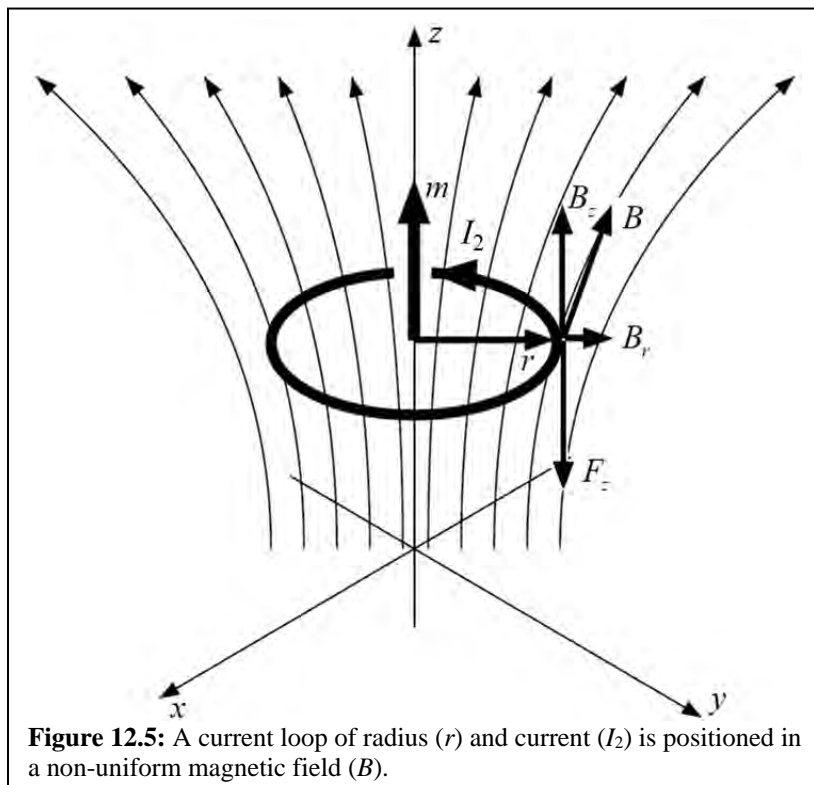


Figure 12.5: A current loop of radius (r) and current (I_2) is positioned in a non-uniform magnetic field (B).

The Z-direction Lorentz force (F_z) can be written as a function of the outward radial magnetic flux density (B_r) and the current (I_2). The radial magnetic flux density (B_r) produced from a 2nd magnetic moment (permanent magnet or

coil) can be calculated from the Biot-Savart law, as defined in **Ch.12.a**. When the 2nd magnetic moment is a circular loop and is aligned on the Z-axis, the radial magnetic flux density is constant around the circumference of the 1st circular loop and **Eq. 12.16** can be used. Otherwise, the Biot-Savart law must be used to obtain the magnetic flux density distribution around the current loop.

$$\vec{F}_z = -2\pi r \vec{I}_2 \times \vec{B}_r \quad \text{Z-axis Lorentz force for constant } B_r \quad (12.16)$$

When the 2nd magnetic moment is aligned on the Z-axis, the magnetic field is symmetric about the Z-axis, and the radial magnetic flux density can be defined as a function of the axial magnetic flux density gradient (dB_z/dz). A magnetic flux balance across the current loop gives this relationship, as follows.

$$\pi r^2 B_z = \pi r^2 B_{z+\Delta z} + 2\pi r \Delta z B_r \quad \text{Magnetic Flux Balance} \quad (12.17)$$

$$B_r = -\frac{r}{2} \left(\frac{B_{z+\Delta z} + B_z}{\Delta z} \right) \quad \text{Solving for } B_r \quad (12.18)$$

$$B_r \Big|_{\Delta z \rightarrow 0} = -\frac{r}{2} \frac{dB_z}{dz} \quad \text{Radial magnetic flux density} \quad (12.19)$$

Combining **Eq. 12.16** and **Eq. 12.19** gives the Z-direction Lorentz force (F_z) as the product of the magnetic moment (m_z) and the magnetic flux density gradient (dB_z/dz). This is valid for small current loops where the 2nd order variations in the magnetic field are insignificant, and where both this current loop (I_2) and the source current loop (I_1) are aligned on the Z-axis.

$$F_z = \pi r^2 I_2 \frac{dB_z}{dz} \quad \boxed{F_z = m_z \frac{dB_z}{dz}} \quad \text{Force on a magnetic moment} \quad (12.20)$$

$$F_z = N_2 I_2 a \frac{dB_z}{dz} = N_2 I_2 \frac{d\phi_{12}}{dz} \quad \left[\begin{array}{l} \phi_{12} = B_z a = N_1 I_1 \mathcal{P}_{12} \\ \text{Flux linking coil-2 from coil-1} \end{array} \right] \quad (12.21)$$

$$L_{12} = \frac{N_2(\phi_{12})}{I_1} \quad \phi_{12} = \frac{L_{12} I_1}{N_2} \quad \text{Mutual inductance for 2 coils} \quad (12.22)$$

$$\boxed{F_z = I_1 I_2 \frac{dL_{12}}{dz}} \quad \left[\begin{array}{l} \text{Force between 2 coils. This is also derived by} \\ \text{energy balance in Slemmon [2] and Brauer [9]} \end{array} \right] \quad (12.23)$$

The Z-axis flux density (B_z) for a circular current loop of radius a , was derived in **Eq. 12.5**. This equation can be differentiated to obtain the magnetic flux density gradient (dB_z/dz) on the Z-axis (**Eq. 12.25**).

$$B_z = \frac{\mu_0 a^2 I_2}{2(a^2 + z^2)^{3/2}} \quad \left[\begin{array}{l} \text{Z-axis flux density} \\ \text{for a coil of radius } a, \text{ Eq.12.5} \end{array} \right] \quad (12.24)$$

$$\boxed{\frac{dB_z}{dz} = \frac{\mu_0 a^2 I_2}{2} \frac{(-3z)}{(a^2 + z^2)^{5/2}}} \quad \left[\begin{array}{l} \text{Z-axis flux density gradient} \\ \text{for a coil of radius } a \end{array} \right] \quad (12.25)$$

13. Slot Motor

Two common configurations for the moveable conductor in a circuit breaker are the reverse loop configuration (**Fig. 13.1**) and the reverse loop with a slot motor (**Fig. 13.2**). In both of these configurations, the Lorentz force due to the high fault current produces a high force on the moveable conductor. Electrical switchgear, such as circuit breakers, function by opening electrical contacts quickly to interrupt fault currents. A 3-phase 600 V-RMS 60 Hz system with 100 kA-RMS of available symmetric current, a shorted power factor of 0.15, and a Phase-A closing angle of 0° produces a peak asymmetric fault current of 231 kA in 7.7 ms (Phase-A) and a current rate of rise of 50 kA/ms (Phase-C), from **Eq. 13.1**, (Greenwood, Eq. 3.2.10) [29]. This is typical of a UL or IEC short circuit test for circuit breakers.

$$I(t) = \frac{V}{Z} [\sin(\omega t + \theta - \varphi) - e^{-\alpha t} \sin(\theta - \varphi)] \quad \text{Greenwood [29]} \quad (13.1)$$

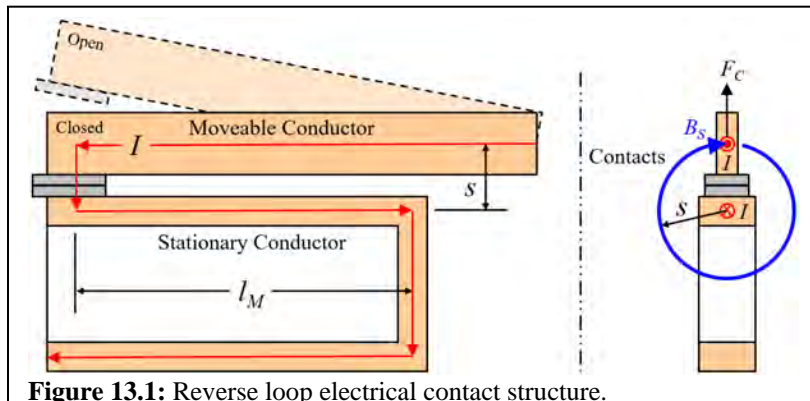
$$V = 600 \quad I_s = 100,000 \quad PF = 0.15 \quad \omega = 377/s \quad \theta = 0^\circ = \text{Closing Angle}$$

$$Z = V/I_s \quad R = (PF)(Z) \quad L = \sqrt{Z^2 - R^2}/\omega \quad \alpha = R/L \quad \varphi = \cos^{-1}(PF)$$

In a circuit breaker, the electrical contacts on a moveable copper conductor must move apart approximately 3 cm in 4 ms to interrupt the fault current and protect the wiring. A high force is required on a moveable conductor to accelerate it and move it quickly to the open position.

a. Reverse Loop Conductors

The reverse loop configuration (**Fig. 13.1**) places a moveable conductor in parallel with a stationary conductor, in which the currents in the conductors are in opposite directions. The significant dimensions are the space (S) between the current paths and the length (l_M) over which the conductors are closely spaced. The current paths are assumed to be in the center of the conductors. The Lorentz force on the moveable conductor (**Eq. 2.28**) is proportional to the current in the moveable conductor, the magnetic flux



density on the moveable conductor from the stationary conductor, and the length of the closely spaced conductors. The magnetic flux density on the moveable conductor is produced by the current in the stationary conductor. The magnetic flux path (B_S) around the stationary conductor intersects with the current in the moveable conductor (shown as the blue circle at radius S in **Fig. 13.1**). When the space (S) between the conductors is much smaller than the parallel length (l_M), the flux density distribution along the length of the conductors can be assumed constant, and the Lorentz force on the moveable conductor can be estimated as follows. Otherwise, the Biot-Savart law (**Ch. 12.a**) is needed to calculate the flux density distribution along the moveable conductor.

The length (l_S) of the circular flux path (**Eq. 13.2**) is the circumference of a circle (of radius S) around the stationary conductor. The magnetic flux density (B_S) in the circular flux path is a function of the magnetic field intensity (H_S) along the circular flux path, as shown below.

$$l_S = 2\pi S \quad \text{Length of the circular flux path} \quad (13.2)$$

$$H_S = \frac{I}{l_S} = \frac{I}{2\pi S} \quad \text{Magnetic field intensity} \quad (13.3)$$

$$B_S = \mu_0 H_S = \mu_0 \frac{I}{2\pi S} \quad \text{Magnetic flux density} \quad (13.4)$$

The Lorentz force vector equation gives an upward force on the moveable conductor (repulsion between the conductors) for the reverse current flow configuration. For parallel current flow, the Lorentz force is downward on the moveable conductor (attraction between the conductors).

$$\vec{F}_C = \vec{I} \times \vec{B}_S l_M \quad \text{Lorentz force (from Eq. 2.28)} \quad (13.5)$$

Combining **Eq. 13.4** and **Eq. 13.5** gives the repulsion Lorentz force for the reverse loop configuration of **Fig. 13.1**. The Lorentz force is proportional to the square of the current (I^2) and the parallel length (l_M) of the conductors, and inversely proportional to the space (S) between the parallel current paths. Also, there are no magnetic materials in this configuration, therefore there is no saturation relative to the current.

$$F_C = \frac{\mu_0 I^2}{2\pi} \frac{l_M}{S}$$

Reverse loop Lorentz force

(13.6)

b. Reverse Loop with Slot Motor

The reverse loop configuration with a slot motor (**Fig. 13.2**) adds a laminated magnetic structure with a slot into which the parallel conductors are placed. The magnetic structure is laminated to minimize steady-state losses due to eddy currents and to eliminate potential delays in producing the magnetic flux due to eddy currents.

The significant dimensions include the air gap across the slot (g), the length of the slot (w), and the thickness of the slot motor legs (t). The purpose of the slot motor is to amplify the magnetic flux density on the moveable conductor. The Lorentz force (Eq. 13.5) on the moveable conductor, due to the slot motor, is proportional to the current (I) in the moveable conductor, the magnetic flux density (B_s) on the moveable conductor, and the length of the slot in the slot motor (w).

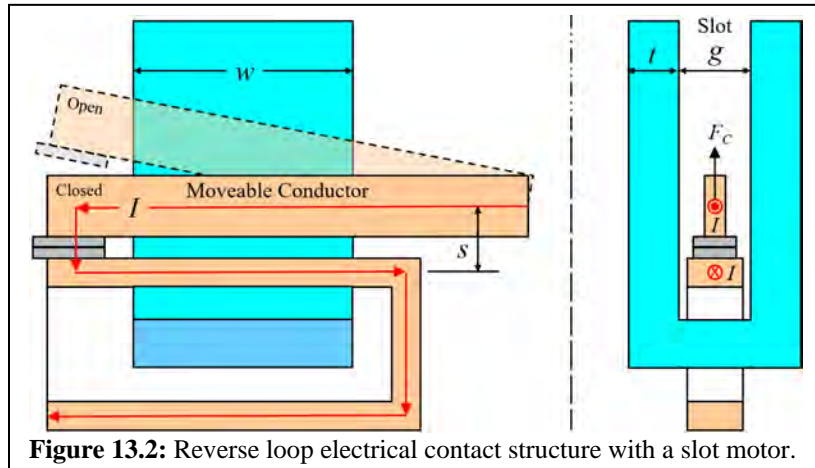


Figure 13.2: Reverse loop electrical contact structure with a slot motor.

The magnetic flux density in the slot motor air gap (g) and the magnetic flux density on the moveable conductor (B_c) can be determined quickly by evaluating the 3 magnetic flux loops and the magnetic flux vector chart shown in Fig. 13.3. The steel relative permeability is approximately 7,000, which can be assumed as infinite when not saturated. The magnetic flux paths

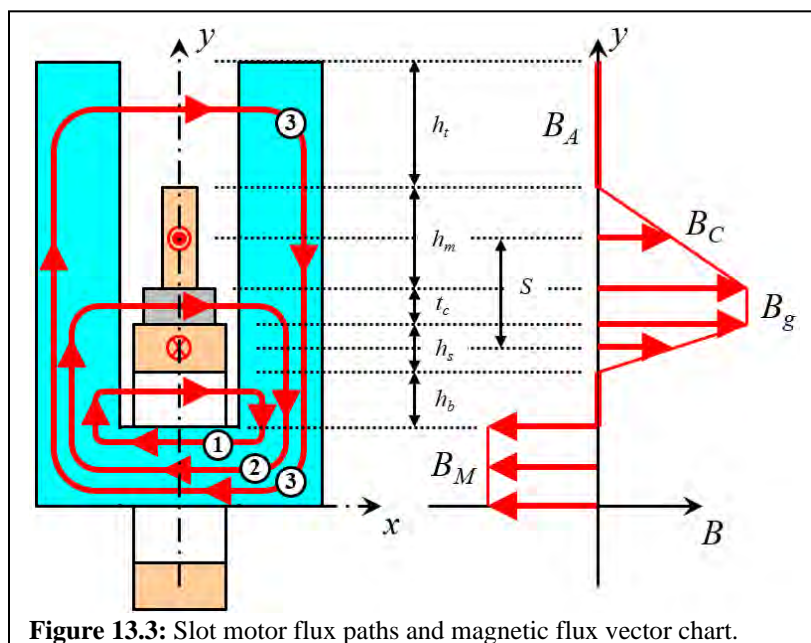


Figure 13.3: Slot motor flux paths and magnetic flux vector chart.

start with loop #1, which is expanded upward to position #2 and then to position #3.

1. Loop #1: Encloses no net current, therefore there is zero flux crossing the slot motor gap in flux loop #1.
2. Loop #2: Encloses the current in the stationary conductor.
3. Loop #3: Encloses no net current, therefore there is zero flux crossing the slot motor gap in flux loop #3.

The observations for each flux loop are reflected in the flux vector diagram at the right side in **Fig. 13.3**. Also, the vertical dimensions are shown, including the height of the moveable conductor (h_m), the height of the stationary conductor (h_s), the thickness of the electrical contacts (t_c), and the space between the parallel current paths (S).

The magnetic flux density across the electrical contacts (B_g) can be calculated from the current (I), the permeability of air (μ_0), the slot motor gap (g), and the magnetic field intensity (H_g), as shown below. The average magnetic flux density on the moveable conductor (B_C) is one half of the flux density across the electrical contacts (B_g). The magnetic flux density in the slot motor (B_M) can be calculated from the air gap magnetic flux density (B_g) and the area ratio ($S w)/(t w)$ for the air gap and the slot motor.

$$H_g = \frac{I}{g} \quad \text{Magnetic field intensity across the gap} \quad (13.7)$$

$$B_g = \mu_0 H_g = \mu_0 \frac{I}{g} \quad \text{Magnetic flux density across the contacts} \quad (13.8)$$

$$B_C = \frac{1}{2} B_g = \frac{\mu_0 I}{2g} \quad \text{Average magnetic flux density on moveable} \quad (13.9)$$

$$\vec{F}_C = \vec{I} \times \vec{B}_C w = \frac{\mu_0 I^2}{2g} w \quad \text{Lorentz force on the moveable} \quad (13.10)$$

$$B_M = B_g \left(\frac{S}{t} \right) = \frac{\mu_0 I S}{2g t} \quad \text{Magnetic flux density in the slot motor} \quad (13.11)$$

The Lorentz force (F_C) on the moveable conductor increases as the slot motor gap (g) decreases and as the length of the slot motor (w) increases. The slot motor flux density (B_M) increases as the slot motor air gap (g) decreases, as the slot motor thickness (t) decreases, and as the space (S) increases between the stationary and moveable conductors.

Comparing the Lorentz forces in **Eq. 13.6** and **Eq. 13.11** shows that the slot motor increases the force. The slot motor length (w) is approximately equal to the parallel length (l_M) of the conductors, and the slot motor air gap (g) is approximately equal to the space (S) between the conductors. Hence, the slot motor increases the Lorentz force by about a factor of 3.

c. Slot Motor Saturation

Saturation of the slot motor can be evaluated in 2 ways.

1. Assume slot motor saturation is a perfect flux limiter ($B_M = B_{Sat}$). This is a conservative assumption, because the actual hardware should have a little higher magnetic flux density.

- a. The flux density in the air gap (B_g , B_C) becomes constant.

$$B_C = \frac{1}{2} B_s = \frac{1}{2} B_M \frac{t}{S} = \frac{1}{2} B_{Sat} \frac{t}{S} \quad (13.12)$$

- b. The Lorentz force on the conductor (F_C) becomes linearly proportional to the current (I) with a constant flux density.

$$F_C = \frac{1}{2} I B_{Sat} w \frac{t}{S} \quad (13.13)$$

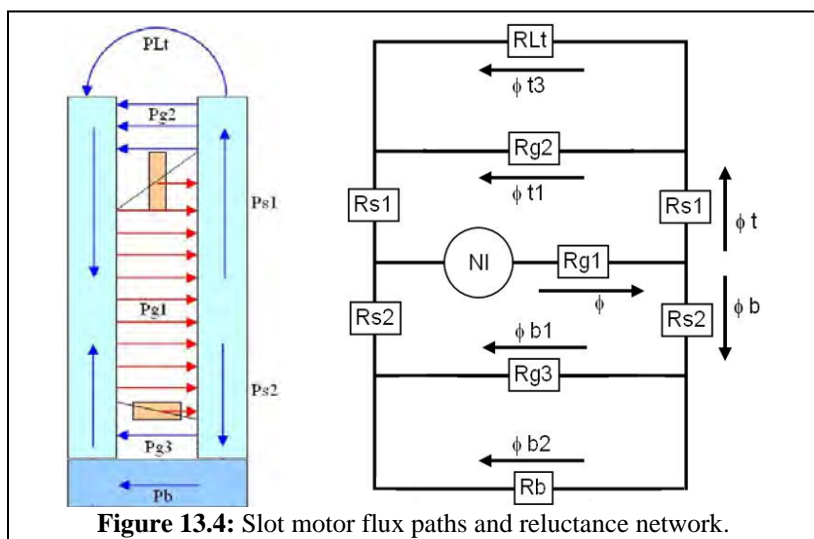
2. The reluctance network shown in **Fig. 13.4** can be solved with non-linear steel magnetic properties, using the dimensions from **Fig. 13.2** and **Fig. 13.3**.

- a. Air reluctance values:

$$\mathcal{R}_{g1} = \frac{g}{\mu_0 S w} \quad \text{Center gap} \quad (13.14)$$

$$\mathcal{R}_{g2} = \frac{g}{\mu_0 h_t w} \quad \mathcal{R}_{g3} = \frac{g}{\mu_0 h_b w} \quad \text{Leg gaps} \quad (13.15)$$

$$\mathcal{R}_{Lt} = \frac{1}{0.24 \mu_0 w + \mu_0 \frac{w}{\pi} \ln \left(1 + 2 \frac{t}{g} \right)} \quad \text{Top} \quad (13.16)$$



b. Steel reluctance values:

$$\mathcal{R}_{s1} = \frac{h_t + h_m}{\mu_r \mu_0 t w} \quad \text{Top of legs} \quad (13.17)$$

$$\mathcal{R}_{s2} = \frac{h_s + h_b}{\mu_r \mu_0 t w} \quad \text{Bottom of legs} \quad (13.18)$$

$$\mathcal{R}_b = \frac{g + t}{\mu_r \mu_0 t w} \quad \text{Bottom} \quad (13.19)$$

d. Example-10 – Slot Motor Force

Calculations were done for the reverse loop contact structure with and without a slot motor. The dimensions are shown in **Fig. 13.5**, with the moveable conductor in the closed position. The Lorentz force and slot motor magnetic flux density are calculated by solving the reluctance network (**Fig. 13.4**) for currents ranging from 1 kA to 45 kA.

The calculated results are listed in **Fig. 13.6** and shown on the graph in **Fig. 13.7**. The results include the Lorentz force with a slot motor, the Lorentz force for the reverse loop alone (no slot motor), the ratio of the Lorentz forces, and the magnetic flux density in the slot motor. The Lorentz force with a slot motor at 1 kA is 3.69 times the Lorentz force for the reverse loop alone (no slot motor) when the slot motor is not saturated, which is very close to the estimated factor of 3 based on assuming an infinite relative permeability for the steel.

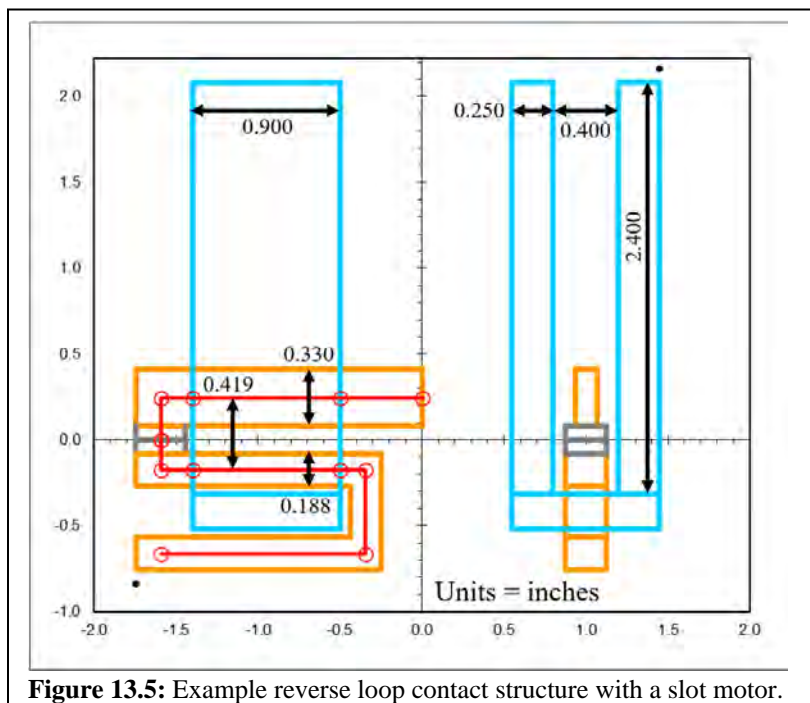


Figure 13.5: Example reverse loop contact structure with a slot motor.

	Slot Motor	Reverse Loop	Ratio	Slot Motor
Current	Force (Fs)	Force (Fr)	Fs / Fr	Flux Density
amperes	N	N	---	T
1,000	1.39	0.376	3.69	0.18
2,590	9.29	2.52	3.68	0.48
6,708	62.2	16.9	3.67	1.22
10,796	157.	43.8	3.58	1.66
17,374	390.	113.	3.43	1.95
27,962	865.	294.	2.94	2.19
45,000	1,730.	761.	2.27	2.39

Figure 13.6: Listing of calculated Lorentz force and flux density for the example reverse loop contact structure with and without a slot motor.

As described in [Eq. 13.12](#) and [Eq. 13.13](#), when the slot motor is saturated, the magnetic flux density becomes limited and the Lorentz force becomes linearly proportional to the current. At currents greater than 10.8 kA the slot motor is saturated ($B > 1.66$ T). If the slot motor didn't saturate, the flux density at 45 kA would be 6.92 T, but it's only 2.39 T, which demonstrates significant flux limiting, although not perfect flux limiting.

The Lorentz force for the reverse loop alone (no slot motor) remains proportional to the square of the current. Therefore, the ratio of the Lorentz

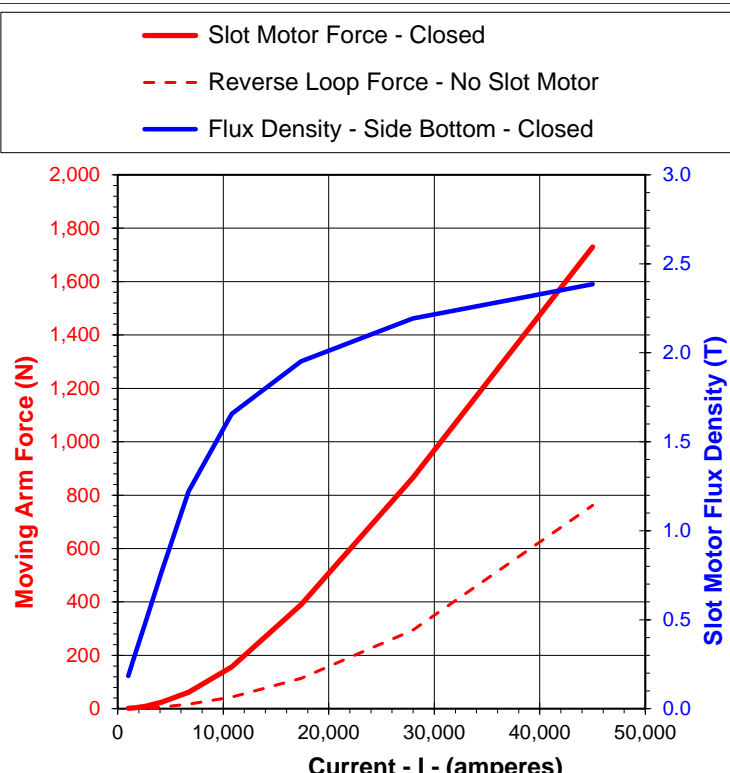


Figure 13.7: Calculation results for reverse loop with a slot motor.

force for the slot motor relative to the reverse loop decreases as the current rises above 10.8 kA. At 1 kA the force ratio is 3.69, at 10 kA the force ratio is 3.58, and at 45 kA, the force ratio is 2.27. Even though the slot motor saturates, the Lorentz force with the slot motor is more than 2x as large as for the reverse loop alone.

e. Contact Forces and Constriction

A mechanical mechanism in a circuit breaker holds the contacts closed with a spring force that exceeds the electromagnetic opening forces discussed earlier in this chapter (the reverse loop force between parallel conductors and the slot motor force). There is also a constriction force that occurs at the electrical contact spot, where the current contracts as it enters the small contact spot and expands when it departs. The contracting current and the expanding current form a reverse current loop at the contact spot that results in a repulsion force (**Fig. 13.8**).

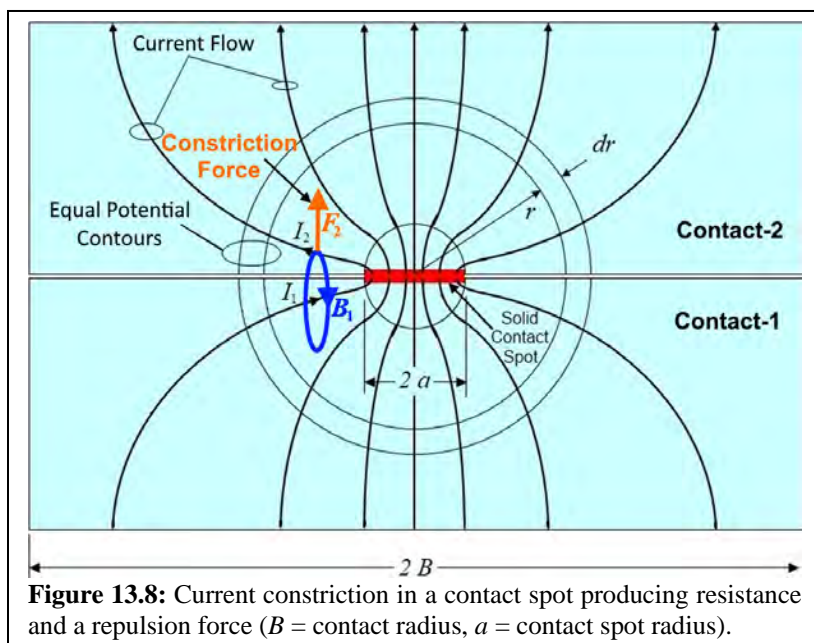


Figure 13.8: Current constriction in a contact spot producing resistance and a repulsion force (B = contact radius, a = contact spot radius).

The spring force is typically large enough to hold the contacts closed during an overload current with sufficient net force to avoid melting (welding) of the contact spot. The constriction force equations are shown below, as reported by Holm [31] for a single contact spot in air (**Eq. 13.20**) and by Slade [32] for 2-3 contact spots in a vacuum (**Eq. 13.22**) (force (N), current (A)). The electromagnetic repulsion forces at 2,590 A, are listed below from **Fig. 13.6**, and from **Eq. 13.21** and **Eq. 13.22**.

$$F_c = (1.0E - 7) I^2 \ln\left(\frac{B}{a}\right) \quad 1 \text{ contact spot (air)} \quad (13.20)$$

$$F_c = (3.56E - 7) I^2 \quad 1 \text{ contact spot for } \ln(B/a) = 3.56 \quad (13.21)$$

$$F_c = (8.0E - 5) I^{1.54} \quad \text{2-3 contact spots (vacuum)} \quad (13.22)$$

Slot motor force at 2,590 A (Fig. 13.6)	= 9.29 N
Reverse loop force at 2,590 A (Fig. 13.6)	= 2.52 N
Constriction force at 2,590 A (Eq. 13.21)	= 2.39 N
Constriction force at 2,590 A (Eq. 13.22)	= 2.99 N

The radius (a) of the contact spot in silver contacts can be calculated as the area in plastic deformation that will support the net force. **Appendix-C** gives the hardness (27 kg/mm^2) (265 MPa) and the electrical conductivity ($6.8E+7 \text{ S/m}$) for silver. Table 21.1a in Slade [32] gives the softening voltage (0.09 V) and melting voltage (0.37 V) for silver. The electrical resistance equation due to constriction is given in Holm [31] as follows (**Eq. 13.23**).

$$R_c = \frac{1}{2\sigma a} \quad \text{Constriction resistance [31]} \quad (13.23)$$

The maximum allowable contact spot resistance to avoid melting can be obtained from the softening voltage and the current.

$$R_c = \frac{0.09}{2590} = 3.47E - 5 \text{ ohm} \quad \text{Softening resistance at 2,590 A} \quad (13.24)$$

The minimum required contact spot radius to achieve the desired contact spot resistance can be obtained from **Eq. 13.23**, as follows.

$$a = \frac{1}{2\sigma R_c} \quad \text{Contact spot radius to achieve } R_c \quad (13.25)$$

$$a = \frac{1}{2(6.8E + 7)(3.47E - 5)} = 2.12E - 4 \text{ m} \quad \text{Contact Spot radius} \quad (13.26)$$

The minimum required net contact force (spring force minus all of the repulsion forces) can be calculated based on the hardness and the contact spot radius. Hardness is measured by applying a force to a surface and dividing the applied force by the area of the permanent deformation spot.

$$H = \frac{F_c}{\pi a^2} \quad F_c = \pi a^2 H \quad \text{Hardness & Contact force} \quad (13.27)$$

$$F_c = \pi (2.12E - 4)^2 (265E + 6) = 37.4 \text{ N} \quad \text{Net Contact force} \quad (13.28)$$

There are some interesting results from these simple calculations, as follows.

- The constriction force is the same order of magnitude as the reverse loop conductor force.
- The constriction force is produced by the contraction and expansion of the current through the contact spot.
- The contact spot is very small. In this case, the contact spot radius is $212 \mu\text{m}$ (0.008 inch).

- The contact springs must produce sufficient net force at the maximum overload current to avoid welding the contacts.

f. Slot Motor Configuration Options

Four alternative slot motor configurations are shown in **Fig. 13.9**. All of the slot motor designs (except Design-D) produce a Lorentz force (F_C) on the moveable conductor in the upward direction.

- The magnetic flux is directed between the stationary and moveable conductors in the slot. Design-A was evaluated in detail in the previous sections.
- The slot motor is inverted from Design-A. This configuration produces the same Lorentz force and the same magnetic flux density in the slot motor as Design-A.
- The stationary conductor with the reverse current is removed from Design-B. Design-C produces the same Lorentz force as Design-B. Excess magnetic flux is produced between the slot motor legs extending below the moveable conductor. As shown, the Design-C slot motor will saturate at a lower current than Design-B. This difference can be minimized by truncating the slot motor legs at the bottom of the moveable conductor. In general, a single current-carrying conductor will move toward the closed end of the slot.
- The slot motor is inverted from Design-C. This configuration produces the opposite direction Lorentz force and magnetic flux density in the slot motor as Design-C. In general, a single current-carrying-conductor will move toward the closed end of the slot.
- The top of the slot motor is closed. This configuration produces the same Lorentz force and half of the magnetic flux density in the slot motor as all the other designs. The added closed end at the top of the slot motor allows the magnetic flux to return through both the top and the bottom of the slot motor.

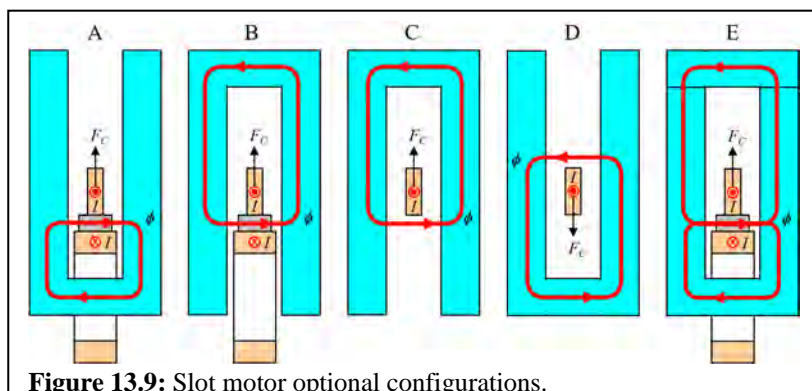


Figure 13.9: Slot motor optional configurations.

14. Thomson Coil

The Thomson Coil actuator was invented by Elihu Thomson (1853-1937). His company, the Thomson-Houston Electric Company, merged with the Edison General Electric Company in 1892 to become General Electric. Elihu Thomson was granted more than 700 patents.

A Thomson Coil actuator consists of a primary coil and an electrically conductive plate closely spaced from the coil with a capacitor connected to the coil (**Fig. 14.1**). When the capacitor is discharged into the coil, the coil current rises and produces an increasing magnetic field. The

increasing magnetic field passes through the electrically conductive plate and produces eddy currents (I_e) in the opposite direction to the primary coil current (I_p), per Lenz's law. The eddy currents interact with the magnetic field to produce a Lorentz force on the electrically conductive plate that is directed away from the coil (repulsion).

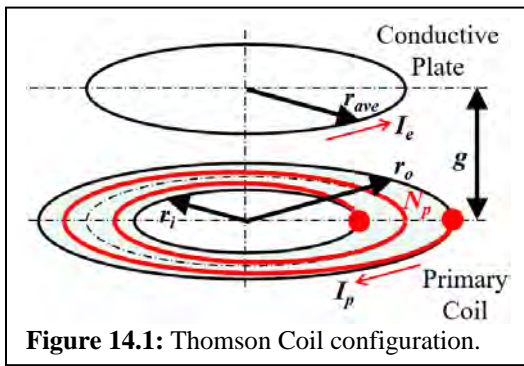


Figure 14.1: Thomson Coil configuration.

The Thomson coil is well known as a high-speed actuator. It produces a very high transient pulse of current and force for applications such as catheter navigation, metal forming, and fast opening of electrical contacts in switches and circuit breakers [41]. Also, steady-state eddy current repulsion is used in levitation systems for MAGLEV trains. Puumala and Kettunen [42] present an alternative configuration in which the conductive plate is replaced with a coil that is driven in series with the primary coil. They show that the series coils give a higher mechanical energy conversion efficiency than the eddy current configuration. Because of the added complexity of a moving contact, this approach is unusual, especially when high currents are involved.

The force between 2 coils is derived as **Eq. 12.23** (shown as **Eq. 14.1**). The axial repulsion force (F_x) is equal to the product of the primary current (I_1), the eddy current in the plate (I_2), and the derivative of the mutual inductance (L_{12} or L_M) in the x-direction. Slemmon [2] and Brauer [9] show the derivation for the force based on an energy balance, where the mechanical energy is equal to the difference between the input electric energy and the stored energy. Roodenburg and Evenblij [41] show the same equation.

$$F_x = I_1 I_2 \frac{dL_M}{dx} \quad (14.1)$$

A major application for the Thomson Coil is for DC circuit breakers. A popular approach is the “parallel hybrid switching configuration” with

electrical contacts in parallel with power electronics to get the best performance from each. Electrical contacts carry current with a small heat dissipation, but switching is slow and typically takes several milliseconds. Power electronics (MOSFET, IGBT, SCR) are capable of very fast switching, but the heat dissipation is high when carrying current. In a parallel hybrid system, the electrical contacts carry the steady-state rated current. At the start of a short circuit, the current commutes into the parallel power electronics, the electrical contacts are opened, and the power electronics switch off (extinguish) the current. The key to this system is to open the electrical contacts and commutate the current very quickly (< 1 ms) because the current rate of rise in a short circuit can be very high. For example, in a 2 kV DC system with 20 kA available and a time constant of 2 ms, the initial current rate of rise is 10 kA/ms. Also, adding 1 mH of inductance in a DC circuit breaker reduces the current rate of rise to 1.7 kA/ms.

Typical excitation circuits are shown in **Fig. 14.2** and **Fig. 14.3** [36] [43], where a precharged capacitor (C_1) is discharged into the primary coil (L_1) through a circuit containing a series resistance (R_1), a diode (D_1), and a thyristor switch (T_1) (electronic trigger) such as a high current SCR. The diode connection in **Fig. 14.3** allows an oscillating current between the stored energy in the inductor and the stored energy in the capacitor. Peng et al. [43] discuss the details of 3 drive circuits with a single capacitor, and 2 drive circuits incorporating 2 capacitors. The single capacitor drive circuit system dynamics result in a coupling between the peak current and the pulse frequency. The 2 capacitor drive circuits give the capability to discharge the 2nd capacitor with a delayed trigger to decouple the peak current and the pulse frequency.

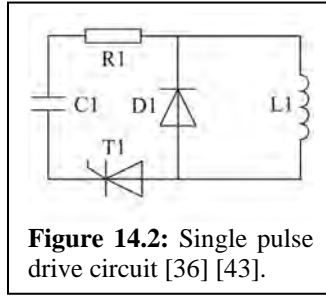


Figure 14.2: Single pulse drive circuit [36] [43].

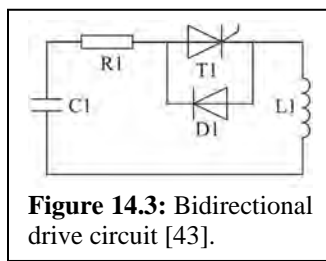


Figure 14.3: Bidirectional drive circuit [43].

The analysis described here was formulated for a spreadsheet. The purpose of the spreadsheet solution was to quickly evaluate design alternatives and capacitor requirements (capacitance, voltage, and size). One of the major factors in the design of a Thomson coil is the size of the capacitor, which depends on the voltage rating and capacitance. The spreadsheet solution takes about 10 seconds. Therefore, many design iterations can be completed quickly. This spreadsheet model was intended as a first cut with sufficient accuracy to determine feasibility and valid trends (“the trend is your friend” because it points the way to performance improvements). A transient FEA model provides the best accuracy and should be used to determine the final design. The FEA model can also include mechanical structural characteristics (mechanical stress, mechanical resonance). The following assumptions make it possible to formulate a spreadsheet model.

- Both the coil and the plate are assumed to be disks, such that the geometry is axisymmetrical. This is by far the more typical configuration.
- A uniform eddy current distribution is assumed in the plate. If the entire plate links all of the magnetic flux, the shorter current path at the inside radius would have less resistance and more current. However, the magnetic flux spreads out and the inside radius links less flux than the center of the plate. Therefore, this assumption is acceptable. Note that a transient FEA model gives the exact solution. Also, the uniform eddy currents in the disk could be limited to the skin depth in the disk (see Ch. 3.h). The skin depth could be determined in a few iterations by assuming the dominant frequency of the system, running the model, and updating the frequency and skin depth based on the resulting current waveform.
- The eddy current path resistance is based on the average radius of the plate, which corresponds with the eddy current distribution assumption.
- There is no steel in the vicinity.
- The current is allowed to be both positive and negative, as with an ideal switch. If an SCR is used, the current cannot go negative so some of the equations concerning the circuit would need to be adjusted.
- The physics are limited to permeance variation. There is no proximity effect in the coil wires. The eddy currents in the plate are solely due to the time-varying current in the coil, and to the plate motion.

a. Flux Paths, Permeance, Inductance

The magnetic field produced by the primary coil can be visualized as shown by the sketch in Fig. 14.4. The sketch shows the magnetic field is concentrated in the center of the coil and spreads out around the coil. It also shows that only some of the magnetic field passes through the conductive plate. This illustrates that the flux paths can't be defined by regular geometric shapes (straight lines and circular arcs, as defined in Ch. 1) to calculate the

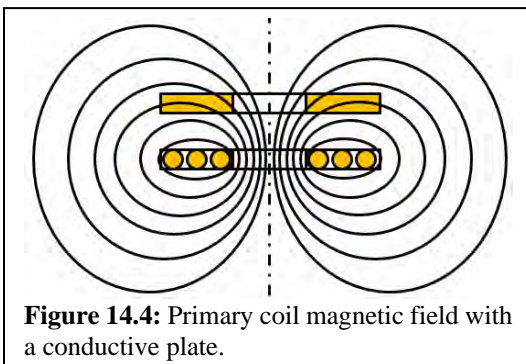


Figure 14.4: Primary coil magnetic field with a conductive plate.

path of the magnetic field in the air. The main challenge in modeling the Thomson coil is defining the permeance of the air flux paths.

The sketch in **Fig. 14.5** shows the three magnetic flux paths for this system. They include, 1) the primary flux path (ϕ_p) passing through the entire space below the primary coil, 2) the eddy current producing flux path (ϕ_e) passing through the conductive plate, and 3) the leakage flux path (ϕ_L) passing through the space between the conductive plate and the primary coil. Based on these definitions, the primary flux is equal to the sum of the eddy-current producing flux and leakage flux, according to the equation shown in **Fig. 14.5**.

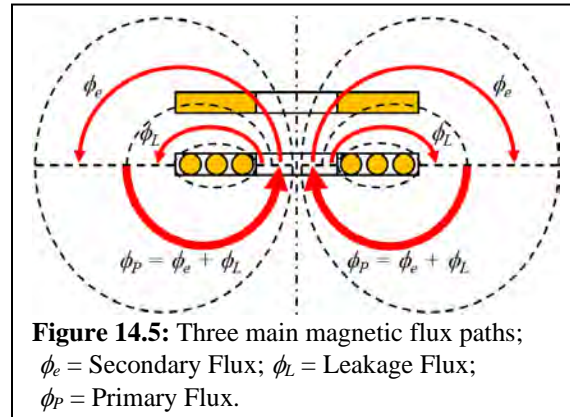


Figure 14.5: Three main magnetic flux paths;
 ϕ_e = Secondary Flux; ϕ_L = Leakage Flux;
 ϕ_p = Primary Flux.

and 3) the leakage flux path (ϕ_L) passing through the space between the conductive plate and the primary coil. Based on these definitions, the primary flux is equal to the sum of the eddy-current producing flux and leakage flux, according to the equation shown in **Fig. 14.5**.

The permeance of the primary flux path (P_p) (**Eq. 14.5**) is defined based on the air core coil inductance (**Ch. 11**).

The leakage flux path permeance (P_L) in **Fig. 14.6** can be defined based on the flux path volume and flux path length. The eddy current flux path permeance (P_e) is defined as the difference between the primary flux path permeance and the leakage flux path

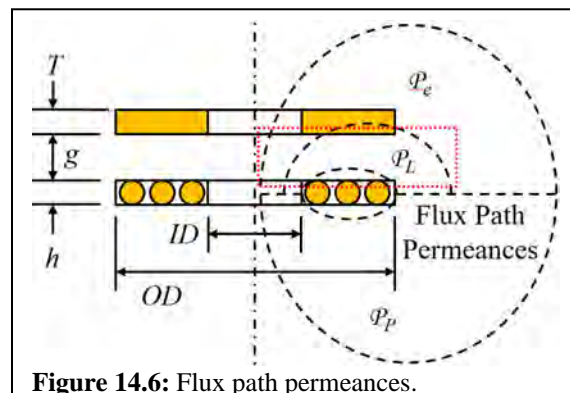


Figure 14.6: Flux path permeances.

permeance (**Eq. 14.10**). The inductance of the primary coil alone can be calculated from the air core coil inductance (**Eq. 14.2**). The total permeance for the primary coil (P_{PT}) can be obtained from the inductance of the primary coil (**Eq. 14.4**), as follows.

$$L_p = K \mu_0 a N_p^2 \left(\frac{D}{\sqrt{D^2 + h^2}} \right) \quad \text{Coil inductance from Eq. 11.5} \quad (14.2)$$

$$L_p = N_p^2 P_{PT} \quad \text{Coil inductance from Eq. 1.27} \quad (14.3)$$

$$P_{PT} = \frac{L_p}{N_p^2} \quad \text{Total permeance} \quad (14.4)$$

$$\boxed{\mathcal{P}_p = 2\mathcal{P}_{PT} = 2 \frac{L_p}{N_p^2}}$$

Permeance of total flux path below or above (14.5)

The permeance of the leakage flux path (**Eq. 14.9**) can be estimated from the volume and length of the leakage flux path, as detailed in **Ch. 1.g**, which is the air gap between the coil and the disk, plus protective or insulation layers, plus (by assumption) 1/3 of the coil conductor thickness and 1/3 of the plate thickness. Also, the equations can be simplified by assuming the inside radius (r_i) of the coil is small compared to the outside radius (r_o) of the coil and setting $r_i = 0$. The geometric terms in the equations below are defined graphically in **Fig. 14.6** (g = air gap, T = plate thickness)

$$v = \pi \left(r_0^2 - r_i^2 \right) \left(g + \frac{h}{3} + \frac{T}{3} \right) \quad \text{Leakage path volume} \quad (14.6)$$

$$v \approx \pi r_0^2 \left(g + \frac{h}{3} + \frac{T}{3} \right) \quad \text{for } r_i \ll r_0 \quad \text{Leakage path volume} \quad (14.7)$$

$$l = r_0 - r_i \approx r_0 \quad \text{for } r_i \ll r_0 \quad \text{Leakage path length} \quad (14.8)$$

$$\boxed{\mathcal{P}_L = \mu_0 \frac{v}{l^2} \approx \mu_0 \pi \left(g + \frac{h}{3} + \frac{T}{3} \right)} \quad \text{Leakage flux path permeance} \quad (14.9)$$

$$\boxed{\mathcal{P}_p = \mathcal{P}_e + \mathcal{P}_L \quad \mathcal{P}_e = \mathcal{P}_p - \mathcal{P}_L}$$

Eddy current flux path permeance (14.10)

As written so far, **Eq. 14.9** allows the leakage flux path permeance (\mathcal{P}_L) to increase beyond the value for the permeance of the entire flux path above the coil (\mathcal{P}_p), which results in a negative eddy-current flux path permeance (\mathcal{P}_e) in **Eq. 14.10**. A negative permeance is meaningless, therefore the maximum leakage permeance (\mathcal{P}_L) must be limited to the permeance above the primary coil (\mathcal{P}_p). This can be accomplished by modeling the leakage flux path permeance with an exponential form, as follows, where g_0 is the starting value for the gap.

$$\boxed{\mathcal{P}_{L0} = \mu_0 \pi \left(g_0 + \frac{h}{3} + \frac{T}{3} \right)}$$

Leakage permeance starting value (14.11)

$$\mathcal{P}_{L\max} = \mathcal{P}_p \quad \text{Leakage permeance maximum value} \quad (14.12)$$

$$\frac{d\mathcal{P}_L}{dg} = \mu_0 \pi \quad \text{Leakage permeance derivative from Eq. 14.9} \quad (14.13)$$

$$\boxed{\Delta\mathcal{P}_L = \mathcal{P}_p - \mathcal{P}_{L0}} \quad \text{Leakage permeance maximum change} \quad (14.14)$$

$$\boxed{\Delta g_M = \frac{\Delta\mathcal{P}_L}{\mu_0 \pi}} \quad \text{Leakage gap maximum change} \quad (14.15)$$

$$\boxed{\mathcal{P}_L = \mathcal{P}_{L0} + \Delta\mathcal{P}_L \left(1 - e^{-(g-g_0)/\Delta g_M} \right)}$$

Leakage permeance (14.16)

$$\frac{d\mathcal{P}_L}{dg} = \Delta\mathcal{P}_L \frac{1}{\Delta g_M} = \Delta\mathcal{P}_L \frac{\mu_0 \pi}{\Delta\mathcal{P}_L} = \mu_0 \pi \quad \text{Leakage permeance derivative} \quad (14.17)$$

The exponential leakage permeance equation (**Eq. 14.16**) provides several advantages and benefits over **Eq. 14.9**. At the initial gap (g_0) it produces the

correct starting value (\mathcal{P}_{L0}) and the correct derivative ($d\mathcal{P}_L/dg = \mu_0\pi$) for the leakage permeance. At an infinite gap, it produces a value equal to the permeance above the coil (\mathcal{P}_p) and the eddy current flux path permeance remains positive. The leakage flux path permeance changes smoothly throughout all possible values for the gap (g), which would not happen if it were truncated at $\mathcal{P}_L = \mathcal{P}_p$. Truncating the leakage permeance would result in a singularity, specifically a very large value for the derivative ($d\mathcal{P}_L/dg$) and an eddy current spike.

The leakage inductance (L_{leak}) is defined as the magnetic flux (ϕ_L) from the primary coil that links only the primary coil (N_p) per ampere of the primary current (I_p).

$$L_{leak} = \frac{N_p \phi_e}{I_p} = \frac{N_p}{I_p} \left(N_p I_p \frac{1}{1/P_L + 1/P_p} \right) \quad \text{Leakage inductance} \quad (14.18)$$

$$L_{leak} = N_p^2 \frac{1}{\frac{1}{P_L} + \frac{1}{P_p}}$$

Leakage inductance (14.19)

The mutual inductance (L_M) is defined as the magnetic flux (ϕ_e) from the primary coil that links the eddy current plate (N_e) per ampere of the primary current (I_p).

$$L_M = \frac{N_e \phi_e}{I_p} = \frac{1}{I_p} \left(N_p I_p \frac{1}{1/P_e + 1/P_p} \right) \quad \text{Mutual inductance } (N_e = 1) \quad (14.20)$$

$$L_M = N_p \frac{1}{\frac{1}{P_e} + \frac{1}{P_p}}$$

Mutual inductance (14.21)

b. System Model Equations

The system model for the Thomson coil is shown in **Fig. 14.7**, from which the 4 loop equations can be written, 1) primary current loop (I_p), 2) primary flux loop (ϕ_p), 3) conductive plate flux loop (ϕ_e), and 4) eddy current loop (I_e). The system equation (**Eq. 14.28**) is obtained by combining the 4 loop equations (**Eq. 14.24 – Eq. 14.27**). Note that the motion of the plate produces a time-varying air gap (velocity) (dg/dt), and as a result, the leakage permeance (\mathcal{P}_L)

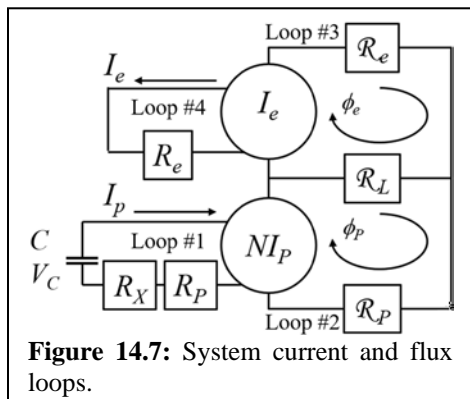


Figure 14.7: System current and flux loops.

and eddy current permeance (\mathcal{P}_e) have a time-varying element in the system equations (**Eq. 14.30** and **Eq. 14.31**) which affects both the primary current and the eddy current. **Fig. 14.7** includes the resistance for the eddy current plate (R_e), the primary coil (R_p), and the extra parasitic resistance (R_x) such as the capacitor ESR, wiring, connectors, and the SCR resistive drop (assumed linear). The equations for the eddy current plate resistance (R_e) and the primary coil resistance (R_p) are shown in **Eq. 14.34** and **Eq. 14.35**.

$$\mathcal{R}_p = \frac{1}{\mathcal{P}_p} \quad \mathcal{R}_L = \frac{1}{\mathcal{P}_L} \quad \mathcal{R}_e = \frac{1}{\mathcal{P}_e} \quad \text{Reluctance} \quad (14.22)$$

$$R_{PX} = R_p + R_x \quad \text{Resistance in Loop #1} \quad (14.23)$$

$$V_C = \left(V_0 - \frac{1}{C} \int I_p dt \right) = I_p R_{PX} + N_p \frac{d\phi_p}{dt} \quad \text{Loop #1 – Sum of V} \quad (14.24)$$

$$N_p I_p = \phi_p (\mathcal{R}_p + \mathcal{R}_L) - \phi_e (\mathcal{R}_L) \quad \text{Loop #2 – Sum of NI} \quad (14.25)$$

$$0 = -\phi_p (\mathcal{R}_L) + \phi_e (\mathcal{R}_L + \mathcal{R}_e) + I_e \quad \text{Loop #3 – Sum of NI} \quad (14.26)$$

$$I_e = \frac{1}{R_e} \frac{d\phi_e}{dt} \quad \text{Loop #4 – Sum of V} \quad (14.27)$$

Combining the 4 loop equations gives the following 2nd order differential equation for the system. The last term in **Eq. 14.30** and **Eq. 14.31** is the result of the motion of the conductive plate. When there is no motion, those terms become zero.

$$A \frac{d^2\phi_e}{dt^2} + B \frac{d\phi_e}{dt} + D \frac{d\phi_e}{dt} = \frac{N_p}{R_{PX}} V_C \quad (14.28)$$

$$A = \frac{N_p^2}{\mathcal{R}_L R_e R_{PX}} \quad (14.29)$$

$$B = \frac{N_p^2}{R_{PX}} \left(\frac{\mathcal{R}_L + \mathcal{R}_e}{\mathcal{R}_L} \right) + \frac{1}{R_e} \left(\frac{\mathcal{R}_L + \mathcal{R}_p}{\mathcal{R}_L} \right) + \frac{N_p^2}{R_e R_{PX}} \frac{d}{dt} \left(\frac{1}{\mathcal{R}_L} \right) \quad (14.30)$$

$$D = \left(1 + \frac{\mathcal{R}_e}{\mathcal{R}_L} + \frac{\mathcal{R}_e}{\mathcal{R}_p} \right) \mathcal{R}_p + \frac{N_p^2}{R_{PX}} \frac{d}{dt} \left(\frac{\mathcal{R}_e}{\mathcal{R}_L} \right) \quad (14.31)$$

Resistance:

The resistance for the primary coil (R_p) and the eddy current plate (R_e) are calculated as follows.

$$r_{ave} = \frac{r_o + r_i}{2} \quad \text{Average radius of plate and primary coil} \quad (14.32)$$

$$l = 2\pi r_{ave} \quad \text{Average circumference of plate and primary coil} \quad (14.33)$$

$$R_p = \frac{N_p l}{\sigma \pi d^2 / 4} \quad \text{Primary coil resistance (} d = \text{wire diameter)} \quad (14.34)$$

$$R_e = \frac{l}{\sigma(r_o - r_i)T} \quad \left[\begin{array}{l} \text{Eddy Plate Resistance, } T = \text{Plate Thickness} \\ \text{or } T = \text{Skin Depth as discussed earlier} \end{array} \right] \quad (14.35)$$

Magnetic Force:

The current in the primary coil and the eddy current in the conductive plate can be calculated by solving the system equation (**Eq. 14.28**) with a time step technique, and substituting the result back into the loop equations. The force between the primary coil and the conductive plate can then be determined from **Eq. 14.1** based on the primary current (I_p), the eddy current (I_e), and the derivative of the mutual inductance (dL_M/dg), where the mutual inductance (L_M) is defined in **Eq. 14.21**.

$$F_M = I_p I_e \frac{dL_M}{dg}$$

Magnetic Force from **Eq. 14.1**
(14.36)

Mechanical Motion:

The equations of motion (**Ch. 7.a**) show that the summation of the forces (F) acting on a mass (m) causes the mass to accelerate (a) (**Eq. 14.37**). The total mass being accelerated includes the conductive plate (m_e , **Eq. 14.44**), and all of the parts that are attached to the conductive plate. The forces include the magnetic force (F_M), the spring force (F_S), and other resisting forces, such as the atmospheric force (F_{atm}) on a vacuum contact bottle.

$$\sum F = F_M - F_S - F_{atm} = ma \quad \text{Inertia force balance} \quad (14.37)$$

$$a = \frac{F_M - F_S - F_{atm}}{m} \quad \text{Acceleration} \quad (14.38)$$

$$\Delta v = a \Delta t \quad \text{Change in velocity} \quad (14.39)$$

$$\Delta x = v_{ave} \Delta t \quad \text{Change in position} \quad (14.40)$$

Temperature Rise:

The temperature rise during the operation of the Thomson coil can be calculated as shown in **Ch. 5.b**. The operation of a Thomson coil starts with the discharge of a capacitor into the primary coil. This results in a very short (on the order of milliseconds) transient current pulse in the primary coil and a very short transient eddy current pulse in the conductive plate. During the short pulse, there is no significant heat transfer by convection or radiation to the surrounding environment. Therefore, all of the heat can be assumed to be absorbed by the coil and the conductive plate. The temperature rise can be calculated for the primary coil (ΔT_p) and the eddy current plate (ΔT_e), as follows.

$$Q_p \Delta t = m_p c_{pp} \Delta T_p \quad \text{Energy absorbed by the primary coil} \quad (14.41)$$

$$Q_p = I_p^2 R_p \quad \text{Heat dissipation in the primary coil}$$

Δt = Time interval

m_p = Mass of the primary coil

c_{PP} = Specific Heat of the primary coil

ΔT_p = Temperature Rise of the primary coil

$$Q_e \Delta t = m_e c_{pe} \Delta T_e \quad \text{Energy absorbed by the conductive plate} \quad (14.42)$$

$$Q_e = I_e^2 R_e \quad \text{Heat dissipation in the conductive plate}$$

Δt = Time interval

m_e = Mass of the conductive plate

c_{pe} = Specific Heat of the conductive plate

ΔT_e = Temperature Rise of the conductive plate

The mass of the primary coil and the conductive plate can be calculated as follows (**Eq. 14.43** and **Eq. 14.44**). The thermal and electrical properties for various materials, including the specific heat (c_p), and density (ρ), are listed in **Appendix-C**.

$$m_p = \rho_p N_p l \pi d^2 / 4 \quad \text{Mass of primary coil} \quad (14.43)$$

ρ_p = Density of the conductive plate

$$m_e = \rho_e \pi (r_o^2 - r_i^2) T \quad \text{Mass of conductive plate} \quad (14.44)$$

ρ_e = Density of the conductive plate

- Approximate Formulae for Verification

It is often useful to derive approximate solutions to verify the approach. Here, a solution is provided first for the current waveform, then for the Lorentz force.

--- Linear RLC System Dynamics, Over Damped, Under Damped

The solution to the differential equations can be checked by comparison to published results, FEA results, test results, or another analysis method. The Thomson Coil is an RLC system, which has the following solution for constant RLC values. The inductance changes with the motion of the conductive plate and the resistance in the semiconductors is nonlinear. However, the characteristics of an RLC system with constant values can be used to define the general shape of the current pulse and to verify the time step solution. The RLC free dynamic system response is described by the following equation.

$$L_{\text{leak}} \frac{dI_p}{dt} + I_p R_{PX} + \frac{1}{C} \int I_p dt = 0 \quad \text{Free dynamic system} \quad (14.45)$$

$$I_p = A e^{st} \quad \text{Exponential solution} \quad (14.46)$$

The exponential solution can be substituted into the free dynamic equation to determine the exponent (s).

$$\left(L_{\text{leak}} s + R_{PX} + \frac{1}{C s} \right) A e^{st} = 0 \quad \text{Free dynamic system} \quad (14.47)$$

$$L_{\text{leak}} s^2 + R_{\text{PX}} s + \frac{1}{C} = 0 \quad \text{Rearrange to solve for } s \quad (14.48)$$

$$s = \frac{-R_{\text{PX}} \pm \sqrt{R_{\text{PX}}^2 - 4(L_{\text{leak}}/C)}}{2L_{\text{leak}}} \quad \text{Quadratic solution for } s \quad (14.49)$$

$$s = \frac{-R_{\text{PX}} \pm \sqrt{\left(\frac{R_{\text{PX}}}{2L_{\text{leak}}}\right)^2 - \frac{1}{L_{\text{leak}}C}}}{2L_{\text{leak}}} \quad \text{Rearranged} \quad (14.50)$$

- If the square root term is positive (+) the system is **overdamped** (or aperiodic) and the system response follows an exponential decay with no oscillation.
- If the square root term is negative (-) the system is **underdamped** (or pseudo periodic) and the system response includes an oscillation.
- If the square root term is zero (0) the system is **critically damped** (or aperiodic) and the system response follows a short exponential decay with no oscillation.

$$\omega_N = \sqrt{\frac{1}{L_{\text{leak}}C}} \quad \text{Natural (resonance) frequency} \quad (14.51)$$

$$f_N = \frac{\omega_N}{2\pi} \quad \text{Hz} \quad \text{Natural (resonance) frequency} \quad (14.52)$$

When the system resistance (R_{PX}) is set equal to the critical damping (R_C), the square root term will equal zero, and the critical damping can be defined as follows.

$$\left(\frac{R_C}{2L_{\text{leak}}}\right)^2 = \frac{1}{L_{\text{leak}}C} = \omega_N^2 \quad (14.53)$$

$$R_C = 2\sqrt{\frac{L_{\text{leak}}}{C}} = 2L_{\text{leak}}\omega_N \quad \text{Critical Damping} \quad (14.54)$$

The ratio of the system resistance (R_{PX}) to the critical damping (R_C) is the damping ratio (ξ).

$$\xi = \frac{R_{\text{PX}}}{R_C} = \frac{1}{2} R_{\text{PX}} \sqrt{\frac{C}{L_{\text{leak}}}} \quad \text{Damping Ratio} \quad (14.55)$$

The system resistance (R_{PX}) can be written as a function of the damping ratio (ξ) and the critical damping (R_C). The solution for (s) can then be written as a function of the damping ratio (ξ) and the natural frequency (ω_N), as follows.

$$R_{\text{PX}} = \xi R_C = 2L_{\text{leak}}\xi\omega_N \quad (14.56)$$

$$s = -\xi\omega_N \pm \omega_N\sqrt{\xi^2 - 1} \quad \xi > 1, \text{overdamped} \quad (14.57)$$

$$s = -\xi\omega_N \quad \xi = 1, \text{critically damped} \quad (14.58)$$

$$s = -\xi\omega_N \pm j\omega_N\sqrt{1 - \xi^2} \quad \xi < 1, \text{underdamped} \quad (14.59)$$

The slower response systems produce less eddy currents and less force. Therefore, the higher speed underdamped systems are more useful for Thomson Coil applications. The solution for the underdamped system response is as follows.

$$\omega_D = \omega_N\sqrt{1 - \xi^2} \quad \text{Damped natural frequency} \quad (14.60)$$

$$I_p = A e^{-\xi\omega_N t} e^{\pm j\omega_D t} \quad \text{Underdamped solution} \quad (14.61)$$

$$e^{j\theta} = \cos(\theta) + j\sin(\theta) \quad \text{Euler Identity} \quad (14.62)$$

The underdamped system response can be written in the following form, with the magnitude (A) and the phase angle (α) between the voltage and current, by incorporating the Euler identity.

$$I_p = A e^{-\xi\omega_N t} \cos(\omega_D t + \alpha) \quad \text{Underdamped solution} \quad (14.63)$$

The magnitude (A) and the phase angle (α) can be determined from the initial conditions of the primary current. The phase angle (α) is determined at $t = 0$, where the primary current is zero.

$$I_p|_{t=0} = A \cos(\alpha) \quad \text{Eq. 14.63 (at } t = 0) \quad (14.64)$$

$$I_p|_{t=0} = 0 \quad \text{Initial Primary Current} \quad (14.65)$$

$$\cos(\alpha) = 0 \quad \text{Combine Eq. 14.64 and Eq. 14.65} \quad (14.66)$$

$$\alpha = \frac{\pi}{2} \quad \text{Phase angle} \quad (14.67)$$

The magnitude (A) can be determined at $t = 0$, based on the rise rate or derivative of the primary current. The initial rise rate of the current is defined by Faraday's Law, as follows.

$$V_C = L_{\text{leak}} \frac{dI_p}{dt} \quad \text{Faraday's Law (at } I_p = 0, t = 0) \quad (14.68)$$

$$\left. \frac{dI_p}{dt} \right|_{t=0} = \frac{V_C}{L_{\text{leak}}} \quad \text{Initial current rise rate (at } t = 0) \quad (14.69)$$

The derivative of the underdamped solution (Eq. 14.63) (at $t = 0$) is combined with Eq. 14.69.

$$\left. \frac{dI_p}{dt} \right|_{t=0} = A\omega_N \left(\xi \cos(\alpha) + \sqrt{1 - \xi^2} \sin(\alpha) \right) \quad (14.70)$$

$$\frac{V_c}{L_{leak}} = A\omega_N \left(\xi \cos(\alpha) + \sqrt{1 - \xi^2} \sin(\alpha) \right) \quad (14.71)$$

Eq. 14.67 and **Eq. 14.71** are combined to determine the magnitude (A).

$$\frac{V_c}{L_{leak}} = A\omega_N \sqrt{1 - \xi^2} = A\omega_D \quad \text{Combine Eq. 14.67 and Eq. 14.71} \quad (14.72)$$

$$A = \frac{V_c}{L_{leak}\omega_D}$$

Magnitude

(14.73)

The linear RLC system dynamic response is defined as follows, by combining **Eq. 14.63**, **Eq. 14.67** and **Eq. 14.73**.

$$I_p = \frac{V_c}{L_{leak}\omega_D} e^{-\xi\omega_N t} \cos\left(\omega_D t + \frac{\pi}{2}\right)$$

Linear RLC system response

(14.74)

--- Approximate Lorentz Force estimate:

The repulsion Lorentz force on the plate can be estimated from the primary coil current (I_p) and the eddy current (I_e) in the conductive plate. This can be approximated by assuming a uniform eddy current distribution and dividing the eddy current into separate sections that align with each turn of the primary coil, and assuming that each turn of the primary coil interacts only with the eddy current section directly across the air gap (g). This simplifying assumption is acceptable as a quick approximation, because the distance to the next turn is larger, relatively, and the force due to the next turn is relatively smaller. The magnetic flux density (**Eq. 14.75**) acting on the eddy current from the primary current is defined by the circular flux path around each winding of the primary current at a radius equal to the air gap (g). Note that this approximation tends to underestimate the force, since the interaction is limited to turns facing each other

$$B_p = \mu_0 H = \mu_0 \frac{I_p}{2\pi g} \quad \text{Primary flux density on the eddy current} \quad (14.75)$$

$$F = \frac{I_e}{N_p} B_p N_p l = I_e \mu_0 \frac{I_p}{2\pi g} 2\pi r_{ave} \quad \text{Lorentz force estimate} \quad (14.76)$$

$$F = \mu_0 I_e I_p \frac{r_{ave}}{g} \quad \text{approximate Lorentz force estimate} \quad (14.77)$$

c. Solutions and Results

A Thomson Coil **Example Model** was defined with the following dimensions, capacitance, voltage, primary coil winding, and electrically conductive plate. An additional mass and spring force are specified that can represent a mechanical mechanism for the system. The parasitic resistance can include the capacitor ESR, wiring, connectors, and SCR effective resistance.

Input Values – Capacitor:	<u>Example Model</u>
Capacitor Voltage (V_C)	= 350 V
Capacitance (C)	= 0.01 F
Parasitic Resistance (R_X).....	= 0.002 ohm

Input Values – Primary Coil Winding:

Coil Inside Diameter (ID).....	= 50.8 mm
Coil Outside Diameter (OD).....	= 127.0 mm
No. of Turns (N_P).....	= 15 turns
Wire Size (AWG).....	= 11 AWG
Height of Wire (h)	= 2.3 mm

Input Values – Electrically Conductive plate (same ID and OD as the coil):

Plate Thickness (T).....	= 12.7 mm
Air Gap – Plate to Coil (g)	= 2.5 mm
Plate Material	= Aluminum

Input Values – Additional mass and spring force due to the mechanism:

Additional Moving Mass (m)	= 1.5 kg
Additional Spring Force (F_S).....	= 500 N
Additional Atmospheric Force (F_{atm})	= 250 N

The following basic characteristics are calculated from the input values. The leakage inductance and the mutual inductance are for the initial air gap between the primary coil and the conductive plate.

Spreadsheet Calculated Values – (from the above input values):

Winding Resistance (R_P)	= 1.73E-2 ohm
Winding Inductance (L_P) (no plate).....	= 20.9 μ H
Leakage Inductance (L_{leak}) (at $t=0$)	= 5.77 μ H
Mutual Inductance (L_M) (at $t=0$)	= 1.27 μ H

$$\text{Damping Ratio } (\xi) \dots \xi = \frac{1}{2} R_{PX} \sqrt{\frac{C}{L_{leak}}} = 0.402$$

Natural Resonance Frequency (ω_N).....	= 4160. 1/sec ($f_N = 662$ Hz)
Plate – Resistance (R_e).....	= 1.63E-05 ohm
Plate – Mass (M_e)	= 0.367 kg

The purpose of using a Thomson Coil is to achieve very fast operation. The critical performance is the time needed to achieve the minimum and maximum displacements. Additional performance issues include the velocity, the peak primary coil current, the peak eddy current, the peak repulsion force, and the temperature rise of the primary coil and conductive plate. The results for this system are listed in **Fig. 14.8**.

	<u>x-min</u>	<u>x-max</u>
Displacement	1.0 mm	7.0 mm
Time.....	0.696 ms	3.26 ms
Velocity	2.70 m/s	1.86 m/s
Peak eddy current	102 kA	
Peak primary current	8.22 kA	
Peak force	14.7 kN	
Conductive plate temperature rise	0.2 °C	
Primary coil temperature rise.....	7.9 °C	

Figure 14.8: Time step solution results for the **Example Model**.

An energy balance was done to check these results, by comparing the energy discharged from the capacitor with all of the energy dissipations and stored energies in the system (**Fig. 14.9**). The small energy balance error (< 4.3%) validates the modeling method.

The calculated performance results curves are shown in **Fig. 14.10** (primary current, eddy current, and force) and **Fig. 14.11** (velocity, and displacement of the conductive plate versus time).

	<u>x-min</u>	<u>x-max</u>
Mass kinetic energy	$\frac{1}{2}(m_e + m)v^2$	6.81 J
Spring potential energy	$(F_S + F_{atm})\Delta g$	0.75 J
Eddy current plate	$\int I_e^2 R_e dt$	63.2 J
Primary coil	$\int I_p^2 R_p dt$	451. J
Parasitic resistance	$\int I_p^2 R_x dt$	52.1 J
Total Energy Dissipated or Stored	574. J	608. J
Capacitor discharge	$\frac{1}{2}C(V_{C0}^2 - V_{Ci}^2)$	600. J
Error – Total energy vs. Capacitor discharge	-4.3%	-0.7%

Figure 14.9: Energy balance for the **Example Model**.

The energy balance error is very small (< 4.3%).

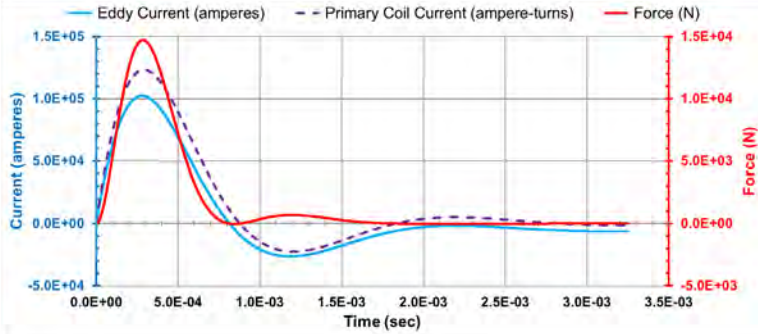


Figure 14.10: Thomson Coil Example Model time step performance calculation – primary current, eddy current and force versus time.

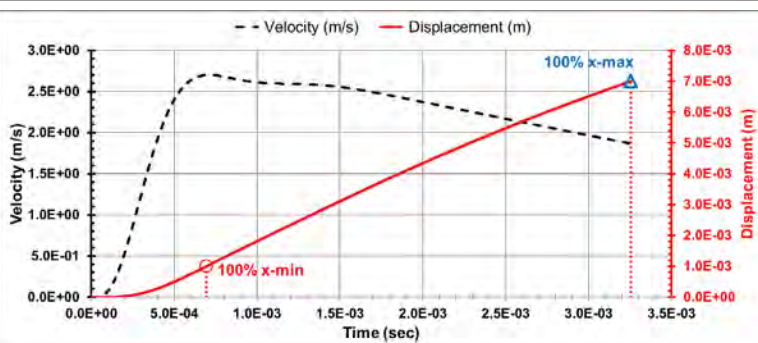


Figure 14.11: Thomson Coil Example Model time step performance calculation – velocity and displacement versus time.

The differential equation (Eq. 14.28), the loop equations, and the mechanical motion equations were discretized and solved with a time step technique. The starting value for the time increment (Δt) was set equal to the smaller of the time constant for the primary current rise (τ_{rise} , Eq. 14.78) or half of the oscillation period (τ_N , Eq. 14.80). The time increment was reduced by a factor of 10 several times, and the selected value was determined based on achieving a small energy balance error, as listed in Fig. 14.12.

$$\tau_{rise} = \frac{L_{leak}}{R_{PX}} \quad \text{Current rise time constant (14.78)}$$

$$\tau_{rise} = \frac{5.77E-6}{1.93E-2} = 2.99E-4 \text{ sec} \quad \text{Current rise time constant (14.79)}$$

$$\tau_N = \frac{1}{2f_N} \quad \text{1/2 oscillation period} \quad (14.80)$$

$$\tau_N = \frac{1}{2(662)} = 7.55E-4 \text{ sec} \quad \text{1/2 oscillation period} \quad (14.81)$$

$$\tau_{inc} = \text{Min}(\tau_{rise}, \tau_N) = 2.99E-4 \text{ sec} \quad \text{Baseline time increment (14.82)}$$

Δt Time Increment	Energy Balance Error % at $x\text{-min}$	Energy Balance Error % at $x\text{-max}$
($\tau_{inc} = 2.99E-4$ s)		<u>Example Model</u>
$\tau_{inc} / 10$	4.3%	7.1%
$\tau_{inc} / 100$	-3.6%	0.0%
$\Delta t = \tau_{inc} / 1000$	-4.2%	-0.6%

Figure 14.12: Solution Energy Balance Error for the Example Model. The smallest Error is with ... $\Delta t = \tau_{inc} / 1000$.

- Comparison to Linear RLC System

A simple check of the primary current waveform from **Fig. 14.10** is shown below in **Fig. 14.13**, where the time step solution primary current waveform (RED) correlates very well with the linear RLC system response (BLUE). The leakage inductance for the time step solution increases as the conductive plate moves away, which results in decreased current and decreased frequency, as can be observed in **Fig. 14.13**. The linear RLC solution (**Eq. 14.74**) gives only the primary current. The time step solution (**Eq. 14.28**) gives the primary current, eddy current, leakage flux, and mutual flux.

- Effect of Mechanical Motion

Calculations were done for the same system without the motion terms (the last term in **Eq. 14.30** and **Eq. 14.31**). The results in **Fig. 14.14**, show the comparison to the results in **Fig. 14.8** (which includes the motion terms). This shows that eliminating the motion terms increases the primary current and the eddy current by 1%, increases the force by 2%, increases the velocity by 4% to 13%, and reduces the time to achieve a displacement by 1.3% to 6.2%.

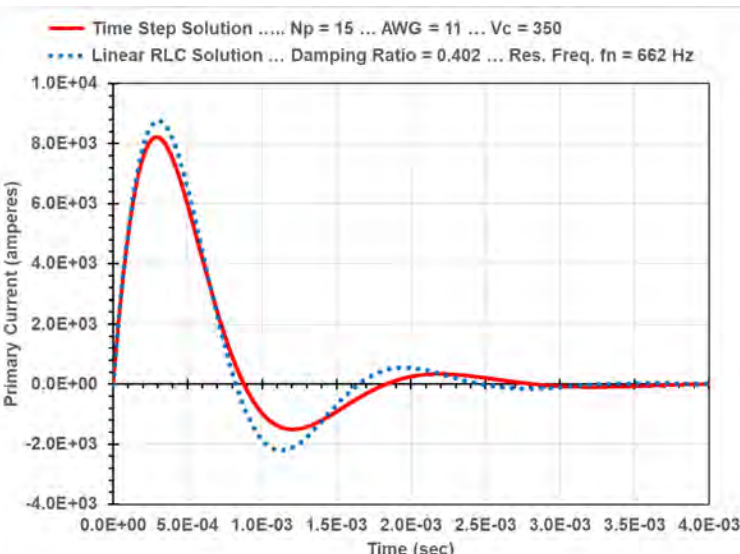


Figure 14.13: Primary current waveform (RED) and linear RLC current waveform (BLUE) for the Example Model – Damping Ratio $\xi = 0.402$.

	<i>x-min</i>	Example Model	<i>x-max</i>
Displacement	1.0 mm		7.0 mm
Time.....	0.687 ms	-1.3%	3.05 ms -6.2%
Velocity	2.81 m/s	+4.1%	2.11 m/s +12.8%
Peak eddy current	103. kA	+1.0 %	
Peak primary current	8.30 kA	+1.0%	
Peak force	15.0 kN	+2.0%	

Figure 14.14: Results without the motion terms. Positive % difference means the value is larger than for the complete results from **Fig. 14.8.**

d. Comparison to FEA and Testing

A Thomson Coil actuator was designed, constructed, and tested at North Carolina State University (NCSU) [36] to quickly open and close an electrical contact in a vacuum interrupter. The design and analysis work was done with a transient Finite Element Analysis for a **Base Design** and a **Prototype Design**. This section shows that the spreadsheet calculations compare very well with the FEA simulations and test results published in [36].

The design characteristics for both NCSU designs are listed below, including the dimensions, capacitance, voltage, primary coil winding, electrically conductive plate, additional mass, and spring force. The parasitic resistance in the **Base Design** includes only the capacitor ESR. The spreadsheet and FEA results for the **Base Design** are listed in **Fig. 14.15**, where acceptable agreement is shown between the spreadsheet and FEA results for the peak primary current, the peak repulsion force, and for the elapsed time at 1.0 mm and 3.0 mm displacement.

Input Values – Capacitor:	Base Design	Prototype Design
Capacitor Voltage (V_C)	= 500 V	300 V
Capacitance (C)	= 0.002 F	0.002 F
Parasitic Resistance (R_X).....	= 0.275 mΩ	10.0 mΩ

Input Values – Primary Coil Winding:

Coil Inside Diameter (ID).....	= 12 mm	12 mm
Coil Outside Diameter (OD).....	= 80 mm	80 mm
No. of Turns (N_P).....	= 10 turns	11 turns
Wire Size (AWG).....	= 10 AWG	7 AWG
Height of wire (h)	= 2.6 mm	4.6 mm

Input Values – Electrically Conductive plate (same ID and OD as the coil):

Plate Thickness (T)	= 4 mm	4 mm
Air Gap – Plate to Coil (g)	= 3 mm	3 mm
Plate Material	= Copper	Copper

Input Values – Additional mass and spring force due to the mechanism:

Additional Moving Mass (m)	= 1.0 kg	0.5 kg
Additional Spring Force (F_S).....	= 300 N	300 N
Additional Atm. Force (F_{atm}).....	= 70 N	70 N

Spreadsheet Calculated Values – (from the above input values):

Winding Resistance (R_P)	= 4.74E-3 ohm	2.60E-3 ohm
Winding Inductance (L_P) (no plate) ..	= 3.35 μ H	3.90 μ H
Leakage Inductance (L_{leak}) (at $t=0$) ...	= 1.58 μ H	2.07 μ H
Leakage Inductance (L_{leak}) (at x_{max}) ..	= 2.13 μ H	2.54 μ H
Mutual Inductance (L_M) (at $t=0$)	= 0.274 μ H	0.276 μ H
Damping Ratio (ξ).....	= 0.089	0.196
Natural Resonance Freq. (ω_N)	= 17,800. 1/sec	15,500. 1/sec
Plate – Resistance (R_e).....	= 1.83E-05 ohm	1.83E-5 ohm
Plate – Mass (M_e)	= 0.176 kg	0.176 kg

Results	Base Design		
	Spreadsheet	FEA	
Capacitor Voltage	volts	500	500
Parasitic Resistance	$m\Omega$	0.275	0.275
Displacement	mm	1.00	1.00
Elapsed Time	ms	0.53	0.40
Velocity	m/s	2.91	---
Displacement	mm	3.00	3.00
Elapsed Time	ms	1.18	1.00
Velocity	m/s	3.09	---
Peak Primary Current	kA	15.1	15.0
Peak Force	kN	23.4	24.0
Energy Error	%	0.2%	---

Figure 14.15: Comparison between the spreadsheet and FEA results. There is acceptable agreement between the spreadsheet and FEA results. The difference in elapsed time may be due to the assumption of a constant spring force in the spreadsheet, rather than the nonlinear spring force of a bellville washer that was used by NCSU.

The calculated performance curves from the spreadsheet for the **Base Design** [36] are shown in **Fig. 14.16** (primary current, eddy current, and force versus time) and **Fig. 14.17** (velocity, and displacement of the conductive plate versus time). The system is lightly damped ($\xi = 0.089$).

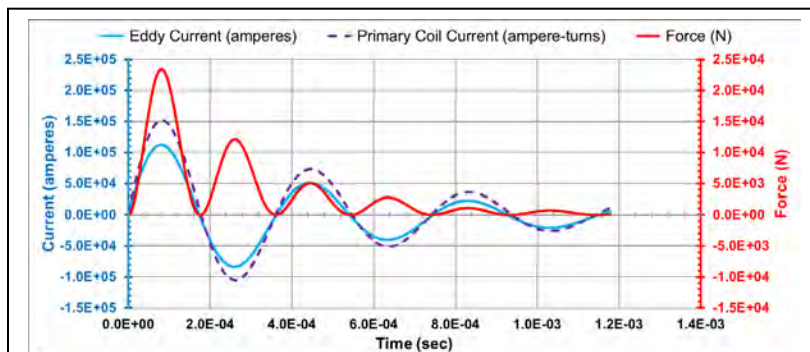


Figure 14.16: **Base Design** time step performance calculation – primary current, eddy current, and force versus time.

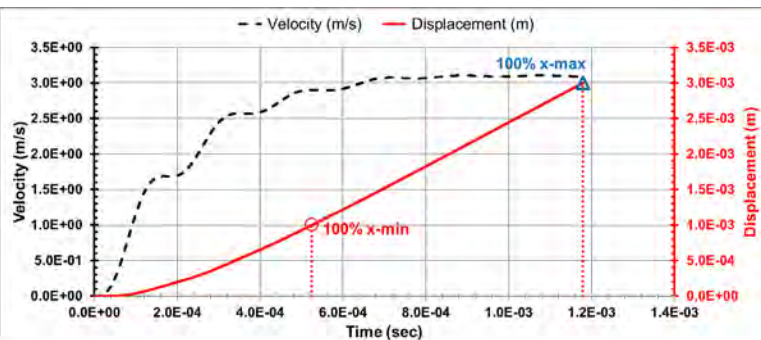


Figure 14.17: Base Design time step performance calculation – velocity and displacement versus time.

Fig. 14.18 shows a good correlation between the time step solution primary current waveform (RED) and the linear RLC system response (BLUE) for the **Base Design**. The leakage inductance for the time step solution increases as the conductive plate moves, which results in decreased current and decreased frequency.

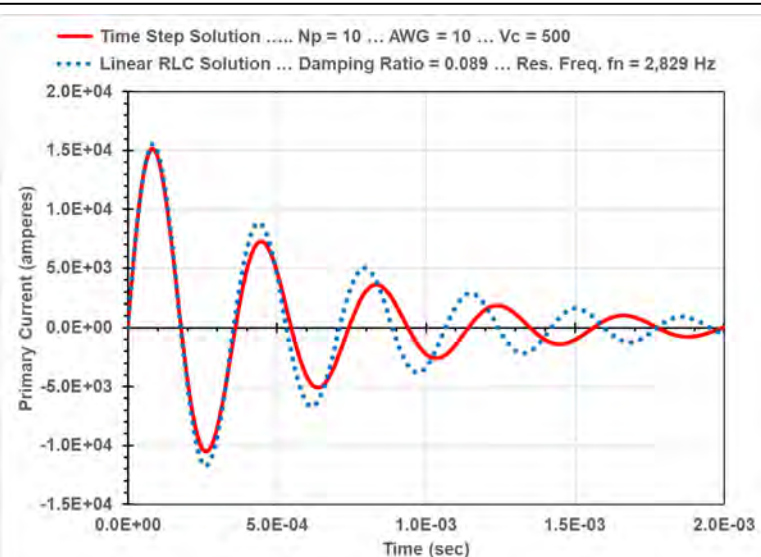


Figure 14.18: Base Design primary current waveform (RED) and linear RLC current waveform (BLUE) – Damping Ratio $\xi = 0.089$.

The spreadsheet and FEA results for the **Prototype Design** [36] are listed in **Fig. 14.19**. The system is lightly damped ($\xi = 0.196$). To achieve the same elapsed time results, the spreadsheet capacitor voltage had to be increased from 300 V to 355 V, or the parasitic resistance had to be reduced from 10.0 $\text{m}\Omega$ to 5.5 $\text{m}\Omega$. With those small modifications, the spreadsheet calculations correlate very well with the FEA results.

Results		Prototype Design		
		Spreadsheet	FEA	
Capacitor Voltage	volts	300	355	300
Parasitic Resistance	$\text{m}\Omega$	5.5	10.0	10.0
Displacement	mm	1.00	1.00	1.00
Elapsed Time	ms	0.90	0.87	1.00
Velocity	m/s	1.30	1.24	1.3
Displacement	mm	2.20	2.20	2.20
Elapsed Time	ms	2.10	2.25	2.00
Velocity	m/s	0.68	0.49	1.3
Peak Primary Current	kA	7.57	8.19	---
Peak Force	kN	7.20	8.43	---
Energy Error	%	0.8%	0.3%	---

Figure 14.19: Comparison between the spreadsheet and FEA results.

The **Prototype Test** results [36] and the spreadsheet calculation results are listed in **Fig. 14.20**. The prototype was operated 10 times at 360 V and consistently produced the listed elapsed times. To achieve the same elapsed time results, the spreadsheet capacitor voltage had to be increased from 360 V to 425 V, or the parasitic resistance had to be reduced from 12.0 $\text{m}\Omega$ to 7.0 $\text{m}\Omega$. With those small modifications, the spreadsheet calculations correlate very well with the test results.

Results		Prototype Test		
		Spreadsheet	Test	
Capacitor Voltage	volts	360	425	360
Parasitic Resistance	$\text{m}\Omega$	7.0	12.0	12.0
Displacement	mm	1.30	1.30	1.30
Elapsed Time	ms	0.87	0.85	1.00
Velocity	m/s	1.75	1.68	---
Displacement	mm	3.10	3.10	3.10
Elapsed Time	ms	2.14	2.24	2.00
Velocity	m/s	1.08	0.92	---
Energy Error	%	0.5%	0.3%	---

Figure 14.20: Comparison between the spreadsheet calculations and the NCSU test results [36].

The spreadsheet calculation for the Thomson Coil leakage inductance is 2.1 μH (with a 1.3 mm air gap) and 2.5 μH (with a 3.1 mm air gap to the conductive plate). The FEA simulations at NCSU [36] used a Thomson Coil inductance of 3 μH – 7 μH , which correlates very well with the 3.9 μH spreadsheet calculation (without the conductive plate). NCSU also included parasitic inductance (1.3 μH in the trigger circuit and 0.6 μH in the Thomson Coil circuit), which was not included in the spreadsheet model. This might account for some of the results differences. Overall, the spreadsheet solution is sufficiently accurate and fast (10 seconds solution time), to quickly determine trends that can point the way to performance improvements – “The trend is your friend”.

15. Magnetic Field Sensors

This chapter is an overview of magnetic field sensors. The primary purpose is to briefly describe the various techniques that can be used to measure a magnetic field.

a. Variable Inductor and Transformer

Reluctance based actuators (**Ch. 2**) can also perform as position sensors. These actuators produce a force across an internal air gap based on the rate of change of the air gap permeance ($d\mathcal{P}_g/dg$) (**Eq. 2.7**). The inductance of the actuator is proportional to the air gap permeance ($L_g = N^2 \mathcal{P}_g$) (**Eq. 1.27**), which is inversely proportional to the length of the air gap (l or g). Therefore, a reluctance actuator is a variable inductor, and it can function as a position sensor by driving the actuator coil with a small AC voltage and monitoring the coil current (or impedance). At an open gap, the current is high (low inductance and low impedance), and at a closed gap the current is small (high inductance and high impedance). The characteristics are nonlinear, but a calibration curve can be developed by measuring the current at several positions. Therefore, a separate position sensor might not be necessary.

A transformer with a moveable core, one primary coil and one secondary coil will produce an output voltage in proportion to the engagement (or position) of the moveable core within the 2 coils. Improved linearity can be achieved by shaping the core poles and by shaping the coils (varying the coil turns in the direction of the core motion).

An LVDT (Linear Variable Differential Transformer) is a commercially available position sensor based on an adjustable core transformer. The typical construction uses a moveable core, one primary coil, and two secondary coils (one secondary coil on each side of the primary coil). The core may have shaped poles and the coils may have varying turns to achieve excellent linearity. Connecting the secondary coils in series gives a differential output voltage. These sensors have excellent linearity. A detailed discussion of the LVDT is presented by Brauer [9].

b. CT, Rogowski Coil, Search Coil

Details of the current transformer (CT) and Rogowski coil were discussed in **Ch. 9**. A current transformer, Rogowski coil, and search coil (also known as pickup coil) are all based on the same magnetic physics.

A **current transformer (CT)** is a transformer with a very low resistance secondary (winding and secondary load). The secondary current (I_2) is proportional to the primary current and the turns ratio ($I_1 N_1/N_2$). If the total secondary resistance ($R + R_2$) is 10% of the secondary inductive impedance

(ωL_2) , the magnitude error is 0.5%, and the phase angle error is 5.7 degrees (**Eq. 9.29**). A high inductance low resistance secondary winding is typically achieved with a high permeability core. The maximum primary current sensing capability of a CT is limited by the saturation of the magnetic core, and the minimum primary current sensing capability of a CT is limited by the coercivity of the core.

A **Rogowski coil** is a transformer with an open secondary (infinite resistance). The Rogowski coil configuration (**Fig. 15.1**) is a helical coil with a constant diameter winding (d) and uniform spacing of the windings (N_2) along the circumference of the core. The Rogowski coil is constructed on a nonmagnetic core with the windings encompassing the entire circumferential length of the core. At the end of the last turn, the wire is returned through the center of the core to the position of the first turn.

The return wire in the center of the core eliminates the sensitivity of the coil to an axial magnetic field. The helical winding is effectively one turn in the clockwise direction around the axis of the primary conductor, and the return conductor through the center of the core is one turn in the counterclockwise direction around the axis of the primary conductor. This adds up to zero turns around the axis of the primary conductor and eliminates sensitivity to an axial magnetic field. There is a small sensitivity to an axial magnetic field if the return wire is not exactly located at the average radius (r).

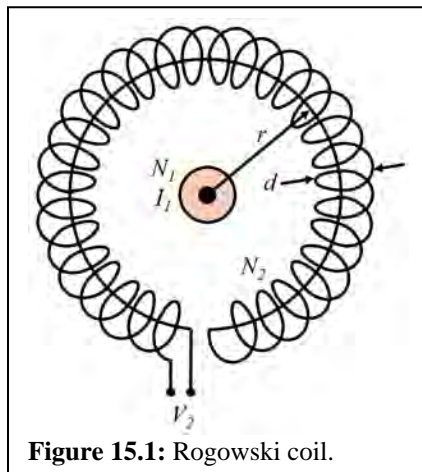


Figure 15.1: Rogowski coil.

An alternative to a return wire through the center of the core is to add an equal number of turns around the core in the counterclockwise direction. This can be done by starting from the maximum clockwise position and simultaneously winding both turns ending at the maximum counterclockwise position. This winding looks like a braid as reported by Wapakabulo and Murgatroyd [40]. They showed that a Rogowski coil with a return wire through the center of the core has a sensitivity to non-uniform fields. The braid Rogowski shows significant improvement.

As shown in **Ch. 9**, the secondary voltage (V_2) is proportional to the primary current, the turns, and the frequency ($I_1 N_1 N_2 \omega$) (**Eq. 9.34**). Therefore, at a constant frequency, the secondary voltage is proportional to the current. However, the secondary voltage is also sensitive to the frequency content of the current. More generally, the secondary voltage (V_2) is proportional to the rate of change of the primary current and the turns ($N_1 N_2 dI_1/dt$) (**Eq. 9.34**). A Rogowski coil typically has a non-magnetic core. Therefore, the Rogowski coil has no sensing limit other than the ability to measure the minimum and maximum secondary voltages (V_2).

Eq. 9.34 can also be obtained by assuming a perfectly centered primary conductor inside a perfectly circular Rogowski coil, as follows. **Eq. 15.4** is identical to **Eq. 9.33** and **Eq. 15.5** is identical to **Eq. 9.34**.

$$H = \frac{N_1 I_1}{2\pi r} \quad \text{Magnetic field intensity in the Rogowski coil} \quad (15.1)$$

$$B = \mu_0 H = \mu_0 \frac{N_1 I_1}{2\pi r} \quad \text{Magnetic flux density in the Rogowski coil} \quad (15.2)$$

$$\mathcal{R} = \frac{l}{\mu_0 A} = \frac{2\pi r}{\mu_0 \pi d^2 / 4} = \frac{8r}{\mu_0 d^2} \quad \text{Reluctance of the Rogowski coil} \quad (15.3)$$

$$\phi = BA = B \frac{\pi d^2}{4} = \mu_0 \frac{N_1 I_1}{2\pi r} \frac{\pi d^2}{4} = \frac{N_1 I_1}{\mathcal{R}} \quad \text{Magnetic Flux (Eq. 9.33)} \quad (15.4)$$

$$V_2 = N_2 \frac{d\phi}{dt} = \frac{N_2 N_1}{\mathcal{R}} \frac{dI_1}{dt} \quad \text{Rogowski voltage (also Eq. 9.34)} \quad (15.5)$$

$$V_{2-PK} = \frac{N_2 N_1}{\mathcal{R}} I_{1-PK} \omega \quad \text{Rogowski peak voltage for } I_1 = I_1 \sin(\omega t) \quad (15.6)$$

A perfectly uniform Rogowski coil winding with no winding gap at the ends of the winding (clockwise end and counterclockwise end) has no sensitivity to the location of the primary conductor. The primary conductor can be located off-center without affecting the Rogowski output voltage (V_2). When the Rogowski coil winding is nonuniform, the Rogowski coil output voltage is sensitive to the location of the primary conductor. This can be visualized by locating the Rogowski coil winding on only half of the core. The output voltage will increase as the primary conductor is moved closer to the side of the core with the windings.

A **search coil** is an open secondary coil. It can be a loop from a single turn of small size wire. The purpose of the search coil is to measure the magnetic flux within the loop. Therefore, it can be wound onto part of a magnetic core to determine the change in the operating magnetic flux by integrating the output voltage (**Eq. 15.7**). It can also be configured as a loose-fitting loop that is placed over a permanent magnet and then removed from the permanent magnet. The magnetic flux in the permanent magnet can be determined by integrating the output voltage pulse (**Eq. 15.7**), which gives the change in magnetic flux as the search coil is placed over or removed from the permanent magnet. The sensing range is $10^{-12} < B < 10^{+2}$ T.

$$\phi = \frac{1}{N} \int V dt \quad \text{Faraday's law} \quad (15.7)$$

c. Wiegand Wire

A Wiegand wire is made of Vicalloy with soft magnetic properties on the inner core and hard magnetic properties on the outer shell. The composition of Vicalloy is 0.03% Carbon, 0.40% Manganese, 0.20% Silicon, 52% Cobalt,

10% Vanadium, and 37.4% Iron. The high coercivity (magnetically hard) outer shell is achieved by twisting the wire under tension to cold-work only the outer shell. The coercivity of the inner core remains small (magnetically soft).

When an external low-level magnetic field is imposed onto a Wiegand wire, the outer shell shields the inner core from the magnetic field. When the external magnetic field becomes large enough, both the outer shell and inner core flip to the polarity of the external magnetic field within a few microseconds. The Wiegand wire will flip back to the original polarity when the reverse external magnetic field is applied. The Wiegand effect includes the flip in magnetic polarity plus a voltage pulse across the two ends of the Wiegand wire, which is related to the Barkhausen effect.

Two alternative sensing configurations are possible; 1) The voltage pulse across the two ends of the Wiegand wire can be sensed directly; 2) the flip in magnetic polarity can be sensed with a coil around the Wiegand wire, in which the fast change in magnetic flux induces a voltage pulse in the coil.

d. Hall Sensor

Edwin Herbert Hall (1855-1938) discovered the Hall effect in 1879 during work on his Ph.D. thesis at Johns Hopkins University. A magnetic field (B_y) in the Y-direction acting on a current (I_x) in the X-direction causes a Lorentz force (F_z) in the Z-direction and results in a Z-direction Hall Voltage (V_H) (Fig. 15.2). The Hall voltage is proportional to the magnetic field and the current. The current is typically a constant bias current, and the Hall voltage is proportional to the magnetic flux density. A detailed discussion of the Hall effect is presented by Brauer [9].

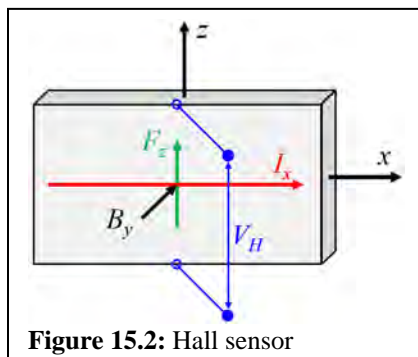


Figure 15.2: Hall sensor

Typical issues and limitations related to Gallium-Arsenide Hall devices and on-chip electronics are listed below.

- Hall chips exhibit an output at zero flux, called zero flux offset. The maximum is 12 mV with a 10 mA bias current. The typical offset is 2 to 5 mV positive or negative. Zero flux offset increases as temperature rises.
- The Hall gain (mV/mT) can be different between chips. The maximum difference can be 2.4:1. The typical difference is 1.5:1.
- Hall gain (mV/mT) decreases with temperature. The typical temperature sensitivity is -0.07 %/°C.
- The on-chip support electronics can limit the frequency response and the maximum magnetic field sensing capability.

The Hall element is nonmagnetic and it has no upper limit due to magnetic saturation. However, it is not perfectly linear, and the gain decreases with increasing temperature. Electronics are typically added to the Hall chip to linearize the output and eliminate the temperature sensitivity. These electronic amplifiers limit the maximum magnetic field sensing capability due to amplifier saturation. The sensing range is $10^{-4} < B < 10^{+2}$ T.

e. SQUID

A SQUID (Superconducting Quantum Interference Device) is based on the phenomena of flux quantization and the Josephson effect in a superconducting closed loop. Traditionally, the SQUID is made of pure niobium and requires cooling to 4°K with liquid helium. A higher temperature design was developed with YBCO which requires cooling to 77°K with liquid nitrogen [34, 35].

A SQUID can detect very low magnetic flux fields and has a sensing range of $10^{-14} < B < 10^{-10}$ T. Sensitivity as low as 5×10^{-18} T has been reported [33]. SQUIDs tend to be used in applications for low magnetic fields ($< 10^{-6}$ G, or $< 10^{-10}$ T), where there is a very low concentration of magnetic material and a need for highly sensitive, precise measurement. Applications include the characterization of materials, geophysics, food contamination detection, and biological responses (such as the human heart, eye, and brain with magnetic fields in the range of 10^{-15} to 10^{-9} T).

f. Fluxgate

A Fluxgate sensor typically is composed of a magnetic core with a square BH loop material, a saturation coil, and at least one sense coil. The saturation coil is connected to an oscillating current source to alternately saturate the core at positive and negative peak currents. Three alternative configurations are discussed below. The sensing range is $10^{-11} < B < 10^{-2}$ T.

The **bar-shaped core** configuration (Fig. 15.3) has a drive coil and one sense coil on a straight core. The drive coil current alternately saturates the magnetic core with positive and negative peak currents. When the drive coil current passes through zero, the magnetic flux density flips from saturation in one direction to saturation in the opposite direction, and the sense coil

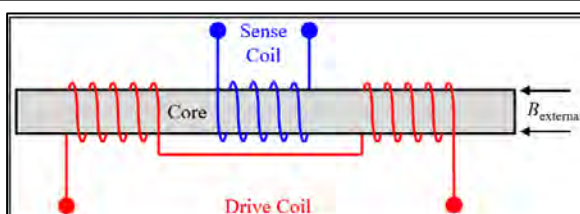


Figure 15.3: Fluxgate sensor – bar-shaped core.

produces a large voltage pulse. A square BH loop flips the saturation direction very quickly and produces a large pulse from the sense coil.

When the external magnetic field is zero, the sense coil voltage pulses are equally spaced in time. When the external magnetic field intensity (H) is non-zero, the net peak field intensity in one direction decreases, and increases in the opposite direction. The time between sense coil voltage pulses decreases in the direction against the external magnetic field and increases in the direction with the external magnetic field. The differential timing between sense coil voltage pulses is proportional to the external magnetic field.

The **ring-shaped core** configuration (Fig. 15.4) has a drive coil and one sense coil on a loop core (rectangular or circular). The drive coil current alternately saturates the magnetic core with positive and negative peak currents. When the core is saturated, the external magnetic field is forced out of the core. When the drive coil current is zero, the external magnetic field is carried by the core. The alternating saturation acts as a gate to exclude or admit the external magnetic flux (a fluxgate).

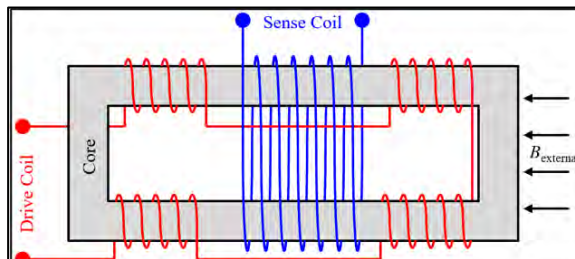


Figure 15.4: Fluxgate sensor – ring-shaped core.

The sense coil produces a voltage pulse as the drive coil current passes through zero and the external magnetic field is allowed into the core and then forced out of the core. The magnetic flux from the drive coil cancels itself out because the sense coil encloses the entire core (there is no net saturation flux). Therefore, the magnitude of the sense coil voltage pulse is proportional to the external magnetic field. The ring-shaped core requires significantly less drive coil current than the bar-shaped core.

The **compass sensor** configuration (Fig. 15.6) has a drive coil and two sense coils on a circular ring-shaped core. It operates the same as the ring-shaped

V1 Sense Coil #1	V2 Sense Coil #2	Earth Field Angle θ (deg)
1.000	0.000	0.0
0.707	0.707	45.0
0.000	1.000	90.0
-0.707	0.707	135.0
-0.707	-0.707	225.0
0.707	-0.707	315.0

Figure 15.5: Example voltage pulse magnitudes and compass angles.

core configuration, except there are two sense coils aligned 90° to each other. The direction of the sense coils relative to the earth's magnetic field can be determined from the arctangent of the ratio of the coil pulses. The sensing direction for each coil is shown in **Fig. 15.6** with the angle relative to the earth's magnetic field. Example voltage pulse magnitudes and calculated compass angles are listed in **Fig. 15.5**.

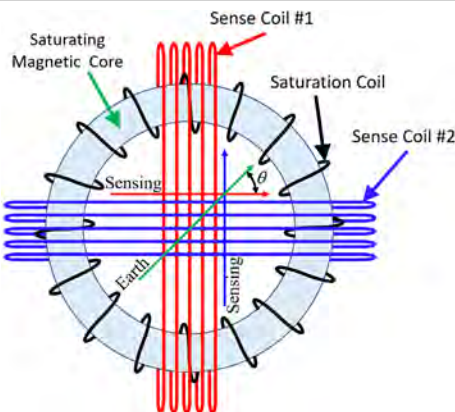


Figure 15.6: Fluxgate ring-shaped compass sensor.

g. Magnetoimpedance (MI)

Panina and Mohri created the term magnetoimpedance (MI) in 1994, and the term giant magnetoimpedance (GMI) in 1995. Magnetoimpedance describes the change in the AC impedance of a conductor when it is exposed to a DC magnetic field. An applied DC magnetic field reduces the magnetic permeability of a magnetic material, which increases the skin effect depth as shown in **Eq. 3.24**, where the skin effect depth (s) is inversely proportional to the square root of the magnetic permeability (μ). The increased skin depth reduces the impedance for high-frequency current. This was first measured in amorphous FeCoSiB wires and ribbons, as described by Barmak and Coffey [37]. At high frequencies (> 100 kHz) the impedance of an amorphous FeCoSiB wire at constant current decreases by 40–60% when the wire is exposed to a small DC longitudinal magnetic field (< 10 Oe).

The MI effect is larger in soft magnetic materials where the domain walls are perpendicular to the direction of the current. When the external DC magnetic field is similar in magnitude to the anisotropy field, the impedance can change by 50%. The impedance of the initial MI sensors was nonlinear (proportional to the square root of the external magnetic field), and a linear MI response has been achieved through the use of different materials [9]. The GMI materials described by Barmak and Coffey [37] are thin-film materials such as FeCuNbSiB or multilayer thin-film materials such as NiFe/Ag or NiFe/Ti where the GMI effect occurs at high frequencies, 10 MHz – 1.8 GHz.

h. Magnetoresistance (MR or AMR)

The first observation of magnetoresistance (MR) was reported in 1857 by William Thomson (Lord Kelvin) [38]. His experiments with iron and nickel showed increased resistance when the current is in the same direction as the magnetic field and decreased resistance when the current is normal (90°) to the magnetic field. He also found that the effect in nickel is greater than in iron. This MR effect is also known as anisotropic magnetoresistance (AMR). Magnetoresistance is caused by the tendency of an electron to follow a curved trajectory as it travels through a magnetic field [39]. The curved trajectory increases the path length of the current, which increases the resistance.

AMR sensors can be made from the same non-magnetic semiconductor material as Hall sensors [9]. Some AMR sensors use a magnetic material such as Permalloy in a meander pattern or a barber pole pattern to enhance the MR effect. The permalloy magnetic material saturates in a high magnetic field, which limits the sensing range. An MR sensor has about 10 times the sensitivity of a Hall sensor, with a sensing range of $10^{-9} < B < 10^{-2}$ T. A detailed discussion of the AMR effects is presented by Brauer [9].

i. Giant Magnetoresistance (GMR)

The giant magnetoresistance (GMR) effect was discovered in 1988 by Peter A. Grünberg and Albert Fert. They shared the 2007 Nobel prize in physics for the discovery of giant magnetoresistance.

GMR sensors are multilayer devices, composed of very thin (nano-meter) layers. They can be visualized as having two ferromagnetic layers (such as iron, nickel, or cobalt) sandwiching a layer of non-magnetic material (such as copper, silver, gold). The magnetic orientation of the 1st ferromagnetic layer is fixed. The magnetic orientation of the 2nd ferromagnetic layer follows the external magnetic field. The electron spin of the current interacts with the electron spin of the ferromagnetic layers. When the ferromagnetic layers have the same magnetic orientation, the electron scattering of the current is minimized, and the electrical resistance is minimized. When the ferromagnetic layers have the opposite magnetic orientation, the electron scattering of the current is maximized, and the electrical resistance is maximized. For this reason, a GMR device is also known as a spin valve, and the technology is also known as spintronics. A GMR sensor has about 10 times the sensitivity of an AMR sensor and about 100 times the sensitivity of a Hall sensor.

A GMR sensor is extremely sensitive compared to an AMR sensor. Therefore, it's feasible to use a GMR sensor without a flux concentrator at low magnetic field levels. A GMR sensor is made with a magnetic material, and it saturates in a high magnetic field. It produces an output signal that is proportional to the absolute value of the applied magnetic field. Therefore, it is typically biased (using a permanent magnet) so that at zero field it produces half of its output voltage. A detailed discussion of GMR is presented by Brauer [9].

j. Other MR (TMR, CMR, BMR, EMR)

Several much larger MR effects have recently been discovered, as reported by S. A. Solin [39] in a 2004 Scientific American article. These effects are briefly described below.

TMR (Tunneling MR): The nonmagnetic metal layer in a GMR sensor is replaced by an insulator. Current flows through the insulator by quantum tunneling of electrons. TMR was first measured by Michel Jullière of INSA at Rennes in 1975.

CMR (Colossal MR): CMR occurs in manganese oxide crystals (manganites). A high external magnetic field (several teslas) causes the nonmagnetic insulating manganite to become metallic and ferromagnetic. The change to metallic significantly reduces the resistance. This transition occurs at cryogenic temperatures ($< 150^{\circ}\text{K}$). CMR was first discovered by G. H. Jonker and J. H. van Santen of Philips, Netherlands, 1950s. It was rediscovered by Sung-Ho Jin of Bell Laboratories and collaborators in 1994.

BMR (Ballistic MR): BMR occurs when a magnetic wire and a magnetic needle are connected at a nano-meter size contact spot. The external magnetic field changes the needle and wire from parallel magnetic polarity (low resistance) to antiparallel magnetic polarity (high resistance). The change in resistance depends on the ballistic travel of electrons across the contact spot. BMR was discovered by N. Garcia, M. Muñoz, and Y. W. Zhao of the Council for Scientific Research (CSIC), Madrid, 1999.

EMR (Extraordinary MR): Magnetoresistance is caused by the tendency of an electron to follow a curved trajectory as it travels through a magnetic field. EMR sensors have been made with a thin film of InSb and with multiple thin layers of InSb and InAlSb. EMR sensors do not contain magnetic materials. Therefore, an EMR sensor has no saturation limit. Long winding electron trajectories reduce the current and increase the resistance. A strong magnetic field can cause the electron trajectories to become helices which results in a very long conduction path and very high resistance. An early prototype achieved a magnetoresistance of 35% in a field of 0.05 T. An EMR sensor operates at temperatures below room temperature ($< 25^{\circ}\text{C}$), and the response is proportional to the square of the magnetic field, which gives good sensitivity, although it is nonlinear.

Appendix-A: Constants

μ_0	= $4\pi E-7$	Henry/m	Permeability of Free Space
μ_0	= 1.0	Gauss/Oersted	Permeability of Free Space
e	= $1.602177E-19$	coulomb	Electron Charge
m_e	= $9.109390E-31$	kg	Electron Mass
h	= $6.626200E-34$	J-sec	Plank's Constant
c	= $2.997925E+8$	m/s	Speed of Light
β	= $9.274000E-24$	A-m ²	Bohr Magneton
g	= 9.806650	m/s ²	Acceleration of Gravity
e	= 2.71828182846	---	Napierian Base
π	= 3.14159265359	---	Pi
$\pi!$	= 7.18808272898	---	Pi Factorial

Appendix-B: Units

Magnetic Flux (ϕ):

1.0	weber	=	$1.0E+8$	line
1.0	weber	=	$1.0E+8$	maxwell
1.0	weber	=	1.0	volt-sec
1.0	weber	=	1.0	henry-ampere
1.0	weber	=	1.0	tesla-m ²

Magnetic Flux Density (B):

1.0	tesla	=	1.0	weber/m ²
1.0	tesla	=	$1.0E+8$	line/m ²
1.0	tesla	=	$1.0E+4$	gauss
1.0	tesla	=	$1.0E+9$	gamma
1.0	gauss	=	1.0	line/cm ²
1.0	gauss	=	6.4516	line/in ²

Magnetomotive or Magnetizing Force (NI):

1.0	ampere-turn	=	0.4π	gilbert
1.0	ampere-turn	=	0.4π	oersted-cm

Magnetic Field Intensity (H):

1.0	ampere-turn/m	=	$4\pi E-3$	oersted
1.0	ampere-turn/m	=	$4\pi E-3$	gilbert/cm
1.0	ampere-turn/m	=	0.0254	ampere-turn/in
1.0	oersted	=	79.5775	ampere-turn/m
1.0	oersted	=	1.0	gilbert/cm
1.0	oersted	=	2.02127	ampere-turn/in

Permeability (μ):

1.0	T-m/ampere-turn	=	$(1.0E+7)/4\pi$	gauss/oersted
1.0	T-m/ampere-turn	=	1.0	weber/ampere-turn-m
1.0	T-m/ampere-turn	=	1.0	henry/m
1.0	T-m/ampere-turn	=	1.0	newton/(A-t) ²
1.0	gauss/oersted (μ_0)	=	$4\pi E-7$	henry/m
1.0	gauss/oersted (μ_0)	=	3.19185	line/ampere-turn-in

Inductance (L):

1.0	henry	=	1.0	volt-sec-turn/ampere
1.0	henry	=	1.0	Weber-turn/ampere
1.0	henry	=	$1.0E+8$	Line-turn/ampere

Energy (*W*):

1.0	joule	=	1.0	watt-sec
1.0	joule	=	1.0	Weber-ampere-turn
1.0	joule	=	1.0	newton-m (N-m)
1.0	joule	=	$1.0E+8$	line-ampere-turn
1.0	joule	=	$1.0E+7$	erg
1.0	kJ	=	0.94783	Btu
1.0	kJ	=	239.01	cal
1.0	Btu	=	778.16	ft-lbf
1.0	Btu	=	252.16	cal

Energy Density (*w*):

1.0	Mega-Gauss-Oersted	=	7.958	kJoule/m ³
1.0	Mega-Gauss-Oersted	=	7958.	tesla-ampere-turn/m
1.0	Mega-Gauss-Oersted	=	7958.	joule/m ³

Power (*P*):

1.0	watt	=	1.0	volt-ampere
1.0	hp	=	745.701	watt
1.0	hp	=	550	ft-lbf/s

Magnetic Moment (*m*):

1.0	emu	=	1.0	erg/Oersted
1.0	emu	=	1.0	erg/Gauss
1.0	emu	=	$1.0E-3$	ampere-m ²
1.0	emu	=	$1.0E-3$	joule/tesla
1.0	emu	=	4π	gauss-cm ³
1.0	emu	=	$4\pi E-10$	weber-m

Force (*F*):

1.0	lb _f	=	16	oz _f
1.0	lb _f	=	4.448	N
1.0	N	=	1.0	kg-m/s ²
1.0	N	=	1000	Dy

Mass (*M*):

1.0	kg	=	2.200462	lb _m
1.0	lb _m	=	454.45	gram
1.0	slug	=	32.174	lb _m
1.0	stone	=	14	lb _m

Length (*l*):

1.0	mil	=	0.001	in
1.0	m	=	39.37	in
1.0	m	=	3.281	ft
1.0	furlong	=	0.125	mile
1.0	lightyear	=	$9.4607E+12$	km
1.0	lightyear	=	$5.8786E+12$	mile
1.0	parsec	=	3.26	lightyear

Wire Area (*a*):

1.0	mil	=	$1.0E-3$	inches = 1.0
1.0	inch	=	1,000	mils
1.0	square mil ($\pi/4 D^2$)	=	$1.0E-6$	in ²
1.0	square mil ($\pi/4 D^2$)	=	0.7854	circular mil (D^2)
1.0	circular mil (D^2)	=	1.273	square mil ($\pi/4 D^2$)
1.0	MCM	=	1,000	circular mills
1.00	$\text{in}^2 (d_B^2)$	=	1,000	$\text{MCM} (1,0000 d_B^2)$
0.25	$\text{in}^2 (d_B^2)$	=	250	$\text{MCM} (1,0000 d_B^2)$
1.0	inch dia. wire (d_B)	=	1,000	$\text{MCM} (1,0000 d_B^2)$
0.5	inch dia. wire (d_B)	=	250	$\text{MCM} (1,0000 d_B^2)$

Frequency:

$$1.0 \quad (f) \text{ Hz} \quad = \quad 2\pi \quad (\omega) \text{ rad/sec}$$

Electrical Resistivity (σ):

$$1.0 \quad \text{ohm-CMF} \quad = \quad 1.6624E-9 \quad \text{ohm-m}$$

(CMF = circular mil per foot)

Electrical Resistance (*R*):

$$\begin{aligned} 1.0 \quad \text{ohm} \quad &= 1.0 & 1/\text{S} \\ 1.0 \quad \text{S} \quad &= 1.0 & 1/\text{ohm} \end{aligned}$$

Hardness:

$$\begin{aligned} 1.0 \quad \text{kg/mm}^2 \quad &= 1.0 & \text{BHN (Brinell)} \\ 1.0 \quad \text{kg/mm}^2 \quad &= 1419.7 & \text{lb}_f/\text{in}^2 \\ 1.0 \quad \text{kg/mm}^2 \quad &= 9.79E+6 & \text{N/m}^2 \end{aligned}$$

Pressure:

$$\begin{aligned} 1.0 \quad \text{MPa} \quad &= 1.0 & \text{N/mm}^2 \\ 1.0 \quad \text{MPa} \quad &= 1.0E+6 & \text{N/m}^2 \\ 1.0 \quad \text{Pa} \quad &= 1.0 & \text{N/m}^2 \\ 1.0 \quad \text{MPa} \quad &= 10 & \text{bar} \\ 1.0 \quad \text{bar} \quad &= 0.1 & \text{MPa} \\ 1.0 \quad \text{bar} \quad &= 1.0E+5 & \text{N/m}^2 \\ 1.0 \quad \text{bar} \quad &= 0.9869 & \text{atm} \\ 1.0 \quad \text{bar} \quad &= 14.505 & \text{lb}_f/\text{in}^2 \text{ or (psi)} \\ 1.0 \quad \text{atm} \quad &= 14.70 & \text{lb}_f/\text{in}^2 \text{ or (psi)} \\ 1.0 \quad \text{inch of H}_2\text{O} \quad &= 0.03613 & \text{lb}_f/\text{in}^2 \text{ or (psi)} \\ 1.0 \quad \text{lb}_f/\text{in}^2 \quad &= 27.678 & \text{inches of H}_2\text{O} \\ 1.0 \quad \text{lb}_f/\text{in}^2 \quad &= 6894.4 & \text{N/m}^2 \end{aligned}$$

Time:

$$1.0 \quad \text{fortnight} \quad = \quad 14 \quad \text{days}$$

Velocity:

$$1.0 \quad \text{furlong/fortnight} \quad = \quad 1.00 \quad \text{cm/min}$$

Appendix-C: Electrical & Thermal Material Properties

		$\frac{1}{\sigma}$ Electrical Resistivity <u>ohm-CMF</u>	σ Electrical Conductivity <u>1/ohm-m</u>	α Temp. Coef. <u>% / °C</u>	k_T Thermal Conductivity <u>W/m-°K</u>	ρ Density <u>kg/m³</u>	c_p Specific Heat <u>J/kg-°C</u>	H Hardness <u>kg/mm²</u>	T_M Melting Temperature <u>°C</u>
Solid Materials									
Silver		8.85	$68.0E+6$	0.380	418.7	10491.	234.	27.	961.
Copper	C10200	10.37	$58.0E+6$	0.393	391.0	8941.	385.	40.	1083.
Brass		37.35	$16.1E+6$	0.150	115.9	8470.	376.	57. - 50.	888.
Nickel		44.9	$13.4E+6$	0.410	49.6	8893.	460.	80.	1454.
Iron		58.4	$10.3E+6$	0.640	75.4	7878.	451.	---	1539.
Chromium		78.2	$7.69E+6$	---	66.9	7212.	460.	---	1843.
Manganese		1114.	$0.54E+6$	---	~5.0	7418.	477.	---	1244.
Aluminum	1100	17.0	$35.4E+6$	0.403	222.1	2718.	961.	23.	657.
	2024	21.0	$28.6E+6$	---	193.3	2774.	961.	47.	638.
	6061	30.0	$20.1E+6$	---	138.5	2691.	961.	47.	649.
	6063	19.9	$30.3E+6$	---	200.4	2713.	962.	25.	652.
Steel	Carbon Steel	114.	$5.26E+6$	0.415	46.7	7833.	510.	90. - 250.	1510.
	400 Stainless	360.	$1.67E+6$	---	24.2	7750.	460.	200.	1482.
	300 Stainless	433.	$1.39E+6$	---	16.3	8027.	502.	80.	1399.
INVAR (Low Thermal Expansion)	NiFe	36-64	494.	$1.22E+6$	---	10.5	8127.	501.	132.
									1427.
Resistance Heating Alloys									
NiCr	80-20	650.	$0.925E+6$	---	15.0	8432.	434.	176.	1399.
NiCrFe	60-15-25	675.	$0.891E+6$	---	13.4	8266.	468.	200.	1349.
NiCrFe	35-20-45	610.	$0.986E+6$	---	21.3	7961.	409.	159.	1379.
NiCrFeAl	74-20-3-3	800.	$0.752E+6$	---	12.7	8127.	434.	~159.	1399.
FeCrAl	72-23-5	812.	$0.741E+6$	---	~12.7	7267.	418.	215.	1510.
Glass		---	---	---	0.98	2500.	1000.	---	---
Epoxy Fiberglass		---	---	---	0.24	---	---	---	---
Plastic		---	$1E-16$ to $1E-11$	---	0.25	1500.	1464.	---	---
Thermal Joint Grease		---	---	---	0.75	---	---	---	---

Appendix-D: Soft Magnetic Materials

Material	Basic Material Property and Cost Data							Force per unit Area $B_{sat}^2/2u_0$ lb/in ²
	B_{sat} Flux Density (H=100 Oe)	u_r Relative Perm.	H_c Coercivity (B=1 T)	Electrical Conduct.	Curie Temp. °C	Density g/cc	Cost \$/lb.	
Copper	---	1.	---	58.00E+6 Oe	7.02m ---	8.9486 0.323 lb/in ³	\$2.80	---
Carbon Steel 1008/1010	1.84	3.29E+3	1.20	8.43E+6 7.13E+6	760 760	7.84 0.283 0.283 0.283 0.283	\$0.35 \$0.44 \$0.44	1347 1261 1261
Carbon Steel 1018/1020	1.78	2.54E+3	1.30	6.18E+6 600.	760 760	7.84 0.283 0.283	\$0.35 \$0.44	195 183
Carbon Steel 1030	1.74	1.16E+3	2.40	5.45E+6	760	7.84 0.283	\$0.44	1205
Carbon Steel 1040	1.65	600.	5.00	10.2E+6	760	7.84 0.283	\$0.44	1083
CH135 (0.005% C Steel)	1.78	4.45E+3	0.61	10.2E+6	760	7.84 0.283	\$0.44	157
Ferrite Phillips® 3C81	0.50	2.70E+3	0.19	1.0	210	4.80 0.173	\$0.44	1261
Ferrite Phillips 3EZ4A	0.41	5.00E+3	0.06	2.0	170	4.80 0.173	\$0.44	183
Ferrite Phillips 4C4	0.38	125.	3.10	10.0E-6	350	4.50 0.163	\$0.44	67 10
Carpenter® 430F Stainless	1.42	1.8E+3	2.00	1.67E+6	671	7.75 0.280	\$0.44	57 8
Carpenter Core Iron 0.06% C	1.70	2.7E+3	1.40	10.0E+6	760	7.86 0.284	\$0.44	802 116
Carpenter 1.0% Si Core Iron A	1.80	4.5E+3	0.90	4.00E+6	810	7.75 0.280	\$0.44	1150 167
Carpenter 2.5% Si Core Iron B	1.80	5.0E+3	0.70	2.50E+6	799	7.65 0.276	\$0.44	1289 187
Carpenter 4.0% Si Core Iron C	1.65	4.0E+3	0.60	1.72E+6	788	7.60 0.275	\$0.44	1289 187
Carpenter HiPerm® 49	1.50	50.0E-3	0.07	2.08E+6	475	8.25 0.298	\$8.25	1083 157
Carpenter HyMu® 80	0.73	200E-3	0.02	1.72E+6	460	8.75 0.316	\$13.99	895 130
Carpenter Hyperco® 50	2.28	8.00E-3	0.60	2.50E+6	940	8.11 0.293	\$47.09	212 31
AK Steel® M-15, 2.7% Si	1.76	8.00E-3	0.35	1.96E+6	800	7.70 0.278	\$0.44	2068 300
AK Steel M-19, 2.7% Si	1.72	8.19E-3	0.36	2.00E+6	800	7.70 0.278	\$0.44	1232 179
AK Steel M-22, 2.0% Si	1.72	7.82E-3	0.39	2.00E+6	800	7.75 0.280	\$0.66	1177 171
AK Steel M-36, 2.0% Si	1.75	7.81E-3	0.50	2.27E+6	800	7.75 0.280	\$0.66	1219 177
AK Steel M-45, 1.6% Si	1.77	7.08E-3	0.81	2.94E+6	800	7.80 0.282	\$0.66	1247 181
Meiglas® Allied 2605CO	1.80	400E-3	0.05	813.E-3	415	7.56 0.273	\$53.98	1289 187
Meiglas Allied 2714A	0.57	1.00E-6	0.01	704.E-3	205	7.59 0.274	\$104.33	129 19

Note:

- This data was collected in 2002.
- The Carbon Steel Electrical Conductivity is estimated based on a linear interpolation between the following two data points.
 - 0.0% C Steel = 9.7 micro-ohm-cm
 - 1.4% C Steel = 40.0 micro-ohm-cm

Appendix-E: BH Curve Fit

The 3-Factor magnetization equation (**Eq. E.1**) from Brauer [9] is shown in the form of relative permeability. The coefficients (k_1 , k_2 , k_3) are based on a curve fit of manufacturer data. The values for RMS Error, maximum permeability ($\mu_{r\text{-max}}$), and saturation flux density (B_{sat}) are from **Eq. E.1**. Saturation is defined here as the point where permeability is 10% of $\mu_{r\text{-max}}$.

$$\mu_r = \frac{B}{\mu_0 H} = \frac{1}{\mu_o \left[k_1 e^{(k_2 B^2)} + k_3 \right]} + 1 \quad (\text{E.1})$$

Material	Curve Fit Coefficients			$\mu_{r\text{-max}}$	B_{sat} Tesla	RMS Error
	k_1	k_2	k_3			
US Steel® 1010 annealed	4.847E+00	1.9080	2.273E+02	3,429	1.79	1.00%
US Steel 1010 cold rolled	3.662E+01	1.3310	5.349E+02	1,393	1.93	0.80%
US Steel 1020 annealed	4.770E+00	2.0550	3.022E+02	2,593	1.77	1.40%
US Steel 1020 cold rolled	1.423E+01	1.6990	8.063E+02	971	1.92	1.20%
US Steel 1030 annealed	5.000E+01	1.3710	6.543E+02	1,146	1.88	1.50%
US Steel 1030 cold rolled	4.000E+01	1.4160	1.212E+03	636	2.00	0.70%
AK Steel® H-0	1.500E-05	4.6500	1.108E+01	71,850	1.85	4.30%
AK Steel M-4	4.242E-03	3.3230	1.358E+01	58,586	1.77	1.65%
AK Steel M-6	1.235E-02	3.0870	9.788E+00	81,203	1.70	1.83%
AK Steel M-15	8.795E-01	2.6660	9.427E+01	8,364	1.61	3.80%
AK Steel M-19	2.150E+00	2.4770	8.303E+01	9,343	1.55	4.00%
AK Steel M-22	2.214E+00	2.4120	9.038E+01	8,595	1.57	3.70%
AK Steel M-36	1.683E+00	2.4320	1.035E+02	7,563	1.62	3.80%
AK Steel M-45	3.500E+00	2.1480	1.248E+02	6,204	1.65	3.80%
AK Steel M-47sp	1.247E-01	3.3350	7.083E+01	11,216	1.60	3.90%
Carpenter® Hiperco® 15	7.510E+00	1.6560	3.787E+02	2,061	1.93	2.24%
Carpenter Hiperco 50A	4.595E-03	2.5360	4.651E+01	17,109	2.13	2.28%
Carpenter HiPerm® 49 annealed	7.214E-03	5.5500	7.256E+00	109,563	1.29	1.80%
Carpenter HiPerm 49 mill processed	5.386E+01	1.0240	1.484E+02	3,935	1.87	3.90%
Carpenter HyMu® 80	5.633E-04	24.5900	1.674E+00	475,082	0.67	2.41%
Carpenter HyMu 800	2.431E-05	31.6600	2.391E+00	332,765	0.68	3.58%
Carpenter Silicon Core Iron B-FM	1.214E+00	2.7950	1.727E+02	4,577	1.60	1.81%
Stainless 416 Metals Handbook	2.044E+01	2.6590	9.934E+02	786	1.52	2.60%
Carpenter Stainless 430F $H_{RB}=78$	4.645E-02	6.9520	4.132E+02	1,927	1.28	2.49%
Carpenter Stainless 430F $H_{RB}=87$	3.164E-02	7.0850	7.271E+02	1,095	1.33	2.42%
Carpenter Stainless 430FR 9.5 mm Dia.	5.588E-02	6.7150	4.009E+02	1,986	1.29	3.07%
Carpenter Stainless 430FR 15.9 mm Dia.	4.403E-02	7.8090	7.184E+02	1,109	1.25	1.11%
Cast Iron Gray Metals Handbook	4.438E+03	0.9405	1.300E+01	180	1.58	4.91%
Cast Iron Nodular Metals Handbook	4.343E+01	2.5510	1.568E+03	495	1.52	1.78%
Hitachi® Finemet® FT-3TL	2.000E-05	9.4950	3.951E+01	20,144	1.35	2.15%
Magnetics® Square Permalloy 80	4.500E-02	9.0910	6.344E+00	124,563	0.89	2.10%
Magnetics Supermalloy®	1.073E-01	9.1760	3.046E+00	252,369	0.79	2.60%
Magnetics Supermendur®	2.248E-05	2.9890	1.124E+01	70,788	2.27	4.00%
Magnetics Kool Mu® 26u	3.125E+03	4.6360	3.048E+04	25	1.06	4.12%
Metglas® 2605S-2	2.031E-05	6.2390	1.881E+00	422,973	1.49	3.45%
Metglas 2605S-3A	5.321E-03	4.2930	1.209E+00	655,384	1.34	2.07%
Metglas 2605SM	5.321E-03	5.7680	1.005E+00	787,833	1.15	4.29%
Metglas 2826MB	2.375E-05	19.1300	8.075E-01	985,477	0.83	2.03%
Micrometals® 26	2.000E+03	1.0920	8.894E+02	276	1.57	3.50%
Micrometals® 52	2.002E+03	1.0230	1.901E+03	205	1.70	2.70%

Appendix-F: Hard-Magnetic Permanent Magnet Materials

Permanent Magnet Type	Br Residual Flux	Hc kGauss	BHmax	u-rec	Recoil Perm.	Tc Curie Temp. °C	Tmax Operating Temp. °C	Density g/cc	Density lb/in ³	Cost \$/lb.	BHmax kJ/m ³
Ceramic 1	2.30	1.86	1.05	1.15	450	300	4.99	0.180	0.2.	\$2.	8.4
Ceramic 8	3.85	2.95	3.50	1.06	450	300	4.99	0.180	0.4.	\$4.	27.9
Ceramic 10	4.20	3.05	4.20	1.06	450	300	4.99	0.180	0.8.	\$8.	33.4
Flexible HF1	2.20	2.00	1.10	1.06	---	100	3.88	0.140	0.2.	\$2.	8.8
Flexible HF2	2.45	2.20	1.40	1.06	---	100	3.88	0.140	0.3.	\$3.	11.1
Flexible HF3	2.65	2.20	1.60	1.06	---	100	3.88	0.140	0.3.	\$3.	12.7
Alnico 5 - Cast	12.50	0.64	5.5	3.70	860	540	7.30	0.263	0.15.	\$15.	43.8
Alnico 5-7 - Cast	13.50	0.74	7.5	3.60	860	540	7.30	0.263	0.30.	\$30.	59.7
Alnico 6 - Cast	10.50	0.78	3.9	2.40	860	540	7.30	0.263	0.20.	\$20.	31.0
Alnico 8 - Cast	8.20	1.65	5.5	2.00	860	550	7.30	0.263	0.18.	\$18.	43.8
Alnico 5 - Sintered	10.80	0.60	3.8	5.20	860	550	7.30	0.263	0.10.	\$10.	30.2
Alnico 8 - Sintered	7.00	1.90	5.0	1.90	860	540	7.30	0.263	0.10.	\$10.	39.8
Sm-Co B15S Bonded	7.95	6.10	14	1.05	720	150	7.00	0.253	0.90.	\$90.	111.4
Sm-Co 18	8.60	7.20	18	1.08	775	250	8.30	0.300	0.100.	\$100.	143.2
Sm-Co 28	10.70	10.30	28	1.05	820	350	8.30	0.300	0.130.	\$130.	222.8
Sm-Co 32H	11.60	9.50	32	1.02	820	350	8.30	0.300	0.140.	\$140.	254.6
Nd-Fe-B B10N Bonded	6.80	5.78	10	1.25	350	150	6.00	0.217	0.60.	\$60.	79.6
Nd-Fe-B 24 UH	10.00	9.60	24	1.10	310	210	7.45	0.269	0.80.	\$80.	191.0
Nd-Fe-B 28 UH	10.90	10.40	28	1.05	310	190	7.45	0.269	0.80.	\$80.	222.8
Nd-Fe-B 32 SH	11.60	11.10	32	1.10	310	180	7.45	0.269	0.90.	\$90.	254.6
Nd-Fe-B 39 H	12.80	12.30	40	1.10	310	150	7.45	0.269	0.80.	\$80.	318.3
Nd-Fe-B 42 H	13.30	12.70	43	1.10	310	120	7.45	0.269	0.80.	\$80.	342.2
Nd-Fe-B 45	13.30	12.90	45	1.10	310	100	7.45	0.269	0.90.	\$90.	358.1
Nd-Fe-B 48	14.10	12.90	48	1.10	310	80	7.45	0.269	0.90.	\$90.	382.0

Note: This data was collected in 2002

Appendix-G: Low Core Loss Magnetic Materials

Note: The **RED** values are estimates based on similar materials.

Material Type	Material ID	ur		Bmax	t	r	εr	d	k	Bsat	Tc
		Relative Permeability	Flux Density T	Lamination Thickness in	Electrical Resistivity ohm·m	Dielectric Constant	Density kg/m³	Thermal Cond. w/m·K	Saturation Flux Density T		
1	Motor Lamination	AK Steel® H-0 - 3.0% Si	71,850	1.00	0.0090	4.50E-07	0.0	7,650	18.0	1.85	749
2	Motor Lamination	AK Steel M-2 - 3.0% Si	55,600	1.00	0.0090	4.80E-07	0.0	7,650	18.0	1.70	746
3	Motor Lamination	AK Steel M-3 - 3.0% Si	65,000	1.00	0.0090	4.80E-07	0.0	7,650	18.0	1.70	746
4	Motor Lamination	AK Steel M-4 - 3.0% Si	58,586	1.00	0.0090	4.80E-07	0.0	7,650	18.0	1.77	746
5	Motor Lamination	AK Steel M-5 - 3.0% Si	69,250	1.00	0.0090	4.80E-07	0.0	7,650	18.0	1.70	746
6	Motor Lamination	AK Steel M-6 - 3.0% Si	81,203	1.00	0.0090	4.80E-07	0.0	7,650	18.0	1.70	746
7	Motor Lamination	AK Steel M-15 - 2.7% Si	8,364	1.00	0.0185	5.10E-07	0.0	7,650	18.0	1.61	746
8	Motor Lamination	AK Steel M-19 - 2.7% Si	9,343	1.00	0.0185	5.00E-07	0.0	7,650	18.0	1.55	746
9	Motor Lamination	AK Steel M-22 - 2.0% Si	8,595	1.00	0.0185	4.40E-07	0.0	7,650	18.0	1.57	746
10	Motor Lamination	AK Steel M-36 - 2.0% Si	7,563	1.00	0.0185	4.00E-07	0.0	7,700	18.0	1.62	746
11	Motor Lamination	AK Steel M-45 - 1.6% Si	6,204	1.00	0.0185	3.40E-07	0.0	7,750	18.0	1.65	746
12	Motor Lamination	Hitachi® UnCut-Core - 3% Si	62,500	1.00	0.0090	4.80E-07	0.0	7,600	18.0	1.70	746
13	Motor Lamination	Hitachi UnCut-Core - 6.5% Si	50,000	0.90	0.0040	8.00E-07	0.0	7,600	18.0	1.60	746
14	Electrical Steel	JFE® - 6.5% Si - 10INEX900	23,000	1.00	0.0040	8.20E-07	0.0	7,490	18.0	1.80	746
15	Electrical Steel	JFE - 6.5% Si - 10INH600	4,000	1.00	0.0040	8.20E-07	0.0	7,530	18.0	1.88	746
16	Electrical Steel	JFE - 6.5% Si - 20INHF1300	4,000	1.00	0.0040	8.20E-07	0.0	7,530	18.0	1.88	746
17	Nano-Crystalline	Finemet® FT-3M	50,000	0.80	0.0007	1.20E-06	0.0	7,300	8.2	1.23	570
18	Nano-Crystalline	Finemet FT-3KL	20,690	1.00	0.0007	1.20E-06	0.0	7,300	8.2	1.23	570
19	Nano-Crystalline	Finemet FT-3KS0T	60,500	0.90	0.0007	1.20E-06	0.0	7,300	8.2	1.23	570
20	Nano-Crystalline	Finemet UnCut-Core F3CC	50,000	0.70	0.0007	1.20E-06	0.0	7,300	8.2	1.23	570
21	Nano-Crystalline	Finemet UnCut-Core FT-3TL	21,145	1.00	0.0007	1.20E-06	0.0	7,300	8.2	1.23	570
22	Nano-Crystalline	Finemet UnCut-Core FT-3TL - New Info	21,145	1.00	0.0007	1.20E-06	0.0	7,300	8.2	1.23	570
23	Nano-Crystalline	Finemet UnCut-Core FT-3TL - CMU Test	26,500	1.00	0.0007	1.20E-06	0.0	7,300	8.2	1.23	570
24	Nano-Crystalline	NASA MANC GR133 Strain Annealed	41	1.00	0.0007	1.20E-06	0.0	7,300	8.2	1.23	570
25	Nano-Crystalline	Vitroperm® 500F	150,000	0.80	0.0008	1.10E-06	0.0	7,600	8.2	1.20	600
26	Nano-Crystalline	MK Magnetics® (Finemet FT3)	21,145	1.00	0.0007	1.20E-06	0.0	7,300	8.2	1.23	570
27	Amorphous	MK Magnetics (26055A1)	600,000	1.00	0.0010	1.30E-06	0.0	7,180	9.0	1.56	395
28	Amorphous	Metglas® - 2605HB1	400,000	1.00	0.0010	1.20E-06	0.0	7,330	9.0	1.63	364

Note: The **RED** values are estimates based on similar materials.

Note: This data was collected in 2018.

Material Type	Material ID	ur		Bmax		t		r		εr		d		k		Bsat		Tc	
		Relative Permeability	Flux Density T	Linear Flux T	Lamination Thickness in	Available	Electrical Resistivity ohm·m	Dielectric Constant	Density kg/m³	Thermal Cond. w/m·K	Saturation Flux Density T	Curie Temp. deg.C							
29	Amorphous Metglas - 26055A1	600,000	1.00	0.0010	1.30E-06	0.0	7.180	9.0	1.56	395									
30	Amorphous Metglas - 26055A3	35,000	1.00	0.0010	1.38E-06	0.0	7.290	9.0	1.41	358									
31	Amorphous Metglas - 2705M	600,000	0.40	0.0010	1.36E-06	0.0	7.800	9.0	0.77	365									
32	Amorphous Metglas - 2714A	1,000,000	0.30	0.0010	1.42E-06	0.0	7.590	9.0	0.57	225									
33	Amorphous Metglas - 2826MB	800,000	0.70	0.0010	1.38E-06	0.0	7.900	9.0	0.88	353									
34	Amorphous Metglas - UnCut-Core AMCCSA1	600,000	1.00	0.0010	1.30E-06	0.0	7.180	9.0	1.56	395									
35	Ceramic Ferrite EPCOS® - N27	2,000	0.35	---	3.00	20.0	4,800	3.6	0.40	220									
36	Ceramic Ferrite EPCOS - N49	1,500	0.33	---	17.00	20.0	4,750	3.6	0.38	240									
37	Ceramic Ferrite EPCOS - N87	2,200	0.33	---	10.00	20.0	4,850	3.6	0.38	210									
38	Ceramic Ferrite EPCOS - N92	1,500	0.33	---	8.00	20.0	4,850	3.6	0.42	280									
39	Ceramic Ferrite EPCOS - N97	2,300	0.33	---	8.00	20.0	4,850	3.6	0.40	230									
40	Ceramic Ferrite Fair-Rite® - 95	3,000	0.30	---	2.00	20.0	4,800	3.6	0.50	220									
41	Ceramic Ferrite Fair-Rite - 98	2,400	0.30	---	2.00	20.0	4,800	3.6	0.50	215									
42	Ceramic Ferrite Fair-Rite - 78	2,300	0.20	---	2.00	20.0	4,800	3.6	0.48	200									
43	Ceramic Ferrite Fair-Rite - 97	2,000	0.30	---	2.00	20.0	4,800	3.6	0.50	220									
44	Ceramic Ferrite Fair-Rite - 77	2,000	0.20	---	1.00	20.0	4,800	3.6	0.49	200									
45	Ceramic Ferrite Fair-Rite - 79	1,400	0.30	---	2.00	20.0	4,800	3.6	0.47	225									
46	Ceramic Ferrite Fair-Rite - 73	2,500	0.15	---	1.00	20.0	4,800	3.6	0.39	160									
47	Ceramic Ferrite Fair-Rite - 52	250	0.20	---	1.00E+07	20.0	4,800	3.6	0.42	250									
48	Ceramic Ferrite Fair-Rite - 51	350	0.10	---	1.00E+07	20.0	4,800	3.6	0.32	170									
49	Ceramic Ferrite Fair-Rite - 44	500	0.10	---	1.00E+07	20.0	4,800	3.6	0.30	160									
50	Ceramic Ferrite Fair-Rite - 46	500	0.10	---	1.00E+06	20.0	4,800	3.6	0.30	140									
51	Ceramic Ferrite Ferrox-Cube® - 3C30	5,900	0.20	---	2.00	20.0	4,800	3.6	0.50	240									
52	Ceramic Ferrite FerroxCube - 3C34	6,500	0.20	---	5.00	20.0	4,800	3.6	0.50	240									
53	Ceramic Ferrite FerroxCube - 3C81	5,500	0.20	---	1.00	20.0	4,800	3.6	0.45	210									
54	Ceramic Ferrite FerroxCube - 3C90	5,500	0.20	---	5.00	20.0	4,800	3.6	0.47	220									
55	Ceramic Ferrite FerroxCube - 3C91	5,500	0.20	---	5.00	20.0	4,800	3.6	0.47	220									
56	Ceramic Ferrite FerroxCube - 3C92	5,500	0.20	---	5.00	20.0	4,800	3.6	0.54	280									

Note: The **RED** values are estimates based on similar materials.

Note: This data was collected in 2018.

Material Type	Material ID	ur	Bmax	t	r	εr	d	k	Bsat	Tc
		Relative Permeability	Linear Flux Density	Available Lamination Thickness in	Electrical Resistivity ohm·m	Dielectric Constant	Density kg/m³	Thermal Cond. w/m·K	Saturation Flux Density T	Curie Temp. deg.C
57 Ceramic Ferrite	Ferrox-Cube - 3C93	5,000	0.10	---	5.00	20.0	4,800	3.6	0.52	240
58 Ceramic Ferrite	Ferrox-Cube - 3C94	5,500	0.20	---	5.00	20.0	4,800	3.6	0.47	220
59 Ceramic Ferrite	Ferrox-Cube - 3C95	5,000	0.20	---	5.00	20.0	4,800	3.6	0.53	215
60 Ceramic Ferrite	Ferrox-Cube - 3C96	5,500	0.20	---	5.00	20.0	4,800	3.6	0.50	240
61 Ceramic Ferrite	Ferrox-Cube - 3T3	4,000	0.20	---	2.00	20.0	4,750	3.6	0.44	200
62 Ceramic Ferrite	Ferrox-Cube - 3T4	1,700	0.20	---	10.00	20.0	4,700	3.6	0.41	220
63 Ceramic Ferrite	Ferrox-Cube - 3T35	2,400	0.20	---	10.00	20.0	4,750	3.6	0.50	240
64 Ceramic Ferrite	Ferrox-Cube - 3T45	1,700	0.20	---	10.00	20.0	4,800	3.6	0.42	300
65 Ceramic Ferrite	Magnetics® - R	4,300	0.25	---	6.00	20.0	4,800	3.6	0.50	230
66 Ceramic Ferrite	Magnetics - P	4,000	0.25	---	5.00	20.0	4,800	3.6	0.50	230
67 Ceramic Ferrite	Magnetics - F	3,800	0.25	---	2.00	20.0	4,800	3.6	0.49	250
68 Iron Powder	Magnetics - Koil-Mu® - Fe Si Al - 125u	125	1.00	---	1.00	20.0	5,790	3.6	1.00	500
69 Iron Powder	Magnetics - Koil-Mu® - Fe Si Al - 60u	60	1.00	---	1.00	20.0	5,790	3.6	1.00	500
70 Iron Powder	Magnetics - Koil-Mu® - Fe Si Al - 26u	26	1.00	---	1.00	20.0	5,790	3.6	1.00	500
71 Iron Powder	Magnetics - Koil-MuHF-Fe Si Al	60	1.00	---	1.00	20.0	6,450	3.6	1.00	500
72 Iron Powder	Magnetics - Edge® - Fe Ni	60	1.50	---	1.00	20.0	8,050	3.6	1.50	500
73 Iron Powder	Magnetics - MPP - Fe Ni Mo	200	0.80	---	1.00	20.0	9,550	3.6	0.80	460
74 Iron Powder	Micrometals® - MS - Sendust - Fe Si Al	125	0.80	---	1.00	20.0	5,790	3.6	1.00	500
75 Iron Powder	Micrometals - MP - Ni Fe Mo	250	0.80	---	1.00	20.0	7,440	3.6	1.00	400
76 Iron Powder	Micrometals - FS - Fe Si	90	0.80	---	1.00	20.0	6,590	3.6	1.00	700
77 Iron Powder	Micrometals - HF - Ni Fe	160	0.80	---	1.00	20.0	6,880	3.6	1.00	450
78 Iron Powder	Micrometals - OP - Fe Si Al Ni	125	0.80	---	1.00	20.0	6,620	3.6	1.00	400
79 Iron Powder	POCO® - NPF - Fe 6.5%Si	90	1.35	---	1.00	20.0	6,670	3.6	1.50	700
80 Iron Powder	POCO - NPF-C - Amorphous	60	1.08	---	1.00	20.0	6,000	3.6	1.20	700
81 Iron Powder	POCO - NPS - Sendust - Fe Si Al	125	0.90	---	1.00	20.0	6,200	3.6	1.00	500
82 Iron Powder	POCO - PPI - Iron	40	1.17	---	1.00	20.0	6,200	3.6	1.30	700
83 Iron Powder	POCO - PHD-40 - Amorphous	40	1.08	---	1.00	20.0	6,400	3.6	1.20	700
84 Iron Powder	POCO - PHD-60 - Iron	60	1.08	---	1.00	20.0	6,400	3.6	1.20	700

Note: This data was collected in 2018.

Note: The Steinmetz coefficients were curve fit to core loss curves from material datasheets.

Material Type	Material ID	Bpk =	Core Loss			Steinmetz Coefficients			Valid Frequency Range			
			Excitation Voltage Wave Form	1 kHz w/kg	10 kHz w/kg	Pc = K (fAa) (BaB) w/kg f(Hz), BT	K	a	b	Min (Hz)	Max (Hz)	RMS Error %
1	Motor Lamination	AK Steel® H-0 - 3.0% Si	Sine	0.6	21.1	744.9	6.600E-04	1.547	2.407	50.0E+0	400.0E+0	6.6%
2	Motor Lamination	AK Steel M-2 - 3.0% Si	Sine	0.8	22.8	618.9	1.061E-03	1.433	2.002	50.0E+0	60.0E+0	7.4%
3	Motor Lamination	AK Steel M-3 - 3.0% Si	Sine	0.9	28.0	831.0	9.365E-04	1.472	2.020	50.0E+0	60.0E+0	6.4%
4	Motor Lamination	AK Steel M-4 - 3.0% Si	Sine	1.4	45.6	1495.5	9.340E-04	1.516	1.968	50.0E+0	60.0E+0	6.1%
5	Motor Lamination	AK Steel M-5 - 3.0% Si	Sine	1.7	59.9	2116.1	9.114E-04	1.548	1.966	50.0E+0	60.0E+0	4.9%
6	Motor Lamination	AK Steel M-6 - 3.0% Si	Sine	2.3	86.4	3277.7	9.234E-04	1.579	1.924	50.0E+0	60.0E+0	3.9%
7	Motor Lamination	AK Steel M-15 - 2.7% Si	Sine	3.2	104.9	3432.7	2.790E-03	1.515	2.111	50.0E+0	400.0E+0	5.6%
8	Motor Lamination	AK Steel M-19 - 2.7% Si	Sine	2.5	83.1	2721.7	2.760E-03	1.515	2.262	50.0E+0	400.0E+0	6.3%
9	Motor Lamination	AK Steel M-22 - 2.0% Si	Sine	3.7	122.6	4012.4	3.130E-03	1.515	2.099	50.0E+0	400.0E+0	5.1%
10	Motor Lamination	AK Steel M-36 - 2.0% Si	Sine	4.5	148.0	4843.5	3.520E-03	1.515	2.055	50.0E+0	600.0E+0	5.2%
11	Motor Lamination	AK Steel M-45 - 1.6% Si	Sine	8.0	261.1	8547.9	5.340E-03	1.515	1.961	50.0E+0	400.0E+0	2.4%
12	Motor Lamination	Hitachi® UnCut-Core - 3% Si	Sine	2.1	103.6	5003.8	4.756E-04	1.684	2.000	1.0E+3	100.0E+3	0.7%
13	Motor Lamination	Hitachi UnCut-Core - 6.5% Si	Sine	0.9	28.4	879.8	7.715E-04	1.491	2.000	1.0E+3	100.0E+3	0.5%
14	Electrical Steel	JFE® - 6.5% Si - 10INEX900	Sine	0.9	34.6	1335.9	3.345E-04	1.587	1.908	2.0E+3	50.0E+3	9.8%
15	Electrical Steel	JFE - 6.5% Si - 10INHF600	Sine	1.2	31.0	830.6	1.566E-03	1.428	2.025	2.0E+3	50.0E+3	11.3%
16	Electrical Steel	JFE - 6.5% Si - 20INHF1300	Sine	2.0	50.1	1239.0	3.068E-03	1.393	1.944	1.0E+3	20.0E+3	7.9%
17	Nano-Crystalline	Finemet® FT-3M	Sine	0.01	0.56	33.0	1.517E-06	1.767	2.142	1.0E+3	300.0E+3	12.1%
18	Nano-Crystalline	Finemet FT-3KL	Sine	0.01	0.44	33.9	3.177E-07	1.890	2.034	1.0E+3	100.0E+3	6.6%
19	Nano-Crystalline	Finemet FT-3K50T	Sine	0.00	0.30	20.1	4.390E-07	1.822	2.074	1.0E+3	100.0E+3	4.7%
20	Nano-Crystalline	Finemet UnCut-Core F3CC	Sine	0.10	3.3	113.0	6.178E-05	1.332	2.000	1.0E+3	100.0E+3	1.5%
21	Nano-Crystalline	Finemet UnCut-Core FT-3TL	Sine	0.01	0.4	20.0	9.619E-07	1.743	2.000	1.0E+3	100.0E+3	0.3%
22	Nano-Crystalline	Finemet UnCut-Core FT-3TL - New Info	Sine	0.01	0.4	21.2	8.153E-07	1.780	2.125	1.0E+3	100.0E+3	4.4%
23	Nano-Crystalline	Finemet UnCut-Core FT-3TL - CMU Test Square	Sine	0.01	0.6	30.7	1.814E-06	1.747	2.155	1.0E+3	50.0E+3	3.1%
24	Nano-Crystalline	NASA MANC GRIC133 Strain Annealed	Sine	0.08	4.3	227.2	1.683E-05	1.723	2.124	1.0E+3	10.0E+3	5.9%
25	Nano-Crystalline	Visoterm® 500F	Sine	0.01	0.70	44.5	1.252E-06	1.802	2.088	2.0E+3	100.0E+3	1.4%
26	Nano-Crystalline	MK Magnetics® (Finemet FT3)	Sine	0.04	1.6	61.1	2.383E-05	1.573	2.083	1.0E+3	200.0E+3	7.3%
27	Amorphous	MK Magnetics (26055A1)	Sine	0.50	9.3	171.9	2.812E-03	1.267	2.216	400.0E+0	40.0E+3	8.2%
28	Amorphous	Metglas® - 2605HB1	Sine	0.27	12.1	546.4	5.122E-05	1.655	1.784	1.0E+3	100.0E+3	23.4%

Note: The **GREEN** values are based on imaginary permeability data.

Note: The Steinmetz coefficients were curve fit to core loss curves from material datasheets.

Material Type	Material ID	Excitation Voltage Wave Form	Bpk = 0.2	Tesla			Valid Frequency Range			RMS Error %
				Core Loss w/kg	Core Loss 1 kHz w/kg	Core Loss 100 kHz w/kg	K	a	b	
29 Amorphous	Merglas - 2605SA1	Sine	0.27	12.1	546.4	5.122E-05	1.655	1.784	1.0E+3	100.0E+3 23.4%
30 Amorphous	Merglas - 2605SA3	Sine	0.09	3.3	117.9	5.520E-05	1.550	2.032	1.0E+3	250.0E+3 15.9%
31 Amorphous	Merglas - 2705M	Sine	0.09	3.2	116.3	5.847E-05	1.559	2.141	5.0E+3	250.0E+3 18.8%
32 Amorphous	Merglas - 2714A	Sine	0.03	1.23	45.6	9.944E-06	1.570	1.700	6.0E+0	250.0E+3 ---
33 Amorphous	Merglas - 2826MB	Sine	0.53	18.5	650.3	1.880E-04	1.546	1.704	6.0E+0	100.0E+3 19.5%
34 Amorphous	Merglas - Uncut-Core AMCC-SA1	Sine	0.49	12.4	315.6	7.364E-04	1.406	2.000	1.0E+3	100.0E+3 1.9%
35 Ceramic Ferrite	EPCOS® - N27	Sine	0.92	14.36	224.9	7.167E-03	1.195	2.115	2.0E+3	200.0E+3 4.3%
36 Ceramic Ferrite	EPCOS - N49	Sine	0.59	8.9	133.7	1.316E-02	1.178	2.694	2.50E+3	500.0E+3 5.9%
37 Ceramic Ferrite	EPCOS - N87	Sine	0.46	7.8	133.9	3.699E-03	1.232	2.291	2.50E+3	200.0E+3 5.8%
38 Ceramic Ferrite	EPCOS - N92	Sine	2.73	24.5	220.7	8.159E-02	0.954	1.914	2.0E+3	200.0E+3 12.3%
39 Ceramic Ferrite	EPCOS - N97	Sine	0.51	8.1	129.1	4.606E-03	1.201	2.228	1.60E+3	200.0E+3 6.2%
40 Ceramic Ferrite	Fair-Rite® - 95	Sine	0.23	4.1	71.6	2.594E-03	1.242	2.531	50.0E+3	200.0E+3 19.5%
41 Ceramic Ferrite	Fair-Rite® - 98	Sine	0.03	1.4	61.4	1.874E-05	1.657	2.532	50.0E+3	200.0E+3 10.3%
42 Ceramic Ferrite	Fair-Rite - 78	Sine	0.14	4.4	141.0	2.976E-04	1.506	2.653	2.50E+3	200.0E+3 14.0%
43 Ceramic Ferrite	Fair-Rite - 97	Sine	0.02	1.0	69.2	3.215E-06	1.819	2.521	50.0E+3	400.0E+3 12.8%
44 Ceramic Ferrite	Fair-Rite - 77	Sine	0.60	13.7	311.1	1.942E-03	1.357	2.261	1.0E+3	100.0E+3 5.7%
45 Ceramic Ferrite	Fair-Rite - 79	Sine	0.08	2.5	81.4	1.683E-04	1.515	2.705	1.00E+3	750.0E+3 26.2%
46 Ceramic Ferrite	Fair-Rite - 73	Sine	0.00	0.30	18.7	4.670E-07	1.800	2.000	10.0E+3	50.0E+3 5.2%
47 Ceramic Ferrite	Fair-Rite - 32	Sine	0.38	6.7	115.3	1.840E-03	1.239	2.000	1.0E+6	1.0E+6 0.0%
48 Ceramic Ferrite	Fair-Rite - 51	Sine	0.85	8.5	85.2	2.130E-02	1.000	2.000	1.0E+3	100.0E+3 0.0%
49 Ceramic Ferrite	Fair-Rite - 44	Sine	0.06	1.7	50.2	5.170E-05	1.477	2.000	1.0E+3	1.0E+6 0.0%
50 Ceramic Ferrite	Fair-Rite - 46	Sine	1.33	13.3	133.2	3.330E-02	1.000	2.000	1.0E+3	100.0E+3 0.0%
51 Ceramic Ferrite	Ferrox-Cube® - 3C30	Sine	0.09	3.3	115.4	1.590E-04	1.550	2.703	25.0E+3	200.0E+3 8.3%
52 Ceramic Ferrite	Ferrox-Cube - 3C34	Sine	0.09	2.8	84.8	2.850E-04	1.486	2.799	25.0E+3	200.0E+3 10.3%
53 Ceramic Ferrite	Ferrox-Cube - 3C81	Sine	0.26	7.9	239.9	5.450E-04	1.481	2.520	25.0E+3	200.0E+3 6.0%
54 Ceramic Ferrite	Ferrox-Cube - 3C90	Sine	0.09	3.1	112.9	1.480E-04	1.558	2.729	25.0E+3	200.0E+3 7.6%
55 Ceramic Ferrite	Ferrox-Cube - 3C91	Sine	0.10	3.5	122.6	2.110E-04	1.550	2.841	25.0E+3	200.0E+3 7.3%
56 Ceramic Ferrite	Ferrox-Cube - 3C92	Sine	0.13	3.1	74.9	1.450E-03	1.383	3.150	25.0E+3	100.0E+3 4.2%

Note: The Steinmetz coefficients were curve fit to core loss curves from material datasheets.

Material Type	Material ID	Excitation Voltage Wave Form	Bpk = 0.2	Tesla			Valid Frequency Range				
				Core Loss w/kg	Core Loss 1 kHz w/kg	Core Loss 100 kHz w/kg	Steinmetz Coefficients PC = K (fA) (B ^a) w/kg f(Hz), B(T)	K	a	b	Min (Hz)
57 Ceramic Ferrite	Ferrox-Cube - 3C93	Sine	0.21	4.4	91.2	4.140E-03	1.318	3.215	25.0E-3	100.0E-3	5.9%
58 Ceramic Ferrite	Ferrox-Cube - 3C94	Sine	0.09	2.9	91.7	2.350E-04	1.504	2.754	25.0E-3	200.0E-3	6.6%
59 Ceramic Ferrite	Ferrox-Cube - 3C95	Sine	0.00	0.5	58.9	2.020E-07	2.079	2.762	100.0E-3	400.0E-3	14.0%
60 Ceramic Ferrite	Ferrox-Cube - 3C96	Sine	0.13	3.1	77.6	1.210E-03	1.396	3.109	25.0E-3	100.0E-3	3.1%
61 Ceramic Ferrite	Ferrox-Cube - 3f3	Sine	0.39	6.1	95.6	7.470E-03	1.193	2.658	25.0E-3	100.0E-3	2.7%
62 Ceramic Ferrite	Ferrox-Cube - 3f4	Sine	1.8	25.3	350.7	9.340E-02	1.142	3.055	25.0E-3	400.0E-3	8.0%
63 Ceramic Ferrite	Ferrox-Cube - 3f5	Sine	0.0000	0.02	10.7	1.420E-11	2.762	2.768	500.0E+3	1.0E+6	13.7%
64 Ceramic Ferrite	Ferrox-Cube - 3f5	Sine	0.43	8.2	153.2	5.650E-03	1.274	2.771	500.0E+3	1.0E+6	7.0%
65 Ceramic Ferrite	Magnetics® - R	Sine	0.04	1.9	86.3	4.310E-05	1.651	2.795	25.0E-3	100.0E-3	10.9%
66 Ceramic Ferrite	Magnetics - P	Sine	0.09	3.2	109.3	1.942E-04	1.532	2.732	25.0E-3	100.0E-3	10.6%
67 Ceramic Ferrite	Magnetics - F	Sine	0.81	11.0	150.0	2.473E-02	1.134	2.700	1.0E+3	100.0E-3	18.5%
68 Iron Powder	Magnetics - Kool-Mu® - Fe Si Al - 125u	Sine	1.62	19.7	240.6	1.955E-02	1.086	1.917	1.0E+3	20.0E+3	3.5%
69 Iron Powder	Magnetics - Kool-Mu® - Fe Si Al - 60u	Sine	1.24	15.7	198.7	1.049E-02	1.103	1.771	1.0E+3	20.0E+3	8.9%
70 Iron Powder	Magnetics - Kool-Mu® - Fe Si Al - 26u	Sine	1.66	17.0	174.9	2.555E-02	1.012	1.752	1.0E+3	20.0E+3	1.8%
71 Iron Powder	Magnetics - Kool-MuHf- Fe Si Al	Sine	0.46	9.0	173.5	1.120E-03	1.287	1.781	60.0E+0	500.0E+3	---
72 Iron Powder	Magnetics - Edge® - Fe Ni	Sine	0.64	12.2	232.1	3.798E-03	1.280	2.309	60.0E+0	500.0E+3	---
73 Iron Powder	Magnetics - MPP - Fe Ni Mo	Sine	0.80	12.4	191.7	9.028E-03	1.190	2.322	60.0E+0	10.0E+3	---
74 Iron Powder	Micrometals® - MS - Sendust - Fe Si Al	Sine	2.20	27.18	335.2	2.502E-02	1.091	1.900	400.0E+0	25.0E+3	7.6%
75 Iron Powder	Micrometals - MP - Ni Fe Mo	Sine	1.30	20.3	315.5	8.389E-03	1.192	1.981	400.0E+0	25.0E+3	12.4%
76 Iron Powder	Micrometals - FS - Fe Si	Sine	5.64	63.5	713.8	9.591E-02	1.051	1.979	400.0E+0	50.0E+3	8.9%
77 Iron Powder	Micrometals - HF - Ni Fe	Sine	3.74	49.1	644.4	5.255E-02	1.118	2.148	400.0E+0	50.0E+3	12.9%
78 Iron Powder	Micrometals - OP - Fe Si Al Ni	Sine	1.79	22.5	282.3	2.842E-02	1.099	2.143	400.0E+0	25.0E+3	7.7%
79 Iron Powder	POCO® - NPF - Fe 6.5%Si	Sine	3.16	47.0	700.0	3.378E-02	1.173	2.216	16.0E+3	100.0E+3	2.6%
80 Iron Powder	POCO - NPF-C - Amorphous	Sine	2.09	31.8	482.1	1.644E-02	1.181	2.057	16.0E+3	100.0E+3	4.3%
81 Iron Powder	POCO - NPs - Sendust - Fe Si Al	Sine	1.83	26.8	392.0	1.664E-02	1.165	2.080	16.0E+3	100.0E+3	2.0%
82 Iron Powder	POCO - PPI - Iron	Sine	8.60	105.5	1295.4	2.181E-01	1.089	2.391	10.0E+3	50.0E+3	8.3%
83 Iron Powder	POCO - PHD-40 - Amorphous	Sine	3.23	65.6	1322.4	7.720E-03	1.308	1.862	5.0E+3	50.0E+3	15.1%
84 Iron Powder	POCO - PHD-60 - Iron	Sine	1.66	43.9	1166.3	1.868E-03	1.424	1.895	5.0E+3	100.0E+3	20.3%

Appendix-H: Wire Insulation

<u>Insulation</u>	<u>Thermal Rating deg.C</u>	<u>NEMA MW 1000</u>	<u>Federal Spec.</u>	<u>Mil-W-583C Class/Type</u>
Plain Enamel	105	MW 1-C MW 2-C	JW 1177/1 JW 1177/2	Class 105 Types T thru T-4
Polyurethane	105	MW 3-C		
Polyurethane Bond	105	MW 15-C	JW 1177/4	
Fomivar	105	MW 1-C	JW 1177/6	
Fomvar Bond	105	MW 29-C		
Poly-Nylon Bond	105			
Polyurethane-Nylon		MW 28-C	JW 1177/9	Class 130
Poly H.T.		MW 75-C		Types B thru B-4
Polyester	155	MW 5-C	JW 1177/10	Class 155
Polyester Epoxy Bond	155			Types L thru L-4
Polyester/Polyimide	180	MW 30-C	JW 1177/12	Class 180
Isoniad	180	MW 30-C	JW 1177/12	Types H thru H-4
Polyester Nylon	180	MW 24-C	JW 1177/11	
Solderable Polyester	180	MW 26-C		
Solderable Polyester Nylon	180	MW 27-C		
Armored Polyester	200	MW 35-C	JW 1177/14	Class 200
Teflon	200			Types K thru K-4
ML	220	MW 16-C	JW 1177/15	Class 220/M thru M-4

Appendix-I: Magnet Wire

Listed below are the bare wire diameter and insulated wire diameter from the MWS Wire Industries wire tables (<https://mwswire.com/>). The insulation thickness is half the difference between the bare and insulated wire diameters.

Wire Size AWG	d_B Bare OD inch	d - Insulated Wire OD (Nominal)				t - Insulation Thickness (Nominal)			
		Single Build inch	Heavy Build inch	Triple Build inch	Quad. Build inch	Single Build inch	Heavy Build inch	Triple Build inch	Quad. Build inch
6	0.1620	0.1648	0.1659	0.1679	0.1685	0.00138	0.00193	0.00293	0.00323
7	0.1443	0.1469	0.1481	0.1492	0.1506	0.00131	0.00191	0.00246	0.00316
8	0.1285	0.1306	0.1322	0.1333	0.1349	0.00106	0.00186	0.00241	0.00321
9	0.1144	0.1165	0.1177	0.1191	0.1205	0.00104	0.00164	0.00234	0.00304
10	0.1019	0.1039	0.1051	0.1064	0.1078	0.00101	0.00161	0.00226	0.00296
11	0.0907	0.0927	0.0938	0.0952	0.0965	0.00099	0.00154	0.00224	0.00289
12	0.0808	0.0827	0.0838	0.0851	0.0864	0.00096	0.00151	0.00216	0.00281
13	0.0719	0.0739	0.0749	0.0762	0.0774	0.00098	0.00148	0.00213	0.00273
14	0.0641	0.0659	0.0675	0.0692	0.0696	0.00092	0.00172	0.00257	0.00277
15	0.0570	0.0587	0.0602	0.0619	0.0625	0.00083	0.00158	0.00243	0.00273
16	0.0508	0.0524	0.0539	0.0554	0.0561	0.00080	0.00155	0.00230	0.00265
17	0.0452	0.0469	0.0482	0.0497	0.0504	0.00083	0.00148	0.00223	0.00258
18	0.0403	0.0418	0.0431	0.0445	0.0454	0.00076	0.00141	0.00211	0.00256
19	0.0359	0.0373	0.0386	0.0399	0.0407	0.00072	0.00137	0.00202	0.00242
20	0.0319	0.0334	0.0346	0.0358	0.0366	0.00073	0.00133	0.00193	0.00233
21	0.0284	0.0298	0.0309	0.0321	0.0330	0.00068	0.00123	0.00183	0.00228
22	0.0253	0.0266	0.0276	0.0288	0.0296	0.00064	0.00114	0.00174	0.00214
23	0.0226	0.0239	0.0249	0.0259	0.0268	0.00067	0.00117	0.00167	0.00212
24	0.0201	0.0213	0.0223	0.0233	0.0242	0.00061	0.00111	0.00161	0.00206
25	0.0179	0.0190	0.0199	0.0209	0.0219	0.00056	0.00101	0.00151	0.00201
26	0.0159	0.0170	0.0178	0.0188	0.0196	0.00054	0.00094	0.00144	0.00184
27	0.0142	0.0153	0.0161	0.0169	0.0177	0.00056	0.00096	0.00136	0.00176
28	0.0126	0.0137	0.0144	0.0152	0.0159	0.00054	0.00089	0.00129	0.00164
29	0.0112	0.0123	0.0130	0.0138	0.0145	0.00053	0.00088	0.00128	0.00163
30	0.0100	0.0109	0.0116	0.0124	0.0131	0.00044	0.00079	0.00119	0.00154
31	0.0089	0.0097	0.0105	0.0110	0.0118	0.00039	0.00079	0.00104	0.00144
32	0.0079	0.0088	0.0095	0.0101	0.0107	0.00043	0.00078	0.00108	0.00138
33	0.0071	0.0078	0.0085	0.0090	0.0096	0.00037	0.00072	0.00097	0.00127
34	0.0063	0.0070	0.0075	0.0080	0.0085	0.00035	0.00060	0.00085	0.00110
35	0.0056	0.0062	0.0067	0.0071	0.0076	0.00030	0.00055	0.00075	0.00100
36	0.0050	0.0056	0.0060	0.0064	0.0068	0.00030	0.00050	0.00070	0.00090
37	0.0044	0.0050	0.0055	0.0059	0.0063	0.00028	0.00053	0.00073	0.00093
38	0.0040	0.0045	0.0049	0.0054	0.0056	0.00027	0.00047	0.00072	0.00082
39	0.0035	0.0039	0.0043	0.0049	0.0049	0.00019	0.00039	0.00069	0.00069
40	0.0031	0.0035	0.0038	0.0043	0.0044	0.00018	0.00033	0.00058	0.00063
41	0.0028	0.0031	0.0034	0.0039	0.0039	0.00015	0.00030	0.00055	0.00055
42	0.0025	0.0028	0.0030	0.0035	0.0034	0.00016	0.00026	0.00051	0.00046
43	0.0022	0.0025	0.0027	0.0032	0.0031	0.00014	0.00024	0.00049	0.00044
44	0.0020	0.0022	0.0025	0.0029	0.0029	0.00011	0.00026	0.00046	0.00046
45	0.00176	0.00192	0.00215	0.00255	0.00260	0.000081	0.000196	0.000396	0.000421
46	0.00156	0.00173	0.00196	0.00235	0.00241	0.000083	0.000198	0.000393	0.000423
47	0.00139	0.00158	0.00178	0.00210	0.00218	0.000093	0.000193	0.000353	0.000393
48	0.00124	0.00140	0.00155	0.00190	0.00190	0.000080	0.000155	0.000330	0.000330
49	0.00110	0.00124	0.00139	0.00170	0.00174	0.000068	0.000143	0.000298	0.000318
50	0.00098	0.00113	0.00128	0.00160	0.00158	0.000073	0.000148	0.000308	0.000298
51	0.00088	0.00103	0.00117	0.00150	0.00148	0.000077	0.000147	0.000312	0.000302
52	0.00078	0.00093	0.00107	0.00140	0.00138	0.000075	0.000145	0.000310	0.000300
53	0.00069	0.00079	0.00090	0.00121	0.00118	0.000048	0.000103	0.000258	0.000243
54	0.00062	0.00070	0.00082	---	---	0.000041	0.000101	---	---
55	0.00055	0.00064	0.00075	---	---	0.000045	0.000100	---	---

The wire insulation breakdown voltage strength is about 120 kV/mm, based on the minimum dielectric breakdown voltage from Essex Wire datasheets (<https://essexwire.com/>) and the nominal insulation thickness.

- Breakdown \approx 4,300 V for 18 AWG Heavy Build ($t = 0.0014$ inch)
- Breakdown \approx 1,700 V for 36 AWG Heavy Build ($t = 0.0005$ inch)

Increased insulation build layers (such as Heavy Build) increases breakdown voltage, prevents shorting turn-to-turn, and increases reliability. The highest breakdown and shorting potential is typically between the first and last turn. The bare wire diameter (d_B) is given in **Eq. I.1**, where the 1/0, 2/0, 3/0 and 4/0 wire sizes correspond to AWG values of 0, -1, -2 and -3, respectively.

$$d_B = 0.008255(1.123)^{-\text{AWG}} \quad \text{m} \quad \text{Bare wire diameter - Exact} \quad (\text{I.1})$$

The maximum current density (J) for long wires (**Eq. I.2**, 10.5% RMS Error) (from UL or IEC standards) is between $3E+6$ A/m² (2,000 A/in²) for 1 AWG and $11E+6$ A/m² (7,000 A/in²) for 18 AWG. Also, the overall diameter and insulation thickness can be estimated with the following curve fit equations (**Eq. I.3 – Eq. I.14**).

$$J < 111,711/d_B^{2/3} \quad \text{A/m}^2 \quad \text{IEC, UL Rated Current Density } (d_B = \text{m}) \quad (\text{I.2})$$

Overall Diameter over Insulation: (for $6 < \text{AWG} < 55$)

$$d = 0.008172(1.1197)^{-\text{AWG}} \quad \text{m} \quad \text{Single Build} \quad \text{RMS Error} = 1.3\% \quad (\text{I.3})$$

$$d = 0.007998(1.1165)^{-\text{AWG}} \quad \text{m} \quad \text{Heavy Build} \quad \text{RMS Error} = 1.5\% \quad (\text{I.4})$$

$$d = 0.007593(1.1112)^{-\text{AWG}} \quad \text{m} \quad \text{Triple Build} \quad \text{RMS Error} = 3.2\% \quad (\text{I.5})$$

$$d = 0.007749(1.1113)^{-\text{AWG}} \quad \text{m} \quad \text{Quad. Build} \quad \text{RMS Error} = 2.5\% \quad (\text{I.6})$$

Insulation Thickness – Single Build: (RMS Error = 10.5%)

$$t = 0.03924(1.0397)^{-\text{AWG}} \quad \text{mm} \quad (\text{for } 6 < \text{AWG} < 32) \quad (\text{I.7})$$

$$t = 0.33361(1.1115)^{-\text{AWG}} \quad \text{mm} \quad (\text{for } 30 < \text{AWG} < 55) \quad (\text{I.8})$$

Insulation Thickness – Heavy Build: (RMS Error = 7.9%)

$$t = 0.06329(1.0360)^{-\text{AWG}} \quad \text{mm} \quad (\text{for } 6 < \text{AWG} < 32) \quad (\text{I.9})$$

$$t = 0.40265(1.0992)^{-\text{AWG}} \quad \text{mm} \quad (\text{for } 30 < \text{AWG} < 55) \quad (\text{I.10})$$

Insulation Thickness – Triple Build: (RMS Error = 7.3%)

$$t = 0.08112(1.0278)^{-\text{AWG}} \quad \text{mm} \quad (\text{for } 6 < \text{AWG} < 29) \quad (\text{I.11})$$

$$t = 0.22173(1.0694)^{-\text{AWG}} \quad \text{mm} \quad (\text{for } 28 < \text{AWG} < 55) \quad (\text{I.12})$$

Insulation Thickness – Quadruple Build: (RMS Error = 7.2%)

$$t = 0.09903(1.0271)^{-\text{AWG}} \quad \text{mm} \quad (\text{for } 6 < \text{AWG} < 29) \quad (\text{I.13})$$

$$t = 0.54250(1.0903)^{-\text{AWG}} \quad \text{mm} \quad (\text{for } 28 < \text{AWG} < 55) \quad (\text{I.14})$$

Appendix-J: Summary of Physics Equations

Magnetic Field

System Performance

$$\phi \quad \text{Flux}$$

$$\text{Wb}$$

$$1\text{a}$$

$$NI \quad \text{MMF}$$

$$\text{A}$$

$$2\text{a}$$

$$NI = \phi R$$

$$3\text{a}$$

$$\sum \phi = 0 \quad \text{Nodal Eq.}$$

$$\text{Wb}$$

$$4\text{a}$$

$$\lambda = N\phi = LI \quad \text{Flux Linkage}$$

$$5\text{a}$$

$$V = \frac{d\lambda}{dt} \quad \text{Faraday's Law}$$

$$\text{V}$$

$$6\text{a}$$

$$V = \frac{d\lambda}{dt}$$

$$7\text{a}$$

System Properties

$$R = \frac{l}{\mu a} \quad \text{Reluctance}$$

$$\frac{\text{A}}{\text{Wb}}$$

$$8\text{a}$$

$$\mathcal{P} = \frac{\mu a}{l} \quad \text{Permeance}$$

$$\frac{\text{Wb}}{\text{A}}$$

$$9\text{a}$$

$$L = \frac{\lambda}{I} = N^2 \mathcal{P} \quad \text{Inductance}$$

$$\text{H}$$

$$10\text{a}$$

Material Properties

$$B = \frac{\phi}{a} \quad \text{Flux Density}$$

$$\text{T}$$

$$11\text{a}$$

$$H = \frac{NI}{l} \quad \text{Field Intensity}$$

$$\frac{\text{A}}{\text{m}}$$

$$12\text{a}$$

$$\mu = \frac{B}{H} \quad \text{Permeability}$$

$$\frac{\text{H}}{\text{m}}$$

$$13\text{a}$$

$$\mu_0 = 4\pi \times 10^{-7} \quad \text{Free Space}$$

$$\frac{\text{H}}{\text{m}}$$

$$14\text{a}$$

$$\mu_r = \frac{\mu}{\mu_0} \quad \text{Relative Permeability}$$

$$15\text{a}$$

Energy

$$w = \frac{1}{2} BH \quad \text{Density}$$

$$\frac{\text{J}}{\text{m}^3}$$

$$16\text{a}$$

$$W = \frac{1}{2} NI\phi \quad \text{Energy}$$

$$\text{J}$$

$$17\text{a}$$

Electric Field

System Performance

$$q \quad \text{Charge}$$

$$\text{c}$$

$$1\text{b}$$

$$V \quad \text{Voltage}$$

$$\text{V}$$

$$2\text{b}$$

$$V = \frac{q}{C}$$

$$3\text{b}$$

$$\sum q = 0 \quad \text{Nodal Eq.}$$

$$\text{c}$$

$$4\text{b}$$

$$5\text{b}$$

$$I = \frac{dq}{dt} \quad \text{Current}$$

$$\text{A}$$

$$6\text{b}$$

$$7\text{a}$$

$$10\text{b}$$

System Properties

$$R = \frac{l}{\mu a} \quad \text{Reluctance}$$

$$8\text{b}$$

$$\mathcal{P} = \frac{\mu a}{l} \quad \text{Permeance}$$

$$9\text{b}$$

$$C = \frac{\epsilon a}{l} \quad \text{Capacitance}$$

$$\text{F}$$

$$9\text{b}$$

$$10\text{a}$$

$$11\text{b}$$

$$D = \frac{q}{a} \quad \text{Flux Density}$$

$$\frac{\text{c}}{\text{m}^2}$$

$$12\text{b}$$

$$E = \frac{V}{l} \quad \text{Field Intensity}$$

$$\frac{\text{V}}{\text{m}}$$

$$\epsilon = \frac{D}{E} \quad \text{Permittivity}$$

$$\frac{\text{F}}{\text{m}}$$

$$\epsilon_0 = 8.85 \times 10^{-12} \quad \text{Free Space}$$

$$\frac{\text{F}}{\text{m}}$$

$$\epsilon_r = \frac{\epsilon}{\epsilon_0} \quad \text{Dielectric Constant}$$

$$14\text{b}$$

Energy

$$w = \frac{1}{2} DE \quad \text{Density}$$

$$\frac{\text{J}}{\text{m}^3}$$

$$16\text{b}$$

$$W = \frac{1}{2} qV \quad \text{Energy}$$

$$\text{J}$$

$$17\text{b}$$

Material properties are the primary difference in these 4 areas of physics. The equations going across all have the same physical meaning.

- Eq. 3a – 3d all represent the characteristic performance equation
- Eq. 9a – 9d all represent the system compliance
- Eq. 13a – 13d all represent the material property

Electric Current

Mechanical

System Performance

I	Current	A	1c	x	Displacement	m	1d
V	Voltage	V	2c	F	Force	N	2d
$V = IR$	Ohm's Law		3c	$F = k x$			3d
$\sum I = 0$	Nodal Eq.	A	4c	$\sum F = 0$	Nodal Eq.	N	4d
			5c				5d
$V = \frac{d(LI)}{dt}$	Induced Voltage	V	6c	$v = \frac{dx}{dt}$	Velocity	$\frac{m}{s}$	6d
$I = \frac{d(CV)}{dt}$	Stored Current	A	7c				7d

System Properties

$R = \frac{l}{\sigma a}$	Resistance	ohm	8c	$k = \frac{Ea}{l}$	Stiffness	$\frac{N}{m}$	8d
$G = \frac{\sigma a}{l}$	Conductance	S	9c	$\frac{1}{k} = \frac{l}{Ea}$	Compliance	$\frac{m}{N}$	9d
			10c				10d

Material Properties

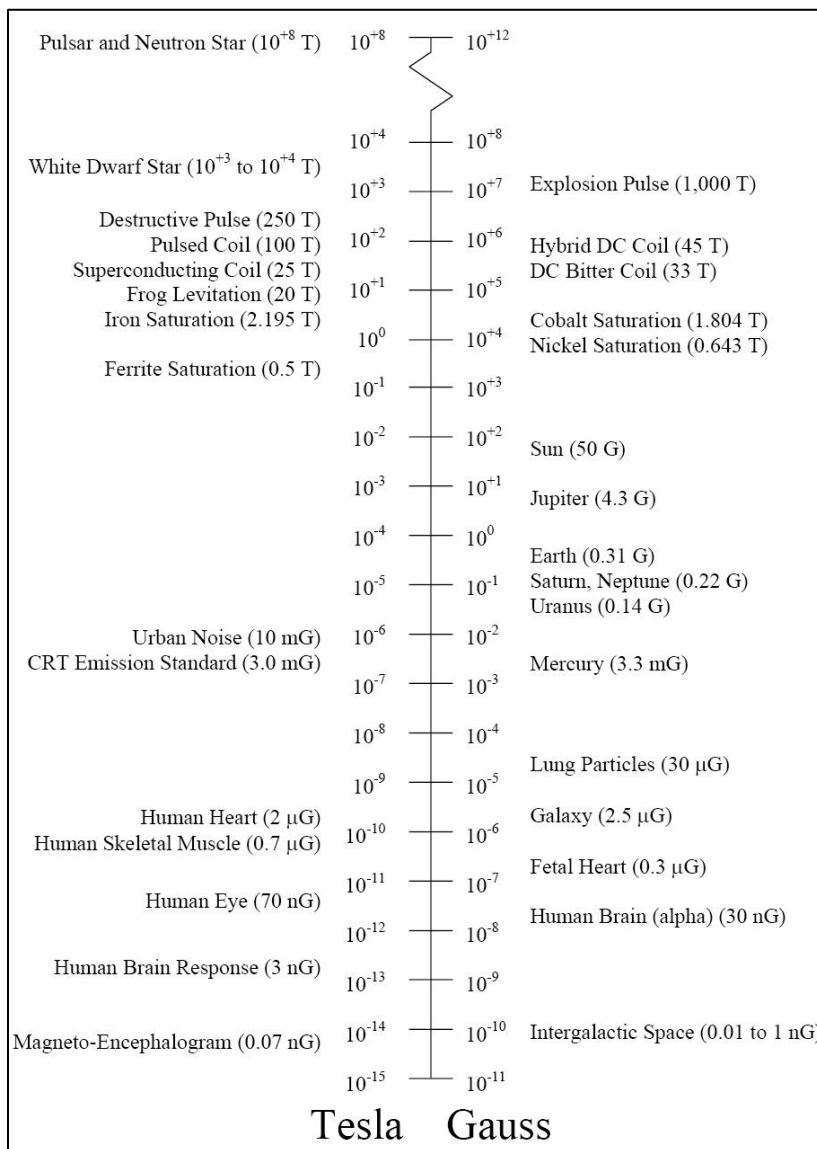
$J = \frac{I}{a}$	Current Density	$\frac{A}{m^2}$	11c	$\varepsilon = \frac{x}{l}$	Strain	$\frac{m}{m}$	11d
$E = \frac{V}{l}$	Field Intensity	$\frac{V}{m}$	12c	$\sigma = \frac{F}{a}$	Stress	$\frac{N}{m^2}$	12d
$\sigma = \frac{J}{E}$	Conductivity	$\frac{S}{m}$	13c	$E = \frac{\sigma}{\varepsilon}$	Elastic Modulus	$\frac{N}{m^2}$	13d
$\sigma_{cu} = 5.80 \times 10^7$	Copper	$\frac{S}{m}$	14c	$E_{Fe} = 2.07 \times 10^{11}$	Steel	$\frac{N}{m^2}$	14d
			15c				15d

Energy

$w = \int EJdt$	Density	$\frac{J}{m^3}$	16c	$w = \frac{1}{2}\sigma\varepsilon$	Density	$\frac{J}{m^3}$	16d
$W = \int VIdt$	Energy	J	17c	$W = \frac{1}{2}Fx$	$\Delta W = F\Delta x$	J	17d

Appendix-K: Range of Magnetic Field Values

Iron, nickel, and cobalt are used in machines (motors, solenoids, actuators, transformers, inductors) that work in the flux density range of 0.5 to 2.0 Tesla (close to a single unit of Tesla). The Earth's magnetic field is 0.31 Gauss (close to a single unit of Gauss). Sensors (Inductive, Hall, MR, GMR, Flux Gate, SQUID) can be designed to work over any part of the entire range. The most unusual item on the chart is "Frog Levitation" at 20 T. A search on "Frog Levitation" will bring up links to further explanations and videos.



References

1. H. C. Roters, *Electromagnetic Devices*, John Wiley & Sons, New York, 1941.
2. G. R. Slemon, *Magnetoelectric Devices: Transducers, Transformers and Machines*, John Wiley & Sons, New York, 1966.
3. B. D. Cullity and C. D. Graham, *Introduction to Magnetic Materials*, 2nd ed., IEEE Press, New Jersey, 2009.
4. J. R. Brauer, “Simple Equation for the Magnetization and Reluctivity Curves of Steel”, *IEEE Transactions on Magnetics*, pp.81, Vol. 11, Jan. 1975.
5. R. J. Parker, *Advances in Permanent Magnetism*, John Wiley & Sons, New York, 1990.
6. L. Gonick and A. Huffman, *The Cartoon Guide to Physics*, Harper Perennial, New York, 1991.
7. R. M. Bozorth, *Ferromagnetism*, IEEE Press, Piscataway, NJ, 1993.
8. W. Yeadon and A. Yeadon, *Handbook of Small Electric Motors*, McGraw-Hill, New York, 2001.
9. J. R. Brauer, *Magnetic Actuators and Sensors*, 2nd ed., John Wiley & Sons, IEEE Press, New Jersey, 2014.
10. J. C. Mallinson, *Magneto-Resistive and Spin Valve Heads, Fundamentals and Applications*, 2nd ed., Academic Press, New York, 2001.
11. R. J. M Konings and O. Beneš, “The Thermodynamic Properties of the f-Elements and Their Compounds. I. The Lanthanide and Actinide Metals”, *Journal of Physical and Chemical Reference Data*, volume 39, number 4, 2010.
12. J. L. Marshall, “A Living Periodic Table”, *Journal of Chemical Education*, volume 77, number 8, 2000.
13. T. Lyman editor, *Metals Handbook*, 8th ed., Vol. 1, “Properties and Selection of Metals”, ASM, 1961.
14. W. Chubberly, Director of Reference Publications, *Metals Handbook*, 9th ed., Volume 3, “Properties and Selection: Stainless Steels, Tool Materials and Special Purpose Metals”, ASM, 1980.
15. US Steel, “Section III Carbon and High Strength Steels, Datasheets for Core Loss, AC Magnetization, DC Magnetization”, Pittsburgh, PA, 1966.
16. G. Engdahl, *Handbook of Giant Magnetostrictive Materials*, Academic Press, New York, 2000.
17. ANSI/NEMA MW 1000-2003, “Magnetic Wire”, Rev. 1, October 25, 2005, National Electrical Manufacturers Association.
18. J. P. Holman, *Heat Transfer*, 5th ed., McGraw-Hill, New York, 1981.

19. M. A. Juds, "A Nonlinear Magneto Dynamic Model for AC Magnets with Shading", *Proceedings of the International Relay Conference*, 1994.
20. L. H. Van Vlack, *Elements of Materials Science*, 2nd ed., Addison-Wesley, 1964.
21. R. Plonsey and R. E. Collin, *Principles and Applications of Electromagnetic Fields*, McGraw-Hill, 1961.
22. H. A. Wheeler, "Simple Inductance Formulas for Radio Coils", *Proceedings of the Institute of Radio Engineers*, vol. 16, no. 10, pp. 1398-1400, Oct. 1928.
23. H. A. Wheeler, "Inductance formulas for circular and square coils," *Proceedings of the IEEE*, vol. 70, no. 12, pp. 1449-1450, Dec. 1982.
24. F. W. Grover, *Inductance Calculations*, Dover Publications, New York, 1973.
25. W. H. Hayt, *Engineering Electromagnetics*, 5th ed., McGraw-Hill, New York, 1989.
26. H. O. Jimenez, "AC resistance evaluation of foil, round and Litz conductors in magnetic components", 2013, Master's Thesis, Chalmers University of Technology, Department of Energy and Environment, <https://hdl.handle.net/20.500.12380/175744>.
27. E. L. Barrios, A. Ursúa, L. Marroyo, and P. Sanchis, "Analytical Design Methodology for Litz-Wired High-Frequency Power Transformers", *IEEE Transactions on Industrial Electronics*, vol. 62, no. 4, pp. 2103-2113, April 2015.
28. M. A. Juds, Z. Xu, M. Rashidi, R. Gao, R. Beddingfield, R. Chattopadhyay, S. Bhattacharya, P. R. Ohodnicki Jr, and K. Byerly, "Leakage Flux Mitigation of Laminated Ribbon Core based Transformer for a Triple Active Bridge DC-DC Converter", Presentation FH-05, MMM-Intermag Joint Conference, Washington DC, January 14-18, 2019.
29. A. Greenwood, *Electrical Transients in Power Systems*, John Wiley & Sons, New York, 1971.
30. R. Beddingfield, "High Power Medium Frequency Magnetics for Power Electronics Applications," Ph.D. Dissertation, Dept. of Electrical and Computer Engineering, North Carolina State Univ., Raleigh, NC, 2018.
31. R. Holm, *Electric Contacts Theory and Application*, 4th ed., Springer-Verlag, New York, 1967, Reprinted 1981.
32. P. Slade, *Electrical Contacts Principles and Applications*, Marcel Dekker, Inc., New York, 1999.
33. S. K. Ran, "Gravity Probe B Examining Einstein's Spacetime with Gyroscopes, an Educator's Guide", NASA, p. 26, 2004.
34. M. S. Colclough, C. E. Gough, M. Keene, et al. "Radio-frequency SQUID operation using a ceramic high-temperature superconductor", *Nature* 328, 47–48, 1987. <https://doi.org/10.1038/328047a0>

35. L. P. Lee, K. Char, M. S. Colclough, and G. Zaharchuk, “Monolithic 77 K dc SQUID magnetometer”, *Applied Physics Letters* 59, 3051, 1991.
36. C. Peng, I. Husain, A. Q. Huang, B. Lequesne, and R. Briggs, “A Fast Mechanical Switch for Medium-Voltage Hybrid DC and AC Circuit Breakers”, *IEEE Transactions on Industry Applications*, vol. 52, no. 4, pp. 2911-2918, July-Aug, 2016.
37. K. Barmak and K. Coffey, *Metallic Films for Electronic, Optical and Magnetic Applications Structure, Processing and Properties*, Woodhead Publishing Limited, 2014.
38. W. Thomson, 1857 XIX, “On the electro-dynamic qualities of metals:— Effects of magnetization on the electric conductivity of nickel and of iron”, *Proceedings Royal Society London* 8: 546–550, <http://doi.org/10.1098/rspl.1856.0144>
39. S. A. Solin, “Magnetic Field Nanosensors”, *Scientific American*, Vol. 291, No. 1 (JULY 2004), pp. 70-77.
40. J. Wapakabulo and P. N. Murgatroyd, “Braid Rogowski coil,” *Electronics Letters*, vol. 35, no. 17, pp. 1445-1446, 19 Aug. 1999.
41. B. Roodenburg and B. H. Evenblij, “Design of a fast linear drive for (hybrid) circuit breakers – Development and validation of a multi domain simulation environment,” *Mechatronics*, Volume 18, Issue 3, 2008, Pages 159-171, ISSN 0957-4158.
42. V. Puumala and L. Kettunen, “Electromagnetic Design of Ultrafast Electromechanical Switches,” *IEEE Transactions on Power Delivery*, vol. 30, no. 3, pp. 1104-1109, June 2015, DOI: 10.1109/TPWRD.2014.2362996.
43. C. Peng, A. Huang, I. Husain, B. Lequesne and R. Briggs, “Drive circuits for ultra-fast and reliable actuation of Thomson coil actuators used in hybrid AC and DC circuit breakers,” *2016 IEEE Applied Power Electronics Conference and Exposition (APEC)*, Long Beach, CA, 2016, pp. 2927-2934, DOI: 10.1109/APEC.2016.7468279.
44. N. Aronhime, V. Degeorge, V. Keylin, P. R. Ohodnicki, and M. McHenry, “The Effects of Strain-Annealing on Tuning Permeability and Lowering Losses in Fe-Ni-Based Metal Amorphous Nanocomposites,” *JOM the journal of the Minerals, Metals & Materials Society*, Vol. 69, July 2017. DOI: 10.1007/s11837-017-2480-x.
45. K. Byerly, P. R. Ohodnicki, S. R. Moon, A. M. Leary, V. Keylin, M. E. McHenry, S. Simizu, R. Beddingfield, Y. Yu, G. Feichter, R. Noebe, R. Bowman, and S. Bhattacharya, “Metal Amorphous Nanocomposite (MANC) Alloy Cores with Spatially Tuned Permeability for Advanced Power Magnetics Applications”, *JOM*, Vol. 70, pp. 879–891, 2018. <https://doi.org/10.1007/s11837-018-2857-5>

Index

- 1st quadrant, 68
2nd quadrant, 68
3rd quadrant, 68
acceleration, 101, 129
Acceleration, 129, 218, 241
actuator, 9, 29, 42, 50, 78, 105, 128, 129, 130, 133, 137, 211, 227, 231
actuator technologies, 50
air core coil, 70, 189, 190, 196, 214
air gap, 8, 24, 25, 29, 35, 36, 37, 38, 39, 41, 42, 51, 54, 55, 56, 68, 73, 74, 84, 85, 86, 116, 117, 118, 119, 120, 125, 126, 128, 130, 133, 140, 141, 189, 203, 204, 205, 222, 231
air-core coil, 9, 189, 191, 197
amorphous, 179, 237
ampere-turns, 14, 16, 29, 37, 42, 83, 85, 91, 93, 97, 98, 118, 121, 123, 126, 143, 148, 154, 161, 162, 185
Ansys-Maxwell, 189, 191, 197
antiferromagnetic, 58
armature, 15, 29, 35, 36, 38, 39, 40, 41, 42, 115, 116, 117, 118, 119, 121, 125, 126, 128, 129, 130, 133
Arrhenius Equation, 108
atomic spacing, 8, 58, 62
atoms, 57, 58, 59
Back EMF, 15, 130, 133
Bethe-Slater curve, 58, 59
BH curve, 8, 79, 122, 143, 183, 188
B-H curve, 16
B-H curve, 17
B-H curve, 21
B-H curve, 22
Biot-Savart law, 9, 195, 196, 197, 200, 202
Biot-Savart Law, 196
capacitance, 24, 31, 32, 36, 212, 223, 227
Capacitance, 24, 31, 36, 133, 223, 227, 258
capacitor, 133, 134, 135, 211, 212, 224
Capacitor, 133, 223, 227
circuit breaker, 201, 208
circuit breakers, 7, 9, 201, 270
Co-energy, 35
coercivity, 8, 59, 60, 63, 67, 75, 77, 81, 82, 83, 85, 151, 183, 232, 234
Coercivity, 60, 67
compass, 11, 195, 236
Conductance, 14, 18, 259
conductive plate, 9, 211, 213, 214, 216, 222, 223, 224, 227, 228
conductivity, 29, 77, 78, 89, 91, 97, 101, 105, 209, 263
constriction force, 208
contact spot, 208, 209, 239
contacts, 9, 137, 201, 204, 208, 209, 210
copper area ratio, 94
core loss, 8, 76, 77, 78, 79, 80, 140, 143, 147, 159, 160, 161, 163, 166, 183, 184, 185, 186, 252, 253, 254
Core Loss, 77, 80, 159, 160, 249, 261
core-type
Transformer, 155, 156, 157, 158, 159, 160, 163, 166, 187
critical damping, 220
critically damped, 220, 221
crystal structure, 8, 57, 59, 60
cup-cone pole, 125
curie point, 62
Curie Point, 61
Curie Temperature, 61
current, 8, 9, 11, 12, 14, 15, 16, 17, 18, 20, 23, 29, 31, 33, 43, 56, 63, 76, 77, 78, 81, 82, 83, 91, 93, 98, 102, 106, 128, 130, 133, 137, 138, 140, 142, 143, 147, 148, 149, 150, 151, 153, 154, 160, 161, 162, 163, 164, 165, 183, 184, 185, 186, 187, 189, 195, 196, 197, 198, 199, 200, 201, 202, 203, 204, 205, 207, 208, 209, 210, 211, 213, 214,

215, 216, 222, 224, 228, 231, 232, 234, 235, 236, 237, 238, 239
current loop, 81, 82, 130, 133, 195, 196, 198, 199, 200, 208, 216
current transformer, 231
Current Transformer, 149, 150, 151
damping ratio, 220
demagnetization, 60, 68, 74, 84, 87
depth of penetration, 78
Depth of Penetration, 78
diamagnetic, 57
dielectric constant, 24, 31
domain boundaries, 59
domain wall, 59
domain walls, 58, 59, 237
domains, 58
drive coil, 140, 141, 142, 143, 144, 184, 185, 186, 187, 235, 236
drive current, 186
eddy current, 76, 77, 131, 165, 211, 213, 216, 217, 218, 222, 224, 226, 228
Eddy Current Core Loss, 76
eddy currents, 8, 9, 75, 76, 78, 92, 164, 183, 185, 202, 211
Eddy currents, 130, 133
Electric Field Energy, 36
Electric Field Force, 36
electromechanical energy, 8, 35, 36
electron orbit, 57
electron spin, 57, 58, 69, 238
Electrostatic Force, 38
energy balance, 59, 107, 224
Energy balance, 36
energy product, 71, 72, 82
Energy Product, 67, 71
Exchange Force, 58
exponential solution, 219
Faraday's law, 92, 145, 165, 167, 233
Faraday's Law, 15, 258
FEA, 55, 123, 183, 189, 190, 191, 197, 212, 213, 227, 229
ferromagnetic, 57, 58, 61, 238, 239
Field Intensity, 17, 20, 258, 259
finite element, 7, 8, 23, 51, 122, 123, 157, 270
Finite element, 8, 55
flux, 7, 8, 11, 12, 14, 15, 16, 17, 20, 22, 23, 24, 25, 26, 27, 28, 29, 31, 38, 40, 43, 51, 54, 55, 61, 62, 63, 64, 69, 70, 72, 74, 75, 78, 79, 81, 85, 87, 91, 92, 93, 116, 117, 118, 119, 120, 121, 122, 123, 125, 126, 128, 137, 141, 145, 147, 149, 150, 151, 153, 154, 155, 156, 157, 159, 160, 161, 162, 163, 164, 165, 166, 183, 184, 185, 186, 187, 188, 189, 195, 196, 197, 198, 199, 200, 202, 203, 204, 205, 207, 210, 213, 214, 215, 216, 222, 233, 234, 235, 236, 238, 247, 260
Flux Density, 16, 17, 20, 21, 22, 33, 52, 53, 60, 67, 159, 160, 197, 242, 258
flux leakage, 51, 55, 147, 153
flux lines, 11, 12, 23, 158
flux linkage, 15, 17, 197
Flux linkage, 15
Flux Linkage, 14, 15, 258
flux path, 9, 11, 12, 24, 25, 26, 27, 28, 29, 31, 85, 116, 117, 118, 120, 121, 125, 141, 147, 153, 157, 161, 162, 164, 184, 189, 202, 214, 215, 216, 222
flux paths, 7, 11, 23, 24, 25, 26, 27, 28, 29, 85, 116, 117, 125, 141, 155, 156, 157, 163, 164, 203, 213, 214
flux plot, 23
Fluxgate, 235
force, 8, 9, 29, 35, 36, 37, 38, 39, 40, 41, 42, 43, 53, 54, 55, 58, 78, 91, 92, 115, 118, 119, 121, 122, 123, 125, 126, 128, 129, 130, 133, 137, 140, 145, 195, 196, 198, 199, 200, 201, 202, 203, 204, 205, 206, 207, 208, 209, 210, 211, 222, 223, 224, 226, 227, 228, 229, 231, 234
force balance, 129, 218
forced convection, 102
free body diagram, 129
free convection, 101, 102
free-body diagram, 129

frequency, 75, 77, 78, 79, 80, 92, 144, 151, 161, 163, 165, 167, 232, 234, 237, 262
 Frequency, 18, 244, 262
 fringing, 24, 26, 37, 38, 40, 41, 54, 55, 116, 118, 120
 fringing flux paths, 24
 Frog Levitation, 260
 Full-wave rectification, 137
 fusing time, 105, 106, 110
 Fusing Time, 105
 giant magnetoresistance, 238
 grain boundaries, 59
 grains, 58
 Grashof number, 101
 Half-wave rectification, 137
 Hall effect, 234
 Hall voltage, 234
 Hall Voltage, 234
 Hard magnetic materials, 57, 67
 hardness, 57, 64, 209
 Hardness, 57, 209, 244
 heat, 7, 57, 60, 91, 92, 93, 101, 102, 103, 105, 107, 109, 111, 145, 164, 270
 heat dissipation, 91, 92, 93, 101, 102, 103, 105, 106, 109, 145, 164
 heat transfer coefficient, 101, 102, 111
 hysteresis, 8, 59, 60, 67, 68, 75, 77, 79, 161, 163, 183, 184, 186
 Hysteresis Core Loss, 75
 hysteresis loop, 59, 60, 67, 75, 79, 161, 163, 183, 184, 186
 Hysteresis Loop Area, 60
 hysteresis loop energy, 60
 imaginary
 Permeability, 79, 80, 253
 Imaginary
 Permeability, 79, 80
 impedance, 31, 79, 92, 93, 102, 138, 148, 231, 237
 inductance, 9, 15, 17, 18, 31, 32, 35, 54, 55, 79, 93, 130, 133, 158, 159, 160, 189, 190, 191, 197, 214, 216, 230, 231, 232
 Inductance, 14, 15, 17, 18, 31, 33, 35, 52, 79, 93, 95, 96, 130, 133, 148, 153, 159, 160, 189, 197, 214, 223, 228, 242, 258, 262
 Inductor, 149, 150, 189, 231
 inertia, 129
 initial permeability, 60
 Insulation Life, 108
 integration drift, 161, 162, 186
 intrinsic
 Magnetic Flux, 69, 70, 81
 Intrinsic
 Magnetic Flux, 67
 Iteration, 20, 118, 143
 leakage, 8, 29, 55, 85, 116, 141, 147, 153, 155, 156, 157, 158, 159, 160, 163, 164, 165, 166, 167, 214, 215, 216
 Leakage, 29, 116, 141, 147, 149, 153, 155, 159, 160, 166, 215, 216, 223, 228, 262
 leakage flux, 29, 116, 147, 153, 155, 156, 157, 158, 159, 160, 163, 164, 165, 166, 167, 214, 215, 216
 leakage flux paths, 29, 156, 157, 164
 leakage inductance, 158
 leakage permeance, 159, 215, 216
 load line, 71, 72, 73, 74, 87
 loop equation, 148, 154
 loop equations, 142, 149, 153, 154, 216, 217, 225
 Lorentz force, 8, 43, 195, 196, 199, 202, 204, 206, 208
 Lorentz Force, 43
 Loss Angle, 80
 loss due to leakage, 160, 163, 165, 166
 loss tangent, 79, 80
 Loss Tangent, 79, 80
 losses, 8, 57, 63, 67, 143, 163, 183, 202
 Losses, 75, 78, 92
 LVDT, 231
 Magnetic Co-Energy, 35
 magnetic dipole moment, 81
 magnetic energy, 35, 59
 magnetic field, 7, 8, 9, 12, 14, 16, 17, 20, 24, 35, 36, 37, 41, 43, 57, 59, 67, 71, 76, 161, 162, 184, 187, 195, 196, 198, 199, 200, 202, 204, 211, 213, 231, 232, 234, 235, 236, 237, 238, 239, 260

magnetic field energy, 8, 35, 36, 37, 41, 43
Magnetic Field Energy, 35
magnetic field intensity, 16, 17, 20, 71, 161, 162, 184, 187, 202, 204, 236
Magnetic Field Intensity, 16, 242
magnetic flux, 7, 8, 9, 11, 12, 14, 15, 16, 17, 19, 20, 21, 23, 24, 29, 31, 36, 37, 40, 41, 42, 54, 56, 61, 62, 69, 70, 71, 72, 74, 75, 76, 78, 79, 85, 92, 93, 96, 116, 118, 119, 121, 122, 128, 131, 133, 137, 140, 142, 144, 145, 147, 148, 151, 153, 154, 156, 158, 161, 162, 167, 183, 184, 185, 186, 187, 189, 190, 195, 196, 197, 198, 199, 200, 201, 202, 203, 204, 205, 206, 207, 210, 213, 214, 222, 233, 234, 235, 236
Magnetic Flux, 11, 14, 16, 18, 19, 20, 21, 33, 67, 86, 233, 242
Magnetic Force, 35, 218
magnetic moment, 9, 81, 82, 83, 195, 196, 198, 199, 200
magnetic polarization, 81
magnetic pole, 12, 83
magnetization, 16, 17, 35, 58, 59, 60, 64, 65, 67, 68, 72, 81, 145, 247, 263
magnetization curve, 16, 17, 35, 72, 145
Magnetizing Force, 14, 20, 21, 22, 242
Magneto-Elastic, 59
magnetoimpedance, 237
Magneto-Mechanical, 59
magnetoresistance, 238, 239
magnetostriiction, 58
Magnetostriction, 59
Major Hysteresis Loop, 60
MANC, 179, 263
mass, 76, 79, 105, 110, 129, 158, 218, 219, 223, 227
mean turn length, 90, 91, 97, 109
mechanical dynamics, 129, 270
mechanical energy, 8, 35, 36, 50
Mechanical Energy, 35, 50
mechanical force, 36, 131, 134
Mechanical Force, 35, 36
Mechanical Position, 35
mechanical strain, 8, 58, 59, 60, 185
minor hysteresis loop, 60, 68, 75
motion, 59, 128, 137, 213, 216, 217, 218, 219, 225, 226, 231
moveable conductor, 201, 202, 203, 204, 206, 210
moveable core, 231
MS-Excel, 186, 197
mutual inductance, 191, 211, 218, 223
nanocomposite, 179
natural convection, 101, 102
natural frequency, 220, 221
normal curve, 70
normal magnetic flux, 70
north, 81
North, 11, 12, 165, 227, 262
NORTH, 12
nuclear spin, 57
Nusselt number, 101
Ohm's Law, 14, 259
operating point, 68, 71, 72, 73, 74, 81, 85, 86, 87, 119
overdamped, 220, 221
paramagnetic, 57
parasitic
 Inductance and Capacitance, 32, 230
Parasitic
 Inductance and Capacitance, 31
parasitic resistance, 217, 223, 227, 229, 230
permanent magnet, 7, 8, 9, 12, 29, 59, 67, 68, 69, 70, 71, 72, 73, 74, 81, 82, 83, 84, 85, 87, 195, 196, 199, 233, 238
permeability, 8, 17, 18, 24, 29, 31, 35, 56, 57, 58, 60, 64, 67, 71, 78, 79, 80, 81, 83, 117, 147, 159, 160, 161, 163, 183, 185, 187, 204, 232, 237, 247, 253
Permeability, 16, 17, 20, 56, 71, 79, 80, 159, 241, 242, 258
Permeability of Free Space, 16, 241
permeance, 7, 11, 14, 17, 24, 25, 26, 27, 28, 29, 31, 37, 39, 40, 41, 43, 51, 55, 71, 73, 83, 85,

- 93, 117, 118, 119, 120, 157,
 158, 159, 214, 215, 226, 231
 Permeance, 11, 14, 17, 18, 19, 24,
 33, 51, 52, 55, 85, 93, 120, 121,
 159, 213, 215, 258
 permittivity, 24, 31
 phasor solution, 143, 145, 148,
 154
 pinned domain, 59
 pole shaping, 128
 Pole shaping, 42, 128
 Pole Shaping, 115, 125
 power loss, 75, 76, 77, 79, 143,
 161, 163, 184
 power output, 8, 149, 150, 151
 primary coil, 147, 151, 156, 157,
 158, 165, 211, 213, 214, 215,
 217, 222, 223, 224, 227, 231
 primary winding, 147, 153, 158,
 159
 proximity effect, 78, 92, 103, 158
 radiation, 101, 102
 real permeability, 79
 Recoil
 Permeability, 67, 71, 84
 recoil line, 68, 72, 73, 74, 82, 85,
 87
 Rectification, 137
 rectifier, 137, 138
 relative permeability, 20, 56, 64,
 117, 159, 161, 163, 186, 187,
 188, 203, 206, 247
 relative permittivity, 24
 reluctance, 7, 8, 14, 17, 29, 36, 37,
 38, 41, 43, 54, 83, 85, 86, 116,
 117, 119, 120, 122, 123, 125,
 126, 140, 141, 142, 155, 205,
 206, 231
 Reluctance, 14, 17, 18, 33, 51, 52,
 85, 86, 116, 120, 148, 153, 217,
 231, 233, 258
 reluctance force, 8, 36, 43
 reluctance network, 117, 119, 140,
 141, 142, 205, 206
 repulsion, 9, 202, 208, 209, 211,
 222, 224, 227
 Residual
 Flux Density, 60, 67
 resistance, 14, 19, 20, 76, 79, 89,
 91, 92, 93, 98, 102, 103, 104,
 106, 130, 142, 143, 145, 147,
 148, 149, 150, 151, 153, 158,
 165, 184, 185, 187, 209, 213,
 217, 219, 231, 232, 238, 239,
 262
 Resistance, 14, 18, 19, 95, 96, 98,
 109, 130, 133, 223, 227, 228,
 244, 259
 resistivity, 63
 reverse loop, 201, 202, 206, 207,
 208, 209
 right-hand rule, 81
 Right-Hand Rule, 43
 RIGHT-HAND RULE, 11
 ring sample, 185
 ripple current, 138
 RLC system, 219, 222, 226, 229
 Rogowski coil, 151, 231, 232, 233,
 263
 Rogowski Coil, 149, 151, 231
 Runge-Kutta, 143, 145
 saturate, 18, 33, 41, 51, 52, 151,
 189, 207, 210, 235
 saturating, 19, 35, 79, 118, 121,
 122, 148, 154
 saturation, 8, 16, 20, 21, 22, 38,
 53, 56, 61, 62, 63, 64, 65, 72,
 92, 117, 118, 121, 122, 123,
 126, 140, 145, 147, 149, 151,
 166, 183, 185, 186, 188, 202,
 205, 232, 235, 236, 239, 247
 Saturation, 16, 33, 42, 60, 64, 121,
 205, 247
 search coil, 231, 233
 secondary coil, 29, 147, 148, 149,
 150, 151, 153, 156, 157, 160,
 162, 165, 231, 233
 secondary winding, 147, 149, 153,
 158, 232
 sense coil, 184, 185, 186, 187,
 235, 236
 sense voltage, 186
 sensors, 7, 8, 9, 231, 237, 238,
 239, 270
 shaded pole, 141, 147
 shading, 8, 137, 140, 141, 142,
 143, 145, 147
 shading ring, 141, 142, 143, 145,
 147
 shading rings, 140, 143
 Shading rings, 140
 sheet current, 195, 196

shell-type
Transformer, 155, 156, 157, 158, 159, 160, 165, 166
skin depth, 78, 237
Skin Depth, 78
skin effect, 8, 78, 92, 103, 104, 107, 158, 237
Skin Effect, 75, 78
skin thickness, 76
slot motor, 9, 201, 202, 203, 204, 205, 206, 207, 208, 210
smoke time, 105, 109, 110, 112
Smoke Time, 105, 110
Soft magnetic materials, 57, 59
South, 12
SOUTH, 12
spin valve, 238
spintronics, 238
Spreadsheet, 20
spring force, 115, 129, 137, 140, 209
SQUID, 235, 260, 262, 263
stationary conductor, 201, 202, 204, 210
steady-state temperature, 102, 103, 104, 109, 110, 111
stray
 Inductance and Capacitance, 31
switchgear, 201
tapered pole, 125, 128
temperature coefficient of resistance, 102, 103
Temperature coefficients, 69
temperature rise, 8, 91, 102, 103, 104, 105, 109, 110, 111, 164, 166, 218, 224
temperature sensitivity, 68, 234, 235
thermal time-constant, 110, 111
Thomson coil, 9, 212, 214, 216, 223, 224, 227
Thomson Coil, 211
time constant, 107, 225
Time Step, 20
torque, 29, 195, 198, 199
trade-offs, 9, 95, 96
transformer, 8, 29, 60, 75, 147, 148, 149, 153, 154, 155, 157, 158, 159, 160, 163, 165, 166, 183, 186, 187, 231, 232
transient Finite Element Analysis, 227
underdamped, 220, 221
unshaded pole, 141, 145
velocity, 15, 129, 130, 133, 216, 218, 224, 226, 228
Visual Basic macro, 197
voltage, 14, 15, 16, 18, 19, 20, 22, 76, 91, 92, 97, 102, 106, 107, 109, 130, 131, 132, 133, 137, 138, 142, 144, 145, 147, 148, 149, 150, 151, 154, 158, 160, 161, 162, 163, 165, 184, 185, 186, 187, 209, 212, 223, 227, 231, 232, 233, 234, 236, 237, 238
Wiegand wire, 233, 234
winding density, 90, 97
wire diameter, 89, 90, 91, 92, 93, 94, 97, 109, 189, 217, 257
wire gage, 89, 95, 96, 97
Wire insulation, 89
wire size, 91, 92, 97, 166

About the Author



Mark A. Juds

Mark is an electro-mechanical engineer with product experience in sensors, actuators, circuit breakers, contactors, mechanisms, hydraulic valve actuators, bimetal actuators, transformers, inductors, electronic packaging (cooling, vibration, shock), finite element magnetics and programming (Visual Basic, Fortran). He has experience working in both the manufacturing and research environments. His strengths include electromagnetics, mechanical dynamics, heat transfer, project management, team leading, mentoring, teaching, and the ability to apply physics to a wide range of engineering problems.

Mark holds an MSME degree in heat transfer and fluid dynamics from the University of Wisconsin-Milwaukee, and a BSME degree from the University of Wisconsin-Madison with specialties in dynamic systems, kinematics, strain energy, and numerical optimization. During the past 37 years at Eaton Research Labs, he focused on designing magnetic and electromechanical devices, where he was granted 123 US and foreign patents. He also has 49 publications with 16 journal papers, 1 book chapter, and 1 book appendix, and has given 63 invited presentations.

Mark's awards include:

- 1999: UWM Mechanical Engineering Department – Alumni Award for Outstanding Achievement
- 2006: Eaton Electrical Group – Community Service Award
- 2010: Engineers & Scientists of Milwaukee – Engineer of the Year
- 2013: UWM CEAS – Meritorious Service Alumnus Award

Mark has been involved as a leader in the following organizations.

- 2003 – 2018: Chair of IEEE Magnetics Chapter for the Milwaukee Section
- 2004 – 2009: Chair of UWM ME Department Industrial Advisory Council
- 2007: Chair of Purdue University CTRC Industrial Advisory Board
- 2009 – Present: Member of Board of Directors for the Kids from Wisconsin

Mark has taught courses in kinematics at MSOE and heat transfer, shock, and vibration in electronic systems at UWM. He also participates in many volunteer activities directed toward mentoring and encouraging students in the areas of science, technology, engineering, and math.

More Praise for the Book

(Continued from the back cover)

I had the privilege to work alongside Mark for a number of years. He was known far and wide as “Mr. Magnetics” for everyone at Eaton, providing his expertise for solving many challenging magnetic and electromagnetic problems. Yet at the same time, he was always approachable and became a mentor for many engineers, showing them the ropes and patiently initiating them to the intricacies of complex electromagnetic systems. It is a rare blessing for future generations that he decided to combine his technical talent and teaching acumen, and put his years of experience down in a comprehensive, yet concise treatise of the subject. His book, “Practical Magnetic and Electromechanical Design”, is bound to be on many a shelf in engineering offices, the kind of monograph with yellowed and dog-eared pages (or nowadays, electronic versions of these hallowed notations found on classic engineering monographs). His approach, based on spreadsheets, provides a welcome combination between the relative simplicity of algebraic formulae and the power of computers. Eventually, any engineer, electrical or mechanical, can develop similar spreadsheets to get a quick grasp of the physics for his or her problem. This is a great complement to the powerful and generally accurate finite element method, which however too often ends up being used like a magical black box with results that are difficult to interpret.

Dr. Bruno Lequesne, PhD, Consultant.

- Research Engineer, GM, Delphi, Eaton (retired)
 - Recipient of the 2016 IEEE Tesla Award
-

I enjoyed every moment of reading and reviewing Mark's book. Every single section is of great value to engineers and practitioners. The really innovative approach that has been brought to the subject is the fine balance between the theory and practice. The book is a masterpiece that contains multiple examples from practice that cannot be found anywhere else in literature. I would expect that Mark's book should become part of the regular curriculum for all Engineering schools across the country. In my opinion, Mark's book should be the reference book in electromagnetics for each and every electrical engineer. Thank you Mark for all this great work.

Dr. Armen Baronian, PhD

- Chief Engineer at Eaton Research Labs
 - Professor of Electrical Engineering at McMaster University
-

Mark Juds' knowledge and experience in the area of **Practical Magnetic and Electromechanical Design** are unmatched. His book shows that accurate magnetic models can be developed from simple flux path geometries for wide-ranging applications. This is a must-read book for those involved in magnetics.

Robert T. Balmer, PE, ScD

- Mechanical Engineering Professor Emeritus, University of Wisconsin-Milwaukee
 - Dean Emeritus, Engineering and Computer Science, Union College, Schenectady NY
-

I have had the privilege of working with Mark Juds on several projects in areas of direct relevance to this book during his time with Eaton. We collaborated together on the design and fabrication of advanced high frequency multi-winding transformers for solar and energy storage grid integration as well as medium voltage filter inductors for large-scale industrial motor drives. I am always impressed with his ability to think pragmatically about electromagnetic components and to distill complex technical and engineering problems to their essence. He also takes a very methodical and stepwise approach to building up complicated designs from their most fundamental elements, only increasing complexity as needed to solve an engineering objective. Our collaborations have had a significant impact on the way that I visualize and approach electromagnetic component designs and I have incorporated this line of thinking into the classes that I have taught over the years on directly related topics. I see this book as a major contribution to the field of magnetics and power electronics as it seeks to share that same approach and perspective with the broader community. For practicing engineers in power electronics and power conversion, this book is definitely a worthwhile and recommended addition to your list of references. And for faculty teaching in related fields, I strongly recommend a detailed review to consider incorporation of the content within your own courses.

Dr. Paul R. Ohodnicki, Jr.

- Associate Professor, Mechanical Engineering & Materials Science
 - Director, Engineering Science Program
-

Mark's book, "Practical Magnetic and Electromechanical Design", provides excellent guidance. I was hired by Eaton Research Labs for high-frequency magnetic design seven months before Mark's retirement. I had the privilege to ask any questions, not only because Mark sat in front of my cubicle, but also Mark is happy to share everything he knows. Whenever I asked a magnetic question, the first question Mark asked me was "If you were a flux line, where would you go?" Then he would pick up a marker pen and went to a whiteboard, and drew the flux lines to teach me how to decouple my question into small pieces that have physical meanings and can be solved by a spreadsheet. As an engineer being good at finite element analysis (FEA) tools, my default setting for analyzing the flux path was simulating with FEA tools first, then optimizing the design based on the FEA results. One may lose his direction with so many FEA results. It's more important to understand the physical meaning before optimizing a design. I was also impressed that Mark never went to a book to search for any equations. Everything is well-organized in his mind. Without a doubt, the results calculated by a spreadsheet are very close to the FEA results and experimental test results. Mark's book, "Practical Magnetic and Electromechanical Design", provides excellent guidance with examples about "If I were a flux line, where would I go?". This book will be the one steering my career shelf. It is the most important of the books that will provide guidance and reference for my work and career.

Dr. Guangqi Zhu, PhD

- Lead Engineer, Eaton Research Labs
 - IEEE Magnetics Chair, Milwaukee Section
-

This work, as always with Mark, is rooted in the fundamentals of physics. Each section is lucid and allows further directed research, if necessary. The book proceeds from the fundamentals and generally as one would learn "magnetics". Uniquely, this book presents the process of the art of magnetic design. It judges what is important and what is not within a particular application type; what materials might be used, how, and with what tradeoffs. Whether the young engineer just beginning practice in magnetic design or the older but less experienced engineer this book should be the second on the bookshelf, right next to a good basic text in physics. This book is loaded with practical, necessary, information not usually presented nor, in some cases, easily found.

Buy two! The first will become ragged much too quickly.

Kurt von Eckroth

- Chief Engineer - Owner of Into 3D
 - WCTC Electrical Engineering Professor
 - Eaton Division Engineering Manager (CTRS)
-

Mark was a mentor who taught me how to look at magnetics from a practical perspective. However, his insights never lack theoretical groundings. In fact, using the approach Mark introduced me to, I can always find my way back to the basic magnetic principles where Maxwell's equations rule. Yet his approach makes magnetics so much easier to understand, and so much more efficient to apply in practical applications. I cannot count how many times I had the eureka moment on a specific magnetics phenomenon, or a particular form of governing equation after a coffee talk with Mark. The way he combines magnetic fields with circuit (permeance) representations makes magnetics equally approachable to electrical engineers who are used to circuit analysis of discrete elements as it is to mechanical engineers who are accustomed to field analysis. Till this day, I still find myself going back to a booklet Mark wrote on magnetics either when trying to understand a problem I encountered in my daily work, or when trying to expand my knowledge of a subtopic for a new project. And I am glad that Mark decided to expand that booklet to the book you are reading now. This book has that same approach to magnetics as Mark has taught me, only in a more concise and systematic way. I hope you find this book useful to you as it has been, and will still be, useful to me.

Dr. Zelin Xu, PhD

- Electromagnetics Engineer at Apple Inc.
-

This book is an invaluable reference tool for every engineer working with magnetic materials and devices. The author's four decades of electro-mechanical and magnetic design experience span a large breadth of product areas including appliance, automotive, aerospace, industrial controls, and electrical protection. His comprehensive understanding of fundamental engineering principles allow this author to present this material in a concise manner that makes it easy to understand for engineers of all disciplines.

Todd King

- Managing Director of Engineering for Power Electronic Products at American Superconductor Corp. – Retired
-

Mark Juds provides over 40 years of practical experience in regards to magnetic applications in one easy to read book. I was fortunate to have the pleasure of working with Mark early in my magnetics career - I know how patient, thorough, remarkable, talented, and unique he is. This book should be a recommended read for both the new engineer fresh out of college as well as the seasoned engineer. As an educational tool in magnetics, it provides an easy to understand explanation and visualization of the invisible, yet powerful world of magnetic flux lines that one can otherwise envision only with aid of iron filings or FEA software.

Mary Jo Vander Heiden

- Staff Engineer: Generac Power Systems
-